HAL
open science

High-pressure and high-temperature synthesis of light perovskite hydrides for hydrogen storage

Julius Andrew Nunez

To cite this version:

Julius Andrew Nunez. High-pressure and high-temperature synthesis of light perovskite hydrides for hydrogen storage. Material chemistry. Université Grenoble Alpes [2020-..], 2022. English. NNT : 2022GRALI026 . tel-03777276

HAL Id: tel-03777276

https://theses.hal.science/tel-03777276v1

Submitted on 14 Sep 2022

HAL is a multi-disciplinary open access archive for the deposit and dissemination of scientific research documents, whether they are published or not. The documents may come from teaching and research institutions in France or abroad, or from public or private research centers.

L'archive ouverte pluridisciplinaire **HAL**, est destinée au dépôt et à la diffusion de documents scientifiques de niveau recherche, publiés ou non, émanant des établissements d'enseignement et de recherche français ou étrangers, des laboratoires publics ou privés.

THÈSE

Pour obtenir le grade de

DOCTEUR DE L'UNIVERSITÉ GRENOBLE ALPES

Spécialité : 2MGE : Matériaux, Mécanique, Génie civil, Electrochimie

Arrêté du 25 mai 2016

Présentée par

Julius Andrew NUÑEZ

Thèse dirigée par **Laetitia LAVERSENNE**

et co-encadrée par **Céline GOUJON**

préparée au sein de l'**Institut Néel, CNRS**

dans **l'École Doctorale I-MEP2 - Ingénierie - Matériaux, Mécanique, Environnement, Energétique, Procédés, Production**

Synthèse haute pression et haute température d'hydrures à structure pérovskite à base d'éléments légers pour le stockage d'hydrogène

High-pressure and high-temperature synthesis of light perovskite hydrides for hydrogen storage

Date de soutenance: 29 mars 2022

devant le jury composé de :

Madame Christelle GOUTAUDIER
Professeure, LMI Villeurbane,
Présidente du jury
Madame Céline DARIE
Professeure, Institut Néel, Grenoble, Examinatrice
Monsieur Julien HAINES
Directeur de recherche, ICGM, Montpellier, Rapporteur
Monsieur Stefan KLOTZ
Directeur de recherche, IMPMC, Paris, Rapporteur
Madame Céline GOUJON
Ingénieure de recherche, Institut Néel, Grenoble
Co-encadrante, Invitée
Madame Laetitia LAVERSENNE
Chargée de recherche, Institut Néel, Grenoble
Directrice de thèse

Acknowledgements

It has been a wild 3.5 years of thesis – experimentation, writing, failing, isolating, travelling, and everything in between.

I would like to thank first my thesis directresses, Dr. Laetitia Laversenne and Dr. Céline Goujon for accepting me as their PhD student. I may be a student coming from a different background (Biochemistry), but they were so patient in teaching me the concepts. They made themselves available when I needed them. I am grateful.

I would like to thank the members of my jury for being present during my thesis defense, Madame Christelle Goutaudier, Madame Céline Darie, Monsieur Julien Haines, and Monsieur Stefan Klotz.

I would also like to acknowledge the members of my Comité de Suivi Individuel: Sophie Rivoirard and Michel Boudard, for guiding me during my four CSI's.

I would like to thank also the organizations involved in my PhD scholarship – the reason why I am in France. I would like to thank the Commission on Higher Education of the Philippines and Campus France of France for giving me the CHED-PhilFrance scholarship. I would like to also thank the University of the Philippines Manila for allowing me to have a study leave from the University. To everyone who helped me with my scholarship documents: Madame Emmanuelle Berretta of Campus France Lyon, Ms. Cara of Campus France Manille, Tope Kliatcho of CHED Philippines, and ate She and tita A of DPSM, UP Manila, thank you very much.

To my family, you are my inspiration. To July, thank you for loving me. You are always patient with me. Thank you for all the calls and for listening to my rants. I always enjoy your company and definitely our travels together. Thank you for coming to Europe twice. It really helped me to remain sane. To my mom and my brothers, thank you for always checking if I am OK. We will see each other soon. To my aunts, uncles, and cousins, thank you for the support and prayers.

Thanks also to everyone in Institut Néel who helped me perform my thesis. To Murielle Legendre, thank you for being so efficient with my experiment requests. To Olivier Leynaud, thank you for teaching me XRD. I learned a lot from you. Thank you to Sebastien Paris and Stephanie Kodjikian for helping me learn SEM and TEM. Thanks to Rémy, Alain, and Christophe for helping me whenever I have troubles with the machines. Thank you Paul Chometon for being patient with me during DSC-TGA measurements. Thank you Emmanuel Verloop for helping me with the autoclave. Thanks to Claire Colin, Pierre Toulemonde, and Salvatore Miraglia for helping me with the HP experiments. Thank you Laurent Joubert for fixing my computer. Thanks Muriel Boyer for helping me with all my documents.

To my friendships2017 of DPSM UP Manila, super thanks. To Hermie, you are one of the most honest, real, and intelligent person I know. Thank you for all the chats and gossips. They really made me laugh. To team Europe, Joanne and Arlou, our Malta trip was amazing. Thank you for being as adventurous as I am. Thanks for checking if I am doing OK. To Kevin, thank you for always being so kind. You are the kindest person I know. I appreciate it. To team

USA, Jireh and Dem, thanks for being available during our calls no matter how early it is in your timezones. Thanks Ji and Dem for the support during chats. Our online “you know” will always be remembered.

To my UPM DPSM colleagues, thank you for all the help whenever I needed them. Thank you Ciara, Astrid, Fatsy, MJ, sir Voltz for answering all my uestions whenever I receive some emails from UPM. You acted like my extended office in DPSM. Thank you for your support.

To my high school friends, Bing and Ling, you’re there for me all throughout since the beginning. I love you both. Thank you for staying. We may not be talking that often anymore but I am sure that we will still love each other no matter what.

To my travel buddies: Rob, Jethro, Arianne, Teki, Marisse, sir Ian, thank you for being there when I wanted to discover the world. Rob, you are the best travel buddy ever. You are so organized and efficient. You are truly a citizen of the world. Thanks for being encouraging and for being patient with me. To sir Jethro, thank you for guiding me here in France. Our Greece trip will always be remembered. It was an adventure. To Arianne, I loved our BeNeLux trip. Thanks for booking Morocco and I am sorry if it ended in a different way. Teki, thanks for the good company in Avignon and Malta. Marisse and Ian, thank you for being good hosts in Sweden. Our Hungary trip was also amazing.

To ate Ems, thank you. I wouldn’t be in France if it wasn’t for you.

To Ivy, Olivier, and Joelle, thank you for being my second home in France. Thank you for the hospitality.

To my labmates in Institut Néel, thank you for keeping me sane. To Vartika, you are my best friend in the lab. We share secrets and I like that. Thank you for always checking if I am OK. To Mads and Kylia, thanks for being there when I have questions. To my gymmates, Bruno and Javier, thanks for motivating me and everyone in the group. To the rest of Légers des PLUM, thank you for the good company during lunch.

To my Latina friends, Andrea and Valentina, our Italy trip was super fun. Thanks for being patient with my Spanish. I appreciate your effort.

To the Filipino students in France, my co-CHED-PhilFrance scholars, Lhordz, Cheryl, Reynand, Alfie, Rhea, thank you for all the helpful chats whenever CHED gets so confusing. Thanks for the company. To Keith and Philip, thank you for showing me Paris. To the Filipino students in Lyon, Aileen, Irina, Justin, Rick, Rommel, Rey, Jocelyn, and Keith, thank you for being my 2nd home in Lyon.

To the Filipino students in Grenoble, thank you for being my constant homesickness reliever. Thank you Lara, Dylan, Gerone, and Cil. You guys are my closest friends here. Thank you for all the trips, food trips, picnics, and board games. To the young masters students I met, Ysabella, Trish, Alfonso, JM, Patrick, Emille, Marielle, Deonne, Rey, Roanne, Jerry, Linnaeus, Criz, and Jerwin, although our interactions were short, I appreciate the small chats and food trips we had. We should go skiing again. Thank you for being my family here.

To my ski buddies, Guillaume, Nathan, Raphael, thanks for the help and the friendship. Thanks for being patient with my French.

To all my Facebook and Instagram followers, thank you for your attention and curiosity. I appreciate all the messages.

And lastly, thank you to all the Filipino taxpayers. You contributed to my education in France. You are part of it. My success is also your success. I will not let you down.

Résumé

L'hydrogène est devenu un important vecteur d'énergie alors que le monde poursuit sa transition vers les énergies renouvelables. Le mode de stockage de l'hydrogène a fortement évolué, passant de l'utilisation de réservoirs de gaz au début du 20ème siècle à l'utilisation de matériaux de stockage de l'hydrogène au 21e siècle. Les hydrures à structure pérovskite basés sur des éléments légers sont des matériaux prometteurs pour le stockage de l'hydrogène en raison de leur capacité gravimétrique élevée en hydrogène. Parmi ceux-ci, les pérovskites à base de magnésium, tels que $NaMgH_3$, ont fait l'objet de nombreuses recherches. Cependant, la mauvaise cinétique de désorption de l'hydrogène et la température opérationnelle élevée restent un défi pour son utilisation pratique.

L'ambition de cette thèse était d'étudier la possibilité de modifier les propriétés structurales et fonctionnelles induites par l'utilisation de hautes pressions sur des hydrures légers cristallisant dans la structure pérovskite. Dans cette étude, la synthèse de plusieurs hydrures à structure pérovskite à base de magnésium, comme $NaMgH_3$, et $KMgH_3$ a été réalisée en utilisant une technique à haute pression et à haute température. L'analyse de la diffraction des rayons X in situ a révélé certaines informations sur la transformation de phase qui se produit avec les précurseurs d'hydrure binaire, ainsi que sur le mécanisme de synthèse dans des conditions extrêmes. Les études de diffraction des neutrons sur poudre à haute pression réalisées à l'Institut Laue-Langevin ont permis la détermination de propriétés mécaniques (module d'incompressibilité) de $NaMgH_3$ et $KMgH_3$.

La substitution de cations sur le site A de la pérovskite a également été effectuée sur $NaMgH_3$ pour diminuer sa température de désorption de l'hydrogène. $NaMgH_3$ substitué par du lithium ($Na_{1-x}Li_xMgH_3$) a été synthétisé à haute pression. L'analyse par calorimétrie différentielle à balayage a confirmé la réversibilité de la désorption d'hydrogène desdits matériaux.

Au cours de ce travail de thèse, nous avons également tenté de synthétiser, sans succès, les composés $LiMgH_3$ et $NaCaH_3$ pourtant prédits comme stables par des études reposant sur des calculs théoriques.

Dans l'ensemble, l'étude de ces pérovskites à base de magnésium ouvre la voie vers l'ingénierie des hydrures avec des propriétés de sorption d'hydrogène adaptées au stockage solide.

Introduction

Il est à la fois facile et difficile d'imaginer un monde dont l'empreinte carbone serait nulle. Avec toutes les nouvelles technologies actuelles dans le secteur des énergies renouvelables, il est facile de penser que toutes les technologies basées sur les combustibles fossiles peuvent être supprimées instantanément et que le monde devient alors meilleur. Mais cela est plus facile à dire qu'à faire. Les défis politiques et économiques jouent également un rôle dans la réalisation d'une société à empreinte carbone nulle. La lumière au bout du tunnel est encore loin, disent-ils, car seuls les pays développés sont capables de faire passer la majorité de leurs sources d'énergie de non renouvelables à renouvelables. Sur une note positive, grâce à l'avancement de la recherche et du développement (R&D) dans le domaine des énergies renouvelables, la technologie finira par atteindre les économies à faible revenu, car les scientifiques s'efforcent de trouver des solutions plus faciles à gérer, moins chères, plus sûres et plus efficaces. C'est la vue d'ensemble...

Pour examiner la situation dans son ensemble, il faut se pencher sur les différentes technologies actuellement disponibles. Les lycéens diront peut-être que les sources d'énergie renouvelables se résument aux centrales solaires, aux centrales hydroélectriques et aux parcs éoliens. Ils sont loin de se douter que la société se dirige lentement vers un avenir où l'hydrogène est un carburant propre.

Le contexte théorique de cette thèse présente l'hydrogène comme un vecteur énergétique pouvant être utilisé pour le transport et l'alimentation à la demande. Étant l'élément le plus léger et le plus abondant qui soit, l'hydrogène a joué un rôle important en tant que vecteur énergétique. Cependant, pour les applications stationnaires et mobiles, l'hydrogène doit être stocké. Pendant la majeure partie du début et du milieu du 20e siècle, l'hydrogène a été stocké dans de grands réservoirs de gaz cylindriques à haute pression. Ce n'est toutefois pas la façon la plus efficace de procéder. Aujourd'hui, l'objectif est de disposer d'un matériau capable de contenir autant d'hydrogène que possible, de fonctionner dans des conditions aussi réduites que possible et de durer longtemps. Dans cette étude, les matériaux appelés hydrures de pérovskite, considérés comme l'une des perspectives de stockage de l'hydrogène à l'état solide, sont présentés et discutés. Ces matériaux existent depuis la fin du 20e siècle et la recherche d'amélioration de leurs performances et de leur efficacité est toujours en cours.

Les hydrures de pérovskite fabriqués à partir de métaux légers semblent prometteurs pour le stockage de l'hydrogène à l'état solide car ces matériaux sont légers et ont une capacité

gravimétrique élevée, ce qui signifie qu'ils peuvent contenir de grandes quantités d'hydrogène par unité de masse du matériau. Ces bonnes caractéristiques ont permis l'essor de la recherche pour synthétiser des hydrures de pérovskite présentant de bonnes performances de stockage de l'hydrogène. Parmi les différentes méthodes de synthèse, les techniques haute pression-haute température permettent d'explorer le comportement des matériaux solides dans des conditions extrêmes. Ainsi, certaines plages de pression et de température peuvent être exploitées pour comprendre le comportement et les caractéristiques de certaines phases métastables, qui ont la possibilité de se transformer en un état plus stable si le processus avait été réalisé dans des conditions ambiantes. De plus, travailler à des pressions extrêmes nous permet d'étudier certains changements structurels dans le solide. Ainsi, nous pouvons comprendre comment les arrangements atomiques peuvent affecter les produits de synthèse.

Ceci étant dit, l'objectif général de cette thèse est de synthétiser des hydrures de pérovskite ($NaMgH_3$, $Na_{1-x}Li_xMgH_3$, $KMgH_3$) en utilisant des techniques de haute pression et de haute température et de relier certaines de leurs propriétés mécaniques et thermiques à leurs performances de stockage d'hydrogène.

Les techniques expérimentales

Les synthèses et les caractérisations ont été réalisées à l'aide de presses à grand volume. Nous mentionnons ici des presses grand volume utilisées dans l'étude qui sont disponibles à l'Institut Néel : la presse CONAC, et la presse belt. Une autre presse utilisée était la presse Paris-Edinburgh (PEP). La PEP a été adaptée aux expériences de XRD qui utilisent des faisceaux de rayons X intenses provenant de sources de lumière synchrotron, ainsi qu'aux expériences de diffraction des neutrons sur poudre (NPD). Les avantages de ce type d'expériences sont les suivants : petits volumes d'échantillons, ce qui permet de réaliser des expériences à des pressions encore plus élevées, et diminution significative des temps d'acquisition.

Toutes les synthèses ont été réalisées en utilisant des précurseurs d'hydrure binaire. Les poudres d'hydrure métallique (NaH, MgH_2, LiH, KH, CaH_2) ont été achetées chez Sigma-Aldrich. Toutes les procédures impliquant ces hydrures ont été réalisées sous atmosphère Ar à l'intérieur d'une boîte à gants maintenue à <1,0 ppm de O_2 et de H_2O. Les autres poudres utilisées étaient BN (Aldrich), Cu (Prolabo), MgO (Alfa Aesar), et NaCl commercial (La Baleine). Pour toutes les préparations d'échantillons impliquant ces poudres, après avoir été

pesées, elles ont été broyées pendant quelques minutes à l'aide d'un mortier et d'un pilon pour obtenir un mélange homogène.

L'analyse par diffraction des rayons X des matériaux sensibles à l'air a été réalisée en transmission à l'aide d'un diffractomètre à rayons X Siemens D5000T. Les échantillons ont été placés dans des tubes capillaires scellés en verre borosilicate d'un diamètre de 0,5 mm ou 0,7 mm, et analysés dans une configuration de capillaire rotatif. Les analyses de données ont été effectuées en utilisant le logiciel DIFFRAC EVA et l'analyse de Rietveld en utilisant la suite FullProf.

Les expériences de diffraction des neutrons sur poudre ont été réalisées au diffractomètre à deux axes D1B de l'Institut Laue-Langevin (ILL), Grenoble, France. Les diagrammes NPD ont été collectés à 27°C (300 K) avec une longueur d'onde de 2.52 Å. Le diffractomètre sur poudre à deux axes D1B à haute intensité de l'ILL couvre une plage angulaire de 0,8° à 128,8° avec un détecteur sensible à la position (PSD) $^{3}He/CF_4$ à haute efficacité. Les mesures sur les hydrures réactifs ont été rendues possibles par un montage spécifique développé par S. Klotz (IMPMC) avec l'aide de C. Payre (ILL). La pastille échantillon, d'une épaisseur de 3,7 mm pour le $NaMgD_3$ et de 3,25 mm pour le $KMgD_3$, a été placée dans un joint en TiZr et a été placée entre des enclumes en diamant fritté. Auparavant, les échantillons originaux, $NaMgH_3$ et $KMgH_3$, ont été deutérés dans un autoclave. Les mesures à la ligne de faisceau ont été effectuées à différentes pressions (0-10,7 GPa pour $NaMgD_3$ et 11,63 GPa pour $KMgD_3$). Les données ont été recueillies pendant environ 2 heures pour les basses pressions et jusqu'à 6 heures pour les hautes pressions (>6 GPa). La détermination de la pression a été effectuée en ajustant le paramètre de réseau de NaCl, utilisé ici comme milieu de transmission de pression et calibrant interne, avec l'équation d'état de Brown. Un affinement de Rietveld utilisant FullProf a été effectué sur les diagrammes de diffraction des neutrons et les paramètres de maille de $NaMgD_3$ et $KMgD_3$ à différentes pressions ont été déterminés. Les données des paramètres de maile ont été utilisées à l'aide de l'équation de Birch-Murnaghan du troisième ordre en utilisant le logiciel EoSFit7-GUI pour calculer le module de compressibilité.

L'étude des propriétés thermiques a été réalisée à l'aide d'un calorimètre Nietzsch DSC 3500 Sirius. Les échantillons ont été chauffés jusqu'à 585°C en utilisant différentes vitesses de chauffage : 5, 10, et 20 K/min sous un flux continu d'azote de 20 mL/min. Les échantillons ont été scellés dans un creuset hexagonal en acier CrNi (AlSl 316L) avec couvercle, appelé "creuset haute pression" et résistant à une pression allant jusqu'à 100 bars. Un disque de scellement en or, qui contient également 26% Ag et 15,5% Cu, a été placé entre le creuset et le couvercle. Un creuset vide a été utilisé comme référence.

Synthèse et caractérisation d'hydrures de pérovskite

Cette partie a démontré les différentes expériences de synthèse réalisées pour synthétiser $NaMgH_3$, $NaMgH_3$ substitué par Li, et $KMgH_3$. Les produits synthétisés par l'autoclave, la presse belt, la presse CONAC et la PEP ont été présentés.

Une caractérisation structurelle du $NaMgH_3$ dans des conditions ambiantes, telle que la XRD et la NPD, a également été réalisée. Les résultats de ces dernières confirment que le $NaMgH_3$ produit dans les expériences ne diffère pas de ce qui a été obtenu dans les expériences publiées. La synthèse de $NaMgH_3$ avec analyse XRD in-situ a également été réalisée en utilisant la PEP à 2, 4 et 7,4 GPa.

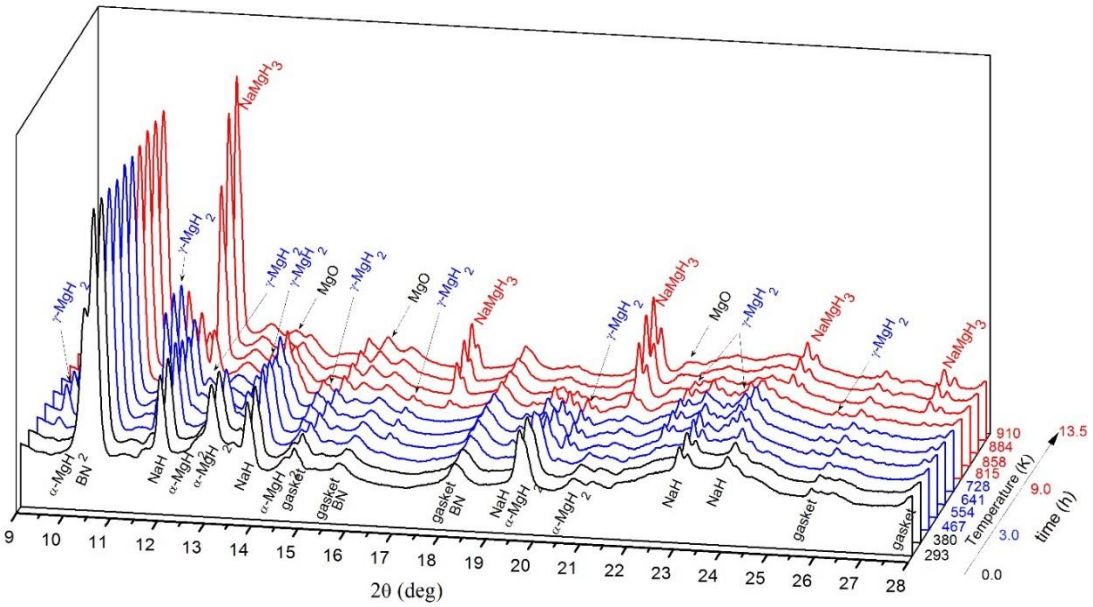

Figure A. Diagrammes XRD recueillis sur la presse Paris-Edinburgh pendant la synthèse de $NaMgH_3$ à ~4GPa à partir d'un mélange de NaH et MgH_2. Les motifs en bleu montrent l'apparence du γ-MgH_2 tandis que les motifs en rouge montrent l'apparence de la pérovskite $NaMgH_3$.

Il est intéressant de noter la transformation de phase de MgH_2 à HP-HT concomitante à la synthèse de $NaMgH_3$. On a émis l'hypothèse que la phase γ de MgH_2 joue un rôle dans la formation de $NaMgH_3$ à partir de NaH et MgH_2 (Figure A et B).

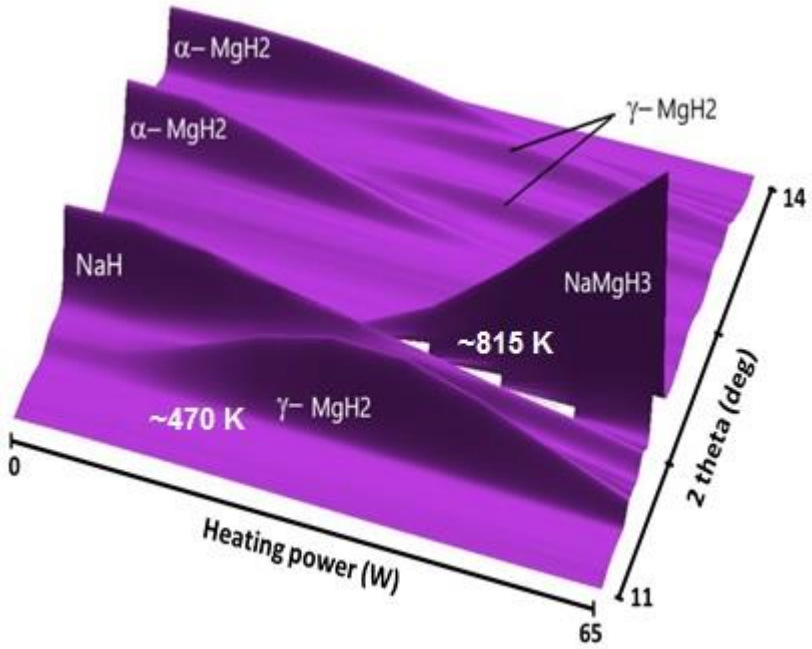

Figure B. Évolution des pics XRD pour $NaMgH_3$ et ses précurseurs en fonction de l'augmentation de la puissance de chauffe à 4 GPa. Les températures de transition ont été obtenues à partir des courbes d'étalonnage du chapitre II.

L'analyse des diffractogrammes du composé $Na_{1-x}Li_xMgH_3$ a montré que les pics associés à la pérovskite se déplacent vers des valeurs 2 thêta plus élevées (Figure C).. Ceci a validé la substitution de Na par Li dans le site A de la structure ABH_3. Le déplacement vers des valeurs 2 thêta plus élevées est attribué à la plus petite taille du Li qui a créé un volume de cellule unitaire contracté. L'analyse de Rietveld a révélé que la substitution maximale de Li effectuée était de 20%.

L'optimisation de la synthèse du $KMgH_3$ a également été réalisée. Ceci a été fait pour minimiser la production d'un produit secondaire, le K_2MgH_4. Les paramètres de maille de $KMgH_3$ obtenue concordent bien avec les valeurs de la littérature.

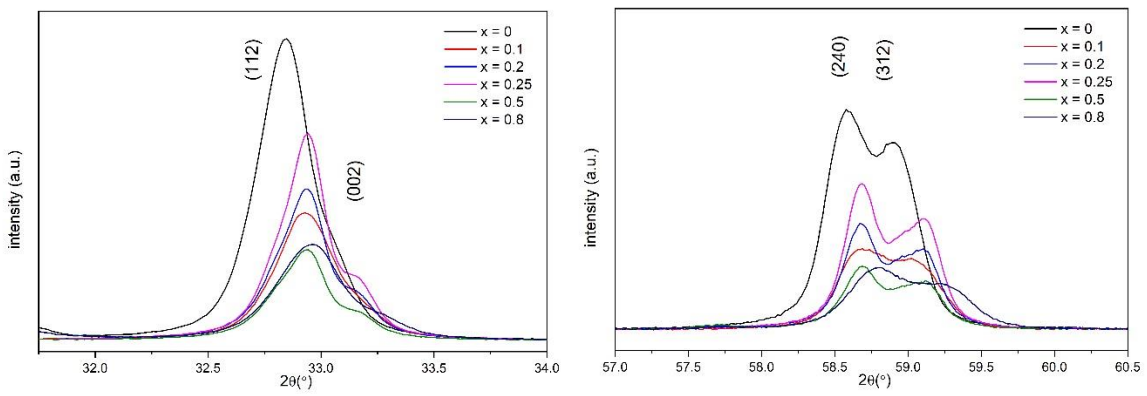

Figure C. Vue rapprochée des pics XRD (112), (002), (240), et (312) associés à $Na_{1-x}Li_xMgH_3$ montrant le décalage vers des valeurs 2 thêta plus grandes.

Étude des changements structurels induits par la haute pression dans les hydrures à structure pérovskite

La diffraction in-situ de neutrons sur poudres à haute pression a permis de déterminer le module de compressibilité du $NaMgD_3$ et du $KMgD_3$. Cette partie nous a également permis d'avancer dans la compréhension des arrangements atomiques, des paramètres de maille, des longueurs de liaison et des angles de liaison impliqués dans la structure pérovskite du $NaMgH_3$ et du $KMgH_3$.

Les études NPD à haute pression ont également montré que $NaMgD_3$ et $KMgD_3$ ne subissaient aucune transition de phase dans la gamme de pression étudiée (jusqu'à 10.7 GPa pour $NaMgD_3$ et 11.6 GPa pour $KMgD_3$). $KMgD_3$ conserve sa structure pérovskite cubique idéale (compression isotrope) alors que $NaMgD_3$ présente des distorsions sous haute pression, sans tendance de tilts de l'octaèdre de MgD_6.

La détermination expérimentale des modules de compressibilité de ces deux composés est une première (Tableau A et B). Ces valeurs expérimentales pourront être utiles pour de futures études liées à d'autres propriétés mécaniques telles que les modules d'Young et de cisaillement, ainsi que d'importantes propriétés thermodynamiques comme Température de Debye, chaleur spécifique, point de fusion, etc.

Tableau A. Module de compressibilité (B_0) et sa dérivée sous pression (B_0') pour $NaMgD_3$.

	Cette étude	Théorie
B_0	43.9(1.3) GPa	38.4 GPa [49], 35.95 GPa [70], 35.9 GPa [209]
B_0'	3.4(3)	3.6 [49]

Tableau B. Module de compressibilité (B_0) et sa dérivée sous pression (B_0') pour $KMgD_3$.

	Cette étude	Théorie
B_0	39.0(7) GPa	34.60-40.84 GPa [53] 35.6 GPa [49] 35.1008 GPa [101]
B_0'	3.5(2)	3.61-3.62 [53] 3.7 [49] 3.57 [101]

Propriétés thermiques des hydrures à structure pérovskite

Le coefficient d'expansion thermique volumique à 300 K de $NaMgH_3$ est rapporté pour la première fois. Le calcul des énergies d'activation du processus de désorption pour le $NaMgH_3$ et le $Na_{1-x}Li_xMgH_3$ n'a pas été possible du fait que la pression d'hydrogène dans le creuset du dispositif de DSC-HP n'était pas maîtrisée (pression autogène). La réversibilité du stockage de l'hydrogène pour ces deux échantillons a également été présentée.

D'autre part, on a constaté que le $KMgH_3$ a une réaction de décomposition en deux étapes. Le mécanisme suggéré est similaire à celui du $NaMgH_3$. De même, le processus de désorption de l'hydrogène du KMg_H3 s'est avéré réversible comme le montrent les données DSC (Figure D) et XRD, avec cependant l'existence d'une réaction secondaire (formation de K_2MgH_4).

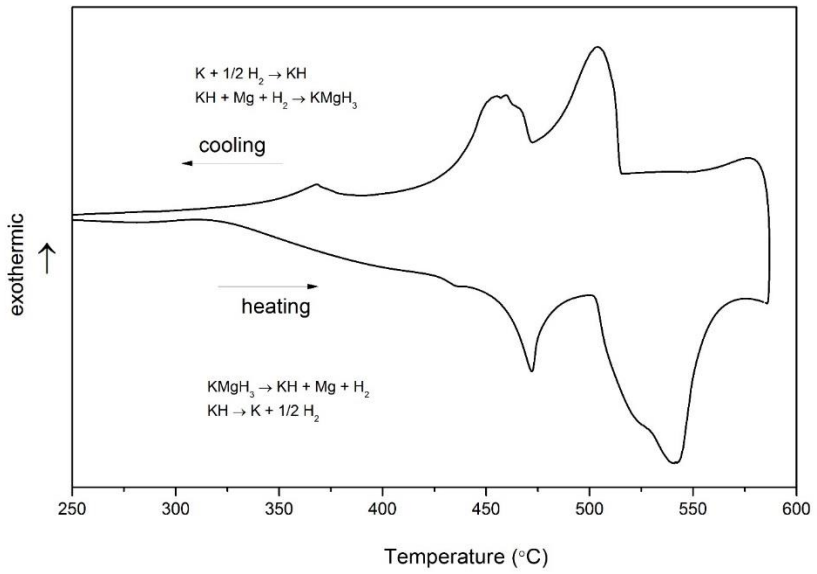

Figure D. Courbe DSC du $KMgH_3$ pendant le chauffage jusqu'à 585°C et le refroidissement jusqu'à la température ambiante.

Conclusion générale et perspectives

Cette recherche de trois ans et demi a été menée pour comprendre le processus de synthèse des hydrures pérovskites, leurs propriétés et leur comportement dans des conditions extrêmes de pression et de température. La possibilité de synthétiser de nouveaux matériaux a également été explorée. Le chapitre I a fourni l'historique et le contexte nécessaires à la nécessité de synthétiser de nouveaux matériaux pour le stockage de l'hydrogène. Les matériaux actuels de stockage de l'hydrogène étant confrontés à certains problèmes concernant leur cinétique et leur thermodynamique, il est toujours nécessaire de modifier certains aspects afin d'obtenir les propriétés idéales envisagées pour un matériau de stockage de l'hydrogène parfait.

Les différentes méthodologies expérimentales présentées dans le chapitre II ont permis d'explorer la synthèse et la caractérisation des hydrures de pérovskite de métal léger pour le stockage de l'hydrogène. Des presses à grand volume ont été utilisées pour permettre la synthèse à des pressions et des températures extrêmes. Des études de diffraction des rayons X et des neutrons sur poudre ont permis d'analyser la structure cristalline des produits. Les propriétés thermiques ont également été étudiées afin d'explorer l'effet de certaines modifications de la structure sur les propriétés de stockage de l'hydrogène des hydrures.

Le chapitre III a présenté et discuté la synthèse et la caractérisation de trois hydrures pérovskites : $NaMgH_3$, $Na_{1-x}Li_xMgH_3$ et $KMgH_3$. Il a été démontré que ces matériaux peuvent

être synthétisés en utilisant l'autoclave, et des presses à grand volume telles que la presse CONAC, et la presse belt. L'analyse de DRX *in-situ* à l'aide de la presse Paris-Edinburgh a permis de comprendre la voie de synthèse du $NaMgH_3$. A 2 GPa (450-780 K) et 4 GPa (460-730 K), il a été observé qu'une transition de phase de MgH_2 de sa phase α à sa phase γ s'est produite avant sa réaction avec NaH pour former la pérovskite $NaMgH_3$. À une pression plus élevée de 7,4 GPa, la pérovskite $NaMgH_3$ n'a pas été synthétisée jusqu'à 650 K. Au lieu de cela, il a été observé qu'une transformation de phase de la phase γ à la phase β de MgH_2 s'est produite. Il a été proposé que γ-MgH_2 soit impliqué dans la réaction avec NaH. La substitution de Na par Li dans $NaMgH_3$ a également été étudiée. La synthèse de $Na_{1-x}Li_xMgH_3$ avec différentes valeurs de x a été réalisée. Les données de DRX ont montré que tous les $NaMgH_3$ substitués par Li avaient des volumes de cellules unitaires plus petits que le $NaMgH_3$ pur en raison de la taille plus petite de l'atome de Li, comme le montre le déplacement des pics DRX vers des valeurs 2 thêta plus élevées. L'affinement de Rietveld des données DRX a montré que la substitution maximale de Li qui peut être faite est de 20%. Il est envisagé de déterminer l'étendue de la substitution de Li à HP-HT en utilisant la DRX *in situ*. De même, il serait intéressant de poursuivre l'analyse du $Na_{1-x}Li_xMgH_3$ en faisant des expériences sur ses propriétés de sorption de l'hydrogène. De même, la production d'un échantillon pur reste un défi qui devra être résolu dans le futur. D'autre part, la dernière partie du chapitre a présenté l'hydrure à structure perovskite cubique, $KMgH_3$. Les conditions de synthèse ont été optimisées afin de ne pas produire un produit secondaire, le K_2MgH_4.

Une propriété mécanique, le module de compressibilité, a fait l'objet du chapitre IV. L'étude de la diffraction des neutrons sur poudre à haute pression a été réalisée sur la ligne D1B de l'Institut Laue-Langevin. L'utilisation d'un instrument à grande échelle a fourni les informations nécessaires pour étudier soigneusement la structure des échantillons d'hydrure à structure pérovskite. Une étude de toute transformation de phase induite par la pression dans le $NaMgH_3$ a été menée. Les résultats obtenus ici ont révélé qu'aucune transformation de phase n'a été observée pour $NaMgH_3$ jusqu'à 10,7 GPa à température ambiante. L'échantillon ne peut pas être indexé dans le groupe spatial *Cmcm* ni dans le groupe spatial $Pm\bar{3}m$. Avec ces données NPD, d'autre part, le module de compressibilité expérimental et sa dérivée sous pression du $NaMgD_3$ ont été obtenus pour la première fois. Le module de compressibilité obtenu est de 43,9(1,3) GPa et sa dérivée sous pression est de 3,4(3). De même, les études de transformation de phase induite par la pression en utilisant la NPD ont révélé qu'aucune transformation de phase ne s'est produite pour le $KMgD_3$ jusqu'à 11,6 GPa. D'après les données NPD, le module de compressibilité expérimental du $KMgD_3$ est de 39,0(7) GPa et la dérivée de pression obtenue

est de 3,5(2). C'est également la première fois qu'un module de compressibilité expérimental pour ce matériau a été rapporté. Ces valeurs seront bientôt publiées dans un article de revue scientifique. Il est envisagé que des études de transformation de phase induite par la pression avec une plus grande gamme de pression et de température soient réalisées pour tous les échantillons présentés.

Dans le chapitre V, les propriétés thermiques des hydrures de pérovskite ont été étudiées par calorimétrie différentielle à balayage (DSC). En raison des incertitudes sur la pression d'H_2, les énergies d'activation des deux étapes de décomposition n'ont pas été calculées. Les résultats de la DSC ont également révélé une décomposition en deux étapes pour $KMgH_3$, similaire à celle de $NaMgH_3$. Tous les échantillons, $NaMgH_3$, $Na_{1-x}Li_xMgH_3$, et $KMgH_3$, ont montré une réversibilité dans la déshydruration, comme le révèlent les résultats de la DSC et de la DRX. La réversibilité observée pour le $KMgH_3$ contredit les données publiées précédemment et peut donc être un bon signe pour susciter de nouvelles recherches sur le $KMgH_3$ pour le stockage de l'hydrogène. En outre, une autre étude de diffraction des neutrons à basse température a permis de déterminer le coefficient volumique d'expansion thermique à 300 K pour la première fois pour $NaMgH_3$.

Dans l'ensemble, ce manuscrit a présenté plusieurs hydrures de métaux légers qui ont été synthétisés dans des conditions extrêmes de pression-température. La méthode de synthèse de nouveaux matériaux à l'aide de l'autoclave, de la presse belt, de la presse CONAC et de la presse Paris-Edinburgh est en effet prometteuse pour la découverte de nouveaux matériaux. Plusieurs tentatives de synthèse de nouveaux matériaux sont présentées en annexe. A la suite de ce travail, il serait intéressant d'essayer d'autres combinaisons de cations pour les sites A et B de la pérovskite. Il serait également intéressant d'étudier le comportement de $NaMgH_3$ et $KMgH_3$ à haute pression et à haute température en utilisant des grands instruments.

Afin d'explorer la possibilité de synthétiser de nouveaux matériaux pour le stockage de l'hydrogène, l'approche de synthèse à haute pression et haute température utilisée dans cette thèse semble très encourageante.

Table of contents

Acknowledgements i
Introduction vi
Les techniques expérimentales vii
Synthèse et caractérisation d'hydrures de pérovskite ix
Étude des changements structurels induits par la haute pression dans les hydrures à structure pérovskite xi
Propriétés thermiques des hydrures à structure pérovskite xii
..... xiii
Conclusion générale et perspectives xiii
Introduction 2
Chapter I. Literature Review 5
I.1. Context 5
I.1.a. The Energy Problem 5
I.1.b. Hydrogen as energy store 7
I.1.c. Hydrogen storage 8
I.2. Perovskite hydrides as hydrogen storage materials 14
I.2.a. Overview of the perovskite structure 14
I.2.b. Perovskite hydrides 16
I.2.c. $NaMgH_3$ 20
I.2.d. Li-substituted $NaMgH_3$ 27
I.2.e. $KMgH_3$ 31
I.3. Binary hydride precursors 34
I.3.a. Magnesium hydride, MgH_2 35
I.3.b. Hydrides of Li, Na, and K 38
I.3.c. Calcium hydride, CaH_2 39
I.4. High-pressure and high-temperature (HP-HT) synthesis of perovskite hydrides 40
I.4.a. Generalities about HP HT 40
I.4.b. The perovskite structure under HP-HT 42
1.4.c. Synthesis of hydrides using HP-HT 44
Chapter Summary 45
Chapter II. Experimental techniques 47
II.1. Materials preparation 47
II.2. Synthesis using HP-HT 47

II.2.a. The CONAC press 47
II.2.b. The Belt press 49
II.3. The autoclave 50
II.4. X-ray diffraction analysis 51
II.4.a. Experimental set up 51
II.4.b. Phase identification and Rietveld refinement 51
II.5. Paris-Edinburgh Press for in situ X-ray diffraction 54
II.5.a. Pressure calibration data for the Paris-Edinburgh Press 59
II.5.b. Temperature calibration data for the Paris-Edinburgh Press 60
II.6. Paris-Edinburgh Press for in situ Neutron powder diffraction 62
II.7. Determination of Thermal Properties 64
II.7.a. Differential Scanning Calorimetry 64
Chapter Summary 64
Chapter III. Synthesis and characterization of perovskite hydrides 65
III. 1. $NaMgH_3$ 65
III.1.a. Preliminary experiments with an autoclave 65
III.1.b. Preliminary experiments with the CONAC Press 66
III.1.c. Structural characterization 66
III.1.d. In-situ study of the synthesis of $NaMgH_3$ under HP-HT 69
III.2. Li-substituted $NaMgH_3$ 74
III.2.a. Synthesis in CONAC press 74
III.3. $KMgH_3$ 79
III.3.a. Synthesis 79
III.3.b Synthesis using an autoclave 79
III.3.c. Synthesis using a large volume press 80
Chapter Summary 83
Chapter IV. Investigation of high-pressure-induced structural changes in perovskite hydrides 85
IV.1. $NaMgH_3$ 85
IV.2. $KMgH_3$ 91
Chapter Summary 95
Chapter V. Thermal properties of perovskite hydrides 97
V.1. Volume thermal expansion coefficient of $NaMgD_3$ at low temperature 97
V.2. Differential Scanning Calorimetry studies 100
V.3. Reversibility of hydrogen storage 103

Chapter Summary 108
General conclusion and perspectives 109
APPENDIX 113
Appendix A. Synthesis and characterization of $LiMgH_3$ 113
Background 113
Experimental 116
Appendix B. Synthesis and characterization of $NaCaH_3$ 120
Background 120
Experimental 122
Appendix C. Synthesis and characterization of $K_{1-x}Li_xMgH_3$ 125
Appendix D. Oral presentations 127
References: 129

List of Figures

- Figure 1. Comparison of volumetric capacities of physical hydrogen storage and materials-based storage [12]. 8
- Figure 2. Kinetic and thermodynamic barriers that need to be overcome to improve a metal hydride's performance as discussed by Wang et al [18]. 11
- Figure 3. Process of hydrogen absorption into the metal crystal to form the metal hydride. .. 11
- Figure 4. Structure of a perovskite showing the BX_6 octahedron and AX_{12} cubo-octahedron. 15
- Figure 5. Estimated formation region of perovskite-type hydrides by Ikeda [48]. 16
- Figure 6. Unit cell of $NaMgH_3$. Blue spheres represent H. [74] 21
- Figure 7. Schematic of the tilting of the MgH_6 octahedron and the plane defined by the triangle of 2 Na and 1 Mg for the movement of H to the adjacent side [41]. 21
- Figure 8. Pressure-composition isotherm (PCI) of $NaMgH_3$ at 400°C (673 K). Point S corresponds to $NaMgH_3$. Point M corresponds to the first dissociation, and point F corresponds to just Na and Mg. Dashed lines are plateau pressures of MgH_2 and NaH at 400°C (673 K) [81]. 23
- Figure 9. Energy values for the different phases of $Na_{1-x}Li_xMgH_3$ as a function of Li concentration [94]. 29
- Figure 10. XRD patterns of $NaMgH_3$ (Li-substituted with x = 0.2) during rehydrogenation up to 350°C from Contreras-Vasquez et al [51]. 30
- Figure 11. Three different phases of $KMgH_3$ named a)Stable, b) US1, and c)US2 in the study of Reshak et al [101]. 33
- Figure 12. Phase transformations of MgH_2 at room temperature based on theoretical (5-8, Ref.[127][143][140][142]) and experimental (1-4, Ref. [128][129][139][130]) data. 36
- Figure 13. Pressure-Temperature phase diagram of the different phases of MgH_2 at high temperature from experimental data [147][144][146][145], including this study. DFT data from Moser et. al [142] are shown in pink. Squares mean either alpha or gamma or both. Yellow circles mean beta. 38
- Figure 14. Schematic representation of the sample in the DAC being compressed by two opposing diamonds (in light blue). 42
- Figure 15. Octahedral tilting (left) and bond length contraction (right) experienced by the BX_6 octahedra in perovskite during compression [173]. 43
- Figure 16. Sample assembly shows the powder sample enclosed in a gold capsule (bottom photo) which is sandwiched between two WC plates (top photo). 48

- Figure 17. The WC plates of the CONAC press (right) is shown where the assembly previously described is placed in the center for high-pressure experiments. 49
- Figure 18. Assembly of the belt press (schematic and actual). 50
- Figure 19. The autoclave used at Institut Néel. 50
- Figure 20. Calculated profiles shown as solid lines and experimental profiles shown as circles for (a) a good fit (b) a peak that has a larger 2θ (c) a peak that has a smaller 2θ (d) a peak with a larger FWHM (e) a peak with a smaller FWHM (f) a calculated intensity that is too high, and (g) a calculated intensity that is too low. 52
- Figure 21. The rotating capillary configuration of the Siemens D5000 diffractometer. An eyepiece is attached to center the capillary prior to measurement. 54
- Figure 22. Cross section of the high-pressure anvils from Besson et al [194]. Shown are the (1) WC anvils (2) sample space (3) toroidal gasket (4) pyrophyllite gaskets and (5) steel rings. 55
- Figure 23. Cross section of the 250 ton press from Besson et al [194]. Shown are the principal parts (1) anvil and sample assembly, (3) main piston, (8) one of four columns, and (6) hydraulic ram. 55
- Figure 24. A VX5 type Paris-Edinburgh Press used at Institut Néel. 56
- Figure 25. The different components in the assembly shown as arranged (left photo) and how they look like using a coin as a scale (middle photo) and clamped anvils with the sample in the middle (right photo) 58
- Figure 26. The Paris-Edinburgh press used for in-situ XRD under high-pressure and high temperature. The two WC anvils where the samples are placed are also shown as an inset. 58
- Figure 27. Pressure calibration curve for the WC anvils used in the Paris-Edinburgh Press. 60
- Figure 28. Temperature calibration curve for the Paris-Edinburgh Press at 2 GPa. 61
- Figure 29. Temperature calibration curve for the Paris-Edinburgh Press at 4 GPa 61
- Figure 30. Instrument layout of the D1B diffractometer at the ILL (top) and the actual experimental set-up (bottom). Small inset shows a sample diffraction pattern. Radial oscillating collimator eliminates parasitic diffraction. Image taken from ILL website. 63
- Figure 31. The Paris-Edinburgh Press (VX5 type) set-up in the D1B diffractometer (left). The sample pellet as it is placed in the TiZr gasket (right). The right photo was taken while the set-up is inside an Ar glovebox. 63
- Figure 32. XRD patterns of products from the $NaMgH_3$ synthesis using the autoclave at 400°C, 70 bar H_2 pressure, using different treatment times 65
- Figure 33. NPD pattern of $NaMgD_3$ at ambient pressure and Rietveld analysis. Refined parameters: a, b, c, X, B_{iso}, and atomic positions. 67

- Figure 34. XRD patterns collected from the Paris-Edinburgh press during the synthesis of $NaMgH_3$ at ~2GPa from a mixture of NaH and MgH_2. Patterns in red show the appearance of the $NaMgH_3$ perovskite. 70
- Figure 35. XRD patterns collected from the Paris-Edinburgh press during the synthesis of $NaMgH_3$ at ~4GPa from a mixture of NaH and MgH_2. Patterns in blue show the appearance of γ-MgH_2 while patterns in red show the appearance of the $NaMgH_3$ perovskite. 71
- Figure 36. XRD patterns collected from the Paris-Edinburgh press during the synthesis of $NaMgH_3$ at ~7.4 GPa from a mixture of NaH and MgH_2. Patterns in blue show the appearance of γ-MgH_2 while patterns in orange show the appearance of β-MgH_2. 72
- Figure 37. Evolution of XRD peaks for $NaMgH_3$ and its precursors with respect to increasing temperature by heating at 4 GPa. 73
- Figure 38. XRD patterns of $Na_{1-x}Li_xMgH_3$ showing the different phases present after synthesis using the CONAC press at 4 GPa and 650°C. X denotes the composition of the starting mixture of precursors. 75
- Figure 39. Closer view of (112), (002), (240), and (312) XRD peaks associated with $Na_{1-x}Li_XMgH_3$ showing the shift in 2 theta values. 76
- Figure 40. XRD pattern of $Na_{1-x}Li_xMgH_3$ with x = 0.1, and Rietveld analysis. 76
- Figure 41. XRD pattern of the synthesis product from the KH:MgH_2 mixture subjected to 400°C and 25 bars D_2 in the autoclave. 79
- Figure 42. XRD pattern of the synthesis product from the KH:MgH_2 mixture subjected to 775°C and 2 GPa for 30 minutes in the CONAC press 81
- Figure 43. NPD pattern of $KMgD_3$ at ambient pressure and Rietveld analysis. 82
- Figure 44. NPD patterns of $NaMgD_3$ (Pnma) up to ~11 GPa (left) and lattice parameters changes (right). The filled symbols were data from the first experiment while the hollow symbols were from the second. 86
- Figure 45. Mg-D and Na-D bond lengths in $NaMgD_3$ (Pnma) during compression in a Paris-Edinburgh Press at room temperature. 88
- Figure 46. EOS curve fit by EOSFit-7GUI software for the relative cell volume (V/V0) vs. Pressure data of $NaMgD_3$. 90
- Figure 47. NPD patterns of $KMgD_3$ up to 11.6 GPa. The peak at $2\theta = 76°$ is for diamond. 91
- Figure 48. EOS curve fit by EOSFit-7GUI software for the relative cell volume (V/V_0) vs. Pressure data of $KMgD_3$. Error bars are too small to be seen. 94
- Figure 49. Unit cell volume of $NaMgD_3$ obtained from low temperature NPD experiments. The EoS curve shown was obtained using EoSFit7-GUI using Salje's equation [214]. 99

- Figure 50. Volume thermal expansion coefficient of $NaMgD_3$ as a function of temperature in Kelvin. 99
- Figure 51. DSC curves of $NaMgH_3$, $Na_{1-x}Li_xMgH_3$, and $KMgH_3$ at a heating rate of 20°C/min. H_2 pressures inside the crucibles are different. 101
- Figure 52. DSC curve of MgH_2 at a heating rate of 10°C/min. 101
- Figure 53. DSC curves of $NaMgH_3$ and $Na_{1-x}Li_xMgH_3$ at different heating rates. T_p = peak temperature. Pressure regulation was not available, therefore comparison is challenging. 103
- Figure 54. DSC curve of $NaMgH_3$ while heating up to 585°C and cooling back to room temperature. Estimated pressure before cooling was 115 bar. 104
- Figure 55. XRD patterns of $NaMgH_3$ before and after DSC up to 585°C. 105
- Figure 56. DSC curve of $Na_{1-x}Li_xMgH_3$ while heating up to 585°C and cooling back to room temperature. Pressure estimation was not possible due to the presence of unreacted MgH_2. 105
- Figure 57. XRD patterns of $Na_{1-x}Li_xMgH_3$ before and after DSC up to 585°C. 106
- Figure 58. DSC curve of $KMgH_3$ while heating up to 585°C and cooling back to room temperature. 107
- Figure 59. XRD patterns of $KMgH_3$ before and after DSC up to 585°C. 108
- Figure 60. Crystal structure of $LiMgH_3$ (R3c)based on the calculations of Li et al [218]. 114
- Figure 61. XRD pattern of the synthesis of $LiMgH_3$ using LiH and MgH_2 at 2 GPa, 400°C (top) and 7 GPa, 650°C (bottom) using the belt press. 117
- Figure 62. XRD patterns obtained in-situ using the Paris-Edinburgh press during the synthesis of $LiMgH_3$ from LiH and MgH_2 at 4 GPa (top) and 7.5 GPa (bottom). 118
- Figure 63. Enthalpy of hydrogen release (ΔH_r) and enthalpy of formation (ΔH_f) of perovskite hydrides from calculations [54]. 122
- Figure 64. Theoretical structure of $NaCaH_3$ [224]. 122
- Figure 65. XRD pattern of the synthesis product at 2 GPa and 650°C using the conac press. 123
- Figure 66. XRD pattern of $K_xLi_{1-x}MgH_3$, x = 0.5, compared to $KMgH_3$. 126

List of Tables

- Table 1. Target gravimetric and volumetric capacities set by the US DOE. 8
- Table 2. Perovskite hydrides experimentally produced(*) and theoretically designed [54]. The corresponding space group is written in parenthesis. 17
- Table 3. Mg-H bond lengths in $NaMgH_3$ from different references. 21
- Table 4. Thermodynamic parameters of the dehydrogenation of $NaMgH_3$. 24
- Table 5. Activation energies of the two-step dehydriding reaction of $NaMgH_3$. 26
- Table 6. Unit cell parameters for $Na_{1-x}Li_xMgH_3$ from NPD data by Martinez-Coronado et al. [71] 28
- Table 7. Desorption temperatures and amount of H_2 release by $Na_{1-x}Li_xMgH_3$ obtained by DSC-TGA. 30
- Table 8. Enthalpy of formation of $KMgH_3$ based on the different pathways shown. 32
- Table 9. Summary of properties of the different binary hydride precursors. 35
- Table 10. Equations of states used for the calibration of pressure of the Paris-Edinburgh Press. 59
- Table 11. Mole fractions of different components from the synthesis of $NaMgH_3$ using the CONAC press at 4 GPa using 30 min treatment time at different temperatures. Quantification was performed by Rietveld refinement of XRD data. 66
- Table 12. Structure parameters of $NaMgD_3$, space group: Pnma. Lattice parameters (Å): a = 5.39996(39), b = 7.68316(56), c = 5.45257(39) 67
- Table 13. Bond lengths and bond angles for $NaMgD_3$. 68
- Table 14. Experimental Unit cell volume of $NaMgH_3$ and its precursors from the in situ experiment performed using the PEP. The unit cell volume of α-MgH_2 is multiplied by 2 because Z = 2, while the rest has Z = 4. 73
- Table 15. Lattice and refinement parameters of $Na_{1-x}Li_xMgH_3$ synthesized using gold capsules in the CONAC 40 press at 4 GPa, 650°C, 2h. The obtained formula of (Na,Li)MgH_3 from the refinements is written in the row named "formula". 77
- Table 16. Mole fractions of the components of the mixture after HP-HT synthesis of $Na_{1-x}Li_xMgH_3$ using CONAC40 at 4GPa, 650C, 2h. 78
- Table 17. Different phases present in the synthesis products from KH:MgH_2 mixture at 4 GPa and 1h using different temperatures. The amount of '+' tells the relative amounts. 80
- Table 18. Lattice parameters of $KMgD_3$ from Rietveld refinement of NPD and XRD data. .. 82
- Table 19. Structure parameters of $KMgD_3$, space group: *Pm*-3*m*. Lattice parameters (Å): a = 4.01962(25). 83

- Table 20. Structural data obtained from Rietveld refinement for $NaMgD_3$ (*Pnma*) at different pressures.....87
- Table 21. Atomic positions of $NaMgD_3$ at different pressures.....87
- Table 22. Bond lengths and bond angles for $NaMgD_3$ (*Pnma*).....89
- Table 23. Bulk modulus (B_0) and its pressure derivative (B_0') for $NaMgD_3$.....90
- Table 24. Structural data obtained from Rietveld refinement for $KMgD_3$ at different pressures. 92
- Table 25. Bulk modulus (B_0) and its pressure derivative (B_0') for $KMgD_3$. 92
- Table 26. Bond lengths and bond angles for $KMgD_3$ at selected pressures.....93
- Table 27. . Optimized lattice parameters and positional parameters of ground state $LiMgH_3$ from Li et al. [218] and Vajeeston et al[49].....114
- Table 28. Synthesis parameters used for the synthesis of $LiMgH_3$ from LiH and MgH_2. 116
- Table 29. Optimized lattice parameters and positional parameters of $NaCaH_3$ from Vajeeston et al [224].....121
- Table 30. Synthesis conditions for the synthesis of $NaCaH_3$ from NaH and CaH_2. 123

Abstract

Hydrogen has become an important vector of energy as the world continues to transition to renewable energy. The way how hydrogen is stored has strongly evolved from using gas tanks in the early 20th century to the use of hydrogen storage materials in the 21st century. Perovskite hydrides based on light metal elements have been one of the promising materials for hydrogen storage due to their high gravimetric hydrogen capacity. Among these, magnesium-based perovskite hydrides, such as $NaMgH_3$, have been investigated extensively. However, poor hydrogen desorption kinetics and high operational temperature remain to be the challenge for its practical use.

The objective of this thesis was to study the possibility of modification of structural and functional properties induced by the use of high pressure on light hydrides crystallizing in the perovskite structure. In this study, the synthesis of several magnesium-based perovskite hydride like $NaMgH_3$ and $KMgH_3$, using high-pressure and high-temperature technique was performed. In-situ X-ray diffraction analysis revealed some information on the phase transformation occurring with the binary hydride precursors, as well as the synthesis mechanism at extreme conditions. Neutron powder diffraction studies at high-pressure performed at the Institut Laue-Langevin enabled the determination of mechanical properties (bulk modulus) of $NaMgH_3$ and $KMgH_3$.

Cation substitution at the A-site of the perovskite was also performed on $NaMgH_3$ to decrease its hydrogen desorption temperature. A lithium-substituted $NaMgH_3$ ($Na_{1-x}Li_xMgH_3$) was also synthesized at high-pressure. Differential Scanning Calorimetry revealed that the hydrogen desorption temperature of the Li-substituted $NaMgH_3$ is lower compared to the pure $NaMgH_3$, which confirmed a destabililization of the material via cation substitution. The reversibility of hydrogen desorption of the said materials is also confirmed by the calorimetric measurements.

During this thesis, we also tried to synthesize, without success, the compounds $LiMgH_3$ and $NaCaH_3$ although predicted as stable by studies based on theoretical calculations.

Overall, the investigation of these light magnesium-based perovskites paves the way to the engineering of hydrides with tailored hydrogen sorption properties.

Introduction

It is both easy and difficult to imagine a world with a zero carbon footprint. With all the new technologies nowadays in the renewable energy sector, it is easy to think that all fossil fuel-based technologies can be scrapped instantly and then the world becomes a better place. This, however, is easier said than done. Challenges in politics and economics also play in the realization of a zero carbon footprint society. The light at the end of the tunnel is still far, they say, as only developed nations are capable of transitioning majority of their energy sources from non-renewable to renewable. On a positive note, through the advancement of research and development (R&D) in the renewable energy field, eventually the technology will trickle down to low income economies as scientists are focused on making solutions that are easier to manage, cheaper, safer, and more efficient. This is the bigger picture…

Looking into the smaller picture involves looking into the different technologies that are currently available. Possibly, high school kids may say that renewable energy sources consist of just solar power plants, hydroelectric plants, and wind farms. Little do they know that society is slowly going into a future with hydrogen – a clean fuel.

The theoretical background of this thesis presents hydrogen as energy carrier which can be used for transportation and on-demand power. Being the lightest and most abundant element there is, hydrogen has played a significant role as an energy carrier. For stationary and mobile applications however, hydrogen needs to be stored. For the most part of the early and mid-20th century, hydrogen has been stored in large high-pressure cylindrical gas tanks. This, however, is not the most efficient way to do it. The goal nowadays is to have a material that can hold as much hydrogen as possible; something that can be operated at the minimal operational conditions as possible; something that can last long. In this study, materials called perovskite hydrides, considered as one of the prospects for solid-state hydrogen storage, are presented and discussed. These materials have been around since the end of the 20th century and the quest to improving the material's performance and efficiency is still ongoing.

Perovskite hydrides made from light metal elements look promising for solid-state hydrogen storage because these materials are lightweight and they have high gravimetric capacity which means they can hold high amounts of hydrogen per unit mass of the material. These good characteristics enabled the outpour of research to synthesize perovskite hydrides

with a good hydrogen storage performance. Among the different synthesis methods, high-pressure high-temperature techniques provide the means of exploring the behavior of solid materials at extreme conditions. With this, certain pressure and temperature ranges can be exploited to understand the behavior and characteristics of some metastable phases, which have the chance to transform into a more stable state had the process been done at room conditions. Moreover, working at extreme pressures allows us to study certain structural changes in the solid. Thus, throwing some light on how the atomic arrangements can affect the synthesis products.

Having said, therefore, the general objective of this thesis is to synthesize perovskite hydrides using high-pressure high-temperature techniques and to relate some of their mechanical and thermal properties to their hydrogen storage performance.

This manuscript consists of five chapters. The first two chapters deal with the background, motivation, literature review, and the experimental techniques employed. Chapter 1 discusses the concept of solid-state hydrogen storage, the role of perovskite hydrides as hydrogen storage materials, and the method of high-pressure synthesis in synthesizing these materials. Chapter 2, on the other hand, describes the experimental methods performed during synthesis of the perovskite hydrides and characterization of the said materials. This chapter is dedicated to the different equipment used, as well as the software and analysis tools employed. In particular, the use of a large-scale instrument at the Institut Laue-Langevin is also highlighted. The different techniques presented here allowed for the determination of certain mechanical and thermal properties of the samples studied.

After presenting the theoretical framework and the experimental techniques employed, the remaining chapters present the results and discussion of each material studied. Chapter 3 describes the synthesis and characterization of $NaMgH_3$, $Na_{1-x}Li_xMgH_3$, and $KMgH_3$, materials that have pretty much received attention in recent years. In this chapter, different high-pressure synthesis techniques are shown. Both the use of autoclave and anvil-type press are presented. Moreover, the formation of $NaMgH_3$ at the high-pressure high-temperature realm has been studied using in-situ X-ray diffraction analysis with a Paris-Edinburgh Press. This provides an understanding as to how phase transformations of the reaction precursors occur at extreme condition and how the synthesis of the perovskite hydride comes about. This chapter also determines the maximum amount of lithium substitution in $NaMgH_3$ and describes its effect in terms of the crystal structure.

The study of one mechanical property, the bulk modulus, of $NaMgH_3$ and $KMgH_3$ is presented in Chapter 4. This is the first time that such experimental data for the bulk moduli of the two perovskites is reported. High-pressure neutron powder diffraction using a Paris-Edinburgh Press at the D1B beamline of the ILL facilitated the exploration of any pressure-induced phase transformation of these materials. Rietveld analysis of the neutron diffraction data provides the information about the arrangement of atoms, bond lengths, bond angles, etc. to help us understand what structural transformation the crystal is going through.

Chapter 5 talks about some thermodynamic properties of the synthesized perovskites in relation to their hydrogen storage performance. Differential scanning calorimetry studies allowed the understanding of how changing the element at the A-site affects the desorption temperature of the perovskite hydride. The obtained temperatures of desorption using different heating rates during measurements were analyzed. The experimental data also shed light on the reversibility of the hydrogen desorption process, which adds to the understanding of the performance of the hydrogen storage material being studied.

General conclusion and perspectives are given at the end of the manuscript. In addition, experimental attempts of synthesis of $LiMgH_3$ and $NaCaH_3$, two promising compounds predicted to be stable by theoretical calculations studies, are described as appendices.

Chapter I. Literature Review

This chapter provides the background of the study. In the first part, the motivation of the research is discussed. Here, the problem that humankind is facing in terms of energy sources is presented. Among the many solutions proposed, the use of hydrogen as energy storage is shown to be a promising one. Different ways of storing hydrogen are discussed and the choice of solid state storage is highlighted.

The second part of the chapter deals with the role of perovskite hydrides as hydrogen storage materials. An overview of the crystal structure of perovskite is presented and this section also provides a literature review of some of the perovskite hydrides already synthesized for hydrogen storage applications, most importantly $NaMgH_3$. Recent developments for $NaMgH_3$, including the modification in the synthesis parameters in order to improve the hydrogen storage performance of the material are also described here.

The final part of the chapter discusses the use of high-pressure high-temperature synthesis techniques. The use of autoclave-type and anvil-type synthesis apparatuses allows for certain processes that normally do not transpire at normal conditions to occur. A lot of perovskite hydrides were synthesized this way and it is interesting to note that high-pressure techniques can pave the way towards synthesizing new materials that have performances better than ever.

I.1. Context

I.1.a. The Energy Problem

In the present day, only less than 15% of the world's energy is produced from renewable sources [1]. Advanced economies such as the European Union has renewable energy penetration of 50% for most of its member states [2]. Majority of the remaining 85% are the culprits of severe waste generation that pose a threat to the environment. Burning coal, for example, in coal power plants is considered to be a very "environmentally dirty" process in energy generation. During this combustion process, CO_2 is formed which then accumulates in the atmosphere and eventually lead to the greenhouse effect. The status quo of burning fossil fuels is not aligned with the principles of sustainable development [1]. Based on the Global

Energy & CO_2 Status Report 2019 of the International Energy Agency (IEA), global energy-related CO_2 emissions in 2018 reached a historic high of 33.1 Gt CO_2, a 1.7% growth. Global annual CO_2 concentration in the atmosphere averaged at 407.4 ppm compared to pre-industrial levels of around 280 ppm maximum. This increase in CO_2 emissions was brought about by the 2.3% annual growth in global energy consumption.

Due to population growth and other socioeconomic factors, the demand for electricity keeps on growing. Soon, the renewable energy sector will get a bigger slice of the pie because the cost of operating renewable energy generators will hopefully become typically lower than fossil-fuel-based thermal generators, and operational costs may decrease due to the growing competition in the power market [3]. Also, non-renewable sources of energy will soon start to dry up. Certain models show the depletion timeframe of non-renewable energy sources like oil, natural gas, uranium, and coal. Based on these models, energy production from uranium will peak by the year 2025, after which depletion of this energy resource will occur. On the other hand, oil production will peak by the year 2060 and after that, oil resources will start to get depleted while natural gas production will start its decline by 2080. Depletion of coal will occur beyond 2100 [4].

Alternative fuels such as biodiesel, hydrogen, and solar fuels (using photo-electrochemical and thermochemical cells) have been developed. Among these key alternatives is hydrogen. It is foreseen to be produced in infinite quantities due to its abundance. However, currently, hydrogen is still produced mainly via natural gas reforming and electrolysis. Still, the spotlight is on hydrogen because there is a potential long-term restriction on greenhouse gases and the rate of technological advancement is increasing [5]. In the European Union, where 20% of energy demand comes from the transport sector, it is projected that in 30 years, renewable fuels such as H_2-biomass, H_2-photovoltaic, electricity-wind/hydro, and electricity-PV, which costs more expensive than gasoline now, will eventually become cheaper and more competitive than conventional gasoline [6]. Likewise, according to the European Commission's High Level Group for Hydrogen and Fuel Cells Technologies, the European Union will attain a Hydrogen-based economy by 2050 and that by 2040, 35% of new vehicles will be run using Hydrogen as fuel [7].

I.1.b. Hydrogen as energy store

Hydrogen is the lightest known element with a molar mass of 1.08 g/mol. In the course of history, energy carriers are being developed in a way that it moves from a more carbon-based fuel to a more hydrogen-rich fuel. The development goes from coal (C) to oil ($-CH_2-$) to natural gas (CH_4) and ultimately to hydrogen (H_2). The chemical energy content of hydrogen per mass is three times larger than that of oil (39.4 kWh/Kg. hydrogen vs. 13.1 kWh/Kg. oil) even if it costs three times as much [8]. This high energy density is one of the advantages of hydrogen when used as an energy carrier in vehicle applications [9]. So economically speaking, being the most abundant element in the universe, hydrogen is a good vector of energy because the benefit outweighs the challenges, which can be solved by further development in technologies.

In the past, hydrogen production is mainly carried out by reacting fossil fuels with water at high temperatures:

$$-CH_2- + 2H_2O \rightarrow 3H_2 + CO_2$$

However, this process requires energy, it uses non-renewable precursors, and it also produces CO_2. The better method is to produce H_2 from non-fossil feedstocks like electrolysis of water in which the energy required for this process comes from renewable sources like wind, solar, or geothermal [8]. Also, when hydrogen is combined with O_2 in a proton exchange membrane fuel cell, water is the only by-product in the power generation process. This process makes it attractive for a zero-emission vehicle [9].

A set of criteria needs to be met for an efficient hydrogen storage system. It should be cheap, and safe. The storage process should allow fast refueling which is also a challenge because the hydrogen absorption process is endothermic. The storage should also be compact and lightweight, but it should have at the same time significant capacity [10]. The U.S. Department of Energy (DOE) identifies gravimetric capacity and volumetric capacity as important parameters for hydrogen storage applications. Gravimetric capacity pertains to the amount of hydrogen that is generated by a given weight of storage material while volumetric capacity is the amount of hydrogen contained in a particular volume of storage material [7][11]. According to the DOE Technology Validation Fleet in 2009, the hydrogen storage targets in terms of gravimetric and volumetric capacities are increased from 2010 to 2015 and finally to an ultimate goal shown in Table 1 [9]. The 2003 targets were higher than these because these

high values were set in order for H storage systems to be equivalent to that of a gasoline fuel system of vehicles.

Table 1. Target gravimetric and volumetric capacities set by the US DOE.

	Units	2010	2015	Ultimate
Gravimetric capacity	wt% H_2	4.5	5.5	7.5
Volumetric capacity	g H_2/L	28	40	70

I.1.c. Hydrogen storage

Hydrogen storage can be performed in several ways. Figure 1 shows a comparison of volumetric capacities of different ways of hydrogen storage. Notice that the amount of hydrogen stored per volume of the material is greater for the materials-based storage. The succeeding sections provide more information about these.

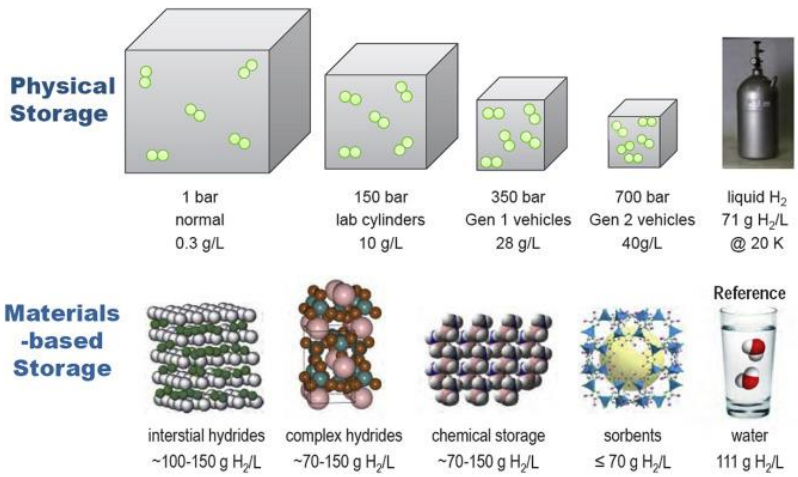

Figure 1. Comparison of volumetric capacities of physical hydrogen storage and materials-based storage [12].

I.1.c.1. Gas storage

Storage of hydrogen fuel for transportation was mainly performed by using storage cylinders. Early versions of these gas vessels were heavy and had only a 0.05 m^3 H gas/kg

cylinder technical efficiency. From the 1960s, these vessels were improved using Cr-Mo alloyed cylinder steels that had an improved efficiency of 0.13 m^3/kg. There was a variation in the exact value, depending on the design code of cylinder fabrication. In the 1970s and 1980s, problems arose when a lot of failures were experienced by hydrogen cylinder vessels, which prompted the questions on its safety. Nowadays, improvements in the cylinder material are constantly being developed such as the use of tanks made of composite materials just like the ones used for compressed natural gas (CNG) and liquefied natural gas (LNG) [13]. However, lightweight carbon fiber, the typical material used to contain hydrogen in vessels for up to 700 bar, is costly, and is more expensive than the plastic gasoline tank. Because hydrogen has a low density of 0.089 g/L at standard temperature and pressure, there is a need to store hydrogen under high pressure in order to fit the configuration of a vehicle [9].

The operating temperature and pressure of a hydrogen storage system depends on the requirements of the cell. Minimum temperature can go as low as -40°C for cold weather operation and maximum temperature is set at 60°C but ultimately can go up as high as 105°C [9][12]. The working pressure on the other hand can vary from 3 bar to 12 bar [9].

With the growing popularity of hydrogen-powered automobile, it should not be forgotten that it can still be dangerous. Hydrogen has the potential to leak outside the tank and it can cause fires and even explosion [14].

I.1.c.2. Liquid state storage

In contrast to the solid state method, liquefaction is a process where liquid hydrogen is stored in cryogenic tanks at 21.2 K. The critical temperature of hydrogen is 33K and because liquid and gas exist very vaguely beyond the critical temperature, liquid hydrogen can only be stored at ambient pressures. To prevent the boil-off of hydrogen, the storage vessels should be ideally spherical. However, fabricating huge spherical containers in more difficult [8]. The regulation of temperature in the vessel is also crucial. For example, if the temperature is <180K, the capacity of a vessel is 71.3 g/L stored hydrogen, and when the temperature is 200K, this decreases to 64.2 g/L [15]. It is the complicated vessel fabrication plus the energy-efficiency of the process of liquefaction and the thermal insulation required for the spherical vessels, that makes this technique a little challenging [8]. In the transportation sector, if hydrogen storage is applied to vehicles, high-pressure tanks and cryo-storage will not be suitable due to their low energy density and also due to safety reasons [16]. Figure 1 demonstrates that physical storage

using high-pressure tanks and liquefying H_2 is less efficient in terms of the amount of H_2 that can be stored [12]. Using materials-based storage in the form of solid materials can be a better option due to a larger volumetric capacity. These materials will be discussed in the next sections.

I.1.c.3. Solid state storage

The first paper related to reversible hydrogen storage material was published in 1958. A zirconium-nickel alloy reacted readily with hydrogen to form a mixture of ZrNiH-$ZrNiH_3$ phases, which also showed reversibility based on its pressure-composition isotherms [17]. This was followed by the Mg_2Ni/Mg_2NiH_4 system which has hydrogen capacity of 3.6 wt.%, which was followed by the development of other materials such as $LaNi_5$, TiFe, $ZrCr_2$, and V [18]. Due to the limitations brought about by simple light metal hydrides, several materials have been synthesized such as complex hydrides, metal alloys [19], 2D layered materials [20], nanocomposites [21], carbon-based nanosheets [22], and metal organic frameworks [23]. Despite all of the available materials, dozens of investigations are still underway on the identification of new materials with high H content that can also have low operating temperatures.

For onboard applications, a hydrogen storage material should operate at 358K and the time it takes to be replenished for another cycle of hydrogenation-dehydrogenation should be within 5 minutes [24]. For Mg-based materials, this is not the case as the temperature for the release of 1 bar hydrogen is 560K. Hydrides of magnesium, lithium, and sodium have a high desorption temperature of greater than 573 K [25]. Strong Mg-H bonds account for this thermodynamic stability. This can be modified by looking at the formation enthalpy (ΔH) and entropy (ΔS) using the van't Hoff equation. On the other hand, the rate of reaction can be modified by looking at the activation energy (E_a). The activation energy can be derived from the Arrhenius equation or in these studies from the Kissinger equation which will be discussed in the succeeding section. Higher ΔH generally means that hydrogen desorption occurs at a higher temperature while high Ea means a slower reaction rate due to the higher kinetic barrier imposed [18]. In order to improve the material's performance, these barriers need to be overcome (Figure 2).

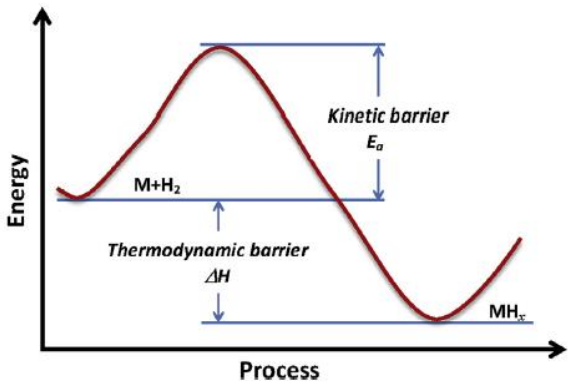

Figure 2. Kinetic and thermodynamic barriers that need to be overcome to improve a metal hydride's performance as discussed by Wang et al [18].

I.1.c.3.a. Metal, Intermetallic, complex hydrides and large surface area materials

It was reported in 1866 by Thomas Graham that palladium had a great absorptive capacity for hydrogen, forming PdH_2 – the first metal hydride [26][27]. Metals reacted with hydrogen to form a solid metal-hydrogen compound is called a metal hydride or metallic hydride [8]. Compounds of hydrogen and the transition metals occur as mono-, di-, or trihydrides (MH_n, n = 1, 2, 3). These binary metal hydrides have their metal lattice similar to the elemental metal's lattice having the hydrogens occupy interstitial sites [28]. Other examples include scandium hydride and titanium hydride [29][30]. When H atoms diffuse into the bulk of the material, the interstitial sites are occupied by these diffusing H atoms (see Figure 3). In the process, a solid solution is formed with a low concentration of H. This is called the α-phase. The H content increases as more energy is added to the system. A hydride phase called the β-phase is formed from nucleation sites which then grows into larger amounts and thus forming a substance that is saturated with H [7].

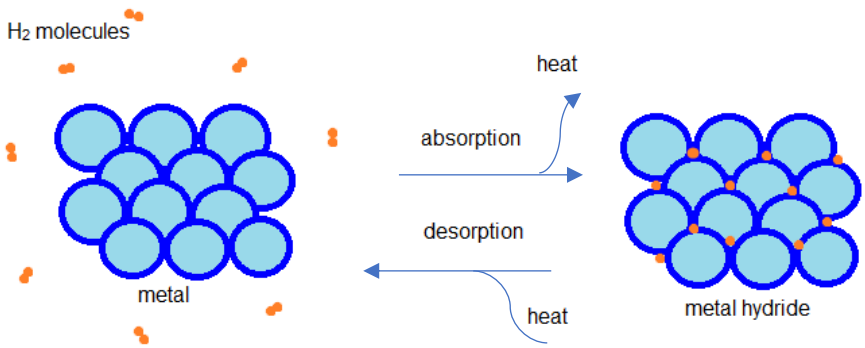

Figure 3. Process of hydrogen absorption into the metal crystal to form the metal hydride.

Intermetallic hydrides have the general formula AB_xH_n, where A is usually an alkaline earth metal or a rare earth metal, and B is usually a transition metal [8]. Contrary to an alloy where there is a continuous composition of a solid solution between A and B, intermetallics have a defined composition of A and B [26]. In AB_xH_n, x can be 0.5,1,2, or 5 while the hydrogen-to-metal ratio can be up to 2 [8]. An example of an intermetallic is $LaNi_5$ that forms a hydride by absorbing more than 6 hydrogens and the absorption-desorption process proceed quickly at room temperature [31].

Complex hydrides were seen in the mid-90's to be a promising group of hydrogen storage materials [32][33]. Complex hydrides are materials that consist of hydrogen and group 1, 2, 3 light metals [16]. In the realm of complex hydrides, materials that were investigated for hydrogen storage applications are alanates, borohydrides, amides, imides, amino boranes and alanes [16]. This type of hydride consists of an electropositive counter ion and a coordination complex, like $[BH_4]^-$ and $[NH_2]^-$, where hydrogen is covalently bonded [10]. Some complex hydrides, such as $NaAlH_4$ and $LiBH_4$ have good hydrogen storage capacities but involve higher operating temperatures because generally complex hydrides have high thermal stability which can hinder its practical use [34][11].

Due to these weak van der Waals forces, hydrogen storage that uses only physisorption occurs only at cryogenic temperatures, usually at 60-120 K. This technique is called cryoadsorption which generally requires adsorbates that have high surface areas for the process to become efficient [35]. The advantages of using this technique are: low operating pressure, low cost of materials, and the simplicity of the design of storage systems. However, the small amount of H_2 gas adsorbed and the low working temperatures are the major drawback of this technique [8].

I.1.c.3.b. How hydrogen is absorbed in metals, alloys, and Intermetallics

The way a hydrogen storage material acts as a "hydrogen sponge" can be generally described in five steps [26].

The first step is the adsorption of molecular hydrogen on the surface. This is called physisorption where hydrogen molecules interact with the surface by weak van der Waals forces. The second and third steps are activation and decomposition of H_2. In the activation

process, any layer of oxides, sulfides, nitrides, etc. will be reduced by hydrogen. Then, H_2 will decompose into H atoms. The fourth step is the formation of a monolayer hydride at the surface through chemisorption. In chemisorption, atomic hydrogen reacts chemically with solid materials to form hydrides [7]. Last is the diffusion of the hydride layer and H- species into the bulk.

The desorption process on the other hand begins when certain changes in the bulk brought about by, say input of energy by heating, force the hydrogen atoms to move to the surface. Hydrogen atoms then recombine to form H_2 and they are released to the environment as H_2 gas. According to Khafidz et al., any of these processes can be the rate-limiting step [25]. Hence, it is important to know which aspect of the material or which aspect of the absorption-desorption process we should look into.

I.1.c.3.c. How hydrogen behaves in complex hydrides

In contrast to hydrogens going into the interstitial sites in the solid, hydrogens involved in hydrogen storage using complex hydrides bind covalently. The stronger hydrogen-host interaction present is the reason why absorbed hydrogens are largely immobile [32]. In the case of the complex hydride, $NaAlH_4$, it gives 5.6 wt.% hydrogen as described in the following reaction: $3NaAlH_4 \leftrightarrow 3\ NaH + 3\ Al + 9/2\ H_2$. It can be seen that a chemical reaction is involved in both the release and reabsorption of hydrogen. Another example is the liberation of 4 moles of H_2 when $LiBH_4$ undergoes hydrolysis: $LiBH_4 + 2H_2O \rightarrow LiBO_2 + 4H_2$ [16]. The hydrolysis reaction has to occur in order for the hydrogen to be released. The rehydrogenation involves heating the remaining product up to 500°C under 800-950 bar H_2 [10].

I.1.c.3.c. Tuning storage performances of hydrides

Some synthesized perovskite hydrides have encountered the same issues of slow kinetics and high thermal stabilities. Generally speaking, some properties can be fine-tuned in order to improve the performance of hydrides. Modifications in the morphology, crystallinity, and chemical reactivity can be achieved by manipulating assembly parameters, synthesis conditions, presence of additives (i.e. adding or substituting ionic species), thermal annealing, and doping [36]. One modification that can be performed is producing powders in

nanocrystalline form. Zaluska et al. used magnesium powders in nanocrystalline form and they found out that the hydrogen storage properties of of MgH_2 were significantly enhanced due to the improvement in its absorption/desorption kinetics [37]. Creating structures in the micro or nano levels decreases the diffusion path lengths for hydrogen and it also reduces the thickness of the hydride layer which is formed during absorption, thus, an improved kinetics [38]. Another technique to improve kinetics is the use of thin films. Novel structures are made in thin films that are beneficial for hydrogen sorption, this being a surface process [25]. Qu et al. produced a very thin Mg layer via magnetron sputtering with improved kinetics and H capacity of 5.5 wt.% [39].

I.2. Perovskite hydrides as hydrogen storage materials

I.2.a. Overview of the perovskite structure

Metal oxides, metal halides, and a few metal carbides may be formed from a reaction of AX_n and BX_m to form ABX_3 where X = O, H, C. These materials with an ABX_3 formula are called perovskite. The name perovskite was derived from the mineral $CaTiO_3$, which is commonly called perovskite [40].

The ABX_3 perovskite crystal structure has a large A cation surrounded by 12 X anions and a small B cation surrounded by 6 X anions [41]. Figure 4 shows the bonding of the B atom with 6 X atoms ([BX_6]-octahedra), and also the A atom at the center of the cube surrounded by 12 X atoms ([AX_{12}]-cubo-octahedra). This ideal perovskite cubic structure has a space group of $Pm\bar{3}m$ where the X atoms are at the middle of the cell edges at 3d (1/2,0,0) while A and B atoms are at the cell center and cell corners, respectively [42]. If the radius of A is smaller than that of B, then the A cations tend to occupy the octahedral sites instead of the cubo-octahedral sites. This structure is known as the inverse perovskite structure or BAX_3 [43].

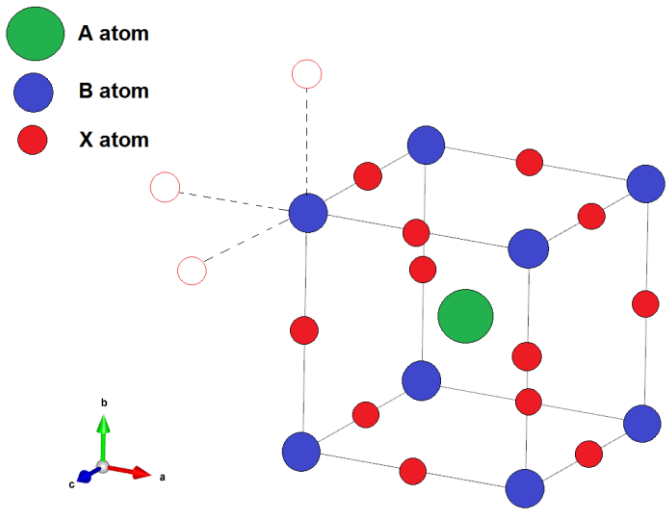

Figure 4. Structure of a perovskite showing the BX_6 octahedron and AX_{12} cubo-octahedron.

Distortion from the ideal cubic structure may occur and these materials can form orthorhombic, tetragonal, or rhombohedral structures [40]. Deviations from a perfect cubic perovskite is determined by a factor called Goldschmidt tolerance factor:

$$t = \frac{(r_A + r_X)}{\sqrt{2}(r_B + r_X)}$$

where r_A, r_B, and r_X are the ionic radii of the cations A and B, and the anion X (usually chalcogen or halogen), respectively. When A and B cations have their ideal equilibrium distances from the X anion, there is no distortion in the unit cell and the symmetry is cubic with space group *Pm-3m*. In this ideal case, t = 1. When the A-X and B-X bond lengths are different from ideal, the symmetry is decreased and t < 1. When t > 1, the structure is usually mixed cubic and hexagonal, or hexagonal close packed. The value of the tolerance factor reflects the geometric stability of a certain crystal structure. A geometric strain is present when the ratio of the ionic radii deviates from the ideal value of t = 1 [44].

Materials that have a perovskite structure include perovskite oxides, ABO_3, that have been well-investigated for their ion-exchange ability for different electro-chemical applications [45]. Another group of materials worth noting are the borohydrides. Schouwink et al. performed calculations based on ionic radii and the Goldschmidt tolerance factor and they were able to map regions where the perovskite structure may exist [46]. Their method was useful for the discovery of new materials having this particular crystal structure for different applications.

I.2.b. Perovskite hydrides

In this section, a general overview of perovskite hydrides is given. The synthesis method and the hydrogen storage mechanism are also discussed in the succeeding subsections.

1.2.b.1 Geometrical considerations

The equation for the Goldschmidt tolerance factor can be rearranged to a linear form:

$$r_B = \frac{(\mathrm{r_A} + \mathrm{r_X})}{\sqrt{2}\,t} - r_X$$

Plotting r_B vs r_A and assuming r_X or r_H to be 0.140 nm (a value that is regularly used in literature and that is based on Shannon effective ionic radii [47]), this equation has a slope of $\frac{1}{\sqrt{2}\,t}$. If t is set at 0.77 and 1.00, we can generate 2 lines with different slopes (shown as the inclined dotted/solid lines in Figure 5) [48]. According to the estimation of Ikeda et al., following Pauling's first rule on stabilization of the polyhedron, the r_B/r_X ratio has an ideal value of 0.414-0.732 and with r_X = 0.140 nm, r_B should be between 0.058 and 0.102 nm which are shown as the 2 horizontal lines in Figure 5. These 2 inclined lines and 2 horizontal lines form a parallelogram, the inside of which represent the region where the perovskite structure may exist [43]. This estimation of the formation region using the Goldschmidt tolerance factor is very useful when trying to predict and synthesize hydrides using group IA and IIA elements with a perovskite-type structure. Also, for t = 0.8-0.89, there is a tetragonal or orthorhombic distortion of the cubic symmetry, which in turn occurs at t = 0.89-1.00. On the other hand, t greater than 1 show the hexagonal variant of the perovskite structure [49].

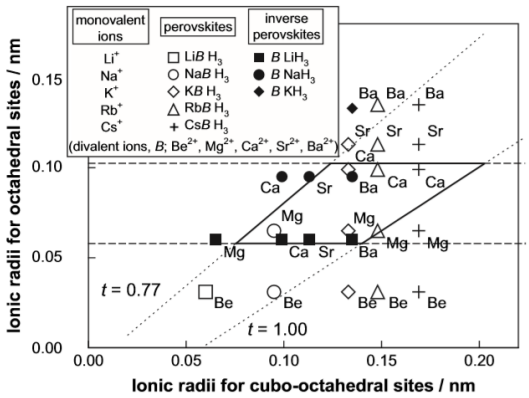

Figure 5. Estimated formation region of perovskite-type hydrides by Ikeda [48].

I.2.b.2 Ab initio calculations

Density functional theory investigations were also done for perovskite hydrides like $CaNiH_3$ [50], $NaBeH_3$ and $LiBeH_3$ [51], $NaMgH_3$ [52], and $KMgH_3$ [53], to determine their structural, elastic, electronic, optical, and thermodynamic properties which can aid in the development and understanding of perovskite materials for hydrogen storage.

Li et al. performed a screening process using computational procedures to determine the hydrides with the highest potential for hydrogen release. Table 2 shows their list of perovskite hydrides, both experimentally produced and hypothetically designed [54]. It can be noticed that there are more hypothetical perovskites than experimentally produced ones. Hence, this is a topic worth looking and exploring to see whether these materials can be synthesized for hydrogen storage purposes.

Table 2. Perovskite hydrides experimentally produced(*) and theoretically designed [54]. The corresponding space group is written in parenthesis.

Be-based	**Mg-based**	**Ca-based**	**Sr-based**	**Ba-based**
*$LiBeH_3$ (*Pnma*)	$LiMgH_3$ (*R*3*c*)	$LiCaH_3$ (*R*3*c*)	*$LiSrH_3$ ($Pm\bar{3}m$)	*$LiBaH_3$ ($Pm\bar{3}m$)
$NaBeH_3$ ($Pm\bar{3}m$)	*$NaMgH_3$ (*Pnma*)	$NaCaH_3$ ($P2_1/c$)	$NaSrH_3$ ($P2_1/c$)	$NaBaH_3$ (*R*3*c*)
$KBeH_3$ ($P2_1/c$)	*$KMgH_3$ ($Pm\bar{3}m$)	$KCaH_3$ (*Pnma*)	$KSrH_3$ (*Pnma*)	$KBaH_3$ (*R*3*c*)
$RbBeH_3$ ($P2_1/c$)	*$RbMgH_3$ ($P6_3/mmc$)	*$RbCaH_3$ ($Pm\bar{3}m$)	$RbSrH_3$ (*Pnma*)	$RbBaH_3$ (*R*3*c*)
$CsBeH_3$ ($P2_1/m1$)	*$CsMgH_3$ (*Pmmn*)	*$CsCaH_3$ ($Pm\bar{3}m$)	$CsSrH_3$ ($Pm\bar{3}m$)	$CsBaH_3$ (*Pnma*)

I.2.b.3 Synthetic hydride perovskites

Ternary light metal hydrides with the perovskite structure such as $LiBeH_3$, $KMgH_3$, $CsCaH_3$, and those with the inverse perovskite structure such as $LiSrH_3$, and $LiBaH_3$, have been synthesized from the late 1960's to the early 1980's [55]. $LiSrH_3$ and $LiBaH_3$ were synthesized from their binary hydride precursors using a thermal analysis apparatus at 650-750°C and 1 atm [56] and they were found to have the inverse perovskite structure [57]. Among the hydrides synthesized presented in Table 2, five of them manifest an ideal $Pm\bar{3}m$ structure: $RbCaH_3$,

$CsCaH_3$, $KMgH_3$, $LiSrH_3$, and $LiBaH_3$ [42]. Some of them will be discussed in the succeeding paragraphs.

$LiBeH_3$ has been synthesized by annealing a mixture of LiH and BeH_2 at 250-425°C and 45 kPa pressure [58], and also by ball-milling and thermal process at 227°C (500K) [59]. X-ray diffraction data shows that $LiBeH_3$ has an ilmenite ($FeTiO_3$ type) structure [58]. Another perovskite in Table 2, $KMgH_3$, was synthesized by ball milling a 1:1 mole ratio of KH and MgH_2 at 400°C (673 K) under 1.0 MPa H_2 pressure for 20 h [60]. Another method of synthesis was reacting K and Mg metals with hydrogen at 15 bar H_2 and 647°C (920K) for 5 min [61]. It was found to have a cubic perovskite structure with space group $Pm\bar{3}m$.

In the early 2000s, two polymorphs of $CsMgH_3$ were synthesized. Renaudin et al. heated CsH and MgH_2 in an autoclave at 327°C (600K) and 150 bars H pressure [62]. The product has an orthorhombic structure with a space group of *Pmmn*. Bertheville et al., on the other hand, used high pressure synthesis. Stoichiometric mixtures of CsH and MgH_2 were placed in a multi-anvil press at 30 kbar pressure and 547°C (820 K) temperature [63]. The $CsMgH_3$ formed has $BaRuO_3$ type structure, rhombohedral symmetry (space group: *R-3m*), while its Ca analogue, $CsCaH_3$, has a cubic perovskite structure, and its Rb counterpart, $RbMgH_3$, has a hexagonal perovskite type structure [63].

Cubic $CsCaH_3$ and hexagonal $RbMgH_3$ were synthesized by Gingl et al. by mixing stoichiometric amounts of the binary hydrides required at 402°C (675 K) under 200 bar H_2 for 10 days [64]. As mentioned, $CsCaH_3$ has a $Pm\bar{3}m$ space group, while $RbMgH_3$ has a $P6_3/mmc$ space group. The Goldschmidt tolerance factor for $CsCaH_3$ is 0.98 which is within the perovskite range while that for $RbMgH_3$ is 1.06, which is not within the range because the Rb ions are just too large. The Ca analogue, $RbCaH_3$, on the other hand, was experimentally synthesized by ball milling Rb and MgH_2 for 1 h and consequently heated overnight at 400°C and 20 bar H_2 pressure [65]. It was shown that $RbCaH_3$ has a simple cubic perovskite structure (space group: $Pm\bar{3}m$). The Goldschmidt tolerance factor of $RbCaH_3$ is 0.928.

Knowing that previously synthesized perovskite hydrides show significant potential for hydrogen storage, it is desirable to continue the search for novel materials that are better and more efficient than what we currently have.

1.2.b.4 Hydrogen storage in perovskites

Perovskite hydrides have a high density of hydrogen which makes them essential in the development of safe, compact, and lightweight hydrogen storage materials for future fuel cells and also for hydrogen combustion applications [43].

Among the synthetic perovskite hydrides, $LiBeH_3$ offers the highest H storage capacity at 15.93 wt. % H [66]. However, Be is very toxic which makes synthesis protocols somewhat complicated. Hence, limited studies on their applicability for hydrogen storage are available [51]. The cubic perovskite $KMgH_3$, on the other hand, according to Ref. [60], shows a one-step decomposition reaction shown below:

$$KMgH_3 \rightarrow K + Mg + 3/2\ H_2$$

Although the theoretical amount of H released is 4.6 wt. %, an experiment at 400°C (673K) showed that only 3.8 wt.% was released due to the presence of small amounts of KH and MgH_2 in the specimen. Furthermore, the dehydrogenation in $KMgH_3$ did not show reversible reactions [60]. For $CsMgH_3$, little is known for its H storage properties and it has not yet been rigorously investigated. However, first-principle calculations by Wang et al. suggest a feasible pathway for the dehydrogenation of $CsMgH_3$ [67]:

$$CsMgH_3 \rightarrow Cs + MgH_2 + 1/2\ H_2$$

In the case of $RbMgH_3$, Wu et al. found that all of its H are desorbed at 392°C while rehydrogenation occurred at 300°C and 20.265 bar [65]. Their temperature programmed desorption (TPD) results show that the dehydrogenation happens in a single step:

$$RbMgH_3 \rightarrow Rb + Mg + 3/2\ H_2$$

On the other hand, $RbCaH_3$ desorbs all of its H in the three-step reaction, as evidenced by the three peaks in Wu et al.'s TPD results, the last of which occurred at 347°C. They also observed that $RbCaH_3$ can be rehydrogenated within the same temperature range 300-400°C and same pressure of 20.265 bar. However, the succeeding dehydrogenation is only about 70% of the first cycle in terms of hydrogen capacity [65].

From the previous examples, it can be seen that perovskite hydrides decompose in different manners. Li et al. studied three hydrogen release pathways through computations [54]. These pathways are:

$$ABH_3 \rightarrow A + B + 3/2\ H_2$$

$$ABH_3 \rightarrow A + BH_2 + ½\ H_2$$

$$ABH_3 \rightarrow AH + B + H_2$$

They suggested that beryllium-based perovskite hydrides and $LiMgH_3$ systems follow the third pathway while the rest, including Mg-based hydrides, follow the second pathway. However, PCT curves from the experiments of Komiya et al indicates that $NaMgH_3$ and $KMgH_3$ follows the third and first pathways, respectively [60].

I.2.c. $NaMgH_3$

I.2.c.1. Crystal Structure

Data from X-ray diffraction (XRD) and neutron powder diffraction (NPD) experiments show that $NaMgH_3$ ($NaMgD_3$ in the case of NPD experiment) has a $GdFeO_3$-type perovskite structure with space group *Pnma* [41][68]. A typical primitive orthorhombic unit cell of $NaMgH_3$ is shown in Figure 6. Shown as green spheres, the Na atom at the A-site is surrounded by 12 H atoms shown in blue. Furthermore, each Mg atom, shown in purple, is bound to 6 surrounding H atoms. Sodium atoms occupy the 4c sites while Mg occupies the 4b sites. The H anion occupies the 4c and 8d sites in the structure and each H is surrounded by 4 Na and 2 Mg cations [69][70]. The tolerance factor of $NaMgH_3$ is 0.87, which is lower than the tolerance factor of an ideal cubic perovskite structure (t = 1.0) [71]. Calculations by Fornari et al. show that lattice distortions from the ideal cubic structure are brought about by Coulombic interactions. With its ionic character, both cations and anions in the structure position themselves in locations that are more favorable, and thus creating the said distortions [72].

Due to the difference in ionic radius of Na and Mg, there is a tendency for the rigid MgH_6 octahedron to tilt which distorts the perovskite structure [69]. This tilting mechanism has an effect to the mobility of H in the structure. Wu et al. determined the effect of temperature on the tilting angle of the MgH_6 octahedron and its eventual effect on H mobility [41]. Table 3 shows the Mg-H bond length in this octahedron. It is interesting to note that the Mg-H bond lengths in $NaMgH_3$ are very close to the 1.94 Å (Mg-H, apical) and 1.97 Å (Mg-H, equatorial) values observed in the crystal of pure tetragonal MgH_2 [73]. For the H ion to move to an adjacent empty site, it must pass through the plane defined by two Na cations and one Mg cation at the center (triangle in Figure 7). If the MgH_6 octahedron is more tilted, it restricts the movement of H to the adjacent site, creating a “bottleneck”, as Wu et al. described it. At higher temperatures, this tilt angle is minimized and it requires a lower activation energy for the movement of H to occur [41].

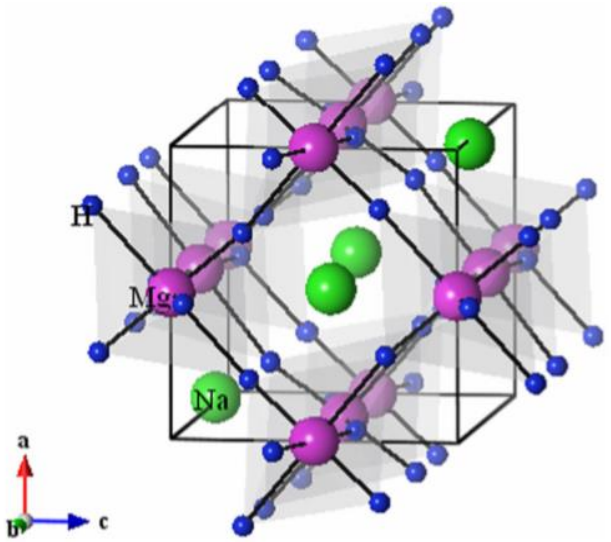

Figure 6. Unit cell of $NaMgH_3$. Blue spheres represent H. [74]

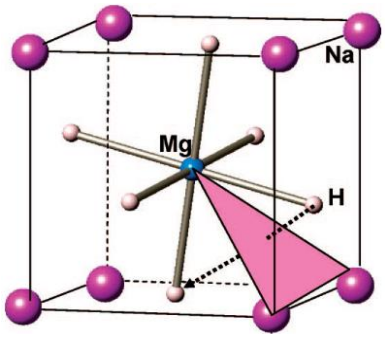

Figure 7. Schematic of the tilting of the MgH_6 octahedron and the plane defined by the triangle of 2 Na and 1 Mg for the movement of H to the adjacent side [41].

Table 3. Mg-H bond lengths in $NaMgH_3$ from different references.

	Ref [75]	**Ref** [68]	**Ref** [41]	**Ref** [69]
Mg-H bond length (Å)	1.75-2.23	1.95-1.98	1.96	1.9572 - 1.9706

I.2.c.2. Synthesis

There are several ways on how to synthesize $NaMgH_3$. Usually, a mixture of the binary hydride precursors are mixed at certain conditions. The reaction

$$NaH + MgH_2 \rightarrow NaMgH_3$$

was investigated by Klaveness et al. and they computed the ΔH for this reaction and it was found to be -143 kJ/mol [76]. For the synthesis, Ikeda et al. used 300 mg of a mixture of NaH and MgH_2 in a planetary ball mill for 20 h at 10 bar H_2 at ambient temperature [47]. Ronnebro et al. prepared $NaMgH_3$ by putting a mixture NaH and MgH_2 in a heated tube furnace for 1 week at 380°C and 70 bar H_2 pressure [68]. Sheppard et al. performed cryomilling of NaH and MgH_2 at -196°C (77K) with subsequent annealing under 50 bar H_2 at 300°C [77]. However, $NaMgH_3$ can also be formed as a secondary product of certain reactions like the synthesis performed by Pottmaier et al. where $NaMgH_3$ was formed as a secondary product of the dehydrogenation reaction between $NaBH_4$ and MgH_2 ,where the major products were mainly NaH, MgB_2, Mg, and H_2 [78].

Mechano-chemical synthesis by mechanical ball-milling has disadvantages. The steel balls can contaminate the sample powders. The process is prone to oxidation. The reaction time is usually long and the products produced have low crystallinity [79]. $NaMgH_3$ was also synthesized by mixing equimolar amounts of NaH and Mg at 480°C under 10 bar H_2 for 24 hours [75]. This method takes a long time and consumes energy due to heating for a prolonged period of time.

A good alternative is the use of a high-pressure press. $NaMgH_3$ has also been synthesized using solid state high-pressure synthesis [80][71]. A mixture of the hydride precursors, NaH and MgH_2, is placed in a metal capsule and is placed in a graphite heater which is then assembled into the large volume press, where it is subjected to high pressure and high temperature. Recently, new hydrides are being synthesized in this manner as it brings an interesting approach compared to conventional methods.

I.2.c.3. Hydrogen Sorption Properties

The hydrogen storage property of $NaMgH_3$ was first reported in 2005 by Ikeda et al [81]. Reversible hydriding and dehydriding processes were confirmed with 6.0 ± 0.3 wt.% of hydrogen released within 8 minutes at 400°C (673 K). Figure 8 shows the pressure-composition (p-c) isotherm of $NaMgH_3$ at 400°C (673 K).

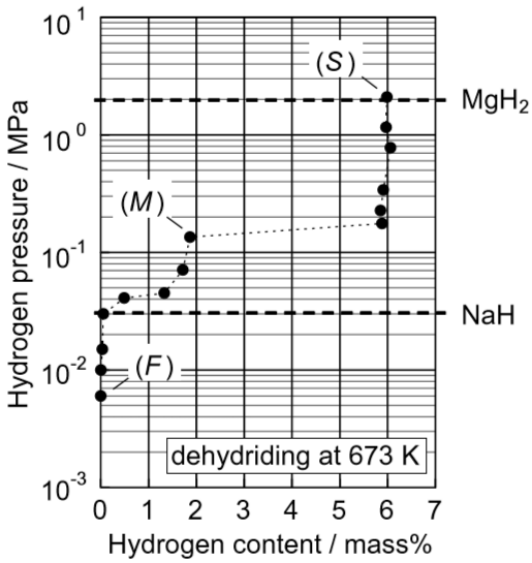

Figure 8. Pressure-composition isotherm (PCI) of $NaMgH_3$ at 400℃ (673 K). Point S corresponds to $NaMgH_3$. Point M corresponds to the first dissociation, and point F corresponds to just Na and Mg. Dashed lines are plateau pressures of MgH_2 and NaH at 400℃ (673 K) [81].

The dehydrogenation of $NaMgH_3$ occurs in two steps. At 400°C (673K), the first plateau at P~1.5 bar H_2 is for the reaction:

$$NaMgH_3 \rightarrow NaH + Mg + H_2$$

While the second plateau at P~0.45 bar H_2 corresponds to

$$NaH + Mg + H_2 \rightarrow Na + Mg + 3/2\ H_2$$

These two reactions were confirmed by XRD data and differential scanning calorimetry (DSC) studies [82]. The XRD data also shows the reemergence of $NaMgH_3$ peaks after rehydriding at 350°C (623K) under 50 bar H_2 pressure, which confirms the reversibility of the process [41].

Several thermodynamic parameters, like enthalpy (ΔH) and entropy (ΔS) for the dehydrogenation of $NaMgH_3$, were also determined. Table 4 summarizes these parameters.

Pottmaier et al. performed dehydriding and rehydriding on $NaMgH_3$ for 15 cycles. However, the hydrogen capacity decreased to 4.0% on the 15th cycle. This was due to the segregation of small isolated blocks of Na after each measurement. Low kinetics was evidenced by the hysteresis observed as the number of cycles increased [69].

Table 4. Thermodynamic parameters of the dehydrogenation of $NaMgH_3$.

	ΔH (kJ/mol)	ΔS (J/K mol)	Reference
$NaMgH_3 \rightarrow NaH + Mg + H_2$	86.6 ± 1.0	132.2 ± 1.3	[77]
	94 ± 15	140 ± 22	[60]
	92	123	[69]
	93.9 ± 0.6	116.2 ± 0.9	[47]
$NaH + Mg + H_2 \rightarrow Na + Mg + 3/2\ H_2$	102.2 ± 0.4	125.9 ± 0.6	[47]

Researchers have tried to investigate the addition of dopants in the synthesis process to produce a product with modified structures and modified properties. In terms of hydrogen storage applications, the transport properties of hydrogen in perovskite hydrides is significant to the kinetics of the hydrogen storage process. Hao et. al. investigated the addition of dopants to $NaMgH_3$ which enhanced the hydrogen diffusion process through additional charged defects, the dominant factor in H transport. Dopants such as Cu, Co, Zr, etc. were able to increase the diffusivity of hydrogen by up to three orders of magnitude compared to the undoped $NaMgH_3$ [83].

Due to the promising potential of $NaMgH_3$ as a hydrogen storage material, researchers have tried to modify $NaMgH_3$ by incorporating different elements or compounds into the perovskite structure to address the issues about its H storage efficiency. Doping is an easy technique that is cheap, and materials can be prepared at ambient conditions. Important parameters that must be taken into consideration are cation radius and cation size variances [36]. Adding dopants into the synthesis process can cause some lattice distortions in the products thereby making the structure less stable. Chaudhary et al. synthesized $NaMgH_3$ via ball-milling with Group IV elements, such as Si, that led to its hydrogen release at lower temperatures [84]. The resulting Si-doped $NaMgH_3$ had an onset desorption temperature which is 80°C lower than pure $NaMgH_3$. Wang et al., on the other hand, used carbon nanomaterials as dopants in their synthesis of $NaMgH_3$ [85]. Their results indicate that addition of carbon nanomaterials reduced the crystallite size of $NaMgH_3$ which can improve dehydriding kinetics. Their DSC analysis also revealed that the doped samples have lower dehydriding temperatures and decomposition activation energies compared to the undoped $NaMgH_3$. The defects brought about by the dopants also improved the maximum amount of hydrogen desorbed up to 3.64%

wt. compared to 3.42% wt. from the undoped sample. Another doped $NaMgH_3$ was prepared by Wang et al. using K_2TiF_6 as dopant [82]. Their XRD analysis revealed that the addition of the dopant caused some variations in the lattice parameters of $NaMgH_3$. This lattice distortion introduced into the system can facilitate better dehydriding for $NaMgH_3$. At 365°C (638K), the doped sample released 3.8% wt. hydrogen compared to 3.5% wt from the pure $NaMgH_3$. Another study from Li et al. showed improved dehydriding-rehydriding kinetics in $NaMgH_3$ [86]. They used in situ embedding of Mg_2NiH_4 and YH_3 nanoparticles into $NaMgH_3$. The Mg_2NiH_4 and YH_3-embedded $NaMgH_3$ showed no peaks for $NaMgH_3$ after dehydriding, indicating that the process is complete. They also performed several cycles at different temperatures of reversible dehydriding-rehydriding reactions for both samples. They were able to observe a continuous decay and reduction in the amount of hydrogen desorbed and absorbed for the pure $NaMgH_3$ while their embedded-$NaMgH_3$ exhibited better kinetics and negligible reduction in activity. More recently, a study of Hang et al. revealed that doping $NaMgH_3$ with a lamellar-structure 2D C-based material called Ti_3C_2 improved the hydrogen storage reversibility, showing 4.6 wt% H_2 capacity after 5 cycles [87].

In essence, doping of materials can either improve or demote certain properties. Normally, dopants are added to hydrogen-storage materials in order to decrease the desorption temperature. However, in the case of the perovskite hydride $MgNiH_3$, its decomposition temperature is -169.86°C (103.29 K) which makes it inappropriate for hydrogen storage. Based from DFT calculations of Abdellaoui et. al., doping $MgNiH_3$ with Co will increase the decomposition temperature to up to 242.15°C (515.30 K) [88]. Therefore, this calls for specific dopants for specific applications [36].

The challenge now is to investigate and develop new materials which can elevate hydrogen storage as the preferred technology and renewable energy source, and have excellent performance in terms of cost of production, ease of fabrication, purity of the material, and storage efficiency.

Using the Kissinger method, the activation energies of the two dehydriding steps from $NaMgH_3$ and doped-$NaMgH_3$ can be compared. All the references in Table 5 used the Kissinger method to determine the activation energy[89][90]. The equation in the Kisssinger method uses the heating rate, υ, and a frequency factor (Arrhenius equation), u_0 :

$$\ln\left(\frac{Tp^2}{\upsilon}\right) = \frac{\Delta E}{RT} + \ln\left(\frac{\Delta E}{Ru_0}\right)$$

where ln $\left(\frac{Tp^2}{\upsilon}\right)$ vs. 1/T are plotted and the slope is $\frac{\Delta E}{R}$, where using R, the gas constant, the ΔE can be calculated, which is the activation energy. It can be seen in Table 5 that doped samples have lower activation energies. Hence, the dehydriding process proceeds easily compared to the undoped $NaMgH_3$.

Table 5. Activation energies of the two-step dehydriding reaction of $NaMgH_3$.

Sample	ΔE_1 (kJ/mol)	ΔE_2 (kJ/mol)	Reference
$NaMgH_3$	180.25	156.23	[89]
C-doped $NaMgH_3$	113.8	126.6	[85]
K_2TiF_6-doped $NaMgH_3$	153.47	117.92	[82]

I.2.c.4. Chemical substitution

Another way of enhancing the dehydriding property of $NaMgH_3$ is by introducing an element into the crystal structure by substitution to produce novel hydrides with new compositions. Tao et. al synthesized K-substituted $NaMgH_3$ using ball-milling technique [91]. They were able to replace 10% of Na with K which resulted to a slight increase in lattice parameters due to the larger ionic size of K. As a result, partial substitution of Na with K allowed the XRD peaks for $NaMgH_3$ to shift to lower 2θ values. Their synthesized $Na_{0.9}K_{0.1}MgH_3$ was observed to have an onset desorption temperature of 157°C (430 K), which is lower compared to 308°C (581 K) of the unsubstituted sample. The substitution with K enabled the kinetics of hydrogen desorption to improve. For the unsubstituted $NaMgH_3$, it took 43 minutes to desorb 3.0% wt. hydrogen at 365°C (638 K). However, for the $Na_{0.9}K_{0.1}MgH_3$ sample, it only took 6 minutes to reach the same amount at the same temperature condition. Their DFT calculations also revealed that their K-substituted $NaMgH_3$ has a higher formation enthalpy in the *Pnma* structure. Hence, a lower stability was observed. These results have proven that partial substitution of Na with K in the $NaMgH_3$ structure can improve the dehydriding properties of the said perovskite material.

Andrada-Chacon et al. prepared several compositions of $NaMgH_3$ with partial substitutions with potassium [80]. Their $Na_{1-x}K_xMgH_3$ ($0 \leq x \leq 1$) samples were synthesized

under high pressure conditions. A mixture of the precursors were sealed in a gold capsule and subjected to high pressure and high temperature conditions (2 GPa and 775°C) using a piston-cylinder press. Their XRD analysis revealed that the Bragg peaks for $NaMgH_3$ have shifted to lower diffraction angles as x increased from 0 to 1 or as the amount of substituted K increased. This is due to the larger ionic size of K. Similarly, the lattice parameters and cell volumes increased as the amount of K substitution increased and there was a shift to lower diffraction angles of the peaks for $NaMgH_3$. Their results have also showed that the orthorhombic distortion of $NaMgH_3$ has been retained even up to x = 0.75. Hence, the K-substituted $NaMgH_3$ samples were refined in the same space group, *Pnma*.

I.2.d. Li-substituted $NaMgH_3$

Lithium has been used to modify the properties of $NaMgH_3$. It is lighter than sodium (A_{Na} = 22.99 u, A_{Li} = 6.94 u). So, once incorporated into the crystal structure, lithium would make the hydride have a higher gravimetric capacity. From here on, the Li-substituted $NaMgH_3$ will be called $Na_{1-x}Li_xMgH_3$, where x denotes the amount of Li substitution.

I.2.d.1. Synthesis

One way to synthesize Li-substituted $NaMgH_3$ is by mechanical milling, where a mixture of NaH, LiH, and MgH_2 is placed in a steel vial with small steel balls and is mechanically milled under either nitrogen [92], hydrogen [89], or argon atmosphere [93]. Another way is to use a high-pressure piston-cylinder press, where the mixture is subjected to to HP-HT conditions of 2 GPa and 750°C [71]. The diffraction peaks for $Na_{1-x}Li_xMgH_3$ with x > 0 slightly shifted to higher 2θ values relative to $NaMgH_3$ due to the partial substitution of sodium by lithium. The smaller ionic radius of Li caused the shrinkage of the cell volume of the perovskite and it becomes more pronounced as more Li is added into the structure. This volume shrinkage is shown in Table 6. The shift in the Bragg peaks here is contrary to the ones observed with K-substituted $NaMgH_3$ where the peaks shifted to lower 2θ values [80].

I.2.d.2. Crystal structure

Neutron powder diffraction data shows that $Na_{1-x}Li_xMgH_3$ also has the perovskite structure and space group *Pnma* [71]. It was noted that the MgH_6 octahedra became more distorted as a result of the smaller Li^+ ionic radius which now occupies the 12-coordinated cubo-octahedral site (A-site). A progressive distortion of this MgH_6 octahedron from x = 0 to x = 0.5 was the consequence of the structural distortion induced by Li as it is being added into the system which was clearly observed in the study as the Mg-H-Mg bond angle changes from 155.12° to 153.64°, for x = 0 to x = 0.5. From Rietveld refinement of NPD data, the maximum Li content obtained was only 0.18 from the nominal x = 0.5. The Goldschmidt tolerance factor of $Na_{1-x}Li_xMgH_3$ is 0.767 for x = 0.50. This is smaller compared to 0.807 of $NaMgH_3$, which means that Li substitution decreases the tolerance factor [89].

Table 6. Unit cell parameters for $Na_{1-x}Li_xMgH_3$ from NPD data by Martinez-Coronado et al. [71]

Nominal composition	x = 0	x = 0.25	x = 0.5
a (Å)	5.4651(6)	5.4656(5)	5.460(1)
b (Å)	7.7026(9)	7.7024(8)	7.698(2)
c (Å)	5.4135(6)	5.4065(6)	5.399(1)
V ($Å^3$)	227.88(4)	227.61(4)	226.96(9)

When x = 0.8, however, the tolerance factor was not within the perovskite range. The cell volume for x = 0.8 was larger than that of the perovskite [93]. This is quite puzzling because as more Li is added into the structure, it is expected that the cell volume would be decreasing, but at x = 0.8, the cell volume increased. This was later explained by first principles calculations by Karfaf et al [94]. According to their calculations, for a $Na_{1-x}Li_xMgH_3$, the space group transforms from *Pnma* to *R3c* at x = 0.7. Figure 9 shows the equilibrium energy obtained using the Murnaghan's equation of state. From this figure, it can be seen that the *Pnma* structure has the lowest energy up to x = 0.7. Beyond this value, the trigonal (*R3c*) structure is the most stable phase. This is a probable explanation why the tolerance factor at x = 0.8 was different from the expected value for a perovskite.

Another interesting thing from Karfaf's calculations is that as pressure is increased for $Na_{1-x}Li_xMgH_3$ samples where x = 0.7, 0.75, and 0.80, the space group reverts back from *R3c* to *Pnma*. The transition pressures are 0.32 GPa, 1.79 GPa, and 4.07 GPa, for x = 0.7, 0.75, and 0.80, respectively. The corresponding volume contraction for these transitions are 2.18%, 2.06%, and 1.84%, respectively [94].

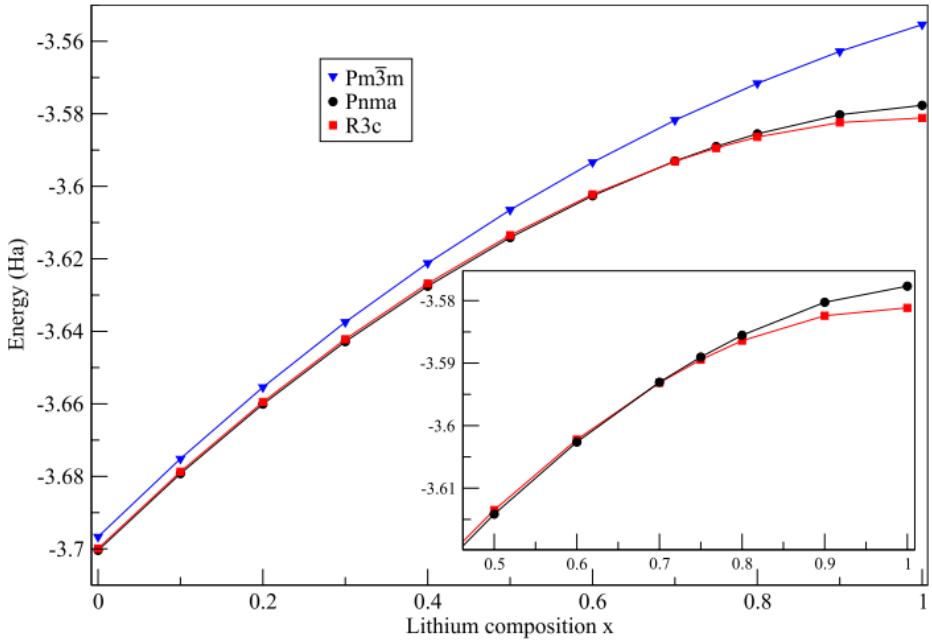

Figure 9. Energy values for the different phases of $Na_{1-x}Li_xMgH_3$ as a function of Li concentration [94].

I.2.d.3. Hydrogen sorption properties

In terms of the dehydriding properties, $Na_{1-x}Li_xMgH_3$ shows promising results. When Na is substituted with Li, the amount of hydrogen per hydride mass increases. As a result of the distortion brought about by Li-substitution, the structural stability of the perovskite decreased, and the hydrogen desorption temperature decreased by as much as 22°C compared to the unsubstituted $NaMgH_3$ [71]. Table 7 shows the behavior of the desorption temperature as a function of x, x being the nominal composition of the reactants.

Table 7. Desorption temperatures and amount of H_2 release by $Na_{1-x}Li_xMgH_3$ obtained by DSC-TGA.

Dehydriding parameters	**Ref.** [71]			**Ref.**[93]				**Ref.** [89]	
	x = 0	x = 0.25	x = 0.5	x = 0	x = 0.2	x = 0.5	x = 0.8	x = 0	x = 0.5
Desorp. H_2 (wt%)	3.41	2.95	2.82	4.6	5.1	5.1	5.2	3.42	4.11
T desorp. (°C)	435	427	413	368-389	364-389	310-369	314-350	--	--

After dehydrogenation, $Na_{1-x}Li_xMgH_3$ can be rehydrogenated by heating up to 350°C under 10 bar H_2. Figure 10 shows XRD patterns that show that the perovskite can be reversibly formed at 350°C.

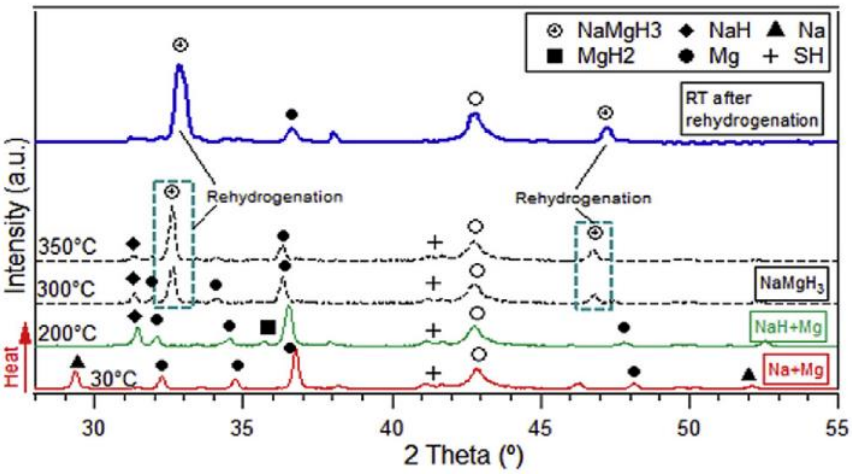

Figure 10. XRD patterns of $NaMgH_3$ (Li-substituted with x = 0.2) during rehydrogenation up to 350°C from Contreras-Vasquez et al [51].

Xiao et. al. used density functional theory to investigate four dehydrogenation pathways and tried to compute for the reaction enthalpy in order to deduce the most feasible reaction pathway [95]. The four possible reaction pathways are as follows:

$$Li_xNa_{1-x}MgH_3 \rightarrow xLi + (1-x)Na + Mg + 3/2\ H_2$$

$$Li_xNa_{1-x}MgH_3 \rightarrow xLiH + (1-x)Na + Mg + (3-x)/2\ H_2$$

$$Li_xNa_{1-x}MgH_3 \rightarrow xLi + (1-x)NaH + Mg + (1 + x/2)\ H_2$$

$$Li_xNa_{1-x}MgH_3 \rightarrow xLiH + (1-x)NaH + Mg + H_2$$

At the decomposition temperature, the Gibbs free energy is just below zero. Therefore it can be said that $\Delta H \cong T\Delta S$. To have a good reversible hydrogen storage material, enthalpy of decomposition should be $30 \leq \Delta H \leq 60$ kJ/mol H_2 provided that T is in the range of 50-150 °C and ΔS is estimated to be 95-140 J/K mol [95][96]. If ΔH is higher than 60 kJ/mol H_2, it would require higher temperature to have appreciable H_2 pressure. On the other hand, if ΔH is less than 30 kJ/mol H_2, there might be a problem in terms of the reversibility of the hydrogen desorption [96].

For pathways 2 and 4, the ΔH of decomposition decreases as Li content increases which means that lower temperatures are needed for higher Li content. It implies that these two pathways are more favorable for the decomposition. Furthermore, between pathways 2 and 4, it is pathway 4 who had a lower calculated energy, making it the most logical pathway to follow [95].

I.2.e. $KMgH_3$

I.2.e.1. Synthesis

Ashby et al. was the first one to synthesize $KMgH_3$ in 1970 [97] but it was Park et al. who first determined it in 1987 to belong to an ideal perovskite structure ($Pm\bar{3}m$) with a Goldschmidt tolerance factor of t = 0.94 [98]. Balawender et al in 1995 reported this to be t = 0.96, while Fornari et al. reported it to be 1.03, and Vajeeston et. al. reported t = 1.01 [99][72][49]. The difference in the reported tolerance factors may be attributed to the different H ionic radius used in the formula. Two reactions were shown in Ashby's investigation that led to the synthesis of this perovskite hydride. The first one was through hydrogenolysis of $KMg(sec\text{-}C_4H_9)_2H$ in benzene solution. The second one was just heat treatment of $KMg(sec\text{-}C_4H_9)_2H$ in mineral oil at 80°C under vacuum. Diffraction data of $KMgH_3$ was similar to $KMgF_3$ and since F- and H- have similar ionic radii, the perovskite structure of $KMgF_3$ was implied also for $KMgH_3$ [97]. Park's synthesis on the other hand was heating different ratios of a $KH:MgH_2$ mixture at 400°C under H_2 pressure. Bastide et. al. did a similar method as Park's but with thermal cycling between 235 and 306°C [100]. Several other investigations were made on $KMgH_3$ that gave a lattice parameter of $a \approx$ 4.010-4.035 Å [53][100][72][76][101][102][98].

$KMgH_3$ was also synthesized by reacting molten K and Mg metals from a mixture of KH and MgH_2 with H_2 gas at 15 Bar pressure and 647°C (920 K) [61]. At this temperature neither of the two binary hydride precursors are stable and this temperature coincides with the melting of Mg, thereby suggesting the said mechanism of $KMgH_3$ formation. On the other hand, small amounts of $KMgH_3$ were produced when KOH and MgH_2 were reacted in a vibratory ball mill at 1000 rpm [103]. Similarly, $KMgH_3$ was a small by-product of the rehydrogenation of ball-milled MgH_2-KOH-graphene at 300°C [104]. Lastly, it was also seen as a by-product of the reaction of LaH_3,MgH_2, and KBH_4 at 434°C (707 K) [105].

During the synthesis of $KMgH_3$, a side product can be formed. This is K_2MgH_4, a Ruddlesden-Popper hydride perovskite with a formula $A_{n+1}B_nH_{3n+1}$, where n =1 [106]. It has a tetragonal structure, which belongs to the I4/mmm space group[107]. It has lattice parameters: a = 4.032-4.036 Å, c = 13.524-13.592 Å [108][107]. Schumacher et al. mentioned that this side product can be formed when $KMgH_3$ is synthesized from the hydrogenation of K and Mg metals, and that the K and Mg mixture is inhomogeneous [61]. It has a theoretical heat of formation of -236.2 kJ/mol for the reaction shown below [109].

$$2KH + MgH_2 \rightarrow K_2MgH_4$$

Table 8. Enthalpy of formation of $KMgH_3$ based on the different pathways shown.

pathway	**ΔH (kJ/mol)**	
	Ref. [110]	Ref. [49]
$KH + MgH_2 \rightarrow KMgH_3$	-28.40	-32.23
$K + MgH_2 + ½ H_2 \rightarrow KMgH_3$	-88.92	-74.87
$KH + Mg + H_2 \rightarrow KMgH_3$	-106.95	-96.02
$K + Mg + 3/2 H_2 \rightarrow KMgH_3$	-167.47	-138.67

The standard enthalpy of formation of $KMgH_3$ was estimated to be -278.4±5kJ/mol by Bouamrane et. al. from experimental enthalpy determination for $KMgH_2F$ and K_2MgF_4 [108]. On the other hand, four possible pathways were proposed for the synthesis of $KMgH_3$. Table 8 shows the calculated enthalpy of formation for each pathway. It can be implied that pathway 4 is the most feasible pathway of synthesis.

I.2.e.2. Crystal structure

The structure of $KMgH_3$ has been studied to determine its stable structure. First-principles calculations were performed to 3 different phases of $KMgH_3$ by Reshak et al [101]. Here, structural, elastic, electronic, and optical properties were determined depending on the structure of each phase. Figure 11 shows the three different phases, including the stable one. Vajeeston et.al. described the stable form to have a $[KH_{12}]$-cubo-octahedral and $[MgH_6]$-octahedral structures, the ideal perovskite-type structure ($Pm\bar{3}m$)[49]. Aside from this stable cubic phase, another $KMgH_3$ phase which is an unusual orthorhombic was observed in another NPD experiment (λ = 1.494Å). This phase was assigned the space group *Pmmm* with lattice parameters: a = 5.227(2), b = 6.935(5), c = 5.100(3) [80].

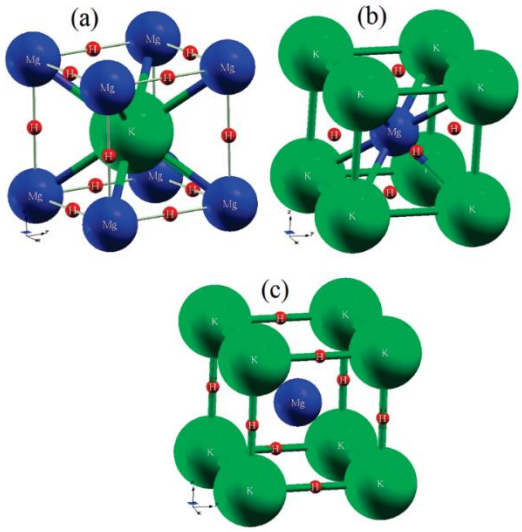

Figure 11. Three different phases of $KMgH_3$ named a)Stable, b) US1, and c)US2 in the study of Reshak et al [101].

DFT studies of electronic properties show that Mg-H bonds have an ionic-covalent nature while that of K with H and K with MgH_6 units have an ionic nature though the charge transfer from both K and Mg toward H is not complete [110][53][111]. Based on electronegativities, the bonding is predominantly ionic in nature [49][101]. Calculations also show that $KMgH_3$ is non-conducting due to a large H-H bond distance [111]. Its Mg-H bond distance is 2.012 Å which is slightly longer than that of MgH_2 (1.95Å) [111].

I.2.e.3. Hydrogen sorption property

Thermal desorption mass spectroscopy shows that this hydride decomposed around 370°C which means that it is relatively stable. PCT experiment showed that $KMgH_3$ had a single-step decomposition process. However, according to Ref. [60], the process is irreversible.

$$KMgH_3 \rightarrow K + Mg + 3/2\ H_2$$

The enthalpy and entropy change, , for $KMgH_3$ decomposition were found to be 110 ± 4 kJ/mol H_2 and 145 ± 5 J/K mol H_2, respectively [60].

I.2.e.4. Substitution

Li et al. performed first-principles studies on an M-substituted $KMgH_3$ named $K_{1-x}M_xMgH_3$ where M are alkali metals Li, Na, Rb, and Cs [112]. Acording to their calculations, all doped $K_{1-x}M_xMgH_3$ samples would favor a dehydrogenation pathway shown below

$$K_{1-x}M_xMgH_3 \rightarrow xMH + (1-x)KH + Mg + H_2$$

And among all the dopants investigated, lithium showed the lowest dehydrogenation reaction enthalpy making $K_{1-x}Li_xMgH_3$ (x = 0.0833 and 0.1667 with *R3c* structure) as the most promising for hydrogen release. They also tried to increase the pressure to 2 GPa and they found in their calculations that all M-doped samples exhibited lower dehydrogenation reaction enthalpy by as much as 0.79 eV, showing that pressure can be used to enhance the dehydriding property.

I.3. Binary hydride precursors

In this section, the different properties of the binary hydrides used as reactants in the study are discussed. Table 9 shows a summary of some of these properties. Each of these hydrides will be discussed in the succeeding subsections

Table 9. Summary of properties of the different binary hydride precursors.

	Space group	Lattice Param. (Å)	$P_{transition}$ (GPa)	$T_{melting}$ (K)	$T_{desorption}$ (K)	B_0 (GPa)	Ref
LiH	$Fm\bar{3}m$	a=4.0811	36 B1→B2	965	993	33	[113][114] [115][116][117]
NaH	$Fm\bar{3}m$	a=4.8812	28.8 B1→B2	905	681	19.4	[118][119] [120][121]
KH	$Fm\bar{3}m$	a=5.575	3-4.9 B1→B2	673	545	15.6±1.5	[122][123] [124][125][126]
MgH_2	$P4_2/mnm$	a=4.5010 c=3.0100	0.6-5.5 α→γ→β		560	50.2-52.57	[127][128][129] [130][131][132]
CaH_2	*Pnma*	a=5.961 b=3.607 c=6.842	15.5	1089	>1273	48.83	[133][134][135]

I.3.a. Magnesium hydride, MgH_2

Magnesium hydride, MgH_2, at ambient pressure and temperature normally exists in its α-phase which is tetragonal in structure, and which belongs to the *P42/mnm* space group. Upon application of pressure at room temperature, MgH_2 transforms into several other phases as observed from several theoretical and experimental studies (Figure 12).

DFT analysis by Vajeeston et al showed that MgH_2 successively transforms from α to γ, and then to β (number 8 in Figure 12) [127]. It was found that α-MgH_2 transforms into γ-MgH_2 which has the orthorhombic α-PbO_2 structure at pressure above 0.39 GPa. The transformation can also occur with ball milling and mechanochemical treatment [136]. The MgH_6 octahedra of the α-phase have similar Mg-H bond lengths in the axial position and equatorial positions (1.94 Å and 1.97 Å, respectively). The MgH_6 octahedra of the γ phase however, has different Mg-H bond lengths that range from 1.91 to 2.0 Å [136]. According to Bastide et al. both α and γ phases coexisted at 2.5-8 GPa and 250-900°C [137]. This coexistence of phases was also observed by El-Eskandarany et al. where reactive ball milling showed that the α and γ phases transform from one form to the other depending on the milling time, i.e. the phase transformation goes back and forth due to the small difference in the energies of the two

phases [138]. Kohlmann et al. observed that no α to γ phase transition was observed up to 9.3 GPa at room temperature (number 3 in Figure 12) [139]. Experiments from a DAC at room temperature, on the other hand, showed an α to γ phase transition between 0.9-9.0 GPa. Beyond 9.0 GPa, another orthorhombic phase (named HP1 with the *Pbc21* space group) existed (number 2 in Figure 12) [129]. Moriwaki et.al. said that the α and γ phases of MgH_2 co-existed at 0.9-9.0 GPa[129].

Aside from the γ phase, other phases were observed at higher pressures. First principle calculations showed that α to γ phase transition occurs at 1.2 GPa while γ to β phase transition occurs at 9.7 GPa. The β-phase belongs to the space group $Pa\bar{3}$ (number 7 in Figure 12) [140]. Vajeeston et al. had both theoretical and experimental data for phase transformations. Experimentally, both α and γ phases coexist up to a certain pressure before the β phase appears at around 10 GPa. Beyond 10 GPa, all three phases transform into an $AuSn_2$-type phase δ', which is a little different from the predicted phase that is orthorhombic (*Pbc21*). At 5.5-9.5 GPa both α and γ phases coexist. At 9.35-10.36 GPa, all three phases coexist (number 4 in Figure 12) [130]. El-Eskandarany et al.'s experiment showed that the cubic β-MgH_2 phase was observed when α-MgH_2 was subjected to cold rolling and high energy ball milling, but decomposed to α and γ phases when annealed at 220°C [141].

In addition, a comprehensive phase diagram was made by Moser et al. using DFT which shows P-T relationship and the different phases present [142]. This is shown in Figure 13 as pink circles.

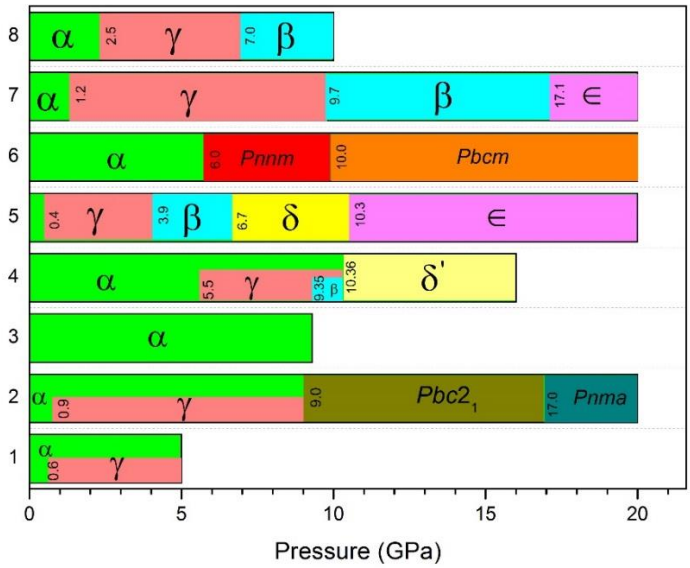

Figure 12. Phase transformations of MgH_2 at room temperature based on theoretical (5-8, Ref.[127][143][140][142]) and experimental (1-4, Ref. [128][129][139][130]) data.

The large discrepancy in the description of MgH_2 P-T phase diagram may be explained on one side by the difficulty of fine calibration in experimental measurements and on the other side, the high metastability of the compounds under extreme conditions. Experiments using HP-HT techniques were performed to obtain information on the α, γ , and β phases of MgH_2 at conditions other than ambient P and T. Figure 13 shows the phase diagram from the results of some experiments with MgH_2, including the one performed in this thesis using a Paris-Edinburgh Press at 2, 4, and 7.4 GPa. Here, the region where either α or γ phase, or a combination of both, was observed is shown as squares. The yellow circles show the region where the β phase was observed. Bortz et al. used a multianvil cell at 2 GPa and 797°C (1070K) to observe this α to γ phase transition. However, the transformation was not complete [144]. Goto et al. found both the α and γ phases at 5 GPa and 950°C [145]. Moser et al. observed the γ phase appearing at 4.3 GPa and 627°C (900 K) [146]. On the other hand, a belt-type HP device was used by Bastide et al. and ex-situ analysis revealed the formation of the β phase at 8 GPa and 800°C. It was also seen as a coexisting phase with α and γ phases at 3.5-4GPa and 800°C. At a lower temperature of 650°C and 4 GPa, it coexisted only with the α phase [137]. Also included in the figure are experimental data from the current study, which somewhat show no consensus with the rest. It has to be noted that utmost care must be considered when comparing in-situ characterization and post-mortem analysis. Our experiments show a larger range of stability of the α-phase which extends up to 100°C and 7.4 GPa, while the β–phase was observed at 7.4 GPa at T>300°C. The existence of the γ-phase at 7.4 GPa and 140°C (413 K) in our experiment is somewhat consistent with the DFT data in the phase diagram in Figure 13 as it is near the γ- β phase boundary. At 7.4 GPa and 279°C (552 K), our experiment is still consistent with the DFT phase diagram as it is near the γ- β phase boundary. The β-phase was experimentally observed by Bastide at 650°C (923K) at 4 GPa, and at 800°C (1073K) at 8 GPa. In comparison, in the present experiment, the β-phase appeared at a lower temperature of 327°C (600K) at 7.4 GPa.

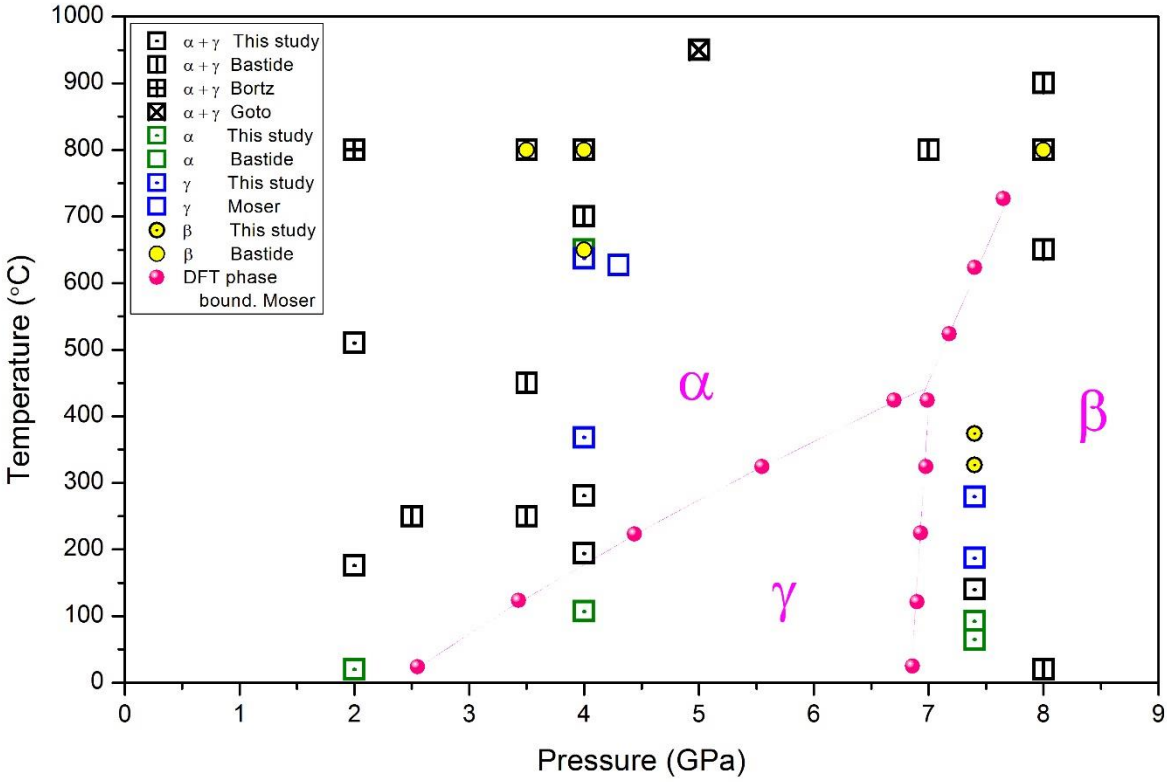

Figure 13. Pressure-Temperature phase diagram of the different phases of MgH_2 at high temperature from experimental data [147][144][146][145], including this study. DFT data from Moser et. al [142] are shown in pink. Squares mean either alpha or gamma or both. Yellow circles mean beta.

According to DFT studies by Emilsson et al., hydrogen desorption energies for all these three phases of MgH_2 are all similar. So, hydrogen desorption for MgH_2 does not depend on the crystal structure [148].

I.3.b. Hydrides of Li, Na, and K

Lithium hydride, sodium hydride, and potassium hydride all have a face-centered cubic (B1 NaCl-type) structure and have the *Fm-3m* space group. At room temperature, B1(NaCl)-B2(CsCl) phase transition occurs at 36 GPa, 29.3±0.9 GPa, and 4.0 GPa, for LiH, NaH, and KH, respectively [114][121][125].

LiH has a melting temperature of 692°C (965 K) and at 20 GPa, the calculated melting temperature is 1277±50 °C (1550±50 K) [117][113]. At ambient pressure, the experimental melting temperature of LiD, on the other hand, was bracketed between 675-700°C (948- 973

K) [149]. On the other hand, NaH has a melting point of 632 °C, while KH has a melting point of 400°C [118][122].

Going down the column of Table 9 while looking at LiH, NaH, KH, it can be noticed that there is a decreasing trend in terms of the melting temperature and the pressure of phase transition as we move from Li to K. The same can be said to the temperature of hydrogen desorption. This can be attributed to the arrangement of these metals in the periodic table, where Li, Na, K all belonging to Group IA metals with the following trend in atomic radius: Li<Na<K.

For its hydrogen desorption property, LiH was found to have a very high dehydrogenation temperature of 720°C (993K) [115]. On the other hand, ball-milled NaH started to desorb hydrogen at 408 °C. It desorbed 3.53 wt% H_2 vs 4.20 wt% theoretical [120]. On the other hand, another experiment showed that under H_2 pressure of 1 bar, NaH decomposes to Na at 427 °C. It also showed that a pressure greater than 106 bar H_2 is needed to prevent decomposition at 632°C [118]. Lastly, the equilibrium between KH and K and H_2 occurs at a hydrogen pressure of 0.305 kPa at 272°C [124].

I.3.c. Calcium hydride, CaH_2

Calcium hydride has an orthorhombic structure and belongs to the *Pnma* space group. At ambient pressure, calcium hydride shows an allotropic transformation at 780 °C similar to the α→β BaH_2 transformation [150][151]. On the other hand, at room temperature, calcium hydride can also undergo pressure-induced phase transformation. At about 15.5-21 GPa, Raman studies using DAC confirmed this phenomenon [133]. Moreover, DFT studies showed a $PbCl_2$-type (Pnma)-to-$InNi_2$-type ($P6_3$/mmc) phase transition at 16 GPa [152]. Similarly, an experiment using DAC confirmed this phase transition using Raman and XRD experiments [153]. The decomposition temperature of CaH_2 at 1 bar H_2 pressure is >1000°C and its melting point is 816°C [134]. Calcium hydride is found to be stable after the HP-HT treatment at 5 GPa pressure and 950°C (1223 K) temperature [145].

I.4. High-pressure and high-temperature (HP-HT) synthesis of perovskite hydrides

I.4.a. Generalities about HP HT

Pressure is a thermodynamic variable that can determine most of a material's properties. It can influence the microstructure, the interatomic interactions, and chemical bonding. Pressure is considered as the amount of force applied to a certain unit of area, but pressure can also be expressed as the amount of energy per unit volume. As an example, when 1 GPa of pressure is applied to a body-centered cubic (BCC) Fe metal, 2 kJ/mol of energy per Fe-Fe bond is applied [154]. So, a pressure of 10 GPa is comparable to energies in a weak chemical bond, while a pressure of 100 GPa is comparable to energies in a strong covalent bond. Knowing the changes in the properties of the material is a good way of understanding the effect of high pressure on chemical bonding [154].

High pressure synthesis can be categorized into two, depending on the way pressure is generated: 1. Autoclave type with gas media, and 2. Anvil-type apparatus [155]. The former works by placing pellets of precursors in an autoclave under gas pressure which is heated for a long time. Deuterides such as Cs_2MgD_4 and Cs_3MgD_5 were synthesized by placing pellets of a mixture of CsD-MgD_2 in an autoclave under 65 bar of D_2 gas at 352°C (625 K) for 5 days [156]. The latter, on the other hand, works generally by placing the powdered samples in capsules placed in anvil cells where it will be subjected to high pressure and high temperature. Sato et al. were able to synthesize novel Mg-Nb hydrides by placing the precursors in NaCl capsules in a multi-anvil cell at 8 GPa and 600°C [157]. The role of HP-HT is significant here as Mg and Nb do not alloy at ambient pressure.

To form a new compound, the product has to have a lower free energy than those of the precursors combined. A general rule requires that the ΔV be negative under pressure for the reaction to proceed forward [158]. Demazeau called it the densification effect, such that for a reaction A + B = AB to occur, $V_A/Z_1 + V_B/Z_2 > V_{AB}/Z_3$ should be the case. This means that application of pressure helps the synthesis of AB [159].

Using high pressure, new materials can be synthesized that were never synthesized before because these conditions were not yet accessible. With high pressure, new materials can be synthesized mainly through four routes as discussed by Zhang et al [160].

First of these four routes is through phase transition. Manjon et al. made a comprehensive review of different phase transitions happening to rare-earth sesquioxides such as Lu_2O_3, Yb_2O_3, Tm_2O_3, Eu_2O_3, etc. Here, they discussed that under high pressure, these

materials tend to transition from a cubic phase to a monoclinic phase and at extreme conditions may further transition to a trigonal phase [161]. Likewise, a high pressure-induced semiconductor-to-metal phase transition was observed by by Lin et al. on an inorganic halide perovskite $Cs_2In(I)In(III)Cl_6$ [162]. With these different phases present, a multitude of synthesis pathways or potential applications can be made available.

Second is by stabilizing new stoichiometries. High pressure can play a role in altering the chemical composition, making it possible to produce compounds with unusual stoichiometries. Struzhkin et al. was able to synthesize NaH_3 and NaH_7 which are quite unusual than the typical NaH [163]. These compounds were only accessible at 40 GPa and 1727°C (2000 K). Another example is in the Ca-H system, where a compounds such as CaH_6 and CaH_{12} exist in the pressure range of 150-200 GPa [162].

Third is by enabling new chemical reactions. As discussed by Zhang et al., high pressure can influence the electronic orbitals of elements and thus, altering their chemical reactivity [160]. As an example, potassium does not react with silver at ambient conditions, but K_3Ag, K_2Ag, and KAg_2 were formed [164]. On the other hand, $MgNi_2$ does not readily react with hydrogen [165][166]. However, with HP-HT conditions of 2.8-7.4 GPa and 300°C, $MgNi_2H_3$ was formed with this mixture of $MgNi_2$ and hydrogen [167].

And fourth is by changing the electronic properties. When interatomic distances are reduced during compression, interatomic interactions become more pronounced, leading to a broadening of the energy bands. These band overlaps can cause pressure-induced phase transitions [160]. Proof to this is the pressure-induced transition in the vicinity of 25-30 GPa of magnetite, Fe_3O_4, where significant changes were seen on its magnetic and electronic properties [168]. In a similar manner, a pressure-induced electronic transition called core-level crossing transition was observed in Iridium metal at pressures of up to 140 GPa [169].

High pressure can also stabilize high and intermediate oxidation states. An example of a high oxidation state element is Fe(V), which can be stabilized at high pressure. On the other hand, an example of an element with an intermediate oxidation state is Cr(IV), the disproportionation of which to Cr(III) and Cr(VI) is prevented at high pressure [158].

As mentioned, compounds that initially cannot be formed at ambient pressures can now yield, upon compression, novel phases that were never observed before. Pressures of up to 100 GPa are now easy to reach with the development of multianvil presses and diamond anvil cells (DACs) [170]. The use of the DAC has some limitations for neutron powder diffraction applications. For this, the Paris-Edinburgh Press was developed. More details will be given in Chapter II.

In the DAC, a sample is placed in between the culet faces (flat faces) of two tiny opposing diamonds (Figure 14). Application of force across the wide face of the diamond would generate immense pressure on the sample though the flat face [171]. In addition to being able to generate pressure, diamonds are also good optical probing windows. It is possible to heat samples up to 6427°C (6700 K) using high-power lasers though the diamond windows even at pressures near 200 GPa [172]. However, with DAC, only small amounts of samples can be analyzed. For a larger sample size, large-volume presses are used to allow experiments on the determination of physical properties of materials under high pressure and high temperature. Millimeter-sized sample holders are used and the highest achievable pressure and temperature are around 40 GPa and 2727°C (3000 K), respectively [171].

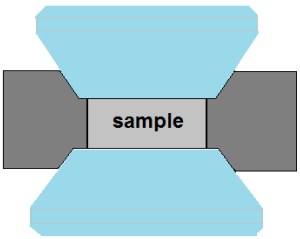

Figure 14. Schematic representation of the sample in the DAC being compressed by two opposing diamonds (in light blue).

I.4.b. The perovskite structure under HP-HT

Compression at high pressures in perovskite structures can provide the way to overcome some steric and electronic limitations in the crystal packing by inducing changes to the metal coordination sphere, changes to the bond lengths, changes to the interoctahedral tilting. Other things that can occur are symmetry-altering phase transitions, local distortions, and partial amorphization [173]. The last one mentioned, amorphization, occurs when the lattice's long-range order begins to be broken due to severe distortions during compression [174]. Two things happen in the lattice upon compression: 1. Octahedral tilting, and 2. Bond contraction (Figure 15). Both phenomena can affect the orbital overlaps and band dispersion in the atoms. These affects the structural and electronic properties of the perovskite. As an example, a change in color indicates a shift in electronic properties. This was observed in Cu(II)-Cl perovskite at elevated pressures. At 4 GPa, the translucent yellow perovskite material

underwent a color change to red, and eventually at 8 GPa to opaque black [175]. As mentioned, these distortions can cause amorphization. In a study by Zhang et al. on the perovskite $CsPbBr_3$, they observed a certain threshold of pressure at 20.0 GPa. Beyond this point, certain peaks in their XRD analysis disappeared which accounts to the amorphization of the perovskite material [174].

In perovskite hydride materials, the location of the H atoms, the tilting of the BH_6 octahedra, the presence of hydrogen vacancies, etc. are among the things to be considered when investigating their hydrogen sorption/desorption kinetics [176]. So, it would be interesting to see the effect of HP on these parameters.

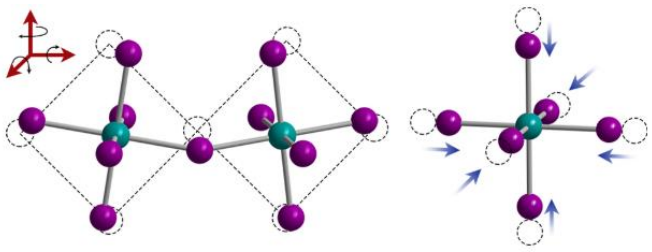

Figure 15. Octahedral tilting (left) and bond length contraction (right) experienced by the BX_6 octahedra in perovskite during compression [173].

In the case of perovskite oxides, ABO_3, the BO_6 octahedra tilt to compensate for any size difference brought about by the ion present on the A-site, and alleviate structural constraints [177]. In the case of the synthesis of a perovskite hydride ATH_3 (A = Li, Na, K, Rb; T = Fe, Co, Ni) by Takagi et al. bond lengths A-H and B-H are also important. Lattice instability has been an issue during compression frustration of the corner-sharing octahedral which makes synthesis difficult. They said that substitution of Li with larger cations would balance the preferred A-H and B-H bond lengths and would therefore lower the tolerance factor to unity [178]. Thus, making way for the synthesis of the target material. Based on this, it would be interesting to see if a certain group of perovskite hydrides can be synthesized by employing the concept of substituting ions in the structure.

1.4.c. Synthesis of hydrides using HP-HT

A lot of hydrides have been synthesized using different high-pressure techniques. Kyoi et al. used a multi-anvil cell with pressures of up to 8 GPa to synthesize magnesium-based hydrides with Zr and Hf [179]. Bertheville et al. also used a multi-anvil cell to synthesize new ternary Cs-Mg hydrides at 3 GPa [63]. Torres et al. prepared a new hydride $Mg_3CuH_{0.6}$ using a novel synthesis procedure using a hydrostatic high-pressure technique with a piston cylinder press at 3.5 GPa [180]. The same piston cylinder was used by the team of Martinez-Coronado to synthesize Mg_2NiH_4 at 2 GPa [181] and by the team of Retuerto to synthesize Mg_2FeH_6 at 2 GPa [79]. Goto et al. synthesized novel Mg-Li and Mg-Pd hydrides using a cubic-anvil-type apparatus at a pressure of 2-5 GPa [182]. Using the same cubic-anvil-type apparatus, Kamegawa et al. synthesized several Mg-based hydride systems with Y, La, Ce, Pr, Sm, Gd, Tb, and Dy at pressures of up to 6 GPa [183]. Novel quaternary hydrides of Mg,Ti with Li, Na, or K, were likewise synthesized using an ultrahigh pressure technique at 8 GPa [184].

High pressure increases the rate of the solid state reactions happening at high temperatures, where the perovskite is formed by ionic diffusion between the component precursors [185]. For the synthesis of a perovskite hydride, ABH_3, four synthesis pathways were proposed by Li et al [54]. These four pathways are the following:

$$A + B + 3/2\ H_2 \rightarrow ABH_3$$
$$A + BH2 + ½\ H_2 \rightarrow ABH_3$$
$$AH + B + H_2 \rightarrow ABH_3$$
$$AH + BH_2 \rightarrow ABH_3$$

The first and last pathways are the ones usually done in experiments. The first pathway was used for the preparation of these perovskite hydrides: $CaNiH_3$ [42], $CaPdH_3$ [186], $BaPdH_3$ and $SrPdH_3$ [187]. The fourth pathway where equimolar mixtures of the binary hydrides were used, on the other hand, was the pathway used for the synthesis of some hydrides such as $BaLiH_3$ [188], $CsCaH_3$, $RbMgH_3$ [64], $SrLiH_3$ and $EuLiH_3$ [189].

Chapter Summary

Solid state hydrogen storage has been studied since the last quarter of the 20th century. The development of efficient hydrogen storage system is still the focus of researchers nowadays as the search for the perfect material that can be synthesized easily, that can store the hydrogen most, that can function at lower temperature, and that can be used for several cycles, is still on.

Perovskite hydrides as hydrogen storage materials have been one of the focus of hydrogen research owing to their lightness, and high gravimetric capacity. Although they show promise in the hydrogen storage field, there are still some issues that need to be addressed in order for these materials to kick off as the perfect material for the job.

In this first chapter, we have presented the state of the art about perovskite hydrides regarding synthesis, crystal structure and hydrogen sorption properties. A focus was made on $NaMgH_3$, $Na_{1-x}Li_xMgH_3$, and $KMgH_3$, which are the subjects of this thesis.

Also, synthesis at high pressure is indeed a very useful technique that enables researches to explore the possibility of existence of certain materials at certain pressure and temperature conditions that were not previously accessible. It is one of the motivation of our work to investigate the synthesis of perovskite hydrides by the use of HP-HT.

The next chapter deals with the experimental techniques that were used to synthesize light metal hydrides. Characterization techniques (X-ray and neutron diffraction, DSC) will be described.

Chapter II. Experimental techniques

In this chapter, we describe the different processes conducted for the synthesis of our perovskite hydrides. We begin with materials preparation and handling. Then, we describe the different high-pressure techniques used. Finally, we present the characterizations performed for the said samples.

II.1. Materials preparation

Metal hydride powders (NaH, MgH_2, LiH, KH, CaH_2) were purchased from Sigma-Aldrich. All procedures involving these hydrides were performed under Ar atmosphere inside a glovebox maintained at <1.0 ppm O_2 and H_2O. Other powders used were BN (Aldrich), Cu (Prolabo), MgO (Alfa Aesar), and commercial NaCl (La Baleine). For all sample preparations involving these powders, after weighing, they were ground first for a couple of minutes using a mortar and pestle to have a homogenous mixture.

II.2. Synthesis using HP-HT

In this work, most of the synthesis and characterizations were performed using large volume presses. Here, we mention two large volume presses used in the study which are available at Institut Néel: CONAC press, and belt press.

II.2.a. The CONAC press

The CONAC press used in Institut Néel came from the Societe Savoisienne de Verins Hydrauliques, Albertville. It has a maximum working pressure of 6 GPa and a maximum temperature of 1200°C. The maximum amount of sample is about 690 mm^3. About 1.5 g of a given sample was encapsulated in a capsule made of either gold or platinum. The capsule was then assembled according to Figure 16 and was placed in between the two WC plates as shown in Figure 17. The pressure was increased to the desired pressure, in tons, at a rate of 7 tons/min.

Then, the temperature was increased using a graphite heater at 50 W/min (Joule effect). Pressure and temperature were controlled using a PID (proportional integral derivative) controller. The HP-HT state was held for the desired duration (e.g. 2h), after which a quench was performed. This temperature quenching is essential to prevent the reversibility of chemical reactions at high pressures [158]. Afterwards, the pressure was slowly decreased at a rate of 7 tons/min. The gold capsule was retrieved from the assembly and was opened, under argon atmosphere in a glovebox, to recover the sample for further analysis.

Pressure and temperature values were determined using calibration curves performed prior to experiments. For this press, pressure calibration was performed using small wires of Bi, Tl, and Ba placed in the middle of the sample assembly, which have known phase transition pressures. A copper wire pierced into the sample assembly was used to measure the variation in resistance to monitor the pressure of the phase transition, when the pressure was increased little by little. Temperature calibration was performed using a BN sample in a gold capsule. A K-type thermocouple is pierced into the sample assembly to measure directly the temperature of BN at different values of heating power.

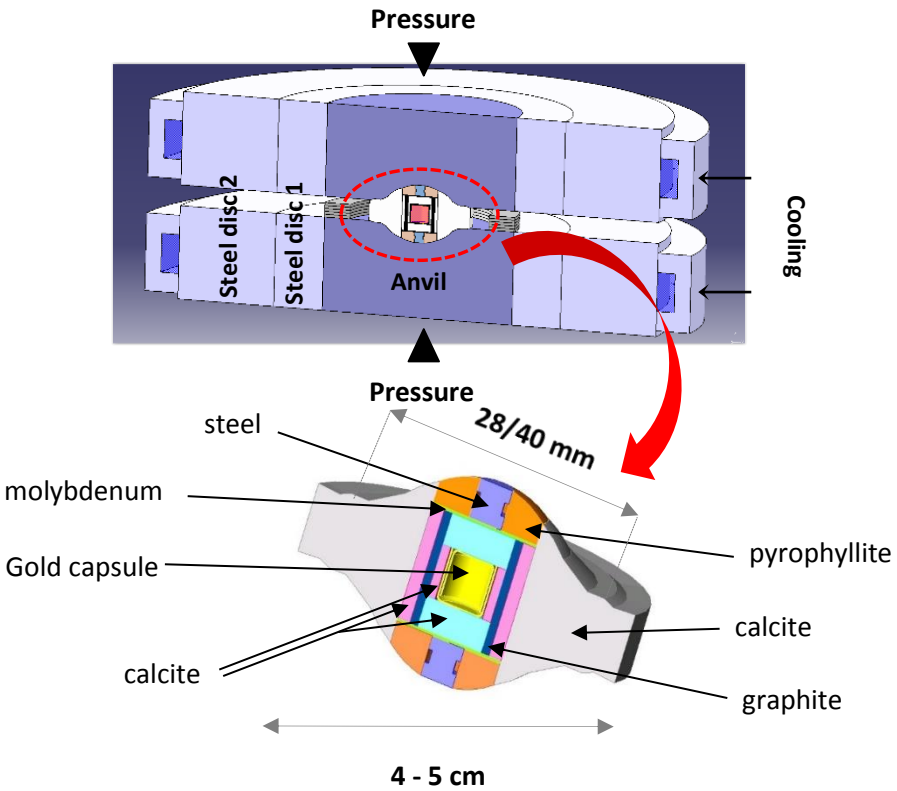

Figure 16. Sample assembly shows the powder sample enclosed in a gold capsule (bottom photo) which is sandwiched between two WC plates (top photo).

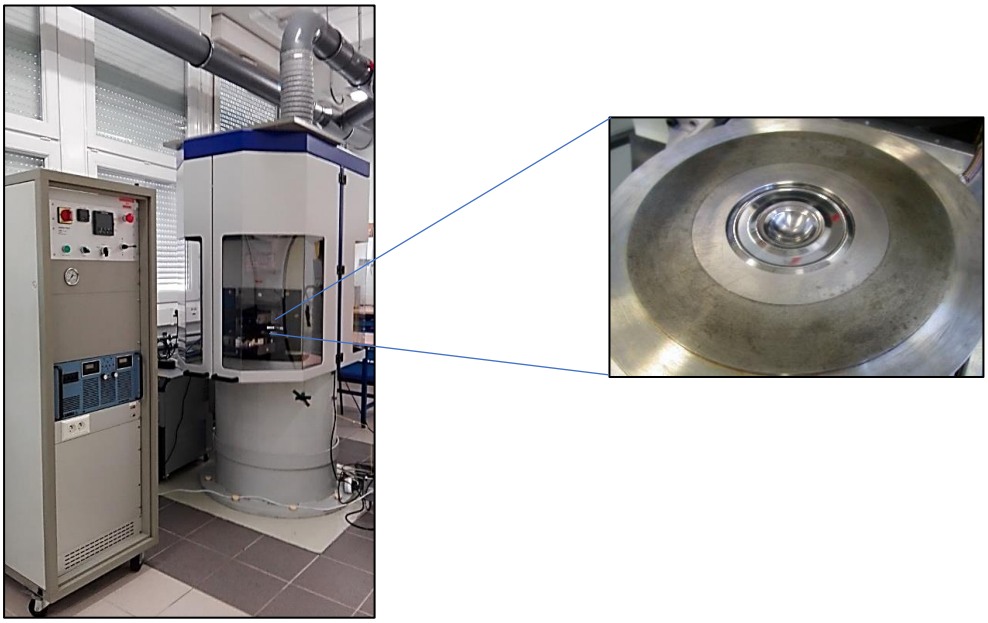

Figure 17. The WC plates of the CONAC press (right) is shown where the assembly previously described is placed in the center for high-pressure experiments.

II.2.b. The Belt press

About 200 mg of a given sample was encapsulated in a capsule made of either gold or platinum. The capsule was then assembled according to Figure 18. The capsule is smaller compared to the ones used in the CONAC press with dimensions of just 6mm x 3mm, which can hold only about 30 mm^3 of the sample. The belt press was used for the preliminary experiments and optimization of synthesis parameters because it only requires a small amount of sample. The pressure and temperature program is similar to the used in the CONAC press except that the speed of increase/decrease of pressure was 5 tons/min. The gold capsule was retrieved from the assembly and was opened to recover the sample for further analysis. Pressure and temperature values were determined using calibration curves performed prior to experiments. The pressure and temperature calibration methods and concepts were similar to the ones performed with the CONAC press. The difference is just the manner of assembly of the Cu wire and the thermocouple due to the difference of shape and configuration of the sample assembly.

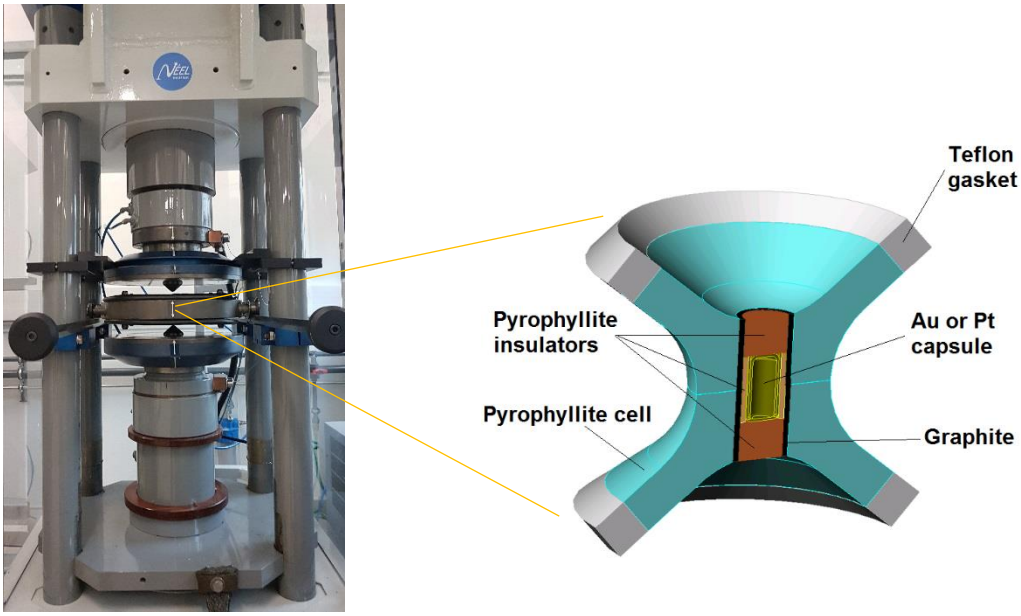

Figure 18. Assembly of the belt press (schematic and actual).

II.3. The autoclave

The high-pressure reactor available at Institut Néel is made of 316 stainless steel and can resist up to 600°C and 200 bar H_2.

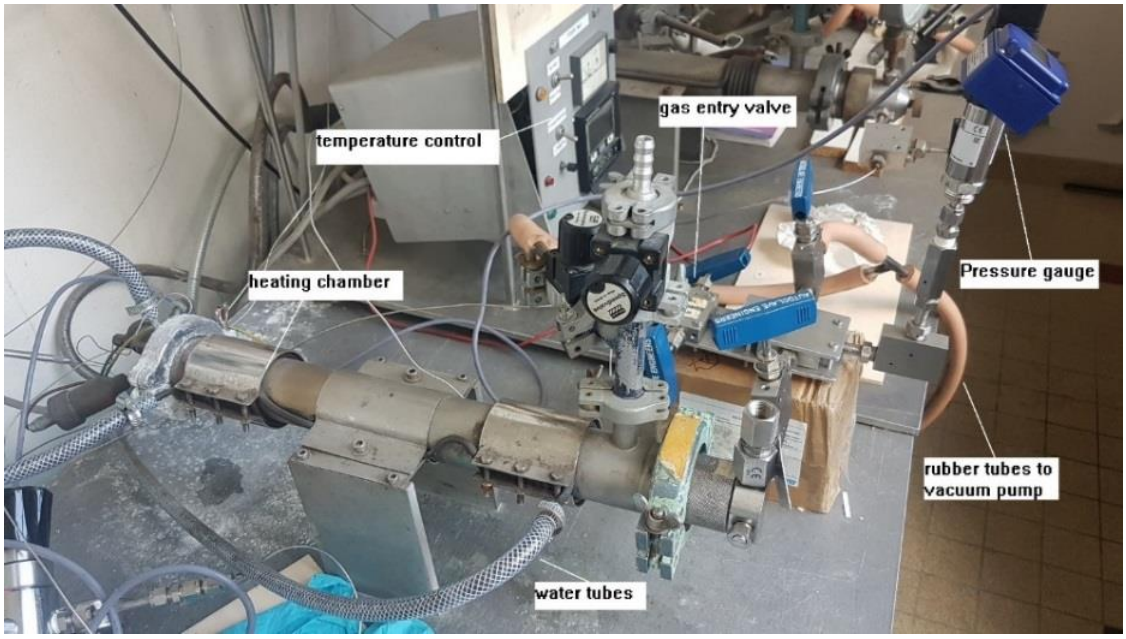

Figure 19. The autoclave used at Institut Néel.

For the synthesis of $NaMgH_3$, about 100 mg of an $NaH:MgH_2$ mixture was pressed into 5mm pellets and placed in an alumina crucible protected by a glass tubing and silica wool. The tube assembly was placed inside the autoclave and closed air-tight inside an Ar glovebox. Different samples were heated for 24h, 48h, and 6.5 days, all at 400°C under 70 bar H_2 pressure (with several purges prior to filling with gas). The autoclave setup is shown in Figure 19.

The autoclave was also used to deuterated samples before NPD measurements. In the case of $NaMgH_3$, the deuteration was performed at 325°C for 8 days under D_2 pressure of 40 bars with purging of D_2 gas every 2 days. In the case of $KMgH_3$, the deuteration was performed at 290°C for 4 days under D_2 pressure of 50 bars with purging of D_2 gas every 24 hours.

II.4. X-ray diffraction analysis

II.4.a. Experimental set up

X-ray diffraction analysis of air-sensitive materials was performed in transmission using a Siemens D5000T X-ray diffractometer. Samples were placed in a sealed borosilicate glass capillary tubes with a diameter of either 0.5 mm or 0.7 mm, and analyzed in a rotating capillary configuration (Figure 21). The scan performed was from 10° to 90° 2θ values with a step size of 0.016° using Cu Kα =1.54247 Å and was done for 12 h 19 minutes. Non-air-sensitive powders were analyzed using a Bruker D8 Endeavor X-ray diffractometer. Samples were placed in a standard sample holder. The scan performed was from 10° to 90° 2θ values with a step size of 0.01° using Cu Kα =1.54247 Å. Data analyses were performed using DIFFRAC EVA Software and Rietveld analysis using FullProf suite.

II.4.b. Phase identification and Rietveld refinement

Phase identification was performed using the EVA software. The PDF-4+ database of ICDD (International Center for Diffraction Data) was used in the EVA software to identify the phase of each corresponding peak in a given XRD diffractogram. Afterwards, Rietveld refinement was performed. In Rietveld refinement, the measured intensity at each point in the pattern is considered. Here, structural model parameters, as well as instrumental parameters, are adjusted until the computer software obtains a least-square best fit between the

experimental and calculated patterns. Originally developed for neutron powder diffraction data analysis, this method is now heavily used for X-ray data analysis [190][191]. The FullProf software was used for Rietveld refinement. The peak shape function used was Npr = 7 (Thompson-Cox-Hastings). Refined parameters include the lattice parameters a, b, and c. Also, the shape factors, X, Y, and GauSiz were refined. When applicable, the temperature factor, Bov is also refined. For the U,V, and W parameters, an .irf file was used based on a previously performed experiment with a silicon calibrant. Background points were selected manually using WinPlotr.

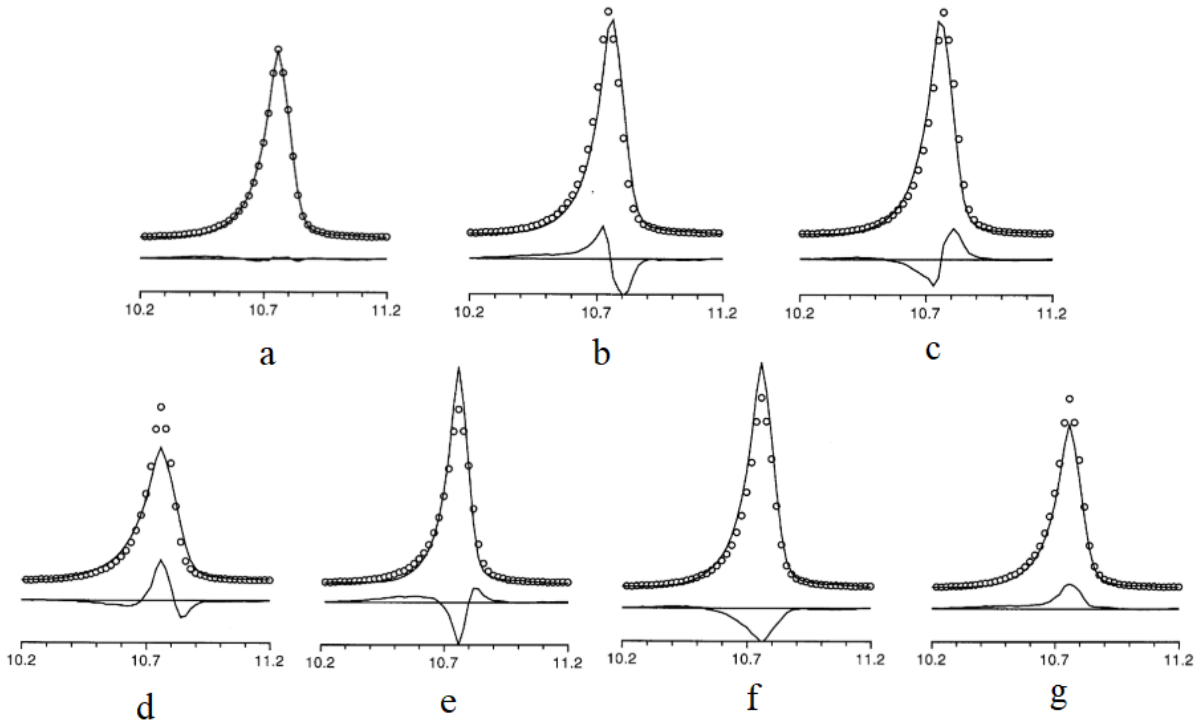

Figure 20. Calculated profiles shown as solid lines and experimental profiles shown as circles for (a) a good fit (b) a peak that has a larger 2θ (c) a peak that has a smaller 2θ (d) a peak with a larger FWHM (e) a peak with a smaller FWHM (f) a calculated intensity that is too high, and (g) a calculated intensity that is too low.

All equations and comments in this section were obtained from the Rietveld refinement guidelines of Mccusker et. al [192].

The correction of 2θ due to displacement of the sample for the Debye-Scherrer geometry with a capillary sample is

$$\Delta 2\theta = \frac{x \sin 2\theta - y \cos 2\theta}{R}$$

Where x and y are displacements of the capillary and R is the radius of the goniometer circle.

The equation for the Gaussian component of the peak shape shows the variation of the FWHM as a function of 2θ:

$$FWHM^2 = U\,tan^2\theta + V\,tan\theta + W$$

and the equation for the Lorentzian part:

$$FWHM = X\,tan\theta + {}^{Y}/_{cos\theta}$$

Profile parameters such as peak width, asymmetry, and peak intensity can be refined once the peak positions have been matched correctly. Figure 20 b and c show a peak mismatch. It shows a -/+ or +/- difference profile. It means that we have to adjust the 2θ values of the calculated peak. When the mismatch has been solved, we can look at the parameters that require further refinement and they can be identified by closely looking at the difference profiles. Figure 20a shows a good fit where the difference profile resembles a flat line. Figure 20 f and g show a difference in intensity of the calculated peak, one being higher than the experimental peak(f) and the other being lower than the expected (g). Figure 20 d and e show the effect of incorrect peak widths (FWHM). The difference profile shows a characteristic "-/+/- or +/-/+" pattern.

During the refinement, the quantity S is minimized where S is:

$$S = S_y + c_w S_G$$

Where c_w is the weighting factor that allows a weighting of the geometric observations `data-set' with respect to the diffraction data-set, S_y is the weighted difference between the observed and calculated diffraction patterns, S_G is the weighted difference between the prescribed and calculated geometric restraints.

The agreement of the calculated and experimental patterns are given a numerical value in terms of R. The weighted-profile R or R_{wp} is defined as:

$$R_{wp}\left\{\frac{\sum_i w_i[y_i(obs) - y_i(calc)]^2}{\sum_i w_i[y_i(obs)]^2}\right\}^{1/2}$$

where y_i(obs) is the observed intensity at step i, y_i(calc) is the calculated intensity , and w_i is the weight. This R_{wp} value should approach the statistically expected R value, R_{exp}:

$$R_{exp} = \left[\frac{(N-P)}{\sum_i^N w_i[y_i(obs)]^2}\right]^{1/2}$$

Where N is the number of observations and P is the number of parameters. The R_{exp} value describes the quality of data. The ratio of R_{wp} and R_{exp} is the goodness of fit. This is shown as:

$$\chi^2 = \frac{R_{wp}}{R_{exp}}$$

A good fit is when χ^2 is close to 1. This is a good indicator of the quality of refinement but it should not be overinterpreted. There should be a good and logical chemical sense of the structural model. The interatomic distances, bond angles, chemical composition, and other cell and atomic parameters should be reasonable.

Figure 21. The rotating capillary configuration of the Siemens D5000 diffractometer. An eyepiece is attached to center the capillary prior to measurement.

II.5. Paris-Edinburgh Press for in situ X-ray diffraction

Those in the field of Earth Sciences and Mineralogy are concerned with structural information and characterization of matter under extreme conditions of pressure and temperature – the same condition there is in the deep portion of the planet Earth. Due to this interest, there is a need to develop high-pressure and high-temperature techniques that can mimic the same conditions of the Earth's interior [193]. Materials that were synthesized at high

pressure and high temperature conditions can still remain intact and stable once the pressure and temperature are quenched. A popular example of this is diamond, which can in fact persist indefinitely [170]. However, some phases are not recoverable at ambient conditions especially those undergoing phase transitions. Some quenched samples may have slight differences in some properties like the degree of cation order and H-bonding configurations. Hence, it is better to obtain in situ X-ray or neutron diffraction data for these kind of samples to really investigate certain phenomena at high pressure and temperature conditions [193].

In the early 90's, the use of Diamond Anvil Cells had some limitations for neutron powder diffraction applications because it requires larger sample size and other high-pressure techniques had some problems with background scattering from the sample with pressures of just up to 3 GPa. So, in 1992, Besson et al. developed a compact 50 kg cell that consisted of a toroidal anvil which is compressed by a small hydraulic press (250 tons) [194]. This setup was remarkable at that time due to its compactness and applicability for neutron diffraction studies. Figure 22 shows the sample cell and Figure 23 shows the press which is a Type V press with four outside columns. This is the earliest "Paris-Edinburgh" press (PEP) developed by scientists from Paris, France and Edinburgh, UK.

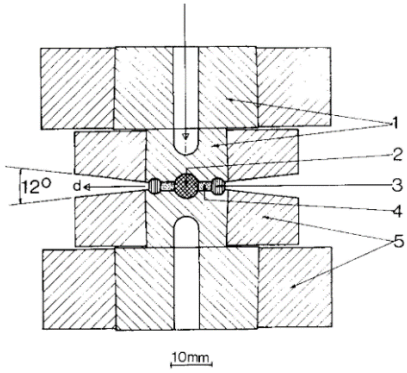

Figure 22. Cross section of the high-pressure anvils from Besson et al [194]. Shown are the (1) WC anvils (2) sample space (3) toroidal gasket (4) pyrophyllite gaskets and (5) steel rings.

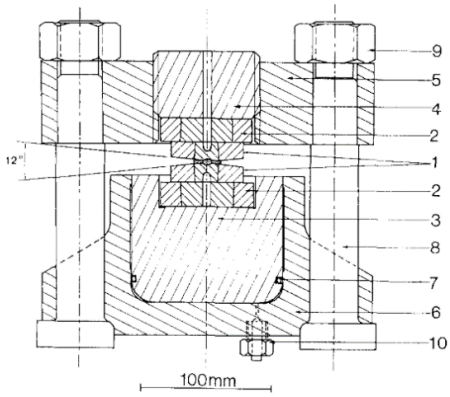

Figure 23. Cross section of the 250 ton press from Besson et al [194]. Shown are the principal parts (1) anvil and sample assembly, (3) main piston, (8) one of four columns, and (6) hydraulic ram.

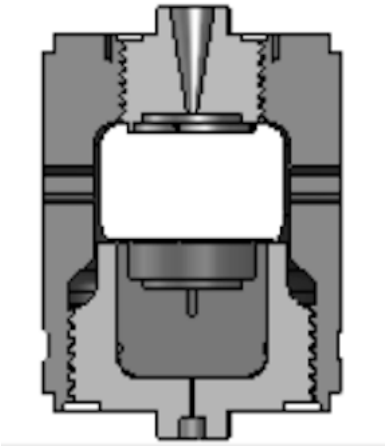

Figure 24. A VX5 type Paris-Edinburgh Press used at Institut Néel.

The PEP has been adapted to XRD experiments that use intense X-ray beams from synchrotron light sources. A different type of PEP that is called a VX5 type has only 2 columns on the sides to allow diffraction without blockage (Figure 24) Advantages of these types of experiments include small sample volumes, which allow experiments at even higher pressures, and significant decrease in acquisition times [195]. The standard design of the Paris-Edinburgh Press has a limited pressure and temperature domain (8 GPa and1927°C (2200 K)) and investigators wanted to expand their curiosity into materials synthesized at even more extreme conditions. There was great interest in in situ studies of new superhard materials, minerals in deep-Earth conditions, and physicochemistry of materials [196]. For this reason, some improvements and modifications were made with the PEP.

New design in cell assembly with internal heating and with new method of temperature measurement was done on the PEP[193]. Also the capability of the press to gather low-temperature data down to -163°C (110 K) was also developed [197]. In 2005, Le Godec et al. developed a compact PEP that was able to reach pressures of up to 25 GPa and temperatures as high as 2027°C (2300 K). It was used at the ID27 beamline of the European Synchrotron Radiation Facility (ESRF) for in situ XRD experiments [196]. In 2007, Morard et al. improved the PEP set-up by using sintered diamond anvils which enabled them to investigate by in-situ X-ray measurements difficult samples such as liquid Fe-FeS eutectic systems under extreme conditions of pressure and temperature (P = 17 GPa, T = 1027°C (1300K)) [195]. Another remarkable setup was presented by Toulemonde et. al where they have developed an in situ XRD set up using a PEP with a laboratory-sized microbeam monochromatic X-ray source [198]. This was their solution to the problem of having limited beamtime access in large synchrotron facilities. This developed facility was also used in exploring P-T phase diagrams

of different compounds and can also be used in the synthesis of metastable phases under high pressure that are up to now remain unexplored. In our study, PEP was used for in-situ neutron diffraction and XRD experiments in the laboratory.

Assemblies used in HP synthesis experiments require a gasket with the following characteristics: good electric and thermal insulation, high mechanical strength and stability at high pressure and temperature, has the ability to deform plastically without breaking, and has minimal absorption for X-ray and/or neutrons [193].

The experimental set-up conceived at Institut Néel is a VX5 type with only 2 columns on the sides (Figure 24). It is mounted on 2 stages that move vertically and horizontally to align the sample with the X-ray beam. The pressure is increased using a manual hydraulic piston pump from 0 to about 350 bar in increments of about 50 bar. The oil pressure (in bar) and sample pressure (in GPa) are calibrated using calibrants such as NaCl, Cu, BN, and MgO. During experiments, X-rays ($\lambda\alpha_1$= 0.559421 Å, $\lambda\alpha_2$= 0.563813 Å) coming from an Incoatec Ag microfocus X-ray source hits the sample precisely at the center. The position of the sample was centered using a diode. The diffracted rays were then collected by a MarXperts mar345s fast image plate detector. The patterns generated in the detector were azimuthally integrated and analyzed using the Dioptas software to determine the lattice parameters of the compounds. Each measurement was performed for at least 2 hours. The pressure was not regulated during X-ray exposure. So, the average of the initial and final pressure was used as the reported pressure for each run.

At high-temperature conditions, the temperature was increased using a power supply from 0 W to about 100 W that generates a current that flows into the sample that generates the heat. Any high-temperature experiment must be performed on the same day. The temperature increase program should be well-planned and must be finished on the same day because stopping the heating mechanism may affect the sample as some phases may appear or disappear depending on their stabilities.

The power coming from the power supply and the corresponding sample temperature were calibrated using the same calibrants stated above, which are discussed in the succeeding section. Lattice parameters were again determined and the appropriate equations of state (EOS) were used in the analysis.

Samples were placed in a BN capsule and were then assembled according to Figure 25. The boron-epoxy gasket is 5mm wide and the hollow part has a diameter of 1.5 mm. The BN capsule was enclosed in a graphite capsule which is in contact with molybdenum disks which in turn are in contact with a steel ring at the outermost part. These will ensure the conduction

of current during the high-temperature experiment in which electrical current is applied (heating by Joule effect). The MgO powder placed inside the steel rings serve as an insulator to protect the anvils from overheating, to ensure that the sample inside is being heated and that only few amount of heat is escaping. The assembled gasket is placed and fixed between two WC anvils using a clamp Figure 25. This fixes the tiny pieces in position to prevent oxidation. The fixed anvils were then placed in the Paris-Edinburgh press shown in Figure 26. Here, the press is a Type VX5 press that only has two columns on the side, instead of four. The metal parts that fix the anvil in place were removed prior to increase in pressure in the press.

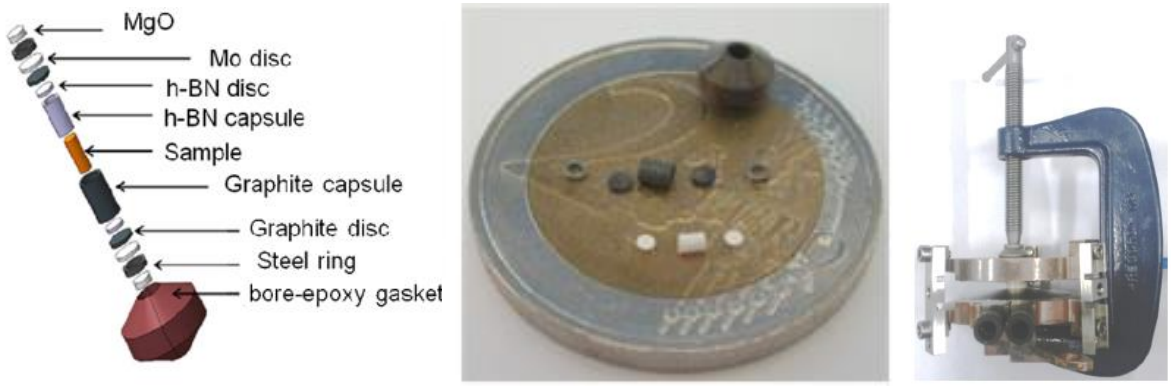

Figure 25. The different components in the assembly shown as arranged (left photo) and how they look like using a coin as a scale (middle photo) and clamped anvils with the sample in the middle (right photo)

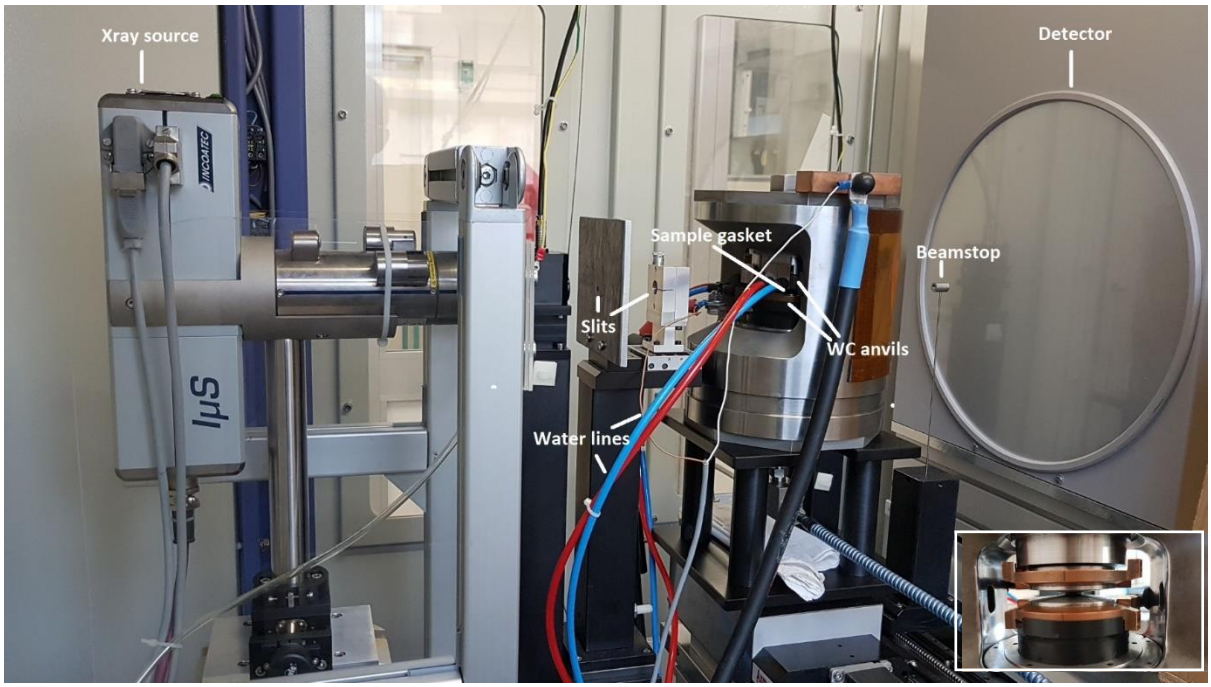

Figure 26. The Paris-Edinburgh press used for in-situ XRD under high-pressure and high temperature. The two WC anvils where the samples are placed are also shown as an inset.

II.5.a. Pressure calibration data for the Paris-Edinburgh Press

Similar to the other presses mentioned, calibration is performed using a mixture of standard samples. Here, a mixture of NaCl, MgO, and Cu was prepared having a mass ratio of 48.8:13.7:37.5. The mixture was placed in a BN capsule and were then assembled according to Figure 25. Pressure was calibrated first. The same procedure in terms of pressure increase in section II.5 was performed. XRD patterns for each pressure step were analyzed using PowderCell to determine the lattice parameters of each component. The obtained lattice parameters were fitted using the equations of states shown in Table 10 to obtain the relationship between the oil pressure (O.P.) of the pump in bar and the actual sample pressure (S.P.) in GPa. A polynomial fit was performed and the final curve is shown in Figure 27. The obtained polynomial fit was further used to determine the experimental conditions without the use of internal calibrants. The sample pressure obtained has an uncertainty of ± 0.02 GPa. The equation of the polynomial fit obtained is:

$$S.P. = [0.03197(\pm 0.00047) \times O.P.] - [0.000030(\pm 0.000002) \times O.P.^2]$$

Table 10. Equations of states used for the calibration of pressure of the Paris-Edinburgh Press.

	Author	**Ref.**
NaCl	Brown	[199]
	Birch	[200]
	Decker	[201]
MgO	Utsumi et.al.	[202]
	Saxena et.al.	[203]
Cu	Greef et.al.	[204]

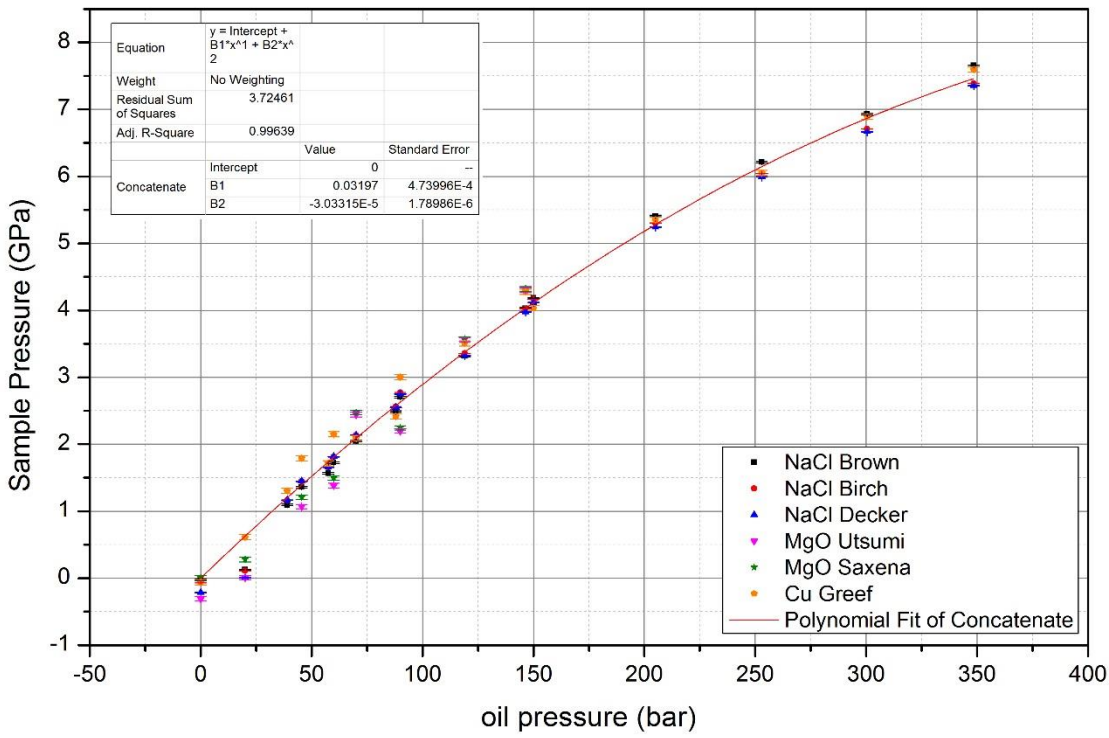

Figure 27. Pressure calibration curve for the WC anvils used in the Paris-Edinburgh Press.

II.5.b. Temperature calibration data for the Paris-Edinburgh Press

A mixture of NaCl, MgO, and Cu was prepared having a mass ratio of 48.8:13.7:37.5. The mixture was placed in a BN capsule and were then assembled according to Figure 25. The same procedure in terms of pressure increase was performed as described in section II.5. The temperature calibration was performed at 2 and 4 GPa. The pressure was set based on the calibration curve previously obtained in section II.5.a. Once the target pressure is reached, the heating power is increased step by step. XRD patterns for each heating power step were analyzed using PowderCell to determine the lattice parameters of each component. The obtained lattice parameters were fitted using the equations of states shown in Table 10 to obtain the relationship between the heating power and the actual sample temperature. A linear fit was performed and the final curve is shown in Figure 28 and Figure 29. Only the data points from Cu and MgO were used in the linear fit as NaCl has a lower thermal expansion coefficient [205]. The temperature obtained from the equation in Figure 28 has an uncertainty of ± 4°C. The equation for the calibration at 2 GPa is:

$$Temperature\ (°C) = 10.43403(\pm 0.36139) \times Power + 20$$

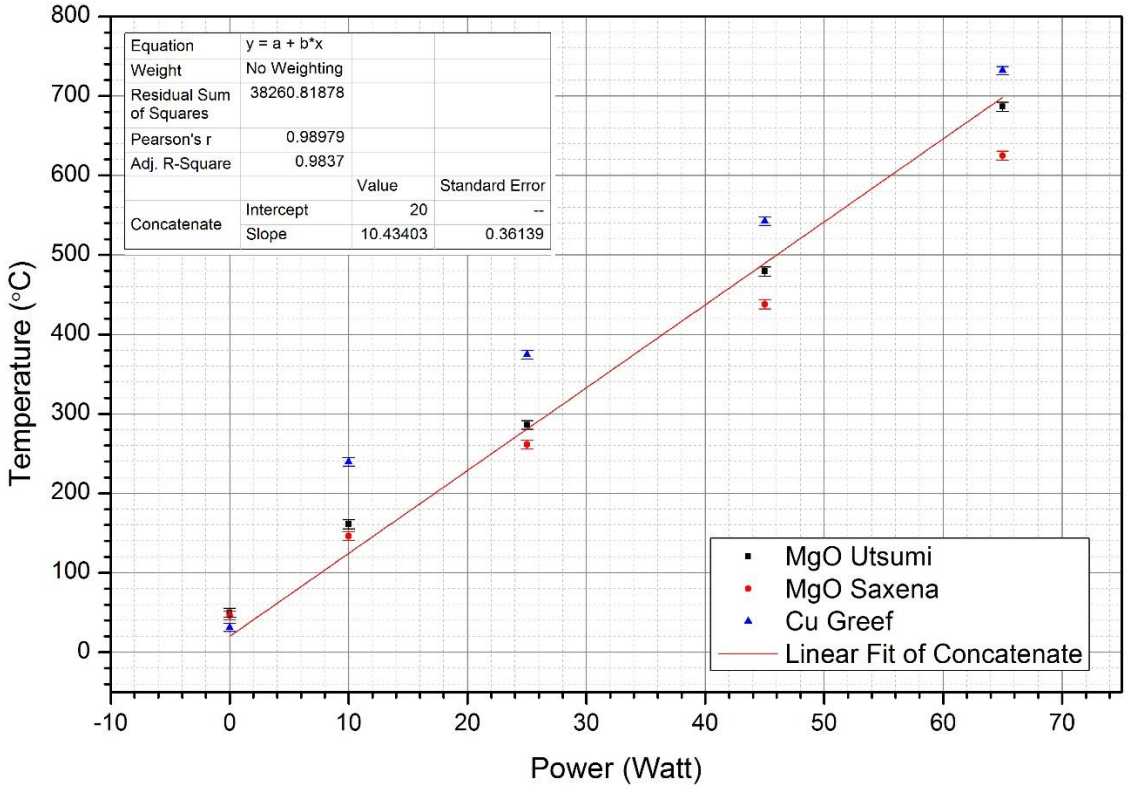

Figure 28. Temperature calibration curve for the Paris-Edinburgh Press at 2 GPa.

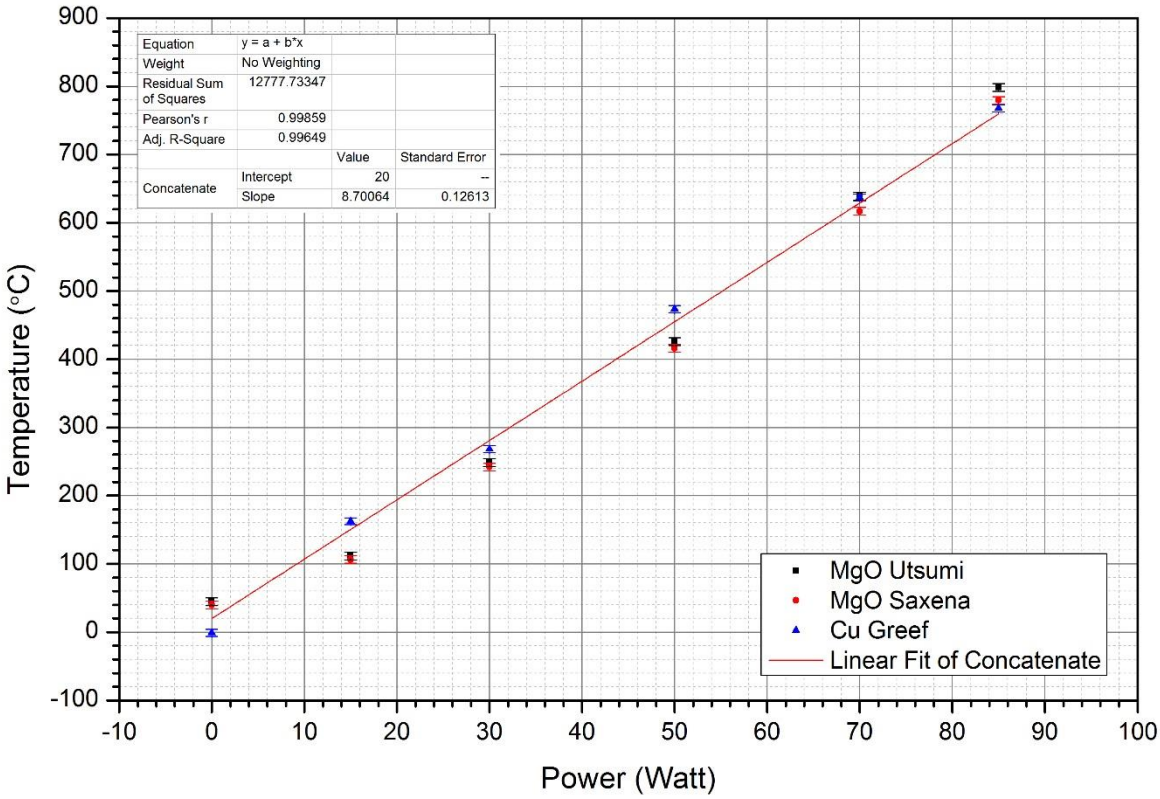

Figure 29. Temperature calibration curve for the Paris-Edinburgh Press at 4 GPa

The temperature obtained from the equation in Figure 29 has an uncertainty of ± 1°C. The equation for the calibration at 4 GPa is:

$$Temperature\ (°C) = 8.70064(\pm 0.12613) \times Power + 20$$

II.6. Paris-Edinburgh Press for in situ Neutron powder diffraction

Neutron powder diffraction experiments were done at the D1B two-axis diffractometer of the Institut Laue-Langevin (ILL), Grenoble, France. NPD patterns were collected at 27°C (300 K) with a wavelength of 2.52 Å selected by a pyrolytic graphite (002) monochromator. The flux at the sample is 7.9 x10^6 n/cm^2s. The D1B high intensity two-axis powder diffractometer at the ILL covers an angular range of 0.8° to 128.8° with a high efficiency $^3He/CF_4$ position sensitive detector (PSD). The schematic set-up of the D1B instrument is shown in Figure 30.

Measurements on reactive hydrides was made possible by a specific set-up developed by S. Klotz (IMPMC) with the help of C. Payre (ILL).

The sample pellet, which is 3.7 mm thick for $NaMgD_3$ and 3.25 mm thick for $KMgD_3$, was placed in a TiZr gasket and was placed in between sintered diamond anvils (Figure 31). The sample, gasket, and anvils were prepared in an argon glove box. The assembly was clamped in the glove box before transferring to the PEP to avoid oxidation. Prior to this, the original samples, $NaMgH_3$ and $KMgH_3$, were deuterated in an autoclave using the method described in II.3.

Measurements at the beamline were performed at different pressures (0-10.7 GPa for $NaMgD_3$ and 11.63 GPa for $KMgD_3$). Data were collected for about 2 hours at low pressures and up to 6 hours for high pressures (>6 GPa). The pressure transmitting medium used was NaCl which was about 50% v/v of the pellet. Pressure determination was performed by fitting the lattice parameter of NaCl, used here as a pressure transmitting medium and internal calibrant, with the Brown's equation of state [199].

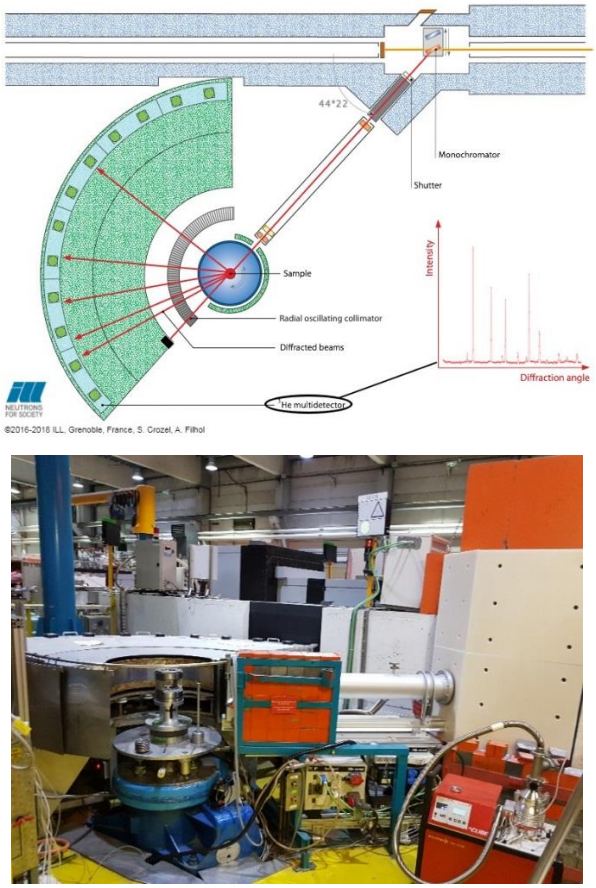

Figure 30. Instrument layout of the D1B diffractometer at the ILL (top) and the actual experimental set-up (bottom). Small inset shows a sample diffraction pattern. Radial oscillating collimator eliminates parasitic diffraction. Image taken from ILL website.

Figure 31. The Paris-Edinburgh Press (VX5 type) set-up in the D1B diffractometer (left). The sample pellet as it is placed in the TiZr gasket (right). The right photo was taken while the set-up is inside an Ar glovebox.

II.7. Determination of Thermal Properties

II.7.a. Differential Scanning Calorimetry

Investigation of the thermal properties was performed using a Nietzsch DSC 3500 Sirius. The samples were heated up to 585°C using different heating rates: 5, 10, and 20 K/min under a continuous nitrogen flow of 20 mL/min. The samples were sealed in a CrNi steel (AlSl 316L) hexagonal crucible with lid, so called "high pressure crucible" and resistant to pressure up to 100 bars. A gold sealing disk, which also contains 26% Ag and 15.5% Cu, was placed between the crucible and the lid. An empty crucible was used as reference. 5.5 mg of sample was used for $NaMgH_3$ and $(Na,Li)MgH_3$ while 3.1 mg was used for $KMgH_3$.

Chapter Summary

In this chapter, the techniques implemented for the study of lightweight hydride perovskites are described. It covers the synthesis process based on high pressure with the description of the materials preparation, the use of the autoclave and large-volume presses. The use of the Paris-Edinburgh Press for in-situ analysis of synthesis products was also presented.

Structural and thermal characterizations allowed a deeper investigation of the perovskite products. A detailed description of the experimental protocols for the pressure-induced phase transformation studies was provided, as well as a description of the Rietveld analysis performed.

Chapter III. Synthesis and characterization of perovskite hydrides

This chapter presents the results and discussion of the three main materials that were successfully elaborated namely, $NaMgH_3$, $Na_{1-x}Li_xMgH_3$, and $KMgH_3$. Here, the manner of synthesis will be discussed and structural investigations at ambient conditions will be presented. In addition to these compounds, time and energy were dedicated in an exploratory work for the synthesis of two perovskite hydrides predicted to be stable by *ab initio* calculations but were never formed experimentally. Unfortunately, it was not conclusive and this part of the work on $LiMgH_3$ and $NaCaH_3$ is proposed in appendices I and II, respectively.

III. 1. $NaMgH_3$

III.1.a. Preliminary experiments with an autoclave

As shown in Figure 32, $NaMgH_3$ was successfully synthesized from NaH and MgH_2 under H_2 atmosphere at 400°C and 70 bars H_2. Peaks for $NaMgH_3$ belonging to the *Pnma* space group were observed. The compound is formed after a 24h treatment. However, a pure $NaMgH_3$ phase was not produced. Peaks for unreacted NaH and MgO originating from the MgH_2 reactant were present. The results obtained were consistent with the synthesis performed by Bouamrane et al. at 480°C, 10 bar H_2 pressure and 24 h treatment time [75].

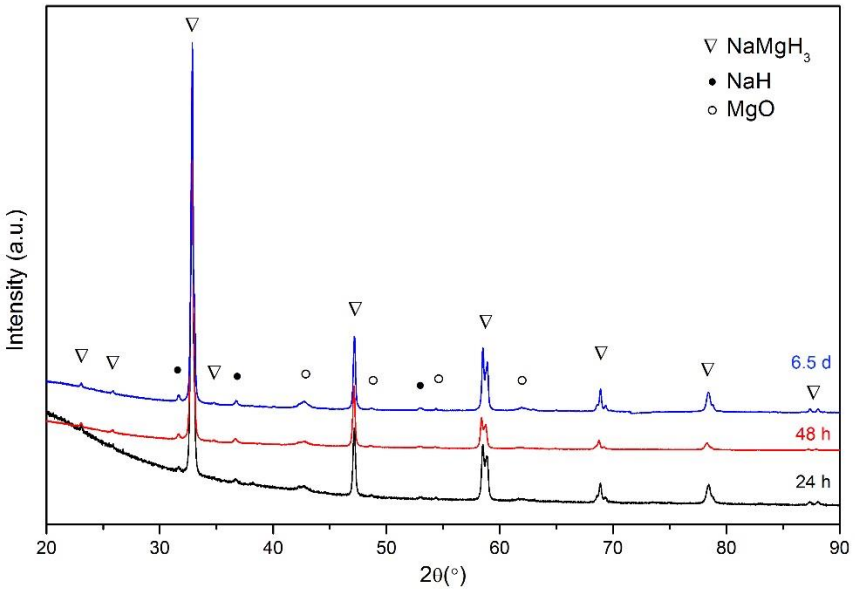

Figure 32. XRD patterns of products from the $NaMgH_3$ synthesis using the autoclave at 400°C, 70 bar H_2 pressure, using different treatment times

III.1.b. Preliminary experiments with the CONAC Press

The synthesis of $NaMgH_3$ from binary hydrides, NaH and MgH_2, was first attempted using the CONAC Press. Synthesis conditions, such as temperature and treatment time, were optimized in the process. Preliminary experiments were performed at a pre-selected pressure of 4 GPa for 30 minutes. The temperature was varied from 450°C to 650°C. Based on the phase quantification during Rietveld refinement of XRD patterns of the products (Table 11), the temperature for the succeeding experiments was set at 650°C because it produced the most $NaMgH_3$ in the set. Then the treatment time was changed from 30 minutes to 4 hours. Rietveld refinement of the XRD pattern revealed that more $NaMgH_3$ was formed at longer treatment time. However, more MgO was also formed at prolonged treatment time. With this, the standard treatment time was fixed at 2 hours. So, all succeeding syntheses using the CONAC press were set at 4 GPa, 650°C, and 2 hours.

Table 11. Mole fractions of different components from the synthesis of $NaMgH_3$ using the CONAC press at 4 GPa using 30 min treatment time at different temperatures. Quantification was performed by Rietveld refinement of XRD data.

	450°C 30 min	**550°C 30 min**	**650°C 30 min**	**650°C 4 h**
$NaMgH_3$	0.20(1)	26.78(29)	78.72(71)	85.19(70)
NaH	48.02(1.11)	34.99(42)	8.66(68)	2.38(12)
α-MgH_2	31.87(74)	22.66(25)	3.55(13)	-
γ-MgH_2	15.94(37)	9.08(21)	-	-
MgO	2.26(5)	6.49(17)	9.07(67)	11.88(24)
Mg	1.71(4)	-	-	-
R_{wp}	*4.37*	*13.3*	*8.45*	*10.4*
χ^2	*9.89*	*6.37*	*4.28*	*3.83*

III.1.c. Structural characterization

Rietveld analysis was performed on the NPD patterns collected to identify the lattice parameters of $NaMgD_3$. Figure 33 shows the NPD pattern of $NaMgD_3$ placed in a vanadium

cylinder at room temperature. The structure parameters are presented in Table 12, while bond lengths and bond angles are shown in Table 13, all of which coincide with literature data.

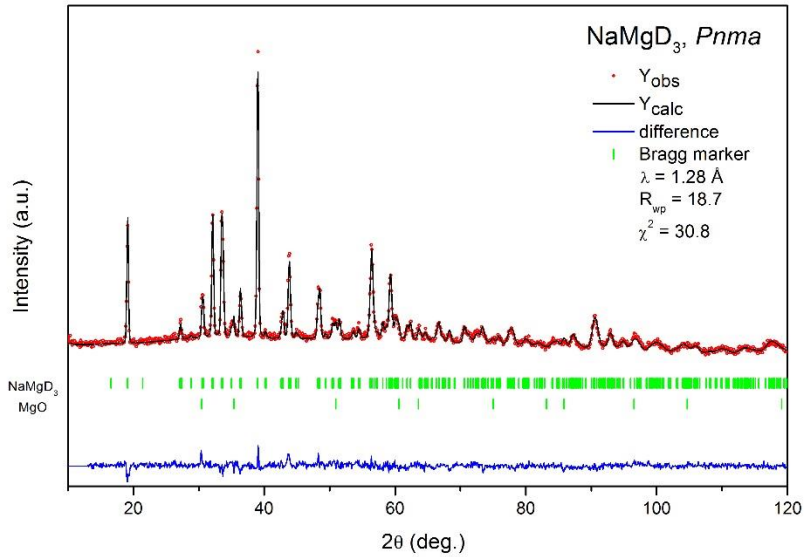

Figure 33. NPD pattern of $NaMgD_3$ at ambient pressure and Rietveld analysis. Refined parameters: a, b, c, X, B_{iso}, and atomic positions.

Table 12. Structure parameters of $NaMgD_3$, space group: *Pnma*. Lattice parameters (Å): a = 5.39996(39), b = 7.68316(56), c = 5.45257(39)

	This study	**Ref.** [41]	**Ref.** [68]
	25°C (298 K)	**27°C (300 K)**	**25°C (298 K)**
Na (*4c*) *x*	0.02120(267)	0.0215(2)	0.015(2)
y	0.25	0.25	0.25
z	0.00937(368)	-0.0040(2)	-0.018(2)
Mg (*4b*) *x*	0.0	0.0	0.0
y	0.0	0.0	0.0
z	0.5	0.5	0.5
D1 (*4c*) *x*	-0.01734(162)	-0.0175(3)	0.064(1)
y	0.25	0.25	0.25
z	0.42637(157)	0.4273(3)	0.483(1)
D2 (*8d*) *x*	0.29321(82)	0.2889(1)	0.292(1)
y	0.03659(67)	0.0374(1)	0.040(1)
z	0.70911(85)	0.7106(1)	0.708(1)

The experimental mean Mg-D bond length of 1.96461 Å is longer than that of MgD_2 (1.9351-1.9549 Å) [144]. In the $NaMgH_3$ perovskite, the Mg-H bond distance is shorter than the Na-H bond distance [206]. This was the case for $NaMgD_3$ as the mean Na-D bond length is 2.58924 Å, as compared to the mean Mg-D bond length of 1.96461 Å. Furthermore, mean Mg-D and Na-D bond lengths for $NaMgD_3$ at 0 GPa agree well with those from Wu et al. and Andrada-Chacon et al [41][80]. In an ideal ABX_3 cubic perovskite, the A-X and B-X bond distances fit very well in the equation [41]:

$$d_{A-X} = \sqrt{2(d_{B-X})}$$

This is not the case for $NaMgD_3$. Hence, it cannot be indexed in the $Pm\bar{3}m$ space group. The bond lengths obtained from Rietveld refinement show that the structure of the $NaMgD_3$ product had some distortion in the unit cell, deviating from the ideal cubic structure.

Table 13. Bond lengths and bond angles for $NaMgD_3$.

	This study P = 0 GPa	**Ref.**[41] **0 GPa**	**Ref.**[80] **0 GPa**
Bond lengths (Å)			
Mg-D1 2x	1.9637(18)	1.9624(3)	1.964(3)
Mg-D2 2x	1.954(5)	1.9604(1)	1.96(1)
Mg-D2 2x	1.977(5)	1.9632(1)	1.99(1)
mean Mg-D	1.965	1.9620	1.97
Na-D1	2.26(2)	2.3378(3)	2.35(3)
Na-D1	2.541(19)	2.5454(3)	2.60(3)
Na-D1		2.9660(3)	
Na-D1		3.0762(3)	
Na-D2 2x	2.370(15)	2.3486(2)	2.32(2)
Na-D2 2x	2.654(12)	2.6763(2)	2.70(2)
Na-D2 2x	2.741(16)	2.6986(2)	2.74(2)
Na-D2 2x		3.2005(2)	
mean Na-D	2.541	2.7311	2.56
Bond angles (°)			
D1-Mg-D1	180.00(17)	180	180.0(3)
D1-Mg-D2 2x	90.9(4)	90.73(6)	89.5(9)
D1-Mg-D2 2x	90.3(3)	90.66(7)	91.8(8)
D1-Mg-D2 2x	89.1(3)	89.27(6)	90.5(9)
D1-Mg-D2 2x	89.7(4)	89.34(7)	88.2(8)
D2-Mg-D2 2x	90.7(3)	90.708(13)	91.1(8)
D2-Mg-D2 2x	180.0(4)	180	180.0(1)
D2-Mg-D2 2x	89.3(3)	89.292(1)	88.9(8)
Mg-D1-Mg	155.99(7)	156.27(9)	157.5(1)
Mg-D2-Mg	154.85(19)	155.53(6)	154.4(4)
mean Mg-D-Mg	155.42	155.90	155.9

III.1.d. In-situ study of the synthesis of $NaMgH_3$ under HP-HT

In an attempt to investigate the pressure-temperature synthesis conditions of $NaMgH_3$, in-situ XRD measurements were performed at three different pressures (2, 4, 7.4 GPa) while the temperature is increased using the Paris-Edinburgh press at Institut Néel.

Figure 34 shows the different XRD patterns collected as temperature increases from room temperature to 677°C (950 K) while the pressure is set at 2 GPa. The initial pattern at 20°C (293 K) shows peaks from the starting reactants: NaH and MgH_2. It is important to note that at this pressure and temperature, only the α-MgH_2 was observed as it is the stable structure under ambient conditions. No γ-MgH_2 was observed at room temperature. The peaks for other components of the sample assembly, such as BN and the gasket, were also visible.

At a higher temperature of about 176°C (449 K), peaks for the γ-MgH_2 were observed. This means that there was a phase transformation from the α-phase to the γ-phase of MgH_2 at a temperature between 20°C (293K) and 176°C (449K). This is consistent with both the DFT data and experimental (Figure 13) phase diagrams of MgH_2 as the P-T condition lies within the region where both the α-phase and the γ-phase exist. This new phase was present up to a temperature of 510°C (783 K) – a temperature at which the α-phase may have still been co-existed with the γ-phase to some extent. Peaks for NaH were still visible up to this temperature. At 593°C (866 K), remarkable peaks attributed to the $NaMgH_3$ perovskite were observed. This means that $NaMgH_3$ formation occured between 510°C (783 K) and 593°C (866 K) at 2 GPa. This is consistent from the synthesis performed by Martinez-Coronado et al., where they observed $NaMgH_3$ at 2 GPa and 750°C (1023 K) [71] and with the synthesis performed by Andrada-Chacon et al., where they synthesized $NaMgH_3$ at 2 GPa and 775°C (1048K) [80]. Furthermore, peaks for NaH and the phases of MgH_2 were hardly observed which supports the complete conversion of the precursors into $NaMgH_3$. Increasing the temperature further to 677°C (950 K) allowed the peaks for the perovskite to increase in intensity signifying an improved crystallinity.

It was also observed that MgO was formed at higher temperatures. Nevertheless, the synthesized $NaMgH_3$ was found to be stable even when the sample was quenched to room temperature and pressure.

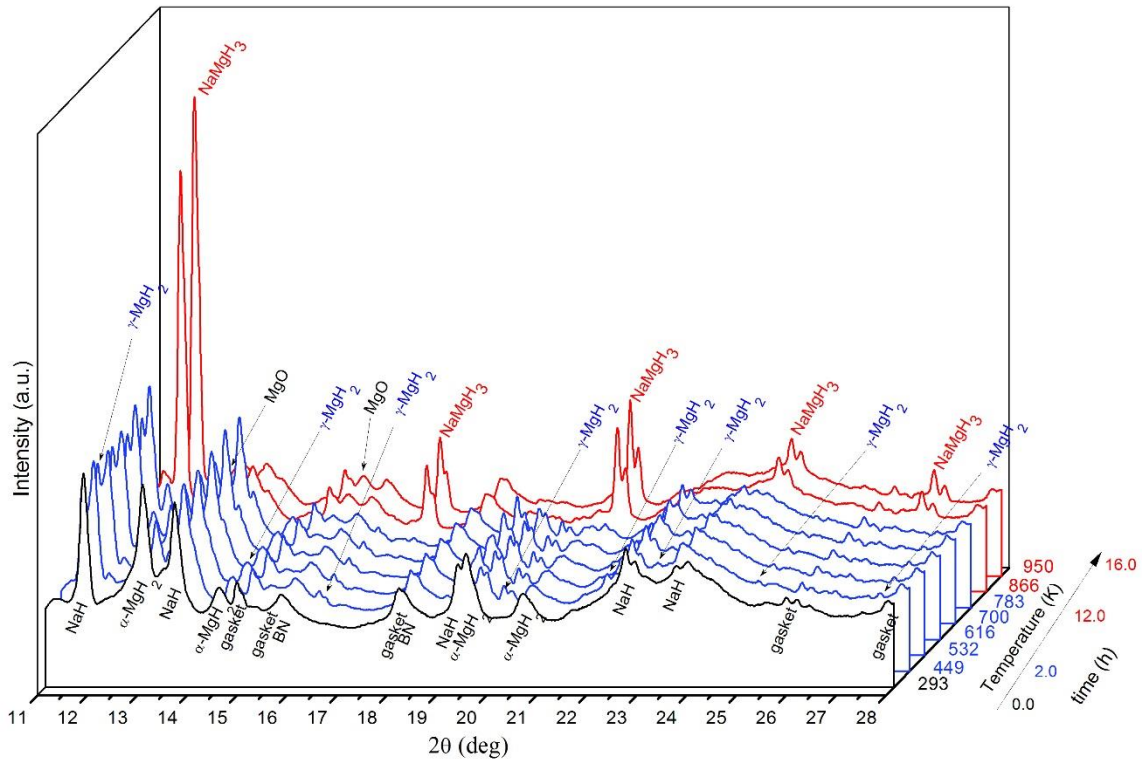

Figure 34. XRD patterns collected from the Paris-Edinburgh press during the synthesis of $NaMgH_3$ at ~2GPa from a mixture of NaH and MgH_2. Patterns in red show the appearance of the $NaMgH_3$ perovskite.

When the pressure was increased to 4 GPa, a similar sequence of appearance of phases was observed. Figure 35 shows the evolution of the XRD peaks associated with each phase as the system is being heated at 4 GPa. It can be seen that the peaks associated with $NaMgH_3$ were first seen at a lower temperature of between 455-542°C (728-815 K), compared to 510-593°C (783-866 K) at 2 GPa. However, this comparison is vague as the temperature steps in the two experiments are not the same.

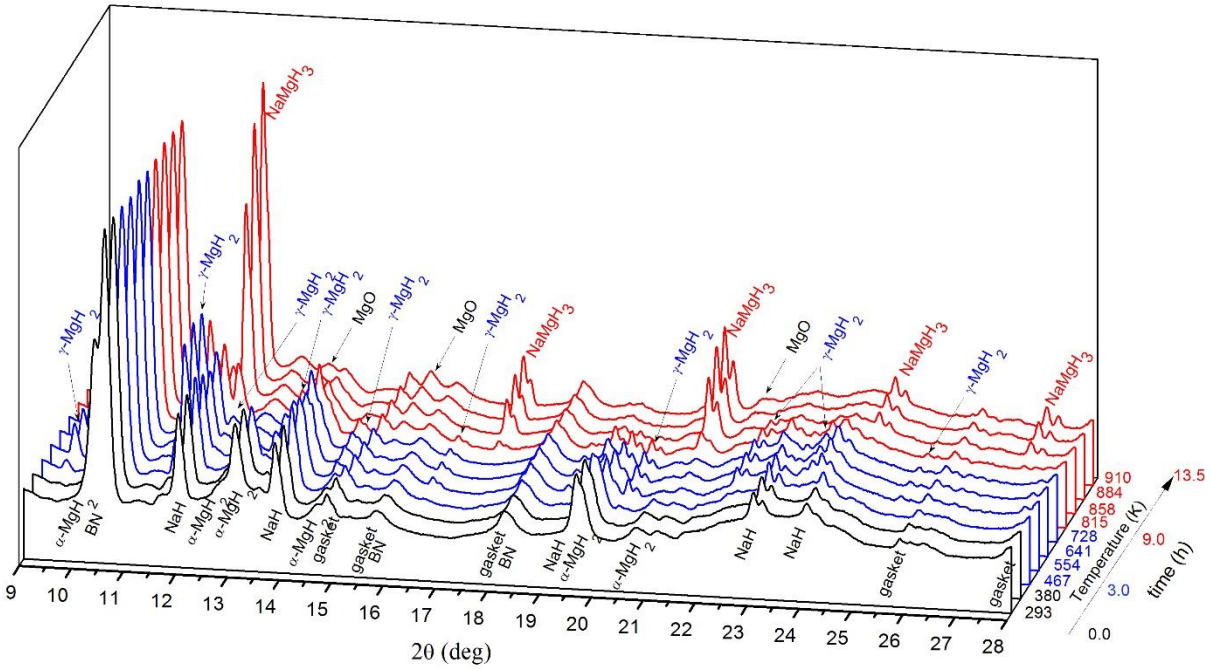

Figure 35. XRD patterns collected from the Paris-Edinburgh press during the synthesis of $NaMgH_3$ at ~4GPa from a mixture of NaH and MgH_2. Patterns in blue show the appearance of γ-MgH_2 while patterns in red show the appearance of the $NaMgH_3$ perovskite.

The same synthesis approach was performed at a high pressure of 7.4 GPa. Figure 36 shows the XRD patterns taken at different temperatures. The initial patterns shown in black show similar peaks to that for 2 GPa and 4 GPa in terms of the phases present. However, beginning at 140°C (413 K), the α-phase was transformed to the γ-phase. The co-existence of the two was not observed at this temperature. The XRD patterns for 140-279°C (413 K – 552 K), shown in blue, show the peaks for γ-MgH_2. At 327°C (600 K), the appearance of the peaks associated with the β-phase was observed. Furthermore, in the current experiment, increasing the temperature to 374°C (647 K) did not produce the $NaMgH_3$ perovskite and the β-phase persisted. It is interesting to see whether the β-phase will persist when the temperature is raised to temperatures higher than 527°C (800K), the temperature where the perovskite started to form at lower pressure of 2 and 4 GPa.

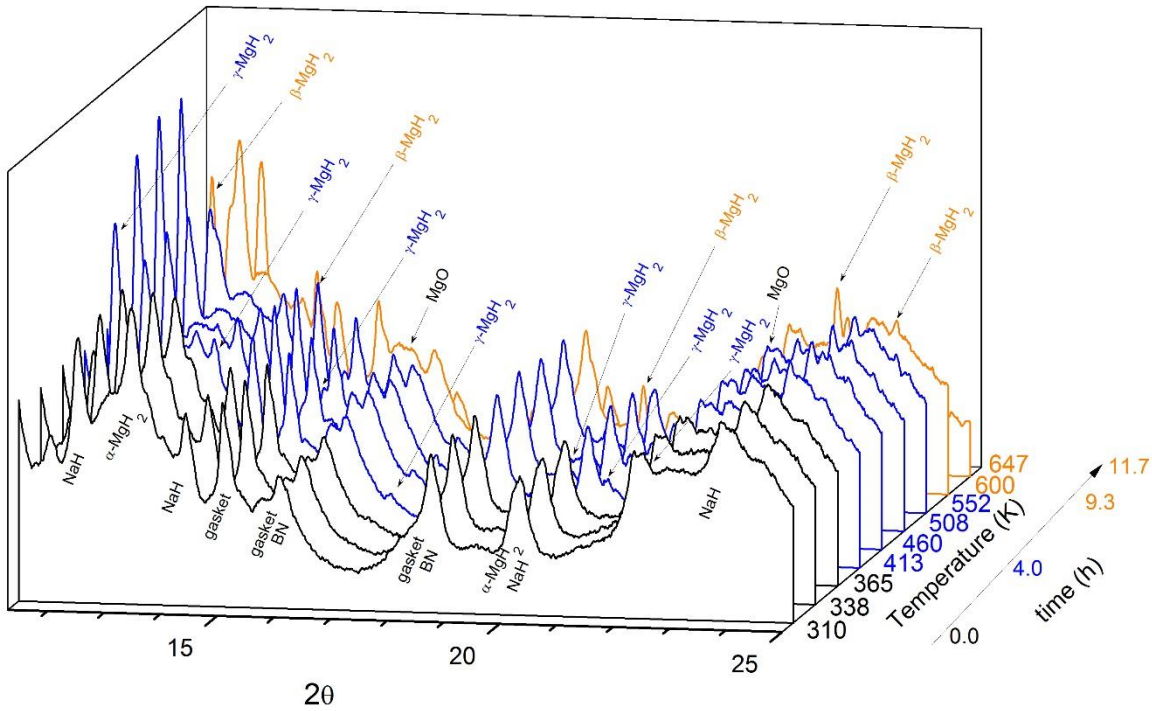

Figure 36. XRD patterns collected from the Paris-Edinburgh press during the synthesis of $NaMgH_3$ at ~7.4 GPa from a mixture of NaH and MgH_2. Patterns in blue show the appearance of γ-MgH_2 while patterns in orange show the appearance of β-MgH_2.

Figure 37 shows a different view of the evolution of the XRD peaks for the synthesis of $NaMgH_3$ at 4 GPa. The α to γ phase transformation can still be seen as the peaks for α-MgH_2 decrease in intensity up to the midway of the graph at the same time that the peaks for γ-MgH_2 start to emerge. On the other hand, there is a gradual decrease in the intensity of the peak for NaH. The emergence of the $NaMgH_3$ can be seen towards the latter part of the graph.

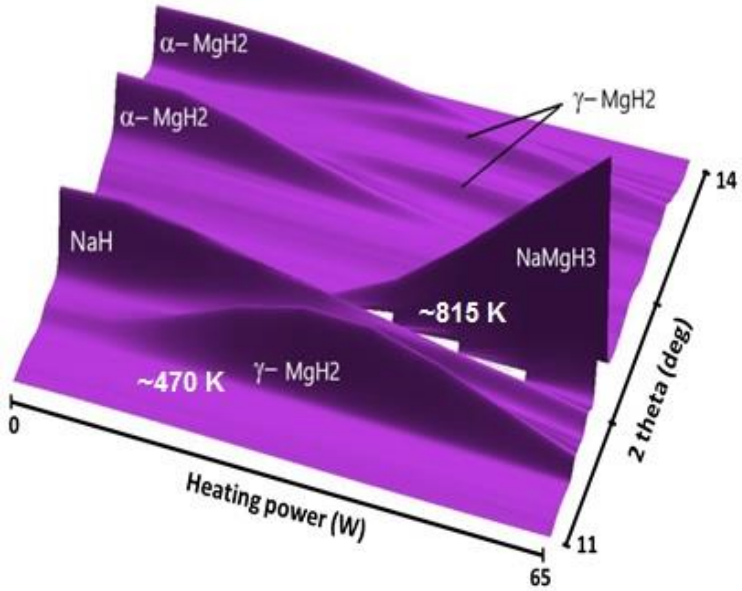

Figure 37. Evolution of XRD peaks for $NaMgH_3$ and its precursors with respect to increasing temperature by heating at 4 GPa.

This research hypothesizes that the formation of $NaMgH_3$ involves the reaction of NaH with γ-MgH_2 at high pressure and temperature. As seen in Figure 37, the peak for $NaMgH_3$ emerges as the peaks for NaH and γ-MgH_2 decreases in intensity. This assumption also lies on the successful synthesis of $NaMgH_3$ using Paris-Edinburgh Press at 2 GPa and 4 GPa in the temperature range where γ-MgH_2 was formed and the absence of reaction at 7.4 GPa. The β-MgH_2 was formed before any reaction with NaH occurred.

Table 14. Experimental Unit cell volume of $NaMgH_3$ and its precursors from the *in situ* experiment performed using the PEP. The unit cell volume of α-MgH_2 is multiplied by 2 because Z = 2, while the rest has Z = 4.

Hydride	Pressure (GPa)	Temperature (K)	Unit Cell Volume (Å^3)
$NaMgH_3$	4	815	213.43
NaH	4	554	101.68
α-MgH_2	4	554	58.39 x 2
NaH	4	815	104.59
γ-MgH_2	4	815	113.92
NaH	4	300	100.45
*β-MgH_2	3.84	300	109.92
NaH + α-MgH_2	4	554	218.46
NaH + γ-MgH_2	4	815	218.51
NaH + β-MgH_2	4	300	210.37

*calculated [127]

Table 14 shows the unit cell volume of $NaMgH_3$ and its precursors from *in situ* experiments using the PEP. Demazeau mentioned that a reaction will occur *in situ* under pressure if the volume of the product is less than the sum of the volumes of individual precursors ($\Delta V<0$) [158]. In Table 14, it can be seen that the volume of $NaMgH_3$ (213.43 $Å^3$) is less than the sum of the volumes of NaH and γ-MgH_2 (218.51 $Å^3$) and that of NaH and α-MgH_2 (218.46 $Å^3$), while it is not the case with that of β-MgH_2. Hence, this supports the hypothesis that the mechanism of $NaMgH_3$ synthesis involves the reaction of NaH with γ-MgH_2 and that is why $NaMgH_3$ was not formed with β-MgH_2.

The in-situ XRD experiments at HP-HT performed at different pressures (2, 4, and 7.4 GPa) from the equimolar NaH:MgH_2 mixture led to the following observations:

- The α-γ phase transformation of MgH_2 occurred within ~140-190°C for the 3 pressures used in the experiment. This is consistent with the fact that the two structures have a small energy difference.
- The $NaMgH_3$ phase was observed at temperatures beyond ~540-590°C at 2 and 4 GPa. It was not observed at 7.4 GPa but the β-phase appeared at ~320°C.
- Smaller steps in the heating process during the PEP experiments within the same day were not possible due to time constraints.

III.2. Li-substituted $NaMgH_3$

This section discusses the synthesis of $Na_{1-x}Li_xMgH_3$ perovskite with different values of x. Here, the A-cation of the perovskite was substituted by a smaller cation; in this case, NaH was partly replaced by LiH as starting material to enable the substitution of Na by Li. In $Na_{1-x}Li_xMgH_3$, x denotes the amount of Li substitution. X-ray diffraction analysis was performed to determine the extent of Li substitution.

III.2.a. Synthesis in CONAC press

The synthesis of $Na_{1-x}Li_xMgH_3$ was performed using gold capsules in the CONAC 40 press at 4 GPa and 650°C for 2 hours. Figure 38 shows the XRD patterns of the different synthesis products. The black pattern corresponds to the unsubstituted $NaMgH_3$ or x = 0, as

discussed in section III.1. For the sake of clarity, $Na_{1-x}Li_xMgH_3$ pertains to the target composition while $(Na,Li)MgH_3$ stands for the resulting perovskite.

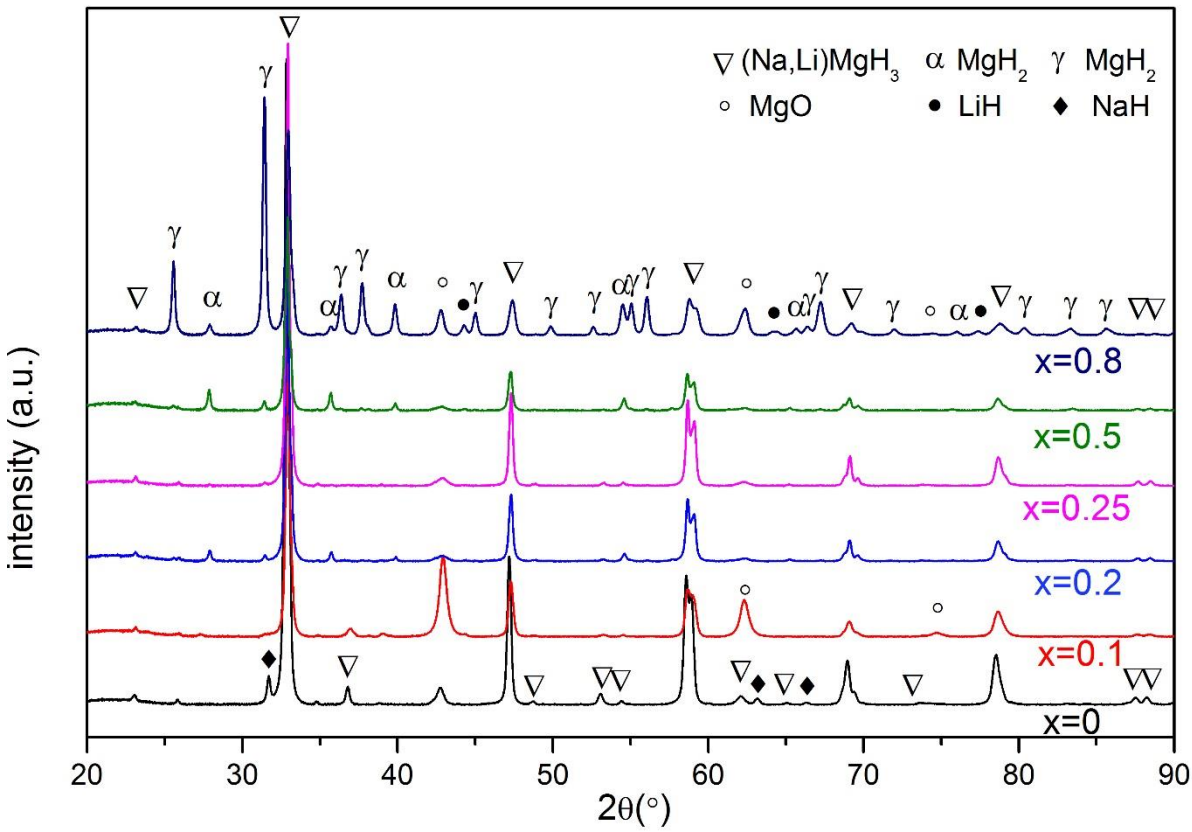

Figure 38. XRD patterns of $Na_{1-x}Li_xMgH_3$ showing the different phases present after synthesis using the CONAC press at 4 GPa and 650°C. X denotes the composition of the starting mixture of precursors.

There are also several peaks that are minor phases found in the XRD patterns of $Na_{1-x}Li_xMgH_3$ especially with x = 0.8. These are either oxidized product such as MgO, or unreacted reactants such as MgH_2. The peaks for $NaMgH_3$ shift to higher 2 theta values due to the replacement of Na by Li atoms (Figure 39). The (112) diffraction peak of $NaMgH_3$ at 32.8°, for example, was shifted higher by 0.2-0.3% for all the $Na_{1-x}Li_xMgH_3$ samples. Ikeda et al. observed a 0.8% shift to higher 2 theta value for the same (112) peak for ball-milled $Na_{1-x}Li_xMgH_3$ with x = 0.5 using the same Cu Kα radiation [92]. This shift is brought about by the smaller size of Li relative to Na. This shift also confirmed the substitution of Na by Li in the perovskite structure of the present study. The Li substitution was also confirmed by Rietveld refinement (Figure 40), where the obtained unit cell volumes for $(Na,Li)MgH_3$ were smaller compared to $NaMgH_3$. Table 15 shows the refined parameters for $(Na,Li)MgH_3$ after Rietveld refinement of XRD data. The lattice parameters are also shown for each sample.

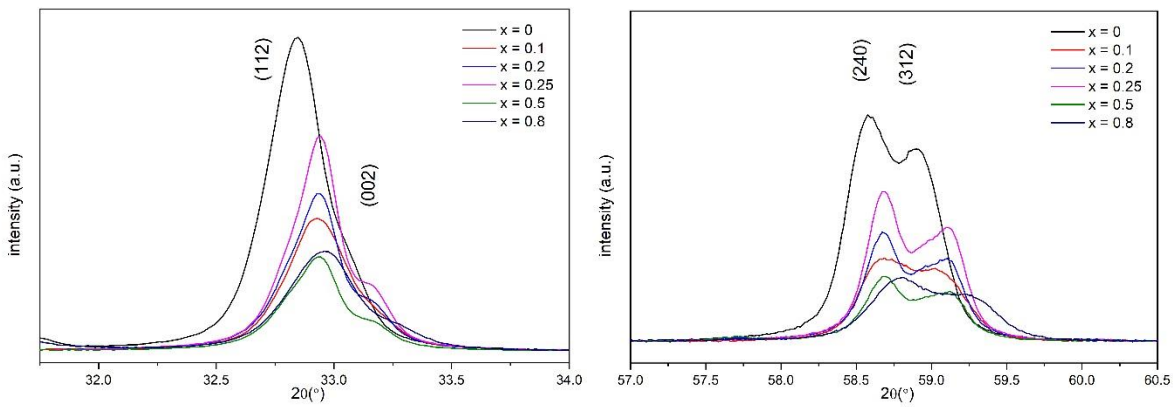

Figure 39. Closer view of (112), (002), (240), and (312) XRD peaks associated with $Na_{1-x}Li_XMgH_3$ showing the shift in 2 theta values.

Atomic positions from NPD data, however, were not available. The initial unit cell volume of $NaMgH_3$ is 227.399(7) $Å^3$.For samples with x = 0.1-0.8, the unit cell volume decreased by at least ~1$Å^3$, which is comparable to the ~0.2 and ~0.8 $Å^3$ volume decrease observed in literature for x = 0.25 and 0.5, respectively [71]. The sample at x = 0.25 decreased in volume by 0.6% relative to $NaMgH_3$. Theoretical calculations by Fornari et al. showed that the volume decrease at x = 0.25 is 3.6% [72]. Along the series of Li substitution beginning with x = 0.1 going up to x = 0.8, it is expected that the unit cell volume will significantly decrease as the amount of Li substituted increases. This is not the case of the present study as the unit cell volume did not significantly decrease further. It is evident in Figure 39 that the Bragg peaks for the perovskite with x = 0.1-0.8 do not vary significantly with each other in terms of peak positions. This explains why the Li-substituted samples have similar unit cell volumes. On the other hand, the occupancy factors for both Na and Li are also shown in Table 15. Here, it can be seen that the

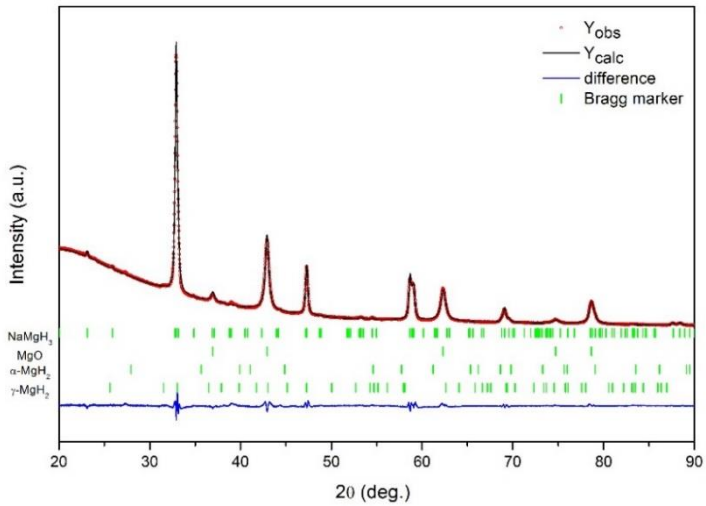

Figure 40. XRD pattern of $Na_{1-x}Li_xMgH_3$ with x = 0.1, and Rietveld analysis.

Table 15. Lattice and refinement parameters of $Na_{1-x}Li_xMgH_3$ synthesized using gold capsules in the CONAC 40 press at 4 GPa, 650°C, 2h. The obtained formula of $(Na,Li)MgH_3$ from the refinements is written in the row named "formula".

	$NaMgH_3$	**x = 0.1**	**x = 0.2**	**x = 0.25**	**x = 0.5**	**x = 0.8**
***a* (Å)**	5.4593(1)	5.4531(1)	5.4537(1)	5.4528(0)	5.4527(1)	5.4524(1)
***b* (Å)**	7.7001(2)	7.6893(1)	7.6881(1)	7.6873(1)	7.6878(1)	7.6883(2)
***c* (Å)**	5.4095(1)	5.3994(1)	5.3952(1)	5.3948(0)	5.3946(1)	5.3940(1)
V ($Å^3$)	227.399(7)	226.399(6)	226.217(4)	226.135(3)	226.139(6)	226.114(9)
Occ Na	0.500	0.443(3)	0.445(2)	0.442(1)	0.424(3)	0.40(1)
Occ Li	0.000	0.057(3)	0.055(2)	0.058(1)	0.076(3)	0.10(1)
formula		$Na_{0.89}Li_{0.11}MgH_3$	$Na_{0.89}Li_{0.11}MgH_3$	$Na_{0.88}Li_{0.12}MgH_3$	$Na_{0.84}Li_{0.16}MgH_3$	$Na_{0.80}Li_{0.20}MgH_3$
ATZ	201.27	194.00	194.155	193.82	191.22	187.29
ρ (g/cm^3)	1.470	1.423	1.424	1.423	1.404	1.375
Rp	13.2	14.0	12.7	10.4	18.8	26.8
Rwp	8.96	10.2	7.78	7.12	10.8	17.9
Rexp	3.60	3.12	3.59	3.00	4.83	9.75
χ^2	6.19	10.6	4.71	5.64	4.97	3.37

amount of lithium substituted is about 10% for x = 0.1-0.25. It reaches 20% when x = 0.8. In comparison, Martinez-Coronado et al. obtained 18% substitution when x = 0.5. From Rietveld refinement of their NPD data, the occupancy of Li for x = 0.25 and x = 0.5 were 0.04 and 0.18, respectively [71]. Therefore, the same trend was obtained in this study where the amount of Li substitution reaches a certain limit – in this case ~20%. This saturation of Li-substitution at higher values of x is also the reason why their unit cell volumes are similar. The same difficulty in substituting a significant amount of Li was observed. Furthermore, when x = 0.5 and 0.8, the formation of the perovskite $(Na,Li)MgH_3$ seemed to be less in terms of the relative amount of the products and precursors. Table 16 shows the relative amount of each phase in terms of mole fractions obtained from Rietveld refinement. When x = 0.8, the relative amount of the perovskite is less and a lot of unreacted species are present as seen from the extra XRD peaks in Figure 38 for x = 0.8. Because of the limited amount of NaH in the starting mixture, and the inability to further incorporate Li beyond 20%, the amount of $(Na,Li)MgH_3$ produced is limited. In Table 16, it can be seen that only 19.44 mole % of the perovskite was produced

when x = 0.8. A lot of the precursors remained unreacted. For the sample with x = 0.1, oxidation might have occurred during sample handling because of the high relative amount of MgO in the sample. For x = 0.2-0.25, no NaH and LiH peaks were seen confirming the reaction of these species to form (Na,Li)MgH_3. As the amount of LiH in the starting mixture was increased, in the case of x = 0.5 and x = 0.8, it became more difficult for Li to be incorporated in the perovskite structure. Thus, we see significant amounts of unreacted precursors after the synthesis.

Table 16. Mole fractions of the components of the mixture after HP-HT synthesis of $Na_{1-x}Li_xMgH_3$ using CONAC40 at 4GPa, 650C, 2h.

Compound	**$NaMgH_3$ x = 0.0**	**x = 0.1**	**x = 0.2**	**x = 0.25**	**x = 0.5**	**x = 0.8**
(Na,Li)MgH_3	69.36(0.61)	52.75	81.78(1.04)	88.17(0.95)	58.20(2.87)	19.44(1.19)
NaH	11.55(0.24)	0.00	0.00	0.00	0.00	0.00
MgO	10.80(0.21)	46.56	8.22(0.20)	9.77(0.17)	10.20(0.66)	2.77(0.19)
α-MgH_2	8.28(0.17)	0.06	7.64(0.15)	1.04(0.08)	14.59(0.74)	24.19(1.35)
γ-MgH_2	0.00	0.62	2.36(0.11)	1.02(0.08)	4.80(0.32)	18.38(1.05)
LiH	--	0.00	0.00	0.00	12.21(3.24)	35.21(4.83)

Thus, the solubility limit of incorporation of Li in the $NaMgH_3$ *Pmma* structure has been determined to be 20%. The experimental data does not show a significant difference for x = 0.1, 0.2, and 0.25, which leads to the extent of substitution of about 11%. The extent of substitution increases to 16% and 20% for x = 0.5 and x = 0.8, respectively but the conversion rate of the reaction is very low. Even at high concentration of LiH in the starting mixture, no $R3c$ structure is visible in contrast to ab initio predictions.

III.3. $KMgH_3$

III.3.a. Synthesis

This section discusses the different methods of synthesizing $KMgH_3$. Several attempts were performed using either the autoclave, the belt press, or the CONAC press.

III.3.b Synthesis using an autoclave

A 1:1 $KH:MgH_2$ mixture was formed into 5 mm pellets and were placed in an autoclave for 4 days at 400°C under 25 bars D_2 pressure with purging every 24h. The results of the XRD analysis of the sample show that the product was not pure. From the XRD pattern in

Figure 41, aside from peaks for $KMgD_3$ ($Pm\bar{3}m$), peaks for K_2MgD_4 were also seen. Unreacted MgH_2 and an oxidized product, MgO, were also seen.

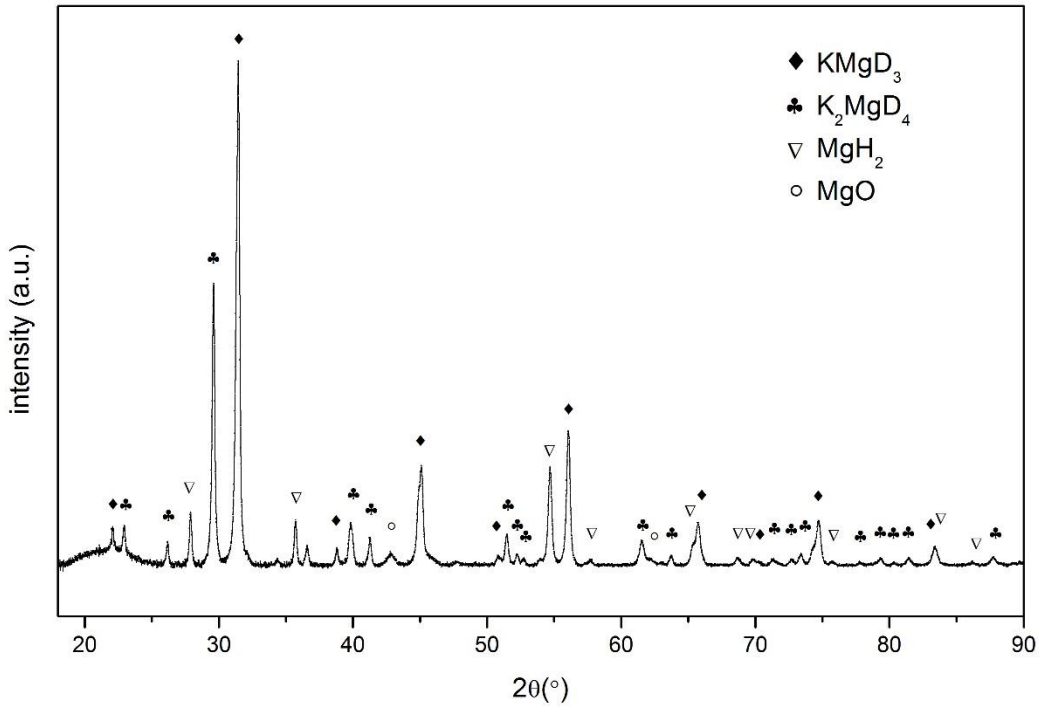

Figure 41. XRD pattern of the synthesis product from the $KH:MgH_2$ mixture subjected to 400°C and 25 bars D_2 in the autoclave.

K_2MgD_4 has a tetragonal structure (*I*4/*mmm* space group) [107]. It has lattice parameters: a = 4.032-4.036 Å, c = 13.524-13.592 Å [108][107]. This side product can be formed when $KMgH_3$ is synthesized from the hydrogenation of K and Mg metals [61]. The presence of K_2MgD_4 was the motivation to search for alternative synthesis routes.

III.3.c. Synthesis using a large volume press

Using the belt press, preliminary experiments were performed to optimize the synthesis temperature. Experiments were performed using a 1:1 KH:MgH_2 mixture in gold capsules using the belt press in a trial-and-error fashion to obtain an optimized product.

The pressure used in the belt press was 4 GPa and treatment time was 1 hour. Table 17 shows the different products observed based on XRD results of different synthesis products at different temperatures. In the table, the '+' signs tell the relative amounts of each component. It can be observed that at lower temperatures, the reaction of the precursors was not complete and an increase in temperature favors the formation of the desired $KMgH_3$ product. However, the presence of a secondary product, K_2MgH_4, and also the reaction of the sample with the gold capsule at 650°C hinder the production of a pure $KMgH_3$ sample. Even when platinum capsules were used, the sample mixture also had a reaction with the capsule at 650°C.

Table 17. Different phases present in the synthesis products from KH:MgH_2 mixture at 4 GPa and 1h using different temperatures. The amount of '+' tells the relative amounts.

	400°C	500°C	650°C
$KMgH_3$	+	+++	+++++
KH	+++	+	-
K_2MgH_4	+	+++	+
MgO	+	+++	+++++
α-MgH_2	+++	+++	+
MgAu	-	-	+
others	-	-	+++

Finally, the $KMgH_3$ synthesis worked, with minimal impurities, when the sample pellet was enclosed in a BN crucible inside a Pt capsule. The synthesis was performed using the CONAC press at 2 GPa, 775°C for 30 minutes. Analysis of the XRD pattern, shown in Figure 42, showed that the main peaks come from the desired synthesis product, $KMgH_3$. Several

XRD peaks attributed to KH and MgO were also seen. Rietveld analysis was performed to determine the lattice parameters and to quantify the phases present.

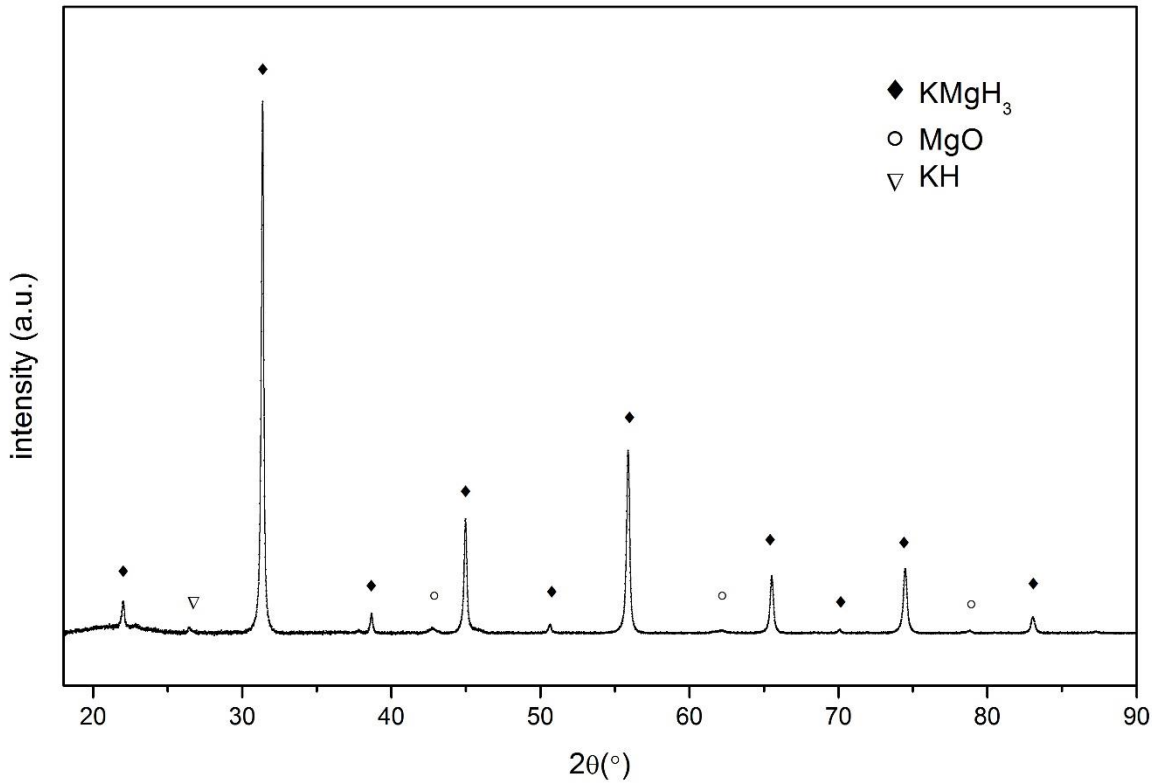

Figure 42. XRD pattern of the synthesis product from the KH:MgH_2 mixture subjected to 775°C and 2 GPa for 30 minutes in the CONAC press

Using the $Pm\bar{3}m$ space group during refinement, quantification revealed that the final product consists of 71.4 mole% $KMgH_3$, 28.2 mole% MgO, and 0.4 mole% KH. The lattice constant obtained was a = 4.021 Å which is consistent with the experimental lattice constant from literature: a = 4.023 Å [98] and a = 4.025 Å [61]. For a complementary description of the structure, neutron diffraction was performed under ambient conditions on the deuterated sample. Rietveld analysis was also performed on the NPD patterns collected to identify the lattice parameters. Table 18 shows the obtained lattice parameters for both XRD and NPD data. Table 19 shows the structure parameters. Figure 43 shows the NPD pattern of $KMgD_3$ at ambient pressure in a vanadium cylinder, with the corresponding phases present. No other $KMgH_3$ phase was observed.

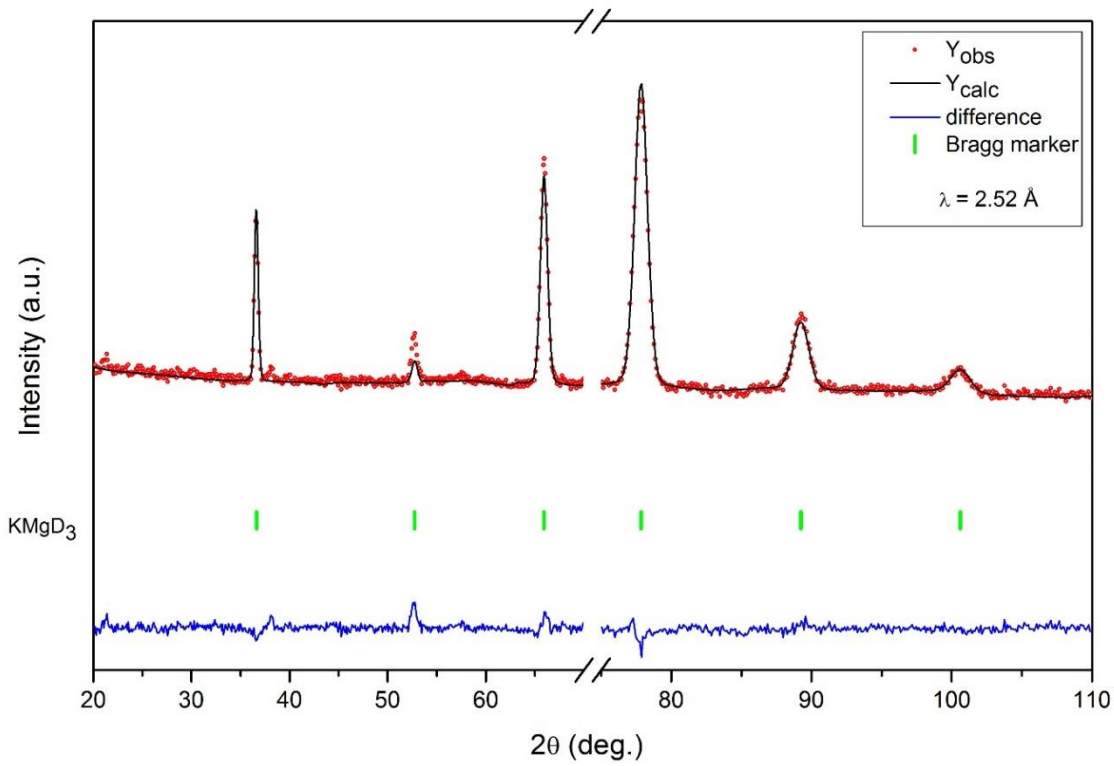

Figure 43. NPD pattern of $KMgD_3$ at ambient pressure and Rietveld analysis.

Table 18. Lattice parameters of $KMgD_3$ from Rietveld refinement of NPD and XRD data.

	NPD	**XRD**
***a* (Å)**	4.01962(25)	4.02134(4)
V (Å^3)	64.947(7)	65.030(1)
R_{wp}	14.7	14.0
χ^2	2.46	9.75

Table 19. Structure parameters of $KMgD_3$, space group: $Pm\bar{3}m$. Lattice parameters (Å): a = 4.01962(25).

	Atomic positions
K (*1b*) *x*	0.0
Y	0.0
Z	0.0
Mg (*1a*) *x*	0.5
Y	0.5
Z	0.5
D (*3d*) *x*	0.5
y	0.5
z	0.0

Chapter Summary

This chapter demonstrated the different synthesis experiments performed to synthesize $NaMgH_3$, Li-substituted $NaMgH_3$, and $KMgH_3$. The products synthesized from the autoclave, the belt press, the CONAC press, and the PEP were presented.

Structural characterization on $NaMgH_3$ at ambient conditions such as XRD and NPD was also performed. Results of these confirm that the $NaMgH_3$ produced in the experiments do not differ from what was obtained in published experiments. Synthesis of $NaMgH_3$ with in-situ XRD analysis was also performed using the PEP at 2, 4, and 7.4 GPa. It is interesting to note that the phase transformation of MgH_2 at HP-HT affects the synthesizability of $NaMgH_3$. It was hypothesized that the γ phase MgH_2 plays a role in the formation of $NaMgH_3$ from NaH and MgH_2.

X-ray diffraction analysis of the synthesized Li-substituted $NaMgH_3$ showed that the peaks associated with the perovskite shifter to higher 2 theta values. This validated the substitution of Na by Li in the A-site of the ABH_3 structure. The shift to higher 2 theta values

is attributed to the smaller size of Li which created a contracted unit cell volume. Rietveld analysis revealed that the maximum Li substitution performed was at 20%.

The optimization of $KMgH_3$ synthesis was also performed. This was done to minimize the production of a side product, K_2MgH_4. The $KMgH_3$ lattice constant obtained agrees well with literature values. The synthesized products are subjected to different characterization experiments which are presented in the succeeding chapters.

Chapter IV. Investigation of high-pressure-induced structural changes in perovskite hydrides

To complement data obtained from X-ray diffraction, the perovskite hydride samples were also investigated using neutron powder diffraction. With this, the atomic structure of the material can be determined accurately, in particular the position of deuterium atoms. A collaboration was established with Gilles Frapper (ICM2P, Poitiers, France) in order to have a theoretical insight on the behavior of hydride perovskites under high pressure. During her internship in Frapper's group, Somayeh Faraji combined DFT calculations and the use of global evolutionary algorithm (USPEX for Universal Structure Predictor: Evolutionary Xtallography) to study stable and metastable phases of several hydride perovskites under pressure. As for $NaMgH_3$ under pressure, a phase transformation (*Pnma* to *Cmcm*) somewhere in the area within 10 GPa was predicted (unpublished). So, it is interesting to compare theoretical and experimental results.

Determining the elastic constants such as the bulk modulus is essential because they are also related to other mechanical properties such as Young's and shear moduli, as well as important thermodynamic properties such as Debye temperature, specific heat, melting point, etc [70][51]. So far, no experimental data on the bulk modulus of both $NaMgH_3$ and $KMgH_3$ is available in literature. The following study presents the first time that these values are reported.

IV.1. $NaMgH_3$

Investigation of pressure-induced structural changes in $NaMgD_3$ was conducted using a PEP on the D1B diffractometer at ILL using the set-up described in section II.6.

Rietveld refinement using FullProf was performed on the neutron diffraction patterns and the lattice parameters of $NaMgD_3$ and $KMgD_3$ at different pressures were determined. The lattice parameter data were fitted using the third order Birch-Murnaghan equation using the EoSFit7-GUI software [207]:

$$P = \frac{3}{2}K_{T_0}\left[\left(\frac{V_0}{V}\right)^{\frac{7}{3}} - \left(\frac{V_0}{V}\right)^{\frac{5}{3}}\right]\left[1 + \frac{3}{4}\left(K'_{T_0} - 4\right)\left\{\left(\frac{V_0}{V}\right)^{\frac{2}{3}} - 1\right\}\right]$$

Where P is the pressure, V is the volume, V_0 is the initial volume, K_{T_0} is the isothermal bulk modulus at standard temperature, K'_{T_0} is the pressure derivative of the isothermal bulk modulus at standard temperature.

The sample consists of a mixture of $NaMgD_3$ and NaCl which acts as a pressure transmitting medium and as an internal calibrant. Figure 44 shows the NPD patterns for $NaMgD_3$ collected at higher pressure up to 10.7 GPa and the lattice parameters as a function of pressure. Only a decrease in the lattice parameters was observed in the pressure range investigated from the two experiments performed using two different assemblies. Moreover, no phase transition was observed up to 10.7 GPa. The peaks attributed to $NaMgD_3$ shifted to higher 2θ values due to the decrease in unit cell volume (Table 20). The intense peak at 75° is from the sintered diamond anvil.

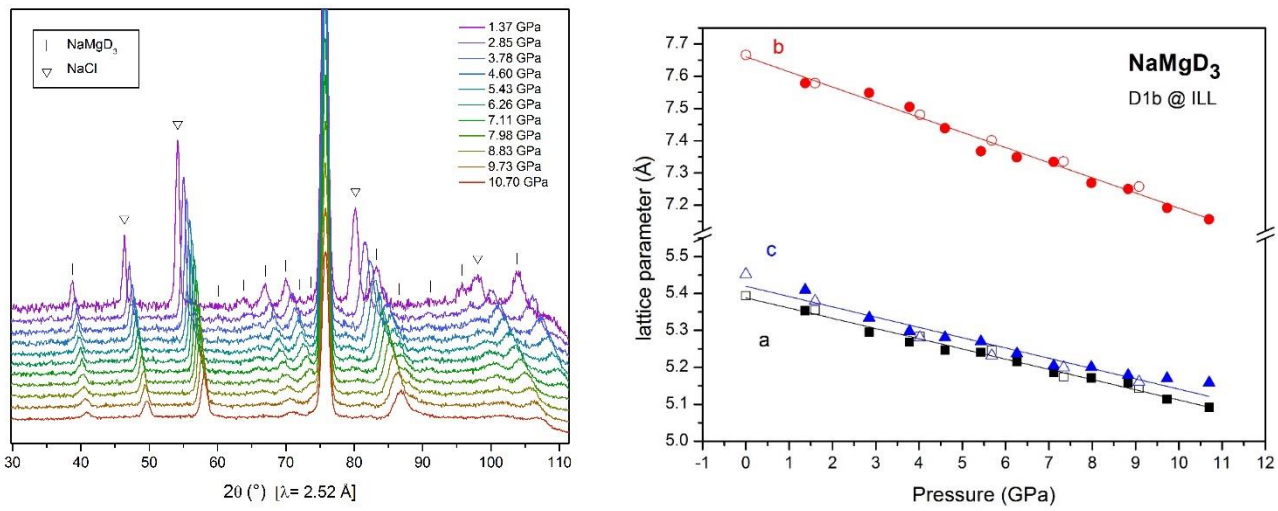

Figure 44. NPD patterns of $NaMgD_3$ (*Pnma*) up to ~11 GPa (left) and lattice parameters changes (right). The filled symbols were data from the first experiment while the hollow symbols were from the second.

Table 20. Structural data obtained from Rietveld refinement for $NaMgD_3$ (*Pnma*) at different pressures.

	P = 0 GPa	**P = 4.6 GPa**	**P = 10.7 GPa**
a **(Å)**	5.39996(39)	5.24285(241)	5.15862(332)
b **(Å)**	7.68316(56)	7.38534(307)	7.15644(301)
c **(Å)**	5.45257(39)	5.30265(262)	5.09220(325)
V (Å^3)	226.220(28)	205.320(163)	187.990(188)
R_{wp}	18.7	20.4	9.61
χ^2	30.8	12.7	17.8

Rietveld refinement summary for $NaMgD_3$ (*Pnma*) at selected pressures is shown in Table 20. Atomic positions are shown in Table 21. The atomic positions were plotted using the VESTA software. No significant tilting of the MgD_6 octahedra was observed at high pressures. Bond lengths and bond angles for $NaMgD_3$ on the other hand are presented in Table 22. Data for the pressure 10.7 GPa was selected as it is the highest pressure attained while that of 4.6 GPa was selected as the middle pressure.

Table 21. Atomic positions of $NaMgD_3$ at different pressures.

	P = 0 GPa	**P = 4.6 GPa**	**P = 10.7 GPa**
Na (*4c*) *x*	0.02120(267)	-0.04292(2116)	-0.07668(1304)
y	0.25	0.25	0.25
z	0.00937(368)	-0.02574(2479)	-0.03341(2399)
Mg (*4b*) *x*	0.0	0.0	0.0
y	0.0	0.0	0.0
z	0.5	0.5	0.5
D1 (*4c*) *x*	-0.01734(162)	0.03020(999)	0.00619(1172)
y	0.25	0.25	0.25
z	0.42637(157)	0.44979(1088)	0.42472(1107)
D2 (*8d*) *x*	0.29321(82)	0.30232(538)	0.30148(645)
y	0.03659(67)	0.04461(661)	0.03095(493)
z	0.70911(85)	0.74998(1062)	0.71674(1008)

For the higher achievable pressure in the experiment, the compressed $NaMgD_3$ structure cannot be indexed in the predicted *Cmcm* space group nor in the $Pm\bar{3}m$ space group which would confirm a structural transition towards the ideal cubic perovskite structure. The bond lengths and bond angles presented in Table 22 show how it deviates from the bond angles in a cubic structure.

When the pressure was increased to 10.7 GPa, the mean Mg-D and Na-D bond lengths decreased as a result of the compression (Figure 45): 1.965 Å and 2.541 Å at P = 0 GPa; 1.89 Å and 2.48 Å at P = 4.60 GPa; and 1.84 Å and 2.44 Å at P = 10.7 GPa.

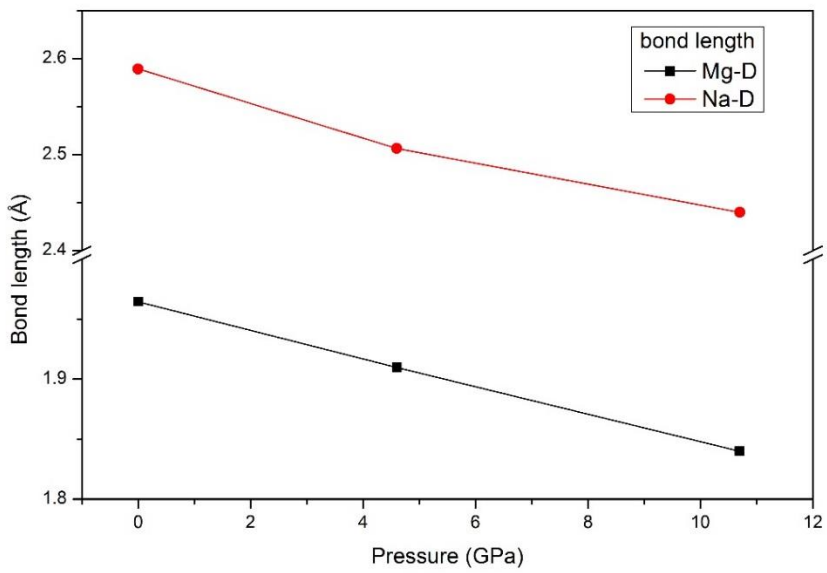

Figure 45. Mg-D and Na-D bond lengths in $NaMgD_3$ (*Pnma*) during compression in a Paris-Edinburgh Press at room temperature.

The D1-Mg-D2 bond angles have values between 89.1(3)° and 90.9(4)° which can be compared to the 88.2°-91.8° range obtained from NPD data by Andrada-Chacon et al [68][68][68][80].

When pressure was increased, the MgD_6 octahedra did not reach the 90° angle in the cubic arrangement, as observed from the D1-Mg-D2 bond angles: 89.1(3)°-90.9(4)° at 0 GPa, 82(3)°-98(3)° at 4.6 GPa, and 87(3)°-93(3)° at 10.7 GPa. It was hypothesized that under compression, $NaMgD_3$ tends to go towards the cubic arrangement but the $NaMgD_3$ phase transformation to the cubic phase was not observed in the pressure range achievable.

From the lattice parameters, the bulk modulus and its pressure derivative were calculated using the EOSFit-7GUI software using 3rd order Birch-Murnaghan equation of state (Figure 46)[208]. The bulk modulus obtained is 43.9(1.3) GPa and its pressure derivative is 3.4(3). The obtained V_0 was 225.5(2) $Å^3$. Table 23 shows the comparison of this experimental data with theoretical data. The experimental bulk modulus is greater than the calculated values from literature. On the other hand, the experimental pressure derivative of the bulk modulus is comparable to the calculated value from theoretical studies.

Table 22. Bond lengths and bond angles for $NaMgD_3$ (*Pnma*).

	P = 0 GPa	**P = 4.60 GPa**	**P = 10.7 GPa**
Bond lengths (Å)			
Mg-D1 2x	1.9637(18)	1.875(9)	1.830(12)
Mg-D2 2x	1.954(5)	2.09(4)	1.92(4)
Mg-D2 2x	1.977(5)	1.71(5)	1.78(5)
mean Mg-D	1.965	1.89	1.84
Na-D1	2.26(2)	2.30(12)	2.36(12)
Na-D1	2.541(19)	2.57(12)	2.22(9)
Na-D1			
Na-D1			
Na-D2 2x	2.370(15)	2.08(9)	2.77(7)
Na-D2 2x	2.654(12)	2.62(10)	2.77(7)
Na-D2 2x	2.741(16)	2.78(12)	1.94(7)
Na-D2 2x			
mean Na-D	2.541	2.48	2.44
Bond angles (°)			
D1-Mg-D1	180.00(17)	180.0(9)	180.0(12)
D1-Mg-D2 2x	90.9(4)	82(3)	90(3)
D1-Mg-D2 2x	90.3(3)	98(3)	87(3)
D1-Mg-D2 2x	89.1(3)	92(3)	90(3)
D1-Mg-D2 2x	89.7(4)	88(3)	93(3)
D2-Mg-D2 2x	90.7(3)	93(4)	91(4)
D2-Mg-D2 2x	180.0(4)	180(4)	180(4)
D2-Mg-D2 2x	89.3(3)	87(3)	89(3)
Mg-D1-Mg	155.99(7)	161.1(4)	155.8(5)
Mg-D2-Mg	154.85(19)	156.0(2)	156.5(19)
mean Mg-D-Mg	155.42	158.6	156.1

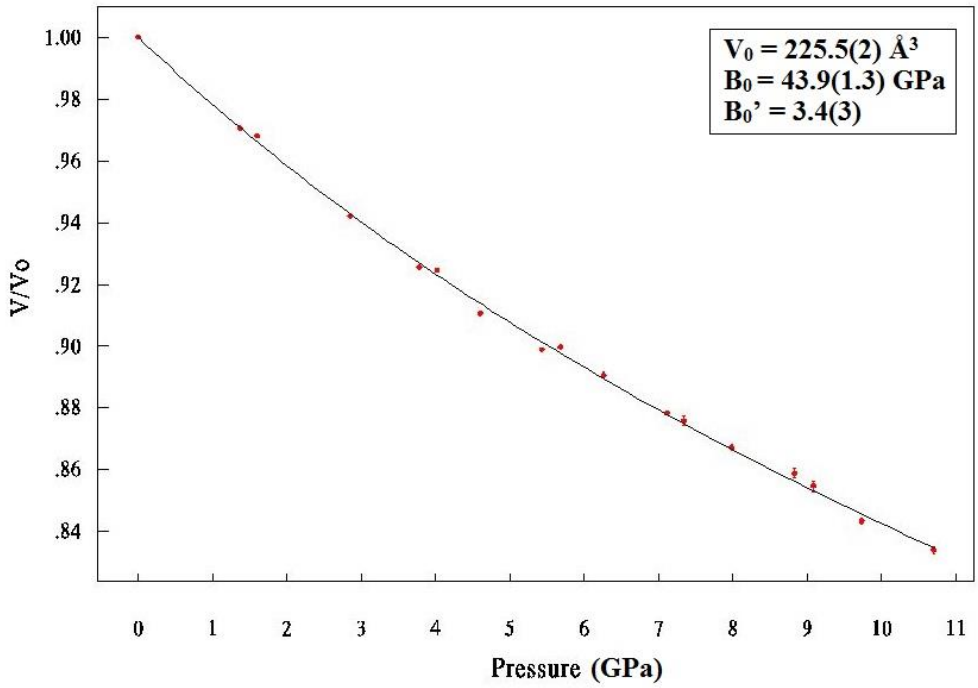

Figure 46. EOS curve fit by EOSFit-7GUI software for the relative cell volume (V/V0) vs. Pressure data of $NaMgD_3$.

Table 23. Bulk modulus (B_0) and its pressure derivative (B_0') for $NaMgD_3$.

	This study	Theoretical
B_0	43.9(1.3) GPa	38.4 GPa [49], 35.95 GPa [70], 35.9 GPa [209]
B_0'	3.4(3)	3.6 [49]

It is interesting to compare also these values to reported bulk modulus values of its precursors, NaH and MgH_2. The reported theoretical and experimental B_0 for NaH are 22.8 and 19.4 GPa, respectively [121]. For MgH_2, the reported values are 50.2-52.57 GPa [131][127][132]. For MgD_2, it was reported to be 49(2) GPa [139]. The experimental bulk modulus of $NaMgH_3$ is closer to that of MgH_2 than that of NaH. This can related to the atomization energy diagrams made by Shinzato et al. that says that $NaMgH_3$ has more resemblance to MgH_2 in terms of chemical bonding than to NaH [206].

To the best knowledge of the research group, this is the first experimental attempt to determine the bulk modulus of $NaMgH_3$. All available data from literature were derived from

calculations. The values of B_0 for $NaMgH_3$ still classify it as soft and compressible. This may be associated with the high ionic character of $NaMgH_3$ [49].

IV.2. $KMgH_3$

Similar to the experiment performed with $NaMgD_3$, $KMgD_3$ synthesized using the CONAC press and deuterated in the autoclave, was analyzed at the D1B beamline of the ILL using the Paris-Edinburgh set-up. Figure 47 shows the NPD patterns for $KMgD_3$ collected up to 11.6 GPa. Only a decrease in the lattice parameters was observed, and no phase transitions, in the pressure range investigated. The peaks attributed to $KMgD_3$ shifted to higher 2θ values due to the decrease in unit cell volume (Table 24). The intense peak at around 76° is from the sintered diamond anvil. The peak at around 79° is actually an overlap of two peaks – one for NaCl and one for $KMgD_3$. These two eventually separated at 3.06 GPa as two peaks started to emerge from this pressure on.

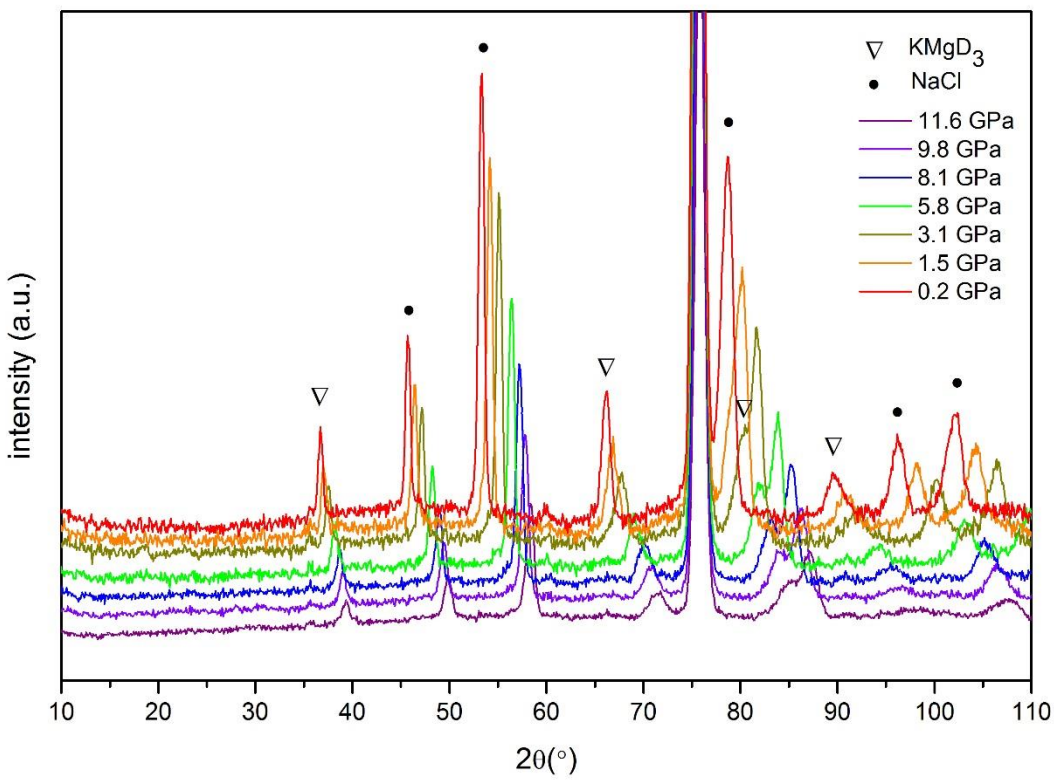

Figure 47. NPD patterns of $KMgD_3$ up to 11.6 GPa. The peak at 2θ = 76° is for diamond.

From the lattice parameters determined from Rietveld analysis, the bulk modulus and its pressure derivative were calculated using the EOSFit-7GUI software using 3rd order Birch-Murnaghan equation of state [208]. The EOS fit is shown in Figure 48 for the relative cell volume versus Pressure data obtained from NPD studies. The bulk modulus obtained from the EOS fit is 39.0(7) GPa and its pressure derivative is 3.5(2). Table 25 shows the comparison of this experimental data with theoretical data. The experimentally determined values agree with the published data. To the best knowledge of the research group, this is the first time that such experimental data are reported. The obtained V_0 was 64.64(3) $Å^3$. It is interesting to compare also these values to reported bulk modulus values of its precursors, KH and MgH_2. The reported values for KH are B_0 = 15.6 ±1.5 GPa and B_0' = 4.0 ±0.5 [125]. For MgH_2, the reported values are 50.2-52.57 GPa [131][127][132]. Moreover, the experimental B_0 of $KMgD_3$ is less than that of $NaMgD_3$, which makes it softer and more compressible than $NaMgD_3$. Bouhadda et al. observed that the Debye temperature, the highest achievable temperature due to a single normal vibration, of $NaMgH_3$ (375°C or 648 K) is greater than that of $KMgH_3$ (115°C or 388 K) which makes $KMgH_3$ softer than $NaMgH_3$ [70][53]. The results of the current study agree with this.

Table 24. Structural data obtained from Rietveld refinement for $KMgD_3$ at different pressures.

	P = 0 GPa	**P = 5.82 GPa**	**P = 11.63 GPa**
***a* (Å)**	4.01962(25)	3.85245(68)	3.74447(130)
V (Å³)	64.947(7)	57.176(18)	52.501(31)
R_{wp}	14.7	9.57	10.4
χ^2	2.46	0.281	0.193

Table 25. Bulk modulus (B_0) and its pressure derivative (B_0') for $KMgD_3$.

	This study	**Theoretical**
B_0	39.0(7) GPa	34.60-40.84 GPa [53] 35.6 GPa [49] 35.1008 GPa [101]
B_0'	3.5(2)	3.61-3.62 [53] 3.7 [49] 3.57 [101]

Upon compression, it is interesting to see its effect on the bonding of atoms in $KMgD_3$. Table 26 shows the bond lengths and bond angles at selected pressures obtained from Rietveld analysis. It can be observed that all 6 Mg-D and all 12 K-D bond lengths are of the same value at a particular pressure. When the pressure was increased, there was a contraction in the bond lengths which is expected because the unit cell volume decreased according to Table 24. At higher pressure, the values of all 6 Mg-D and all 12 K-D bond lengths were still the same, which means that there is an isotropic effect to bond lengths when the pressure was increased, i.e. regardless of the direction (x, y, z) the compressed bond lengths were still the same. This can be related to the ideal perovskite structure of $KMgH_3$. There are 6 Mg-H bonds that form an MgH_6 octahedral structure and there are 12 K-H bonds that form a cubo-octahedral structure. Having a tolerance factor of ~1.0 and its cubic symmetry, that can explain the similarity in the bond lengths observed in the NPD studies. Also, it was observed that at higher pressures, the MgH_6 octahedral structure was maintained as shown in the bond angles of 90° and 180° for the D-Mg-D bonds. This is in contrast to the observed Mg-D bond lengths and bond angles for the high pressure NPD study of $NaMgD_3$, where bond lengths and bond angles changed at higher pressure. In $KMgD_3$ at high pressure, no MgH_6 octahedral tilting was observed. This is consistent with an experiment from literature [80]. Therefore, at high pressure, the kinetics of hydrogen migration in $KMgH_3$ is similar to that at room pressure.

Table 26. Bond lengths and bond angles for $KMgD_3$ at selected pressures.

	P = 0 GPa	**P = 5.82 GPa**	**P = 11.63 GPa**
Bond lengths (Å)			
Mg-D 6x	2.00980	1.92620	1.87225
mean Mg-D	2.00980	1.92620	1.87225
K-D 12x	2.84229	2.72406	2.64776
mean K-D	2.84229	2.72406	2.64776
Bond angles (°)			
D-Mg-D 3x	180.0000	180.0000	180.0000
D-Mg-D 8x	90.0000	90.0000	90.0000
Mg-D-Mg	180.000	180.000	180.000

According to calculations by Vajeeston et al., Mg-H bond lengths for $LiMgH_3$, $NaMgH_3$, and $KMgH_3$ are very similar with values of ~2.00Å, but the Li-H, Na-H and K-H bond distances vary [49]. Comparing the Mg-D bond lengths obtained from NPD studies of $NaMgD_3$ and $KMgD_3$, it can be seen that both of them have Mg-D bond lengths of ~2.00Å (Table 22 and Table 26), which is consistent with Vajeeston's values. The K-H bond length in

$KMgH_3$ is similar to that of KH which results from the weak Mg-H bond and the high polarizability of the hydride ion in the perovskite structure [98]. On the other hand, the Mg-D bonds in the MgD_6 octahedral of $KMgD_3$ have higher bond distance compared to the Mg-H bonds of MgH_2 (a difference of about 0.06Å) [111]. Furthermore, the D-D distance obtained was 2.83783 Å, which is consistent with the 2.845 Å H-H bond distance in $KMgH_3$ from literature [210].

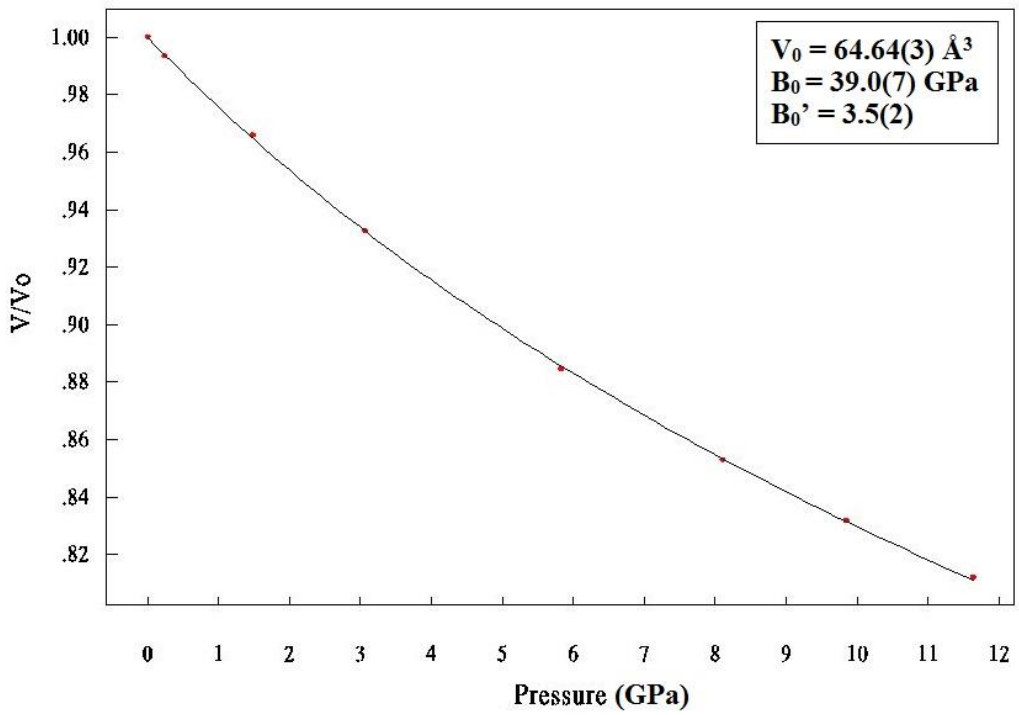

Figure 48. EOS curve fit by EOSFit-7GUI software for the relative cell volume (V/V_0) vs. Pressure data of $KMgD_3$. Error bars are too small to be seen.

Chapter Summary

In-situ high pressure neutron powder diffraction allowed the determination of the bulk modulus of $NaMgD_3$ and $KMgD_3$. This chapter allowed us also to get farther with the understanding of the atomic arrangements, lattice constants, bond lengths, and bond angles involved in the perovskite structure of $NaMgH_3$ and $KMgH_3$.

High pressure NPD studies also discarded the idea of phase transformation in $NaMgD_3$ and $KMgD_3$ in the pressure range studied. $KMgD_3$ maintained its ideal cubic perovskite structure while $NaMgD_3$ remained to have distortions at high pressure.

The determination of the bulk modulus is splendid as no other recent published data show experimental values for the bulk moduli of these materials. With these experimental values, other studies related to other mechanical properties such as Young's and shear moduli, as well as important thermodynamic properties mentioned previously can now be prompted.

The next chapter discusses the thermal properties of the perovskite hydride materials.

Chapter V. Thermal properties of perovskite hydrides

This chapter deals with two types of characterization of thermal properties. The first one is the determination of thermal expansion coefficient of $NaMgD_3$ at low temperature. The second one is related to hydrogen sorption performance.

Aside from neutron studies at high-pressure in Chapter IV, a similar experiment was performed using the same beamline at the ILL. Instead of increasing the pressure, neutron data was collected at low temperatures to see how the unit cell volume of the perovskite behaves at decreased temperatures.

On the other hand, hydrogen sorption properties of the studied perovskites, $NaMgH_3$, $(Na,Li)MgH_3$, and $KMgH_3$ were characterized using differential scanning calorimetry. The hydrogen desorption temperatures of the three are compared and are then related to the cation present in the A-site of the perovskite and the reversibility of hydrogen desorption is investigated.

V.1. Volume thermal expansion coefficient of $NaMgD_3$ at low temperature

Measurements were performed at different temperatures -263°C to 27°C (10-300 K). Rietveld refinement using FullProf was performed on the neutron diffraction patterns and the lattice parameters of $NaMgD_3$ at different temperatures were determined. Coefficient of thermal expansion is usually obtained from the slope of $\frac{\Delta V}{V_0}$ vs ΔT curves [211][212]. For experiments at lower temperature, some equations used for fitting of data do not work in this temperature range. One of the equations that can be used in this temperature range is the Salje equation.

The EosFit7-GUI software was used here and it allows data fitting of V-T data using different equations of states namely: Berman, Fei, Holland-Powell, Salje, etc. [213]. Berman's version is not valid for low temperatures because in his equation, α(T) has a finite value at absolute zero, which should not be the case. With the Fei equation, it is difficult to use this fitting at low temperatures because the coefficient of thermal expansion diverges to infinity when T approaches zero. With the Holland-Powell equation, there is a point at low temperatures that the coefficient of thermal expansion becomes negative. Any further decrease

in temperature tends to increase the unit cell volume, which does not make sense. Among the aforementioned equations, the one from Salje was used in fitting V-T data at low temperatures. Salje et al. suggested the equation below to address the saturation of α at low temperature.

$$V_{0T} = \left[p_0 + p_1\theta_{sat}\coth\left(\frac{\theta_{sat}}{T}\right)\right]^3$$

Here, θ_{sat} is the saturation temperature, while p0 and p1 are just parameter values. This equation can only be used for variation in volume at low temperatures [214][213]. Salje's equation now leads to the expression for the thermal expansion coefficient:

$$\alpha(T) = \frac{3p_1\theta_{sat}^2}{V_{0T}^{1/3}}\left[\frac{coth^2\left(\frac{\theta_{sat}}{T}\right) - 1}{T^2}\right]$$

A low-temperature study was conducted for $NaMgD_3$ at the D1B beamline of ILL to characterize the structural changes down to -263°C (10 K). Unit cell volumes from these measurements can be used for the determination of its volume thermal expansion coefficient, which is defined as $\alpha(T) = V^{-1}\left(\frac{\partial V}{\partial T}\right)_P$. A constraint for α exists and that is $\alpha(T) = \frac{\partial\alpha}{\partial T} = 0$ at absolute zero [213]. For this reason, a lot of equations with different forms were proposed for α taking into account the behaviour of materials at both high and low temperatures.

The unit cell volume obtained from Rietveld refinement of the NPD patterns are shown as a graph in Figure 49 . It was observed that there is a general linear decrease in cell volume as the system is being cooled. This contraction continues until the 100-150 K region, beyond which the decrease in the unit cell volume is no longer proportional to the decrease in temperature. For some solid materials, thermal contraction is achieved above 50-77 K [215].

The values obtained from the EosFit7-GUI software using the Salje equation were: V_0 = 223.14(3) Å^3, θ_{sat}= 161.1(10.6) K. Using these values, the calculated thermal expansion coefficient at 300 K is 6.9 x 10^{-5} K^{-1}. This can be compared to the thermal expansion coefficients of α, γ, and β MgH_2 which range from 2.2 to 4.3 x 10^{-5} K^{-1} [142]. To the best knowledge of the research group, this is the first reported value of α for $NaMgH_3$. According to Salje, the thermal expansion coefficient only becomes zero below ~$\theta_{sat}/10$ which is quite the case as seen in Figure 50.

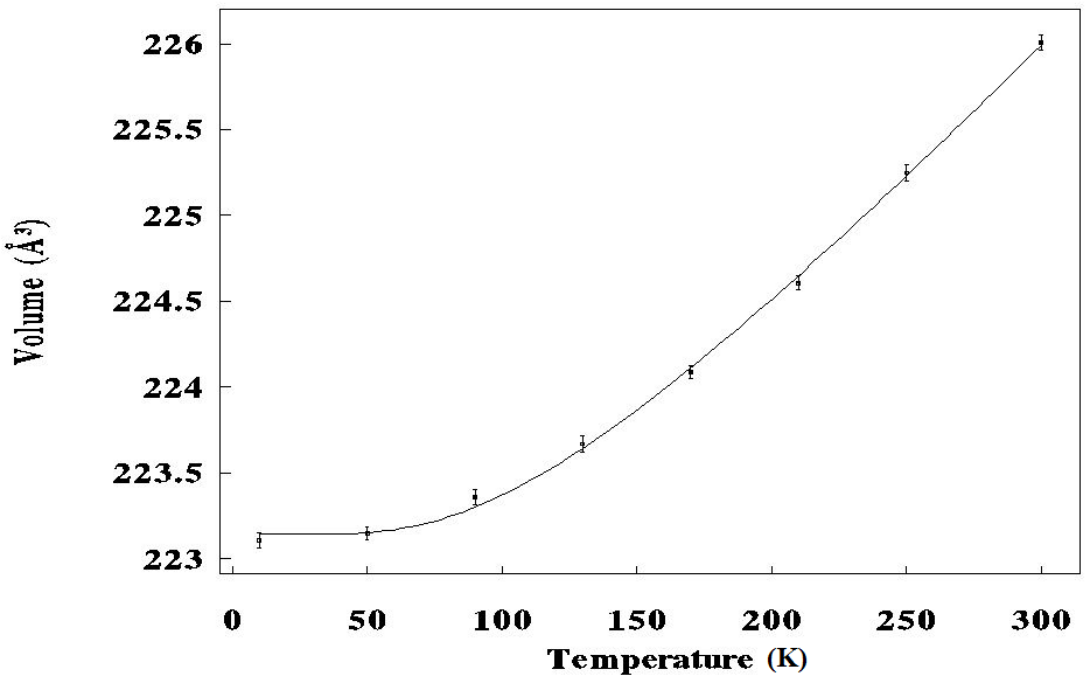

Figure 49. Unit cell volume of $NaMgD_3$ obtained from low temperature NPD experiments. The EoS curve shown was obtained using EoSFit7-GUI using Salje's equation [214].

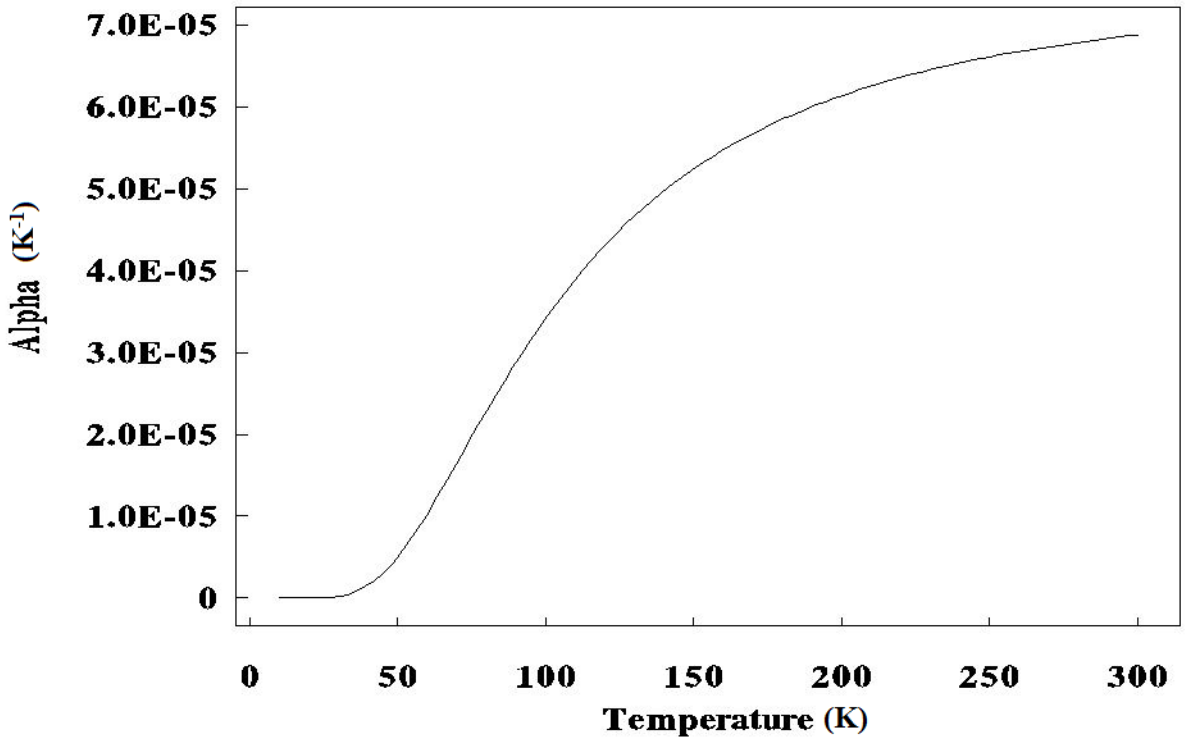

Figure 50. Volume thermal expansion coefficient of $NaMgD_3$ as a function of temperature in Kelvin.

V.2. Differential Scanning Calorimetry studies

The result of the DSC is shown in Figure 51. For $NaMgH_3$, two endothermic peaks corresponding to the 2-step decomposition of $NaMgH_3$ can be seen. The temperatures at the two peaks are 480.7 °C and 529.6 °C which do not agree with literature values: 391.85°C and 405.85 °C at the same heating rate of 20°C/min [91][85]. This is due to the fact that the crucibles used in the previous studies were aluminum crucibles under atmospheric pressure in a constant purge gas flow. In our study, on the other hand, high-pressure cells were used. With this, the volume is kept constant. Therefore, any gas produced during the dehydrogenation process increases the pressure in the crucible. With the increased pressure, the peak temperature associated with the release of gaseous products is shifted to higher temperatures [69][216]. We performed an HP-DSC measurement of MgH_2 at a heating rate of 10°C/min (Figure 52). The peak temperature obtained (460.3°C) is consistent with the HP-DSC result (~457°C) reported in literature at the same heating rate [69].

Compared to the unsubstituted $NaMgH_3$, the DSC curve for $Na_{1-x}Li_xMgH_3$ shows three endothermic peaks: the first one is for the decomposition of MgH_2 (unreacted precursor) while the next two correspond to the 2-step decomposition of $Na_{1-x}Li_xMgH_3$. The peak temperature of MgH_2 is a little different here compared to the peak of pure MgH_2. A difference was also observed in the HP-DSC of MgH_2 in literature as the peak shifted when MgH_2 is in a mixture composed of other gas-producing compounds- that is the measured temperature being pressure dependent [69]. The 3-peak pattern is similar to what was reported in literature [93]. The temperatures of the next two dehydriding peaks are both lower in value compared to pure $NaMgH_3$. If a comparable H_2 pressure prevails in the two experiments, this supports the idea that Li-substitution lowers the thermal stability of the perovskite. The smaller cation placed at some of the A-sites caused a distortion in the unit cell because the site where sodium used to be is now occupied by a smaller lithium, thereby requiring a lower temperature for the hydrogen. Unfortunately, the comparison can only be made if the H_2 pressures in the two sample crucibles were the same.

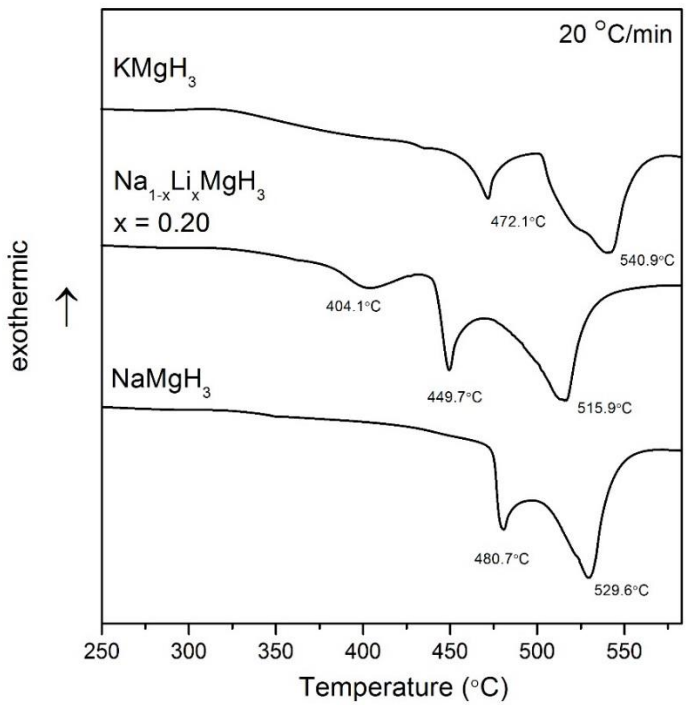

Figure 51. DSC curves of $NaMgH_3$, $Na_{1-x}Li_xMgH_3$, and $KMgH_3$ at a heating rate of 20°C/min. H_2 pressures inside the crucibles are different.

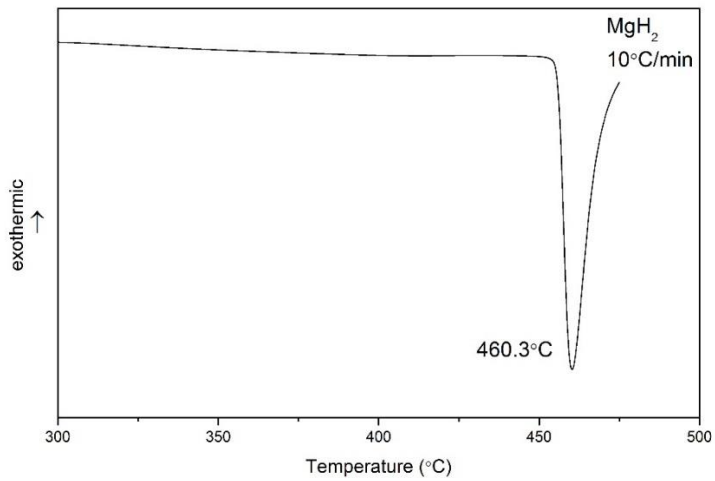

Figure 52. DSC curve of MgH_2 at a heating rate of 10°C/min.

The DSC curve for $KMgH_3$ is interesting as it shows a similar 2-step decomposition similar to $NaMgH_3$. This is contrary to what was suggested in literature where both thermal desorption mass spectroscopy (TDS) and PCI showed a one-step decomposition reaction for $KMgH_3$ [60]:

$$KMgH_3 \rightarrow K + Mg + 3/2\ H_2$$

However, the PCI experiment was performed at 400°C and 0.1 bar. Moreover, the reported decomposition temperature using TDS was around 370°C while the temperatures observed in the current DSC study for $KMgH_3$ were 472.1 °C and 540.9 °C, corresponding to each of the two steps (shift of temperature due to non-ambient H_2 pressure).

In the current study, based on the DSC data, it is suggested that the decomposition of $KMgH_3$ follows the mechanism similar of $NaMgH_3$:

$$KMgH_3 \rightarrow KH + Mg + H_2$$
$$KH + Mg + H_2 \rightarrow K + Mg + 3/2\ H_2$$

Variation in peak temperature at different heating rates using Differential Thermal Analysis can be used to determine the activation energy of certain solid → solid + gas reactions. As mentioned in Chapter I, the Kissinger equation is used to determine the activation energy, Ea, of a decomposition reaction using DTA patterns at different heating rates. Here, Tp is the peak temperature while δ is the heating rate. R is the gas constant while A is a constant. This equation is used by plotting $\ln\left(\delta/T_p^2\right)$ versus $1/T_p$, the slope of which, multiplied by –R, will give us the activation energy. [90]

$$\ln\left(\delta/T_p^2\right) = -E_a/RT_p + \ln(AR/E_a)$$

Energy barriers on each step of the hydrogen release process are considered in the gas-solid phase reactions of Mg-based hydrides. During the release and absorption reactions, the kinetics may be affected by certain metals or hydrides that are forming at the surface, and also the presence of impurities, preventing the diffusion of hydrogen [217]. Moreover, the hydrogen release process in Mg-based hydrides may have a different rate-limiting step, depending on the mechanism of the reaction which is affected by the activation energy of a particular step in the reaction. It is therefore interesting to look into the determination of activation energies for the decomposition steps during the hydrogen release of $NaMgH_3$ and $Na_{1-x}Li_xMgH_3$.

Figure 53 shows the DSC curves of $NaMgH_3$ and $Na_{1-x}Li_xMgH_3$ at different heating rates. The two dehydriding temperatures are labeled as T_{p1} and T_{p2}. T_{p1} and T_{p2} for $NaMgH_3$ observed at a heating rate of 10°C/min are 477.6°C and 526.2°C, respectively. This is consistent with T_{p1} and T_{p2} obtained from HP-DSC using the same heating rate found in literature (~495°C and ~540°C) [69]. It can be observed that T_p increases with the heating rate. However, the two DSC graphs can not be compared directly as the H_2 pressure inside the

sample crucibles were not the same. Unfortunately, pressure regulation in the HP-DSC model used was not available. It is envisioned that we perform the same measurement using an HP-DSC.

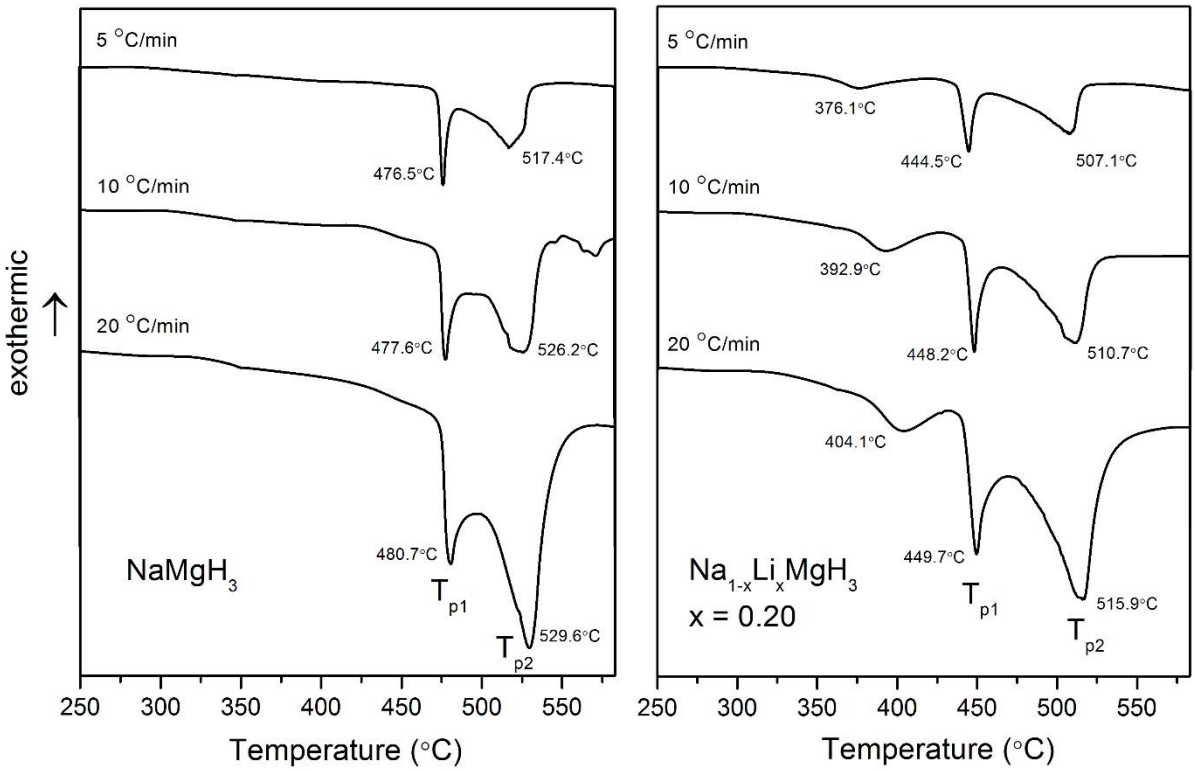

Figure 53. DSC curves of $NaMgH_3$ and $Na_{1-x}Li_xMgH_3$ at different heating rates. T_p = peak temperature. Pressure regulation was not available, therefore comparison is challenging.

Ideally, after cation substitution, a decrease in activation energy would be observed for the desorption process. As much as we wanted to calculate for the Ea, which is part of the objective, due to the uncertainty in H_2 pressure values in the crucible, it is not possible to compare the values obtained for the two decomposition steps. With the use of an HP-DSC, with pressure regulation, values for these could be reported.

V.3. Reversibility of hydrogen storage

Figure 54 shows the DSC curve of $NaMgH_3$ upon heating and cooling. Upon cooling, two exothermic peaks can be seen which are thought to be due to the reabsorption of hydrogen.

Hydrogen absorption requires high pressures of hydrogen [216]. At the start of cooling, the estimated H_2 pressure using the ideal gas equation is 115 bar. A confirmatory XRD analysis was performed to the $NaMgH_3$ sample after DSC.

Figure 55 shows the XRD patterns of $NaMgH_3$ after the DSC analysis compared to the initial sample. The peaks for $NaMgH_3$ can be seen in the XRD pattern of the sample after DSC which means that the desorption of hydrogen is indeed reversible. Thus, the two exothermic peaks during cooling in Figure 54 is confirmed to be the reabsorption of hydrogen to re-form NaH and eventually $NaMgH_3$. However, the process of re-forming $NaMgH_3$ was incomplete. This can be observed in the XRD patterns as several other peaks are present. Products during the 2-step decomposition of $NaMgH_3$, like NaH, MgH_2, and Mg, can be seen in the XRD pattern. There were also some unknown peaks observed, probably coming from the sample holder during the retrieval of the sample. The presence of Mg, MgO, and NaH in the $NaMgH_3$ sample after reabsorption of hydrogen was also observed in the XRD pattern found in literature [93].

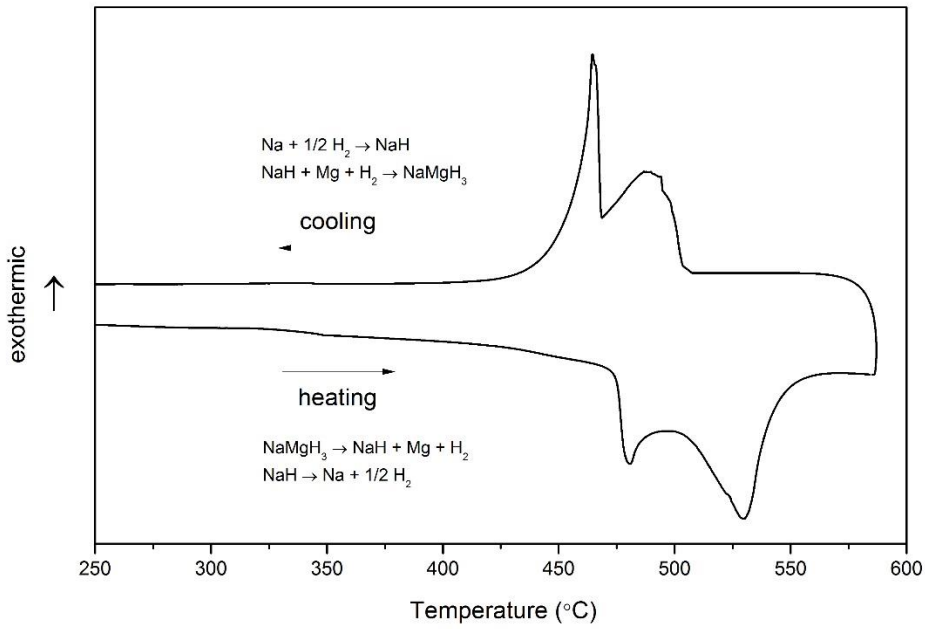

Figure 54. DSC curve of $NaMgH_3$ while heating up to 585°C and cooling back to room temperature. Estimated pressure before cooling was 115 bar.

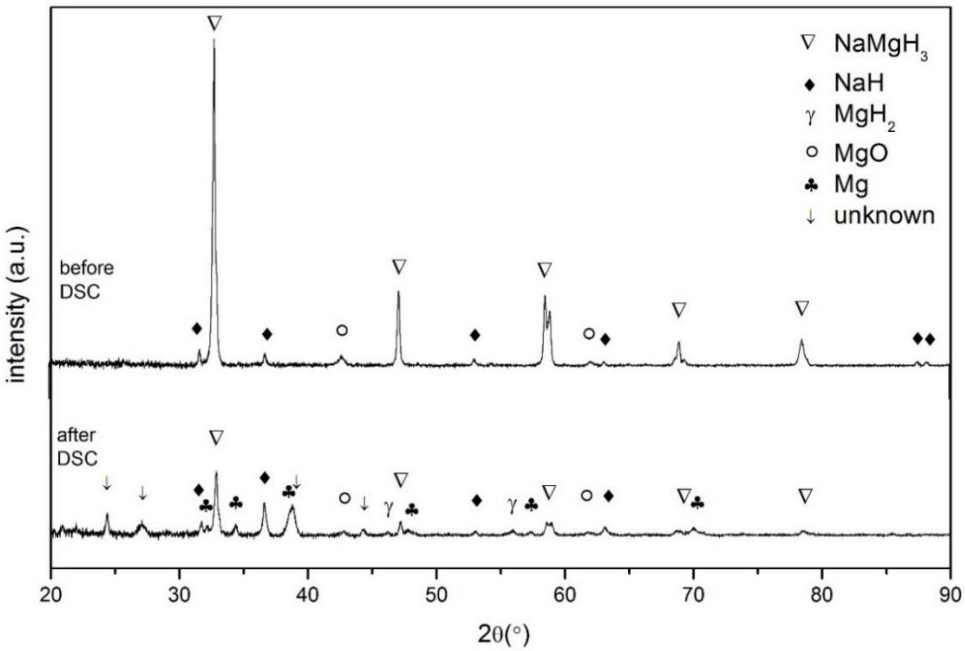

Figure 55. XRD patterns of $NaMgH_3$ before and after DSC up to 585°C.

In a similar manner, $Na_{1-x}Li_xMgH_3$ was also found to have a reversible hydrogen desorption reaction. Figure 56 shows the DSC curve with three exothermic peaks. The smallest peak may be attributed to the MgH_2 impurity. Pressure estimation was not possible due to the presence of both the perovskite and MgH_2.

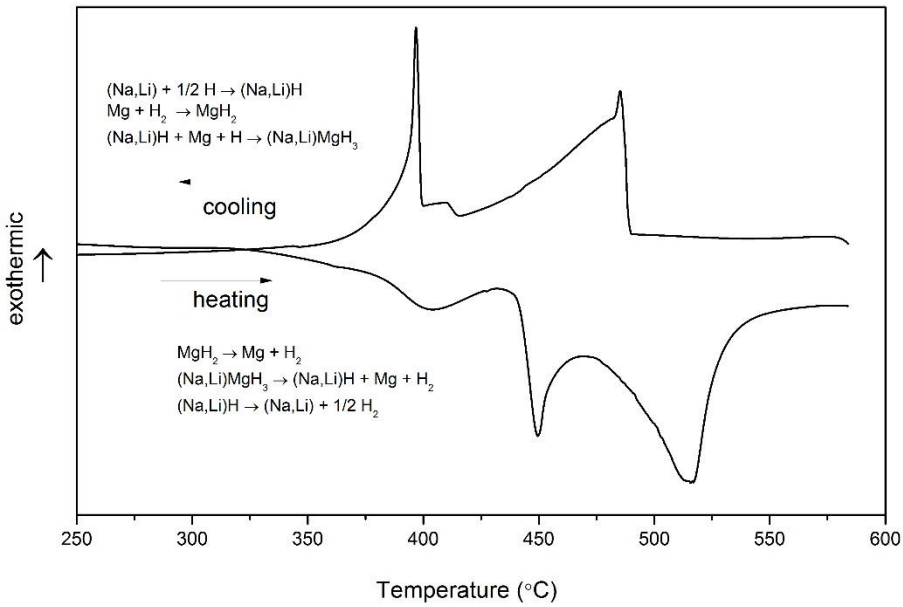

Figure 56. DSC curve of $Na_{1-x}Li_xMgH_3$ while heating up to 585°C and cooling back to room temperature. Pressure estimation was not possible due to the presence of unreacted MgH_2.

Figure 57 shows the XRD patterns of $Na_{1-x}Li_xMgH_3$ after the DSC analysis compared to the initial sample. The peaks for the perovskite can still be seen in the XRD pattern of the sample after DSC which means that the desorption of hydrogen is also reversible for the Li-substituted sample. Therefore, the two main exothermic peaks during cooling in Figure 56 correspond to the reabsorption of hydrogen. Similar to $NaMgH_3$, XRD peaks for $Na_{1-x}Li_xMgH_3$ can still be seen after DSC. The re-formation of MgH_2, on the other hand, was not observed as XRD peaks for Mg were seen instead of peaks for MgH_2. The small peak during cooling in Figure 56 may be something else or MgH_2 was not clearly seen in the XRD profile. It can also be observed that the re-formation of the Li-substituted $NaMgH_3$ has a "cleaner" XRD pattern compared to the unsubstituted one.

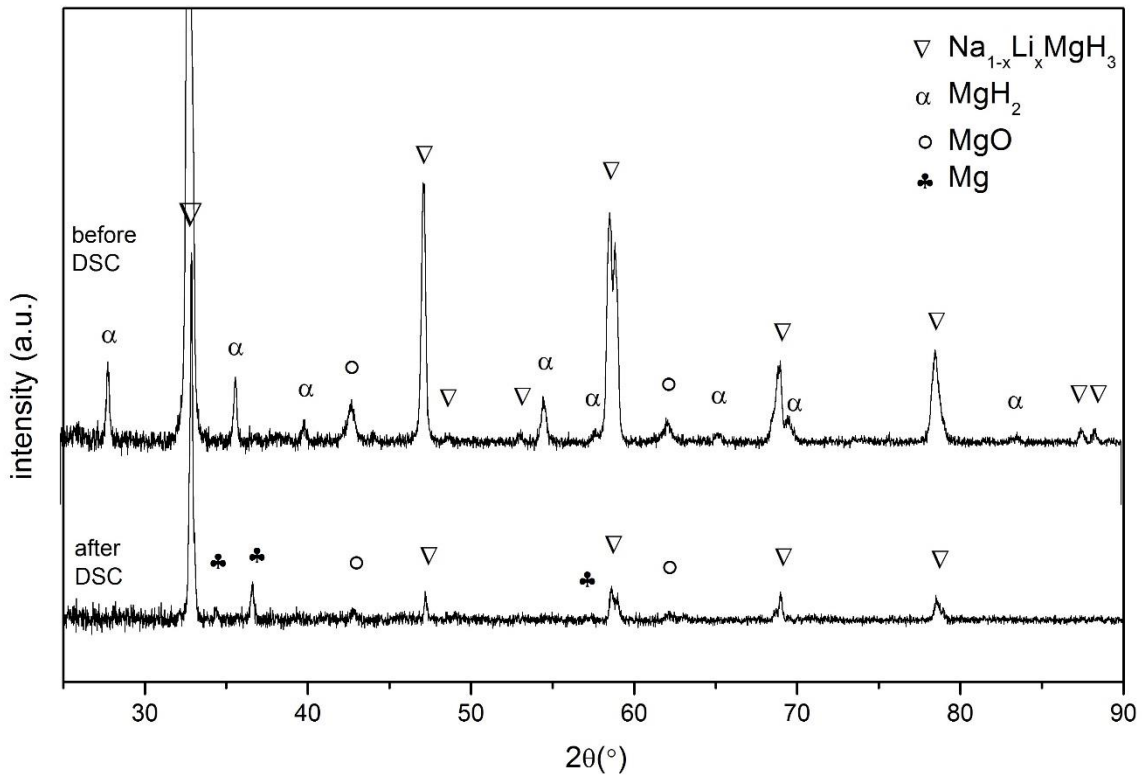

Figure 57. XRD patterns of $Na_{1-x}Li_xMgH_3$ before and after DSC up to 585°C.

Two main exothermic peaks during cooling in Figure 58 suggest that the dehydriding of $KMgH_3$ is reversible. The estimated H_2 pressure at the start of cooling is 49 bar. The suggested reverse mechanism is similar to $NaMgH_3$. There is the re-formation of KH and, eventually, $KMgH_3$. This was contrary to what was reported in literature that the hydrogen

desorption reaction of $KMgH_3$ is not reversible [60]. The third smaller peak is probably the side reaction product, K_2MgH_4, as seen in the XRD pattern in Figure 59.

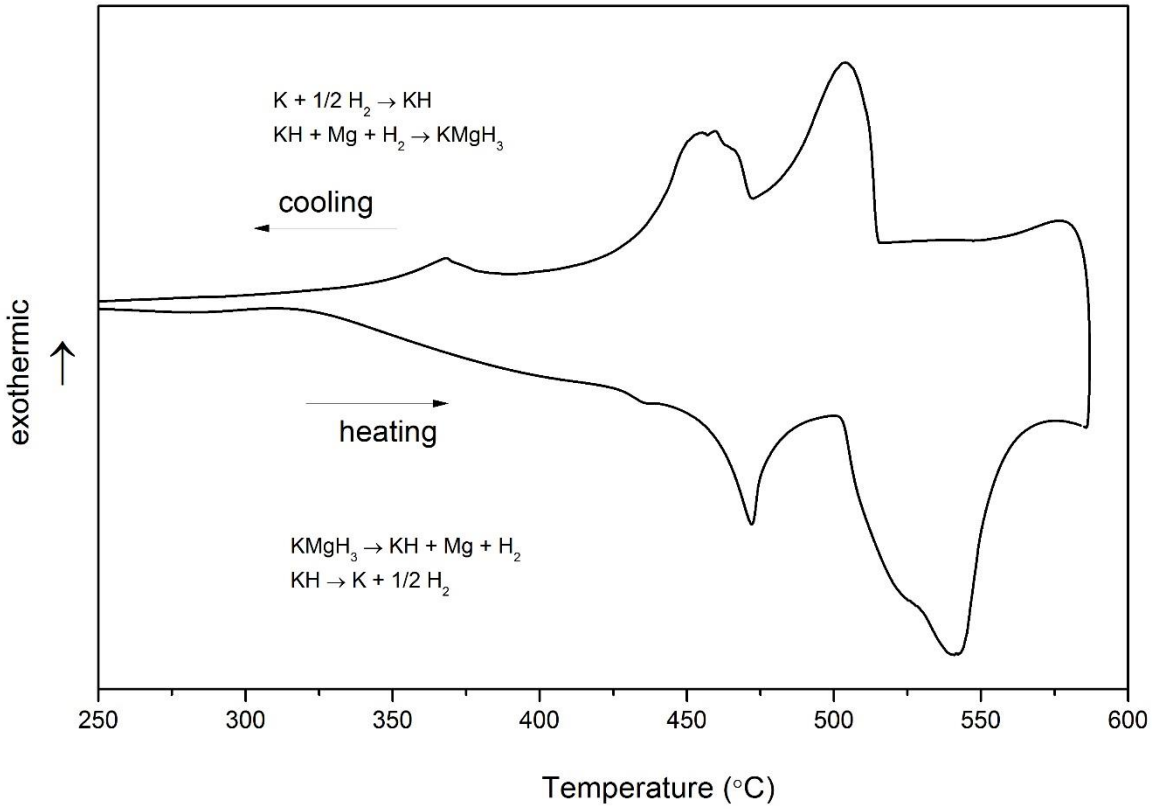

Figure 58. DSC curve of $KMgH_3$ while heating up to 585°C and cooling back to room temperature. Estimated pressure before cooling was 49 bar.

Figure 59 shows the XRD patterns of $KMgH_3$ after the DSC analysis compared to the initial sample. The peaks for $KMgH_3$ can still be seen after DSC. This supports the idea that the hydrogen desorption is reversible at 585°C and 49 bar. However, a side reaction was observed. Peaks for K_2MgH_4 can be seen in the XRD pattern after DSC. Hence, the decreased intensity in the $KMgH_3$ peaks.

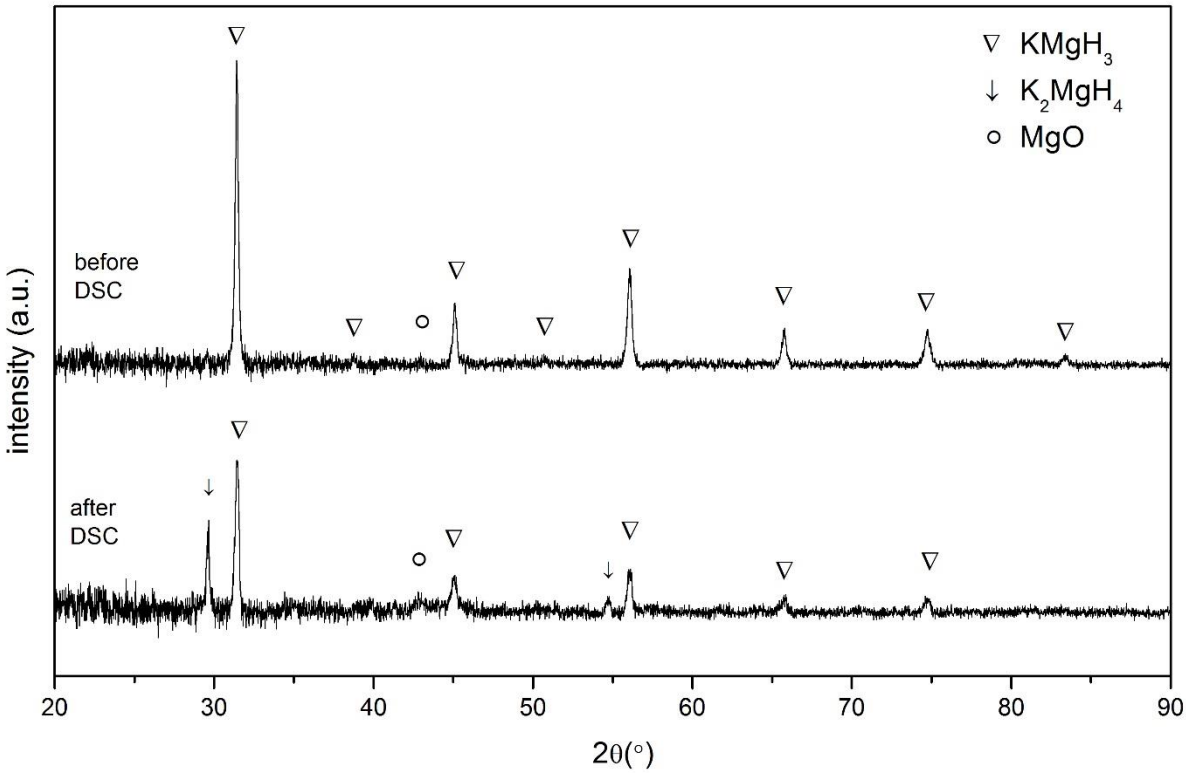

Figure 59. XRD patterns of $KMgH_3$ before and after DSC up to 585°C.

Chapter Summary

The volume thermal expansion coefficient at 300 K of $NaMgH_3$ is reported for the first time. The calculation of activation energies of the desorption process for $NaMgH_3$ and $Na_{1-x}Li_xMgH_3$ encountered some issues due to the fact that the HP-DSC study performed lacked a pressure regulation mechanism. The reversibility of the hydrogen storage for these two samples were likewise presented.

On the other hand, $KMgH_3$ was found to have a two-step decomposition reaction. The suggested mechanism is similar to that of $NaMgH_3$. Likewise, the hydrogen desorption process of $KMgH_3$ was found to be reversible as evidenced by DSC and XRD data, with a little side reaction (formation of K_2MgH_4).

General conclusion and perspectives

This research of three and a half years was carried out to understand the synthesis process of perovskite hydrides, their properties and behavior at extreme pressure and temperature conditions. The possibility of synthesizing new materials has also been explored. Chapter I provided the necessary background and context for the need to synthesize new materials for hydrogen storage. With current hydrogen storage materials facing some issues about their practical applications, there is still a need to modify certain aspects in order to get the ideal properties envisioned for a perfect hydrogen storage material.

With the different experimental methodologies presented in Chapter II, the synthesis and characterization of light metal perovskite hydrides for hydrogen storage were explored. Large volume presses were used to allow the synthesis to happen at extreme pressures and temperatures. X-ray diffraction and neutron powder diffraction studies enabled the analysis of the crystal structure of the products. Thermal properties were also investigated to explore the effect of certain modifications in structure to the hydrogen storage properties of the hydrides.

Chapter III presented and discussed the synthesis and characterization of three perovskite hydrides $NaMgH_3$, $Na_{1-x}Li_xMgH_3$, and $KMgH_3$. It was shown that these materials can be synthesized using the autoclave, and large volume presses such as the CONAC press, and the belt press. In-situ XRD analysis using the Paris-Edinburgh press allowed for the understanding of the synthesis pathway of $NaMgH_3$. At 2 GPa and 4 GPa, it was observed that a phase transition of MgH_2 from its α–phase to its γ–phase occurred before the reaction of it with NaH to form the perovskite $NaMgH_3$. At a higher pressure of 7.4 GPa, the $NaMgH_3$ perovskite was not synthesized. Instead, it was observed that a phase transformation from the γ–phase to the β–phase of MgH_2 occurred. It was proposed that γ–MgH_2 is involved in the reaction with NaH. The substitution of Na with Li in $NaMgH_3$ was also investigated. The synthesis of $Na_{1-x}Li_xMgH_3$ with different values of x was performed. XRD data showed that all Li-substituted $NaMgH_3$ had unit cell volumes that are smaller than the pure $NaMgH_3$ due to the smaller size of the Li atom, as evidenced by the shift of the XRD peaks to higher 2 theta values. Rietveld refinement of XRD data showed that the maximum Li-substitution that can be done is 20%. It is envisioned that the extent of Li-substitution be determined at HP-HT using in situ XRD. Similarly, It would be interesting to continue the analysis of $Na_{1-x}Li_xMgH_3$ by doing experiments on its hydrogen sorption properties. Likewise, the production of a pure

sample remains a challenge that must be solved in the future. On the other hand, the last part of the chapter presented the cubic perovskite hydride, $KMgH_3$. Synthesis conditions were optimized so as not to produce a side product, K_2MgH_4.

One mechanical property which is the bulk modulus was the focus of chapter IV. High-pressure neutron powder diffraction study was performed at the D1B beamline of Institut Laue-Langevin. The use of large scale instrument provided the necessary information needed to carefully study the structure of the perovskite hydride samples. Investigation of any pressure-induced phase transformation in $NaMgH_3$ was conducted. The results here revealed that no phase transformation was observed for $NaMgH_3$ up to 10.7 GPa at room temperature. The sample cannot be indexed in the *Cmcm* nor in the $Pm\bar{3}m$ space group. With this NPD data, on the other hand, the experimental bulk modulus and its pressure derivative of $NaMgD_3$ were obtained for the first time. The bulk modulus obtained is 43.9(1.3) GPa and its pressure derivative is 3.4(3). Likewise, pressure-induced phase transformation studies using NPD revealed that no phase transformation occurred for $KMgD_3$ up to 11.6 GPa. Based on the NPD data, the experimental bulk modulus of $KMgD_3$ was found to be 39.0(7) GPa while the pressure derivative obtained was 3.5(2). This is also the first time that an experimental bulk modulus for this material has been reported. These values will be reported in a scientific journal article soon. It is envisioned that pressure-induced phase transformation studies with a larger pressure and temperature range be performed for all the sample presented.

In chapter V, the thermal properties of the perovskite hydrides were studied using differential scanning calorimetry. Due to uncertainties in H_2 pressure, the activation energies of the two decomposition steps were not calculated. Results of the DSC also revealed a two-step decomposition for $KMgH_3$ similar to $NaMgH_3$. All samples, $NaMgH_3$, $Na_{1-x}Li_xMgH_3$, and $KMgH_3$, showed reversibility in dehydriding, as revealed by results of DSC and XRD. The reversibility observed for $KMgH_3$ contradicts previous published data and therefore may be a good sign to spark new investigations for $KMgH_3$ for hydrogen storage. Moreover, another neutron diffraction study at low temperatures enabled the determination of the volume coefficient of thermal expansion at 300 K for the first time for $NaMgH_3$.

Overall, this manuscript has presented several light metal hydrides that were synthesized at extreme pressure-temperature conditions. The method of synthesizing new materials using the autoclave, the belt press, the CONAC press, and the Paris-Edinburgh Press is indeed promising for the discovery of new materials. Several attempts for the synthesis of

new materials are shown in the Appendix. This is still a work in progress. A ton of work still needs to be done in this area. So, the perspective would be to try other cation combinations for the A-sites and B-sites of the perovskite. It would also be interesting to investigate the behavior of $NaMgH_3$ and $KMgH_3$ both at high pressure and temperature using large-scale instruments.

In order to explore the possibility of synthesizing new materials for hydrogen storage, the high-pressure, high-temperature synthesis approach used in this thesis seemed to be very encouraging.

APPENDIX

Appendix A. Synthesis and characterization of $LiMgH_3$

Background

Complete substitution of sodium by lithium in $NaMgH_3$ was not successful. However, due to the lightweight nature of lithium, the Li-Mg-H system is still an interesting system to look into [218]. One hydride belonging to this system Li-Mg-H is $LiMgH_3$ which has a high gravimetric capacity of 8.8 wt% H_2. This material, according to electronic structure calculations, is an insulator [219].

Previous calculations by Vajeeston et al [49] and Li et al [218] supported the claims that $LiMgH_3$ is of the $LiTaO_3$-type with a *R3c* space group and that it is dynamically stable. The lattice parameters and positional parameters are shown in Table 27 while the crystal structure is shown in Figure 60. Both references in Table 27 show that the lattice parameter is close to 4.9 Å but according to calculations by Pluengphon et al., a = 5.311 Å [220]. According to Li et al., the MgH_6 and LiH_6 have similar shapes and both are distorted octahedra.

Five reaction pathways have been proposed [218].

$$Li + Mg + 3/2\ H_2 \rightarrow LiMgH_3$$
$$LiMg + 3/2\ H_2 \rightarrow LiMgH_3$$
$$LiH + MgH_2 \rightarrow LiMgH_3$$
$$Li + MgH_2 + ½\ H_2 \rightarrow LiMgH_3$$
$$LiH + Mg + H_2 \rightarrow LiMgH_3$$

And all of these pathways have negative calculated Gibbs free energy which means that $LiMgH_3$ can be synthesized.

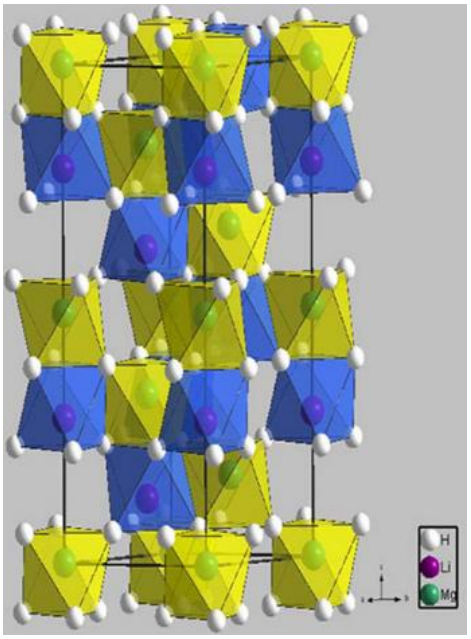

Figure 60. Crystal structure of $LiMgH_3$ (*R*3*c*)based on the calculations of Li et al [218].

Table 27. . Optimized lattice parameters and positional parameters of ground state $LiMgH_3$ from Li et al. [218] and Vajeeston et al[49].

$LiMgH_3$ ($LiTaO_3$, *R*3*c*)	**Ref.** [49]	**Ref.** [218]
Lattice parameters	a = 4.958	a = 4.9226
	c = 13.337	c = 13.2106
Positional parameters	Li (6a): 0.0, 0.0, 0.2887	Li(6a): 0.0,0.0,0.2915
	Mg (6a): 0, 0, 0	Mg(6a): 0.0,0.0,0.0013
	H (18b): 0.0376, 0.3626, 0.5637	H(18b): 0.0361,0.3641,0.0660

The challenge remains in the thermodynamically reversible decomposition of $LiMgH_3$ to LiH and MgH_2, which hinders the synthesis and stable existence of $LiMgH_3$ [218]. The Gibbs free energy of $LiMgH_3$ from the reaction of LiH and MgH_2 presented previously is -10 kJ/mol which is close to zero. Having zero Gibbs free energy means that the process is reversible. Therefore, when $LiMgH_3$ is formed, it can revert back to its precursors. Another thing to note is the enthalpy of reaction (ΔH_{rxn}) calculated by Vajeeston et al for this pathway, which is 4.048 kJ/mol which means it is endothermic [49]. From the formula of Gibbs free energy for any process:

$$\Delta G = \Delta H - T\Delta S$$

For a process to be spontaneous, ΔG should be negative (-). In the reaction of LiH and MgH_2 to form $LiMgH_3$, ΔS is negative (-) due to the formation of a single compound from two precursors. If ΔS is negative, then the second term of the equation above is always positive. Now, if the calculated ΔG of Li et al is correct to be negative, then the ΔH calculated by Vajeeston et al is questionable. Otherwise, if ΔH is indeed positive as suggested by Vajeeston, then ΔG is positive and the pathway is not spontaneous and will never happen.

Another Li-Mg-H compound was studied using first principle predictions. Peltzer y Blanca calculated the ΔG of a theoretical $LiMgH_4$ compound having a cubic structure (P23 space group). However, the calculated ΔG for formation is positive and therefore is not synthesizable [221].

It is hypothesized that it could be possible to synthesize $LiMgH_3$ at HP-HT conditions but since the material decomposes into its hydride precursors, it is impossible to observe the product at ambient conditions. With in-situ X-ray diffraction, it is possible to see the formation of the desired product at HP-HT conditions in order to understand its behavior and its decomposition.

First attempts of synthesizing $LiMgH_3$ happened in the late 1960s. Tanaka et al. performed hydrogenolysis of a mixture of CH_3Li and $(CH_3)_2Mg$ at high temperatures while Coates et al. reported pyrolysis of the n-butyllithium adduct of $(CH_3)_2Mg$, both of which failed to synthesize the desired $LiMgH_3$ [97][222]. Several other attempts have been made, however the product was not successfully synthesized citing a Goldschmidt tolerance factor of t = 0.727 as the reason [92][71][89][93]. This value is not within the tolerance factor fit for a perovskite structure.

Goto et al. tried and subjected a mixture of MgH_2-33 mol% LiH to 5 GPa and 700°C (973 K) for 4h and they were able to synthesize a different product, a Mg-Li hydride with a different composition, Mg_2LiH_5 [182]. They tried equimolar amounts, but they were not able to produce the desired products.

Different synthesis conditions were used in the synthesis of $LiMgH_3$ from LiH and MgH_2 using both the belt press and CONAC press. Table 28 shows the summary of all experiments performed. The old-school approach of trial-and-error was used to optimize the synthesis pressure, temperature, and treatment time.

Figure 61 shows XRD patterns obtained after synthesis using the belt press. The pattern corresponding to the sample treated at 7 GPa and 650°C (bottom) is representative of most of the diffractograms collected on the samples after quenching at room temperature and ambient pressure. It can be seen that there was an α-γ phase transition that occurred with MgH_2. Lithium hydride can still be seen and some oxidation was observed due to the presence of MgO. The diffractogram collected from the sample treated at 2 GPa and 400°C (top of Figure 61) is composed of the reflections assigned to LiH, MgH_2, Li_2O and MgO plus three unidentified peaks. These peaks cannot be assigned to a predicted structure of $LiMgH_3$ and it was not possible to index them. Some experiments performed at 900°C have a lot of unidentified XRD peaks that may have come from the reaction of the sample mixture with the capsule.

Table 28. Synthesis parameters used for the synthesis of $LiMgH_3$ from LiH and MgH_2.

Pressure	Temperature	Time	Press	Capsule
1 GPa	900°C	25 min	belt	Au
2 GPa	400°C	1.5 h	belt	Au
2 GPa	650°C	2 h	belt	Pt
2 GPa	650°C	2 h	CONAC40	Pt
2 GPa	650°C	2 h	CONAC40	Au
2 GPa	900°C	2 h	belt	Au
4 GPa	650°C	30 min	CONAC28	Au
6 GPa	650°C	2 h	belt	Au
6 GPa	900°C	2 h	belt	Au
7 GPa	650°C	2 h	belt	Au
7 GPa	800°C	2 h	belt	Au
7 GPa	900°C	2 h	belt	Au
5.8 GPa	900°C	2 h	CONAC28	Au w/NaCl
5.8 GPa	900°C	2 h	CONAC28	Au w/BN
7 GPa	900°C	2 h	belt	Au w/BN

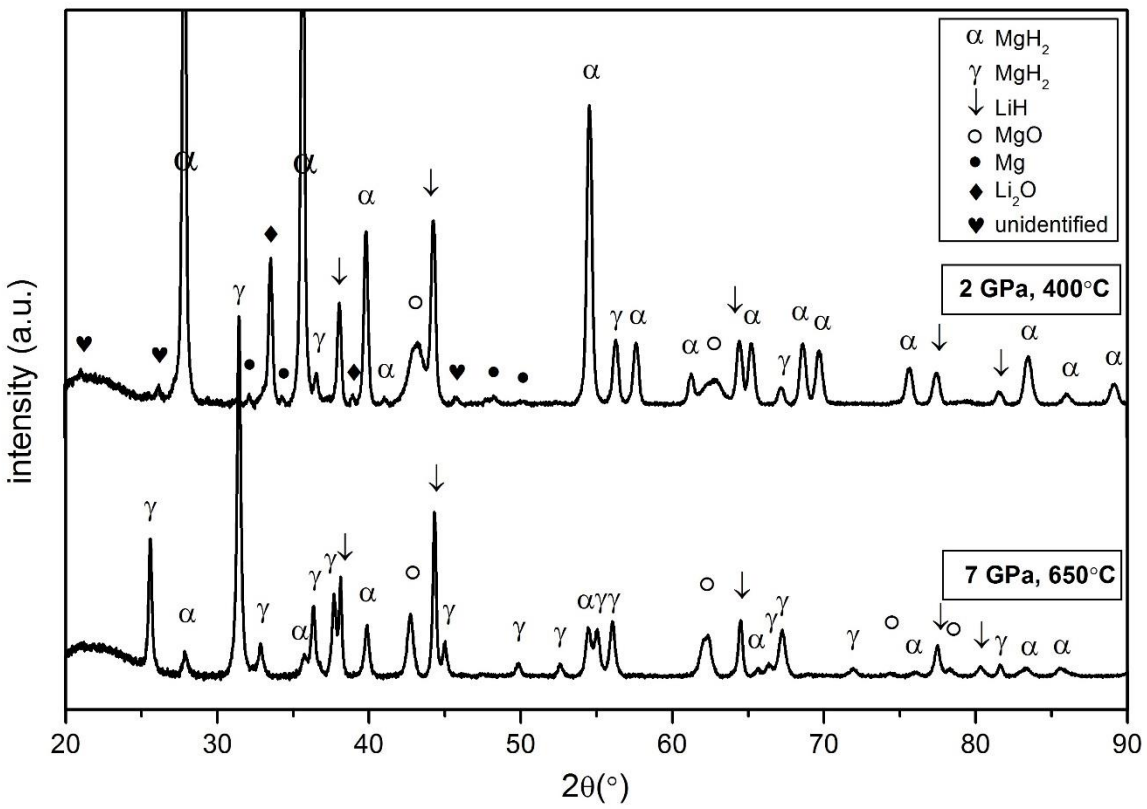

Figure 61. XRD pattern of the synthesis of $LiMgH_3$ using LiH and MgH_2 at 2 GPa, 400°C (top) and 7 GPa, 650°C (bottom) using the belt press.

The parametric study of varying pressure and temperature did not allow to reveal the favorable conditions for the production of $LiMgH_3$. Three hypotheses can be formulated:

1. $LiMgH_3$ cannot be synthesized in the pressure and temperature range investigated.
2. $LiMgH_3$ cannot be synthesized from LiH and MgH_2 in the pressure and temperature range considered.
3. $LiMgH_3$ can be elaborated under HP-HT but is not stable at ambient conditions and cannot be identified on samples brought back to ambient conditions.

Usually, when one of the precursors is thermally unstable, high pressure can aide the synthesis. Given at ambient pressure, $T_{decomposition}$ of the thermally unstable precursor is less than $T_{reaction}$ ($T_{d1} < T_{rxn}$), the reaction would not occur. When the pressure is increased, T_{d1} is also increased, such that it would be possible that $T_{d1} > T_{rxn}$. Then, the reaction could proceed [159]. Hypothesis 3 was tested through in-situ experiment at HP-HT using the PEP at 4 GPa and 7.5 GPa.

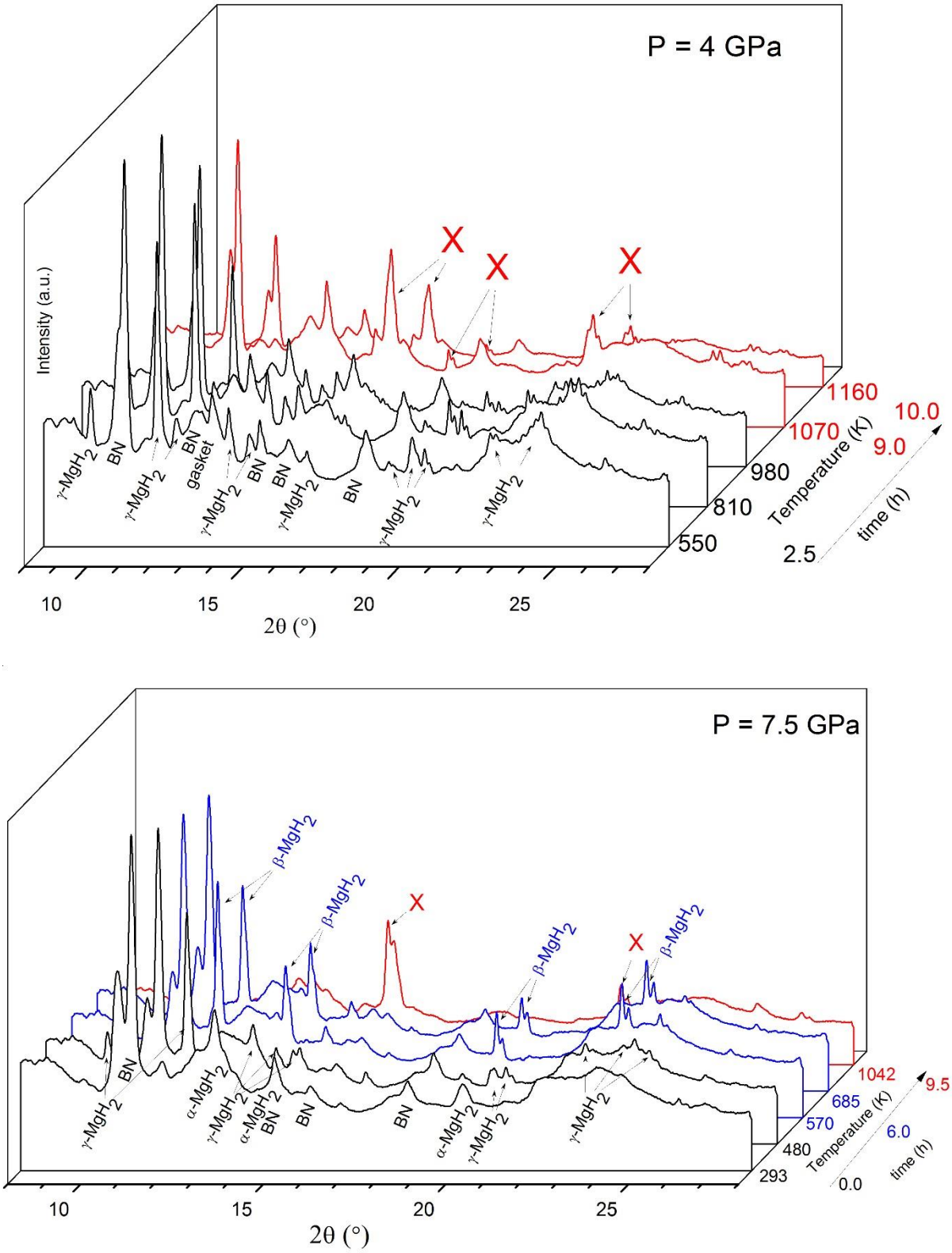

Figure 62. XRD patterns obtained in-situ using the Paris-Edinburgh press during the synthesis of $LiMgH_3$ from LiH and MgH_2 at 4 GPa (top) and 7.5 GPa (bottom).

Figure 62 shows the patterns from the in-situ XRD measurements of the synthesis of $LiMgH_3$ from LiH and MgH_2 using the PEP at 4 GPa and 7.5 GPa. At 4 GPa, the γ-phase of MgH_2 was observed up to ~707°C (980 K), which was not the case with the NaH + MgH_2 mixture in Chapter III, because at this temperature $NaMgH_3$ has already formed. In the case of the LiH + MgH_2 mixture, no reaction was observed at this temperature. When the temperature exceeded ~797°C (1070 K), unknown peaks were observed. This was attributed to the formation of an unknown phase (X-phase) brought about by oxidation and this was previously observed in experiments on pure MgH_2 performed in the same conditions.

Similarly, no reaction was observed when the pressure was raised to 7.5 GPa. The presence of β-MgH_2 was observed beyond ~297°C (570 K). This is consistent with the PEP experiment performed at 7.4 GPa in Chapter III, where the β-phase was observed beyond ~327°C (600 K). When the temperature reached ~769°C (1042 K), X-phase is formed as in the experiment at 4 GPa. Again, these were attributed to the formation of the X-phase.

Referring to the calculated Gibbs free energy and enthalpy of the reaction between LiH and MgH_2 to form $LiMgH_3$ discussed in Chapter I, it is now a question whether the calculations can translate to a synthesizable material. Compared to $NaMgH_3$, the calculated formation enthalpy for $LiMgH_3$ from LiH and MgH_2 is not exothermic. So, this may be the reason why $LiMgH_3$ synthesis has not yet been successfully done experimentally [49].

Due to time constraints of this work, further investigation was not possible. A possible pathway would be to attempt the synthesis starting with other precursors, preferentially using in-situ characterization.

Appendix B. Synthesis and characterization of $NaCaH_3$

Background

Another interesting set of hydrides where alkali metals and alkaline-earth metals are paired are the ones that are calcium-based. In the third column of Table 2, the series of Ca-based hydride can be seen, starting from $LiCaH_3$ up to $CsCaH_3$. It is established that $RbCaH_3$ and $CsCaH_3$ have been experimentally synthesized [54]. However, the first three in the set, $LiCaH_3$, $NaCaH_3$, and $KCaH_3$, have not yet been synthesized, although some fluorinated $KCaH_3$ have been synthesized in the form of $KCaH_{3-x}F_x$ by Bouamrane et al [223]. This opens the opportunity to explore these materials for possible hydrogen storage hydrides.

From the computational screening performed by Li et al., the formation and reaction enthalpies of major perovskite hydrides were plotted in Figure 63. It was noted that among these perovskite systems, $NaCaH_3$ was the most attractive system to investigate due to a low hydrogen release reaction enthalpy of 0.071 eV and a relatively more negative heat of formation (more exothermic) [54].

Vajeeston et al. performed structural optimization calculations of the ground state structures of $NaCaH_3$ which can store theoretically 4.6 wt% H_2 [224]. Their results show two phases of $NaCaH_3$, the α-$NaCaH_3$ ($P\bar{1}$) (Figure 64) and the meta-$NaCaH_3$ (*R3c*). In the α-$NaCaH_3$ phase shown in Figure 64, Vajeeston et al. described that the Na atom is surrounded by 5 H atoms while Ca is surrounded by 7 H atoms. On the other hand, the meta form has 6 H atoms surrounding both Na and Ca, and the NaH_6 and CaH_6 octahedra formed are distorted. The Goldschmidt tolerance factor for this calculated structure is 0.78 which is within the perovskite-like structure. The optimized lattice parameters and positional parameters for $NaCaH_3$ by Vajeeston et al. are presented in Table 29 [224].

For the $NaCaH_3$ synthesis pathways, Vajeeston's team noted two specific pathways that can be related to $NaMgH_3$.

$$MH + CaH_2 \rightarrow MCaH_3$$

$$M + Ca + \frac{3}{2}H_2 \rightarrow MCaH_3$$

Where M represents the alkali metal

These two pathways were experimentally performed for $MMgH_3$ synthesis. However, for $MCaH_3$ synthesis, only the second pathway is deemed feasible. According to their

calculations, the heat of formation for $NaCaH_3$ using pathway1 is 34.45 kJ mol^{-1} (endothermic) while that for pathway2 is -177.79 kJ mol^{-1} (exothermic). The synthesis using metal precursors and H_2 gas is more exothermic. Hence, synthesis may proceed using this route. Also, $MCaH_3$ materials are believed to have a soft and compressible nature due to the low calculated B_0 values from their study and due to the weak M-Ca interaction [224]. Due to its soft character, they added that hydrogen destabilization may occur. However, the Ca-H bonds may be strong so hydrogen release may occur at high temperature. The endothermicity of pathway 1, the softness of $MCaH_3$, and the strong Ca-H interaction are the problems that need to be solved. To the best knowledge of the researcher, no study has been conducted on the synthesis of $NaCaH_3$ using NaH and CaH_2 as precursors nor on its hydrogen storage properties. There is one study by Sartori et al. that wish to form a new hydride from a mixture of NaH, CaH_2, and Al [225]. However, no reaction was observed in their attempt to make a new hydride. The challenge is how to use HP-HT techniques in the synthesis of $NaCaH_3$.

Table 29. Optimized lattice parameters and positional parameters of $NaCaH_3$ from Vajeeston et al [224].

	Lattice parameters	**Positional parameters**
α-$NaCaH_3$ (*P*$\bar{1}$)	a = 6.8555	Na(2i): 0.7257, 0.0131, 0.2737
	b = 7.1940	Ca(2i): 0.1609, 0.6291, 0.7517
	c = 6.8040	H1(2i): 0.9004, 0.5172, 0.6503
	α = 118.59°	H2(2i): 0.3627, 0.8224, 0.0155
	β = 117.01°	H3(2i): 0.2330, 0.8404, 0.3466
	γ = 29.78°	
meta-$NaCaH_3$ (*R3c*)	a = 5.8632	Na(6a): 0.0, 0.0, 0.7826
	c = 15.2174	Ca(6a): 0.0, 0.0, 0.0014
		H(18b): 0.9878, 0.2819, 0.3980

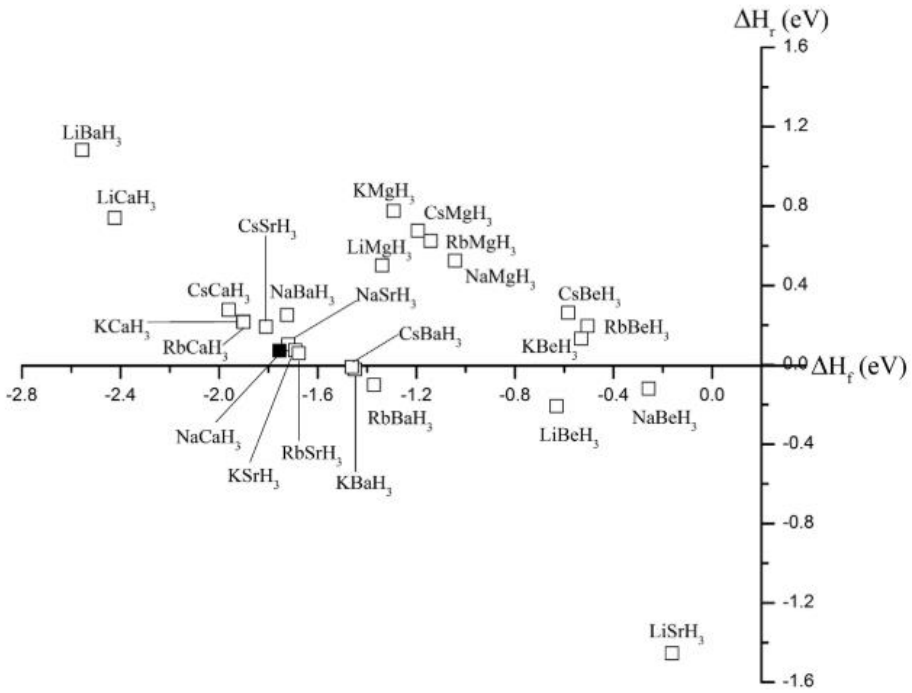

Figure 63. Enthalpy of hydrogen release (ΔH_r) and enthalpy of formation (ΔH_f) of perovskite hydrides from calculations [54].

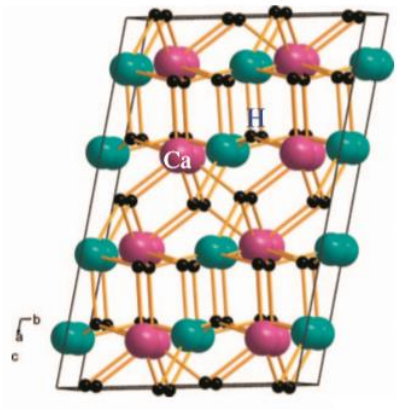

Figure 64. Theoretical structure of $NaCaH_3$ [224].

Experimental

An equimolar NaH:CaH_2 mixture was used for the synthesis. The mixture was placed in a gold capsule and was subjected to HP-HT conditions in the press shown in Table 30. XRD patterns were obtained for each sample. All of the samples showed similar XRD patterns like the one shown in Figure 65. It was observed that the peaks for the NaH and CaH_2 precursors

are the main peaks in the patterns. Therefore, the NaH and CaH_2 precursors did not react at the given pressure and temperature conditions. A little oxidation also occurred due to the appearance of CaO.

Table 30. Synthesis conditions for the synthesis of $NaCaH_3$ from NaH and CaH_2.

Pressure	Temperature	Time	Press
6 GPa	650°C	1 h	belt
6 GPa	900°C	1 h	belt
4 GPa	400°C	1.5 h	belt
2 GPa	650°C	2 h	CONAC40

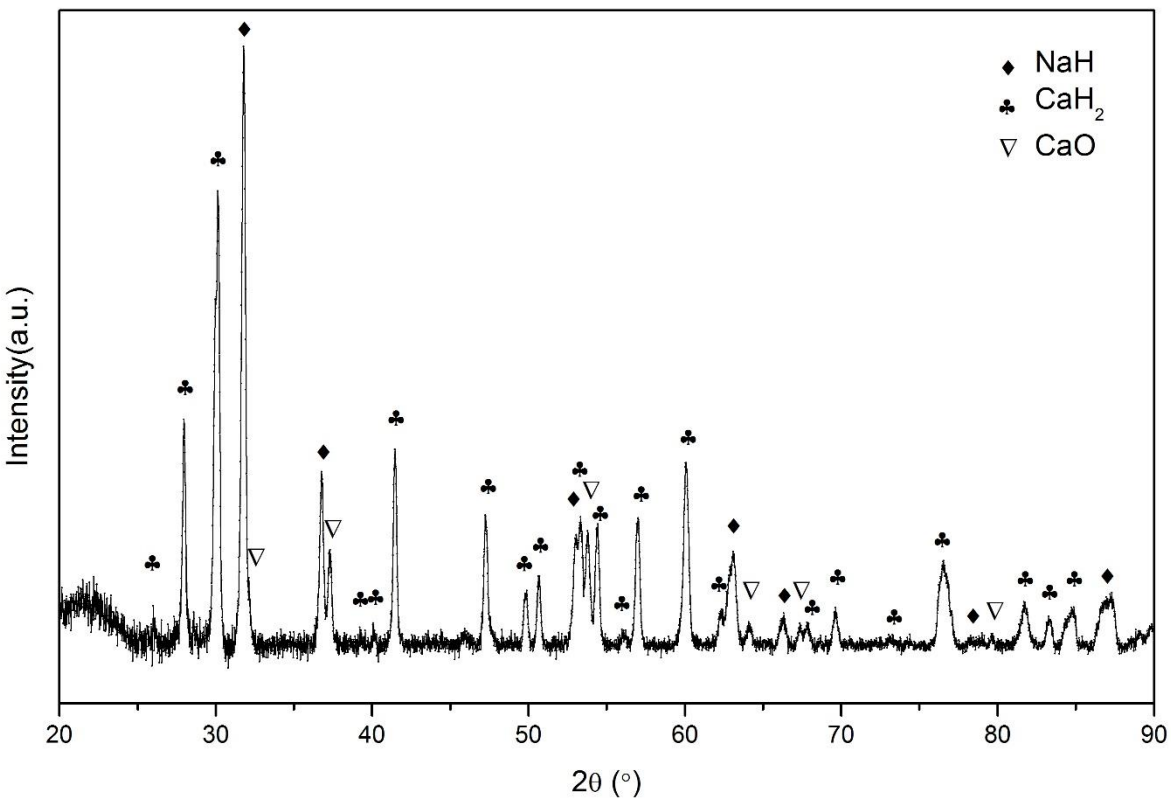

Figure 65. XRD pattern of the synthesis product at 2 GPa and 650°C using the conac press.

The investigation at different pressure and temperature did not give the favorable conditions for the synthesis of $NaCaH_3$. Three hypotheses can be formulated, similar to those in Appendix A:

1. $NaCaH_3$ cannot be synthesized in the pressure and temperature range investigated.

2. $NaCaH_3$ cannot be synthesized from NaH and CaH_2 in the pressure and temperature range considered.
3. $NaCaH_3$ can be elaborated under HP-HT but is not stable at ambient conditions and cannot be identified on samples brought back to ambient conditions.

Because of limited time to complete this work, further experimentation was not performed. A possible alternative would be to synthesize $NaCaH_3$ using other precursors and to analyze using in-situ characterization.

Appendix C. Synthesis and characterization of $K_{1-x}Li_xMgH_3$

As mentioned in chapter I, among the group IA elements, it is Lithium that shows some promise for the improvement of hydrogen release when added to $KMgH_3$ to produce a substituted product $K_{1-x}Li_xMgH_3$ [112]. So a mixture of KH, LiH, and MgH_2 was prepared to have a $K_{1-x}Li_xMgH_3$ product with x = 0.5. The 50%-50% K-Li composition was initially chosen to have a baseline of the extent of Li-substitution possible. The synthesis was performed using the same sample assembly and synthesis parameters for the $KMgH_3$ synthesis in the CONAC press described in section III.3.c. Analysis of the XRD pattern of the obtained product showed no formation of the substituted product (Figure 66). The peaks for the substituted $KMgH_3$ product were the same as the original $KMgH_3$ in terms of peak positions. Normally, when a smaller ion, like Li, substitutes for the bigger K ions, the peak for the perovskite shifts to a higher 2θ values due to the decrease in volume brought about by the substitution. In this case, it can be said that no such thing occurred. The peaks associated with the $KMgH_3$ perovskite had lower intensities mainly due to the decreased amount of KH in the starting mixture. Since the substitution did not occur, the peaks for the unreacted MgH_2 can still be seen in the XRD pattern. Moreover, peaks for K_2MgH_4 were also visible. Contamination with BN from the BN capsule occurred as shown by the BN peaks in the XRD pattern. Several peaks are left unidentified because of the uncertainty on the possible formation of $LiMgH_3$ or Li_2MgH_4 from this mixture, both of which have not yet been synthesized and only theoretical XRD data is present. Further investigation was not performed due to limited time.

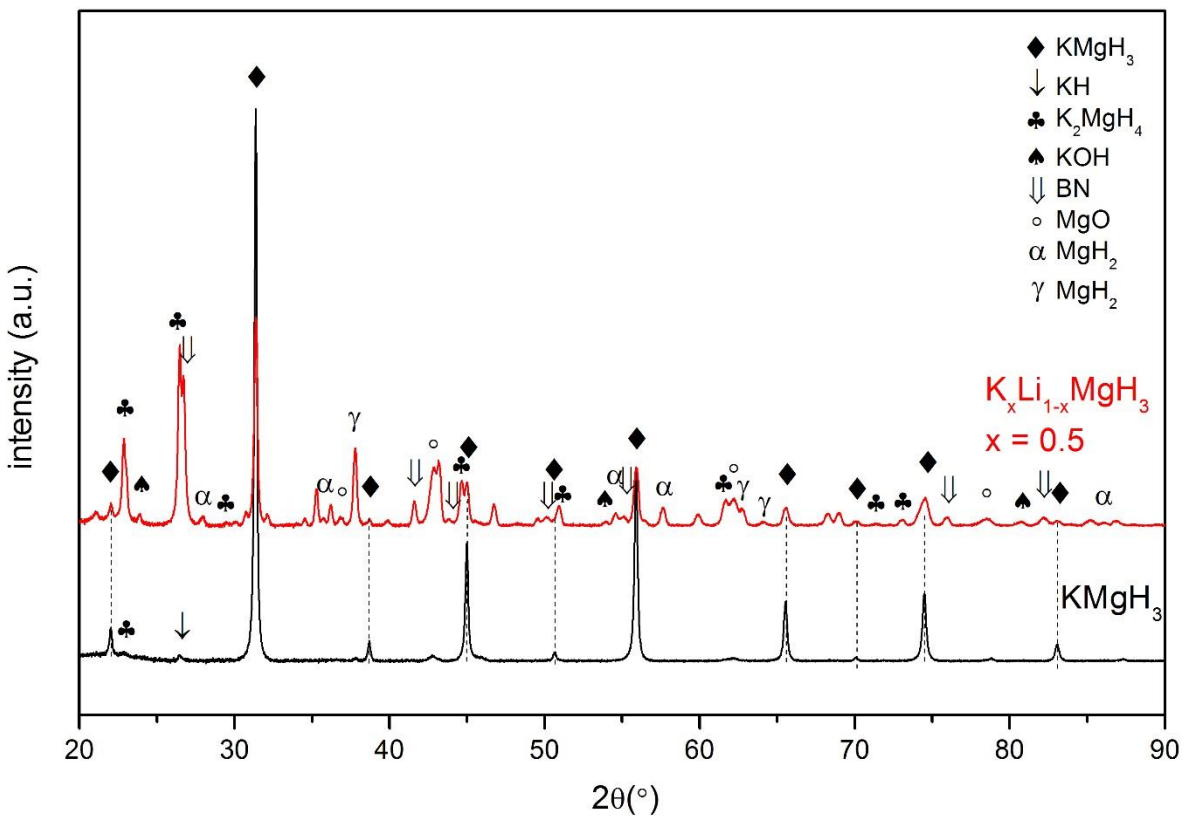

Figure 66. XRD pattern of $K_xLi_{1-x}MgH_3$, x = 0.5, compared to $KMgH_3$.

Appendix D. Oral presentations

The results obtained from this thesis were presented in various international conferences shown below:

Nunez JA, Goujon C, Colin C, Miraglia S, Laversenne L, High-Pressure and High-Temperature Synthesis of $Na_{1-x}Li_xMgH_3$ (x = 0, 0.2, 1.0) for Hydrogen Storage, *First plenary meeting of the FRH2, 31/05 – 04/06, 2021*

Nunez JA, Goujon C, Colin C, Miraglia S, Laversenne L, Synthesis of $Na_{1-x}Li_xMgH_3$ (x = 0, 0.2, 1.0) at Extreme Conditions for Hydrogen Storage Applications, *Conference on Science at Extreme Conditions (CSEC 2021), 25/07 – 30/07, 2021*

Nunez JA, Goujon C, Colin C, Miraglia S, Laversenne L, Neutron Diffraction Study of $NaMgD_3$ at High Pressure, *Journées de la Diffusion Neutronique (JDN 2021), 20/09 – 22/09, 2021*

Nunez JA, Goujon C, Colin C, Miraglia S, Laversenne L, Pressure-induced phase transformation study of $NaMgD_3$ by Neutron Diffraction for Hydrogen Storage Applications, *Philippine Chemistry Congress (PCC 2021), 20/09 – 24/09, 2021*

References:

International Energy Agency (IEA). Global Energy CO_2 Status Report; IEA Publications: Paris, France, 2019

[1] Sheina S G, Pirozhnikova A P and Priss E A 2019 The concept of sustainable development of renewable energy in the modern world *IOP Conf. Ser. Mater. Sci. Eng.* **698**

[2] Erixno O, Rahim N A, Ramadhani F and Adzman N N 2022 Energy management of renewable energy-based combined heat and power systems: A review *Sustain. Energy Technol. Assessments* **51** 101944

[3] Howlader H O R, Adewuyi O B, Hong Y Y, Mandal P, Hemeida A M and Senjyu T 2019 Energy storage system analysis review for optimal unit commitment *Energies* **13** 1–21

[4] Mercure J F and Salas P 2013 On the global economic potentials and marginal costs of non-renewable resources and the price of energy commodities *Energy Policy* **63** 469–83

[5] Balat M 2008 Potential importance of hydrogen as a future solution to environmental and transportation problems *Int. J. Hydrogen Energy* **33** 4013–29

[6] Ajanovic A 2013 Renewable fuels - A comparative assessment from economic, energetic and ecological point-of-view up to 2050 in EU-countries *Renew. Energy* **60** 733–8

[7] Abe J O, Popoola A P I, Ajenifuja E and Popoola O M 2019 Hydrogen energy, economy and storage: Review and recommendation *Int. J. Hydrogen Energy* **44** 15072–86

[8] Züttel A 2004 Hydrogen storage methods *Naturwissenschaften* **91** 157–72

[9] Yang J, Sudik A, Wolverton C and Siegel D J 2010 High capacity hydrogen storage materials: Attributes for automotive applications and techniques for materials discovery *Chem. Soc. Rev.* **39** 656–75

[10] Ley M B, Jepsen L H, Lee Y S, Cho Y W, Bellosta Von Colbe J M, Dornheim M, Rokni M, Jensen J O, Sloth M, Filinchuk Y, Jørgensen J E, Besenbacher F and Jensen T R 2014 Complex hydrides for hydrogen storage - New perspectives *Mater. Today* **17** 122–8

[11] Zhang B and Wu Y 2017 Recent advances in improving performances of the

lightweight complex hydrides Li-Mg-N-H system *Prog. Nat. Sci. Mater. Int.* **27** 21–33

[12] Ren J, Musyoka N M, Langmi H W, Mathe M and Liao S 2017 Current research trends and perspectives on materials-based hydrogen storage solutions: A critical review *Int. J. Hydrogen Energy* **42** 289–311

[13] Irani R S 2002 H ydrogen Storage : High-Pressure Gas *Int. Organ.* 680–2

[14] Toureille A and Touchard G 2021 Problems due to an eventual using of hydrogen in the future *Int. J. Plasma Environ. Sci. Technol.* **15** 1–10

[15] Ahluwalia R K and Peng J K 2008 Dynamics of cryogenic hydrogen storage in insulated pressure vessels for automotive applications *Int. J. Hydrogen Energy* **33** 4622–33

[16] Jain I P, Jain P and Jain A 2010 Novel hydrogen storage materials: A review of lightweight complex hydridespuye *J. Alloys Compd.* **503** 303–39

[17] Hayes H F, Gibb T K P, Libowitz B G G, Hayes F and Gibb T R P 1958 The System of Zirconium-Nickel and Hydrogen **62** 76–9

[18] Wang H, Lin H J, Cai W T, Ouyang L Z and Zhu M 2016 Tuning kinetics and thermodynamics of hydrogen storage in light metal element based systems - A review of recent progress *J. Alloys Compd.* **658** 280–300

[19] Tsukuda R, Yamagishi R, Kameoka S, Nishimura C and Tsai A P 2019 Ability of hydrogen storage CeNi5-xGax and Mg2Ni alloys to hydrogenate acetylene *Sci. Technol. Adv. Mater.* **20** 774–85

[20] Han S A, Sohn A and Kim S W 2017 Recent advanced in energy harvesting and storage applications with two-dimensional layered materials *FlatChem* **6** 37–47

[21] Gao S, Wang X, Liu H, He T, Wang Y, Li S and Yan M 2019 Effects of nano-composites (FeB, FeB/CNTs) on hydrogen storage properties of MgH2 *J. Power Sources* **438** 227006

[22] Alhameedi K, Hussain T, Bae H, Jayatilaka D, Lee H and Karton A 2019 Reversible hydrogen storage properties of defect-engineered C4N nanosheets under ambient conditions *Carbon N. Y.* **152** 344–53

[23] Ma Z, Zou J, Khan D, Zhu W, Hu C, Zeng X and Ding W 2019 Preparation and hydrogen storage properties of MgH2-trimesic acid-TM MOF (TM=Co, Fe) composites *J. Mater. Sci. Technol.* **35** 2132–43

[24] Luo Q, Li J, Li B, Liu B, Shao H and Li Q 2019 Kinetics in Mg-based hydrogen storage materials: Enhancement and mechanism *J. Magnes. Alloy.* **7** 58–71

[25] Nurul N Z, Yaakob Z, Lim K L and Timmiati S N 2016 The kinetics of lightweight

solid-state hydrogen storage materials: A review *Int. J. Hydrogen Energy* **41** 13131–51

[26] Matar S F 2010 Intermetallic hydrides: A review with ab initio aspects *Prog. Solid State Chem.* **38** 1–37

[27] Hall F P 1926 Palladium-hydrogen Equilibrium **451** 1207–19

[28] Switendick A C 1971 Metal Hydrides-Structure and Band Structure * *Int. J. Quantum Chem.* **470** 459–70

[29] Lieberman M L and Wahlbeck P G 1965 The thermodynamics of the scandium-hydrogen system *J. Phys. Chem.* **69** 3514–9

[30] Gibb T R P, McSharry J J and Bragdon R W 1951 The Titanium-Hydrogen System and Titanium Hydride. II. Studies at High Pressure *J. Am. Chem. Soc.* **73** 1751–5

[31] Buschow K H and Van Mal H H 1972 Phase relations and hydrogen absorption in the lanthanum-nickel system *J. Less-Common Met.* **29** 203–10

[32] Eberle U, Arnold G and Von Helmolt R 2006 Hydrogen storage in metal-hydrogen systems and their derivatives *J. Power Sources* **154** 456–60

[33] Bogdanović B and Schwickardi M 1997 Ti-doped alkali metal aluminium hydrides as potential novel reversible hydrogen storage materials *J. Alloys Compd.* **253–254** 1–9

[34] Broom D P and Hirscher M 2016 Irreproducibility in hydrogen storage material research *Energy Environ. Sci.* **9** 3368–80

[35] Hirscher M 2011 Hydrogen storage by cryoadsorption in ultrahigh-porosity metal-organic frameworks *Angew. Chemie - Int. Ed.* **50** 581–2

[36] Hossain A, Roy S and Sakthipandi K 2019 The external and internal influences on the tuning of the properties of perovskites: An overview *Ceram. Int.* **45** 4152–66

[37] Zaluska A, Zaluski L and Ström-Olsen J O 1999 Nanocrystalline magnesium for hydrogen storage *J. Alloys Compd.* **288** 217–25

[38] Jeon K J, Moon H R, Ruminski A M, Jiang B, Kisielowski C, Bardhan R and Urban J J 2011 Air-stable magnesium nanocomposites provide rapid and high-capacity hydrogen storage without using heavy-metal catalysts *Nat. Mater.* **10** 286–90

[39] Qu J, Sun B, Yang R, Zhao W, Wang Y and Li X 2010 Hydrogen absorption kinetics of Mg thin films under mild conditions *Scr. Mater.* **62** 317–20

[40] Chandler C D, Roger C and Hampden-Smith M J 1993 Chemical Aspects of Solution Routes to Perovskite-Phase Mixed-Metal Oxides from Metal-Organic Precursors *Chem. Rev.* **93** 1205–41

[41] Wu H, Zhou W, Udovic T J, Rush J J and Yildirim T 2008 Crystal chemistry of perovskite-type hydride NaMgH3: Implications for hydrogen storage *Chem. Mater.* **20**

2335–42

[42] Sato T, Noréus D, Takeshita H and Häussermann U 2005 Hydrides with the perovskite structure: General bonding and stability considerations and the new representative CaNiH3 *J. Solid State Chem.* **178** 3381–8

[43] Ikeda, K., Sato, T., Orimo S 2008 Perovskite-type hydrides - synthesis, structures and properties *Int. J. Mater. Res.* **99** 471–9

[44] Sato T, Takagi S, Deledda S, Hauback B C and Orimo S I 2016 Extending the applicability of the Goldschmidt tolerance factor to arbitrary ionic compounds *Sci. Rep.* **6** 1–10

[45] Wang Q, Chen Z, Chen Y, Cheng N and Hui Q 2012 Hydrogen storage in perovskite-type oxides ABO 3 for Ni/MH battery applications: A density functional investigation *Ind. Eng. Chem. Res.* **51** 11821–7

[46] Schouwink P, Ley M B, Tissot A, Hagemann H, Jensen T R, Smrčok ̛ubomír and Černý R 2014 Structure and properties of complex hydride perovskite materials *Nat. Commun.* **5** 1–10

[47] Ikeda K, Kato S, Shinzato Y, Okuda N, Nakamori Y, Kitano A, Yukawa H, Morinaga M and Orimo S 2007 Thermodynamical stability and electronic structure of a perovskite-type hydride, NaMgH3 *J. Alloys Compd.* **446**–**447** 162–5

[48] Ikeda K, Kogure Y, Nakamori Y and Orimo S 2007 Formation region and hydrogen storage abilities of perovskite-type hydrides *Prog. Solid State Chem.* **35** 329–37

[49] Vajeeston P, Ravindran P, Kjekshus A and Fjellvåg H 2008 First-principles investigations of the MMgH3 (M = Li, Na, K, Rb, Cs) series *J. Alloys Compd.* **450** 327–37

[50] Benlamari S, Bendjeddou H, Boulechfar R, Amara Korba S, Meradji H, Ahmed R, Ghemid S, Khenata R and Bin Omran S 2018 Structural, electronic, elastic, and thermal properties of CaNiH3 perovskite obtained from first-principles calculations *Chinese Phys. B* **27**

[51] Rehmat B, Rafiq M A, Javed Y, Irshad Z, Ahmed N and Mirza S M 2017 Elastic properties of perovskite-type hydrides LiBeH3 and NaBeH3 for hydrogen storage *Int. J. Hydrogen Energy* **42** 10038–46

[52] Reshak A H 2015 NaMgH3 a perovskite-type hydride as advanced hydrogen storage systems: Electronic structure features *Int. J. Hydrogen Energy* **40** 16383–90

[53] Ghebouli M A, Ghebouli B, Bouhemadou A, Fatmi M and Bin-Omran S 2011 Structural, elastic, electronic, optical and thermodynamic properties of KMgH3 *Solid*

State Sci. **13** 647–52

[54] Li Y, Chung J S and Kang S G 2019 First-Principles Computational Screening of Perovskite Hydrides for Hydrogen Release *ACS Comb. Sci.* **21** 736–42

[55] Orgaz E and Gupta M 1994 Electronic structure of lithium-based antiperovskite hydrides *J. Alloys Compd.* **209** 159–65

[56] Messer C E and Levy I S 1965 Systems of Lithium Hydride with Alkaline Earth and Rare Earth Hydrides *Inorg. Chem.* **4** 543–8

[57] Narayan R and Ramaseshan S 1978 Repulsion Parameters of Ions and Radicals - Application to Perovskite Structures *J. Phys. Chem. Solids* **39** 1287–94

[58] Cantrell J S, Beiter T A, Souers P C and Barry P 1991 Crystallographic studies of compounds from the LiH + BeH2 system *J. Less-Common Met.* **172–174** 213–9

[59] Maienschein J L, Bowers J S, Beiter T A and Cantrell J S 1993 Reactions of lithium hydride and beryllium hydride: thermal studies and identification of products *J. Alloys Compd.* **196** 1–5

[60] Komiya K, Morisaku N, Rong R, Takahashi Y, Shinzato Y, Yukawa H and Morinaga M 2008 Synthesis and decomposition of perovskite-type hydrides, MMgH3 (M = Na, K, Rb) *J. Alloys Compd.* **453** 157–60

[61] Schumacher R and Weiss A 1990 KMgH3 single crystals by synthesis from the elements *J. Less-Common Met.* **163** 179–83

[62] Renaudin G, Bertheville B and Yvon K 2003 Synthesis and structure of an orthorhombic low-pressure polymorph of caesium magnesium hydride, CsMgH3 *J. Alloys Compd.* **353** 175–9

[63] Bertheville B, Fischer P and Yvon K 2002 B. Bertheville , P. Fischer , K. Yvon *J. Alloys Compd.* **330–332** 152–6

[64] Gingl F, Vogt T, Akiba E and Yvon K 1999 Cubic CsCaH3 and hexagonal RbMgH3: New examples of fluoride-related perovskite-type hydrides *J. Alloys Compd.* **282** 125–9

[65] Wu H, Zhou W, Udovic T J, Rush J J and Yildirim T 2009 Crystal chemistry and dehydrogenation/rehydrogenation properties of perovskite hydrides RbMgH3 and RbCaH3 *J. Phys. Chem. C* **113** 15091–8

[66] Mamontov E, Kolesnikov A I, Sampath S and Yarger J L 2017 Hydrogen mobility in the lightest reversible metal hydride, LiBeH3 *Sci. Rep.* **7** 1–7

[67] Wang Z Z, Wang Y F, Tang B Y, Zeng X Q and Ding W J 2008 Theoretical study of the CsMgH3, Cs2MgH4 and Cs4Mg3H10 complex hydrides from first-principles

Phys. Status Solidi Basic Res. **245** 2749–55

[68] Rönnebro E, Noréus D, Kadir K, Reiser A and Bogdanovic B 2000 Investigation of the perovskite related structures of NaMgH3, NaMgF3 and Na3AlH6 *J. Alloys Compd.* **299** 101–6

[69] Pottmaier D, Pinatel E R, Vitillo J G, Garroni S, Orlova M, Baró M D, Vaughan G B M, Fichtner M, Lohstroh W and Baricco M 2011 Structure and thermodynamic properties of the NaMgH3 perovskite: A comprehensive study *Chem. Mater.* **23** 2317–26

[70] Bouhadda Y, Bououdina M, Fenineche N and Boudouma Y 2013 Elastic properties of perovskite-type hydride NaMgH3 for hydrogen storage *Int. J. Hydrogen Energy* **38** 1484–9

[71] Martínez-Coronado R, Sánchez-Benítez J, Retuerto M, Fernández-Díaz M T and Alonso J A 2012 High-pressure synthesis of Na 1-xLi xMgH 3 perovskite hydrides *J. Alloys Compd.* **522** 101–5

[72] Fornari M, Subedi A and Singh D J 2007 Structure and dynamics of perovskite hydrides AMg H3 (A=Na, K, Rb) in relation to the corresponding fluorides: A first-principles study *Phys. Rev. B - Condens. Matter Mater. Phys.* **76** 1–7

[73] Noritake T, Aoki M, Towata S, Seno Y, Hirose Y, Nishibori E, Takata M and Sakata M 2002 Chemical bonding of hydrogen in MgH2 *Appl. Phys. Lett.* **81** 2008–10

[74] Bouhadda Y, Boudouma Y, Fennineche N E and Bentabet A 2010 Ab initio calculations study of the electronic, optical and thermodynamic properties of NaMgH3, for hydrogen storage *J. Phys. Chem. Solids* **71** 1264–8

[75] Bouamrane A, Laval J P, Soulie J P and Bastide J P 2000 Structural characterization of NaMgH2F and NaMgH3 *Mater. Res. Bull.* **35** 545–9

[76] Klaveness A, Swang O and Fjellvag H 2006 Formation enthalpies of NaMgH3 and KMgH3: A computational study *Europhys. Lett.* **76** 285–90

[77] Sheppard D A, Paskevicius M and Buckley C E 2011 Thermodynamics of hydrogen desorption from NaMgH3 and its application as a solar heat storage medium *Chem. Mater.* **23** 4298–300

[78] Pottmaier D, Pistidda C, Groppo E, Bordiga S, Spoto G, Dornheim M and Baricco M 2011 Dehydrogenation reactions of 2NaBH4 + MgH2 system *Int. J. Hydrogen Energy* **36** 7891–6

[79] Retuerto M, Sánchez-Benítez J, Rodríguez-Cañas E, Serafini D and Alonso J A 2010 High-pressure synthesis of Mg2FeH6 complex hydride *Int. J. Hydrogen Energy* **35**

7835–41

[80] Andrada-Chacón A, Alonso J A, Pomjakushin V and Sánchez-Benítez J 2017 High-pressure synthesis and structural characterization of Na1-xKxMgH3 perovskite hydrides *J. Alloys Compd.* **729** 914–20

[81] Ikeda K, Kogure Y, Nakamori Y and Orimo S 2005 Reversible hydriding and dehydriding reactions of perovskite-type hydride NaMgH3 *Scr. Mater.* **53** 319–22

[82] Wang Z, Tao S, Deng J, Zhou H and Yao Q 2017 ScienceDirect Significant improvement in the dehydriding properties of perovskite hydrides , NaMgH 3 , by doping with K 2 TiF 6 *Int. J. Hydrogen Energy* **42** 8554–9

[83] Hao S and Sholl D S 2009 Selection of dopants to enhance hydrogen diffusion rates in MgH2 and NaMgH3 *Appl. Phys. Lett.* **94** 1–4

[84] Chaudhary A, Paskevicius M, Sheppard D A and Buckley C E 2015 Thermodynamic destabilisation of MgH 2 and NaMgH 3 using Group IV elements Si , Ge or Sn *J. Alloys Compd.* **623** 109–16

[85] Wang Z, Tao S, Li J, Deng J, Zhou H and Yao Q 2017 The Improvement of Dehydriding the Kinetics of NaMgH3 Hydride via Doping with Carbon Nanomaterials *Metals (Basel).* **7** 1–10

[86] Li Y, Zhang L, Zhang Q, Fang F, Sun D, Li K, Wang H, Ouyang L and Zhu M 2014 In situ embedding of Mg2NiH4 and YH3 nanoparticles into bimetallic hydride NaMgH3 to inhibit phase segregation for enhanced hydrogen storage *J. Phys. Chem. C* **118** 23635–44

[87] Hang Z, Hu Z, Xiao X, Jiang R and Zhang M 2021 Enhancing hydrogen storage kinetics and cycling properties of namgh3 by 2d transition metal carbide mxene ti3c2 *Processes* **9** 1–13

[88] Abdellaoui M, Lakhal M, Benzidi H, Garara M, Benyoussef A, El Kenz A, Mounkachi O, Loulidi M and Ez-Zahraouy H 2019 Enhancing of hydrogen storage properties of perovskite-type MgNiH3 by introducing cobalt dopant (MgCoxNi1−xH3) using first-principle calculations *Appl. Phys. A Mater. Sci. Process.* **125** 1–8

[89] Wang Z M, Li J J, Tao S, Deng J Q, Zhou H and Yao Q 2016 Structure, thermal analysis and dehydriding kinetic properties of Na1-xLixMgH3 hydrides *J. Alloys Compd.* **660** 402–6

[90] Kissinger H E 1957 Reaction Kinetics in Differential Thermal Analysis *Anal. Chem.* **29** 1702–6

[91] Tao S, Wang Z min, Wan Z zhen, Deng J qiu, Zhou H and Yao Q 2017 Enhancing the dehydriding properties of perovskite-type NaMgH3 by introducing potassium as dopant *Int. J. Hydrogen Energy* **42** 3716–22

[92] Ikeda K, Nakamori Y and Orimo S 2005 Formation ability of the perovskite-type structure in LixNa 1 - XMgH3 (x = 0, 0.5 and 1.0) *Acta Mater.* **53** 3453–7

[93] Contreras Vasquez L F, Liu Y, Paterakis C, Reed D and Book D 2017 Hydrogen sorption properties of LixNa1−xMgH3 (x = 0, 0.2, 0.5 & 0.8) *Int. J. Hydrogen Energy* **42** 22589–97

[94] Karfaf S, Bennecer B, Uur G and Uur 2019 Phase transitions and lattice dynamics in perovskite-type hydride LixNa1-xMgH3 *J. Phys. Condens. Matter* **31**

[95] Xiao X B, Tang B Y, Liao S Q, Peng L M and Ding W jiang 2009 Thermodynamic and electronic properties of quaternary hydrides LixNa1-xMgH3 *J. Alloys Compd.* **474** 522–6

[96] Alapati S V., Johnson J K and Sholl D S 2006 Identification of destabilized metal hydrides for hydrogen storage using first principles calculations *J. Phys. Chem. B* **110** 8769–76

[97] E.C. Ashby, R. Kovar R A 1970 Preparation of Potassium Trihydridomagnesiate, KMgH3 *J. Am. Chem. Soc.* **92** 2182–3

[98] H.H. Park, M. Pezat, B. Darriet P H 1987 The KH-MgH2 system *Rev. Chim. minérale* **24** 525–30

[99] Balawender R., Gupta M., Orgaz E. K L 1995 Electronic structure of KMgH3 , KMgH2F , KMgF3 with the perovskite structure *Acta Phys. Pol. A* **88** 1133–41

[100] Bastide J P, Bouamrane A, Claudy P and Létoffé J M 1987 Elaboration d'hydrures doubles de magnesium et de potassium par réaction entre solides *J. Less-Common Met.* **136**

[101] Reshak A H, Shalaginov M Y, Saeed Y, Kityk I V. and Auluck S 2011 First-principles calculations of structural, elastic, electronic, and optical properties of perovskite-type KMgH3 crystals: Novel hydrogen storage material *J. Phys. Chem. B* **115** 2836–41

[102] Kunkel N, Meijerink A, Springborg M and Kohlmann H 2014 Eu(ii) luminescence in the perovskite host lattices KMgH3, NaMgH3 and mixed crystals LiBaxSr1-xH 3 *J. Mater. Chem. C* **2** 4799–804

[103] Wang H, Zhang J, Liu J W, Ouyang L Z and Zhu M 2013 Improving hydrogen storage properties of MgH2 by addition of alkali hydroxides *Int. J. Hydrogen Energy*

38 10932–8

[104] Leng H, Miao N and Li Q 2020 Improved hydrogen storage properties of MgH2 by the addition of KOH and graphene *Int. J. Hydrogen Energy* **45** 28183–9

[105] Zhang H, Qi J and Ji Z 2019 Synergic improvement on thermal dehydrogenation of the LaH3-MgH2-KBH4 system *Chem. Phys. Lett.* **714** 111–3

[106] Ueda J, Wylezich T, Kunkel N and Tanabe S 2020 Red luminescent Eu2+ in K2MgH4 and comparison with KMgH3 *J. Mater. Chem. C* **8** 5124–30

[107] Bertheville B, Herrmannsdörfer T and Yvon K 2001 Structure data for K2MgH4 and Rb2CaH4 and comparison with hydride and fluoride analogues *J. Alloys Compd.* **325** L13–6

[108] Bouamrane A 1990 Enthalpies Standard de Formation des Composés à Structure Perovskite KMgH3, KMgH2F , KMgHF2, KMgF3 et K 2MgF4 *Thermochim. Acta* **159** 153–62

[109] Klaveness A, Fjellvåg H, Kjekshus A, Ravindran P and Swang O 2009 A semi-empirical approach to accurate standard enthalpies of formation for solid hydrides *J. Alloys Compd.* **469** 617–22

[110] Bouhadda Y, Kheloufi N, Bentabet A, Boudouma Y, Fenineche N and Benyalloul K 2011 Thermodynamic functions from lattice dynamic of KMgH3 for hydrogen storage applications *J. Alloys Compd.* **509** 8994–8

[111] Gupta M and Percheron-Guegan A 1988 Electronic Properties of Light Intermetallic Hydrides: KMgH3 and Lithium Beryllium Hydrides *Chem. Scr.* **28** 117–21

[112] Li Y, Mi Y, Chung J S and Kang S G 2018 First-principles studies of K1−xMxMgH3 (M = Li, Na, Rb, or Cs) perovskite hydrides for hydrogen storage *Int. J. Hydrogen Energy* **3** 2232–6

[113] Ogitsu T, Schwegler E, Gygi F and Galli G 2003 Melting of lithium hydride under pressure *Phys. Rev. Lett.* **91** 1–4

[114] Loubeyre P and Le Toullec R 1998 Equation of state of and from x-ray diffraction to 94 GPa *Phys. Rev. B - Condens. Matter Mater. Phys.* **57** 10403–6

[115] Li-Na Wu, Shao-Yi Wu, Fei-Hu Liu Q Z 2020 Studies of the Electronic, Optical, and Thermodynamic Properties for Metal-Doped LiH Crystals by First Principle Calculations *De Gruyter* **75** 575–86

[116] Priyanga G S, Meenaatci A T A, Palanichamy R R and Iyakutti K 2014 Structural, electronic and elastic properties of alkali hydrides (MH: M = Li, Na, K, Rb, Cs): Ab initio study *Comput. Mater. Sci.* **84** 206–16

[117] Chen Y M, Chen X R, Wu Q, Geng H Y, Yan X Z, Wang Y X and Wang Z W 2016 Compression and phase diagram of lithium hydrides at elevated pressures and temperatures by first-principles calculation *J. Phys. D. Appl. Phys.* **49** 1–10

[118] Humphries T D, Rawal A, Rowles M R, Prause C R, Bird J E, Paskevicius M, Sofianos M V and Buckley C E 2020 Physicochemical Characterization of a Na-H-F Thermal Battery Material *J. Phys. Chem. C* **124** 5053–60

[119] Thakre V and Singh S 2018 Structural properties of some alkali metal hydrides at high temperature and pressure *Acta Phys. Pol. A* **133** 186–93

[120] Humphries T D, Sheppard D A, Rowles M R, Sofianos M V. and Buckley C E 2016 Fluoride substitution in sodium hydride for thermal energy storage applications *J. Mater. Chem. A* **4** 12170–8

[121] Duclos S J, Vohra Y K, Ruoff A L, Filipek S and Baranowski B 1987 High-pressure studies of NaH to 54 GPa *Phys. Rev. B* **36** 7664–7

[122] Pal P, Jain A, Miyaoka H, Kojima Y and Ichikawa T 2020 Eutectic melting in x(2LiBH4-MgH2) hydrogen storage system by the addition of KH *Int. J. Hydrogen Energy* **45** 17000–5

[123] Thakre V and Singh S 2012 Structural analysis of KH at high temperature and pressure *AIP Conf. Proc.* **1447** 97–8

[124] Parry G and Pulham R 1975 Reaction of Hydrogen with Liquid Potassium *J. Chem. Soc. Dalt. Trans.* 446–8

[125] Hochheimer H D, Strössner K and Hönle W 1985 High Pressure X-Ray Investigation *Zeitschrift Phys. Chem.* **143** 139–44

[126] Gou Q, Pei C and Wang X 1993 Theoretical calculation for the equations of state and phase transitions of sodium and potassium hydrides *High Press. Res.* **11** 299–307

[127] Vajeeston P, Ravindran P, Kjekshus A and Fjellvåg H 2002 Pressure-Induced Structural Transitions in MgH2 *Phys. Rev. Lett.* **89** 1–4

[128] Edalati K, Kitabayashi K, Ikeda Y, Matsuda J, Li H W, Tanaka I, Akiba E and Horita Z 2018 Bulk nanocrystalline gamma magnesium hydride with low dehydrogenation temperature stabilized by plastic straining via high-pressure torsion *Scr. Mater.* **157** 54–7

[129] Moriwaki T, Akahama Y, Kawamura H, Nakano S and Takemura K 2006 Structural phase transition of rutile-type MgH2 at high pressures *J. Phys. Soc. Japan* **75** 2–7

[130] Vajeeston P, Ravindran P, Hauback B C, Fjellvåg H, Kjekshus A, Furuseth S and Hanfland M 2006 Structural stability and pressure-induced phase transitions in MgH2

Phys. Rev. B - Condens. Matter Mater. Phys. **73** 1–8

[131] Benyelloul K, Seddik L, Bouhadda Y, Bououdina M, Aourag H and Khodja K 2017 Effect of pressure on structural, elastic and mechanical properties of transition metal hydrides Mg7TMH16 (TM = Sc, Ti, V, Y, Zr and Nb): First-principles investigation *J. Phys. Chem. Solids* **111** 229–37

[132] Kumar E M, Rajkamal A and Thapa R 2017 Screening based approach and dehydrogenation kinetics for MgH2: Guide to find suitable dopant using first-principles approach *Sci. Rep.* **7** 1–11

[133] Li B, Li Y, Yang K, Cui Q, Ma Y and Zou G 2007 Raman evidence of a new high-pressure phase in calcium hydride *J. Phys. Condens. Matter* **19**

[134] Balakrishnan S, Sofianos M V, Paskevicius M, Rowles M R and Buckley C E 2020 Destabilized Calcium Hydride as a Promising High-Temperature Thermal Battery *J. Phys. Chem. C* **124** 17512–9

[135] Djellab S, Bouhadda Y, Bououdina M, Fenineche N and Boudouma Y 2016 Structural, Electronic and Elastic Properties of MgH2, CaH2 and Ca4Mg3H14 for Hydrogen Storage Materials *J. Electron. Mater.* **45** 3935–42

[136] Crivello J C, Dam B, Denys R V., Dornheim M, Grant D M, Huot J, Jensen T R, de Jongh P, Latroche M, Milanese C, Milčius D, Walker G S, Webb C J, Zlotea C and Yartys V A 2016 Review of magnesium hydride-based materials: development and optimisation *Appl. Phys. A Mater. Sci. Process.* **122** 1–20

[137] Bastide J P, Bonnetot B, Letoffe J M and Claudy P 1980 Polymorphisme de l'hydrure de Magnesium sous haute pression *Mat.Res.Bull.* **15** 1215–24

[138] El-Eskandarany M S, Shaban E and Al-Halaili B 2014 Nanocrystalline β-γ-β cyclic phase transformation in reacted ball milled MgH2 powders *Int. J. Hydrogen Energy* **39** 12727–40

[139] Kohlmann H, Zhao Y, Nicol M F and McClure J 2008 The crystal structure of α-MgD2 under high pressure by neutron powder diffraction *Zeitschrift fur Krist.* **223** 706–10

[140] Cui S, Feng W, Hu H, Feng Z and Wang Y 2008 Structural phase transitions in MgH2 under high pressure *Solid State Commun.* **148** 403–5

[141] El-Eskandarany M S, Banyan M and Al-Ajmi F 2018 Discovering a new MgH2 metastable phase *RSC Adv.* **8** 32003–8

[142] Moser D, Baldissin G, Bull D J, Riley D J, Morrison I, Ross D K, Oates W A and Noréus D 2011 The pressure-temperature phase diagram of MgH2 and isotopic

substitution *J. Phys. Condens. Matter* **23** 1–9

[143] Durandurdu M 2014 New high-pressure phase of MgH2: An ab initio constant-pressure study *Epl* **105** 1–6

[144] Bortz M, Bertheville B, Böttger G and Yvon K 1999 Structure of the high pressure phase λ-MgH2 by neutron powder diffraction *J. Alloys Compd.* **287** 4–6

[145] Goto, Y. Kakuta, H. Kamegawa, A. Takamura ,H. Okada M 2001 Synthesis of New Hydrides with Cubic Structures in Mg-Ca-Ni Systems by Using High Pressure *Mater. Trans.* **42** 1850–3

[146] Moser D, Bull D J, Cowpe J S, Roach D L, Ross D K, Noreus D and Tucker M G 2010 An in situ neutron diffraction measurement of the pressure-temperature evolution of a MgD2:TiD2 mixture *High Press. Res.* **30** 643–52

[147] Bastide J, Bonnetot B, Jean-marie L, Claudy P, Min L D P and Thermochimie L De 1980 (Received October 7 , 1980 ; R e f e r e e d) *Magnesium* **15** 1779–87

[148] Emilsson M, Araújo C M and Ahuja R 2006 Hydrogen desorption in high pressure phases of MgH2: A density functional theory based study *AIP Conf. Proc.* **837** 168–72

[149] Zhang J, Zhao Y, Wang Y and Daemen L 2008 Thermal equations of state and melting of lithium deuteride under high pressure *J. Appl. Phys.* **103**

[150] Peterson D T and Fattore V G 1961 Calcium-calcium hydride phase system *J. Phys. Chem.* **65** 2062–4

[151] Peterson D T and Indig M 1960 The Barium-Barium Hydride Phase System *J. Am. Chem. Soc.* **82** 5645–6

[152] Li Y, Li B, Cui T, Li Y, Zhang L, Ma Y and Zou G 2008 High-pressure phase transformations in CaH2 *J. Phys. Condens. Matter* **20**

[153] Tse J S, Klug D D, Desgreniers S, Smith J S, Flacau R, Liu Z, Hu J, Chen N and Jiang D T 2007 Structural phase transition in Ca H2 at high pressures *Phys. Rev. B - Condens. Matter Mater. Phys.* **75** 1–5

[154] Phelan W A, Zahn J, Kennedy Z and McQueen T M 2019 Pushing boundaries: High pressure, supercritical optical floating zone materials discovery *J. Solid State Chem.* **270** 705–9

[155] Kataoka R, Goto Y, Kamegawa A, Takamura H and Okada M 2007 High-pressure synthesis of novel hydride in Mg-Ni-H and Mg-Ni-Cu-H systems *J. Alloys Compd.* **446–447** 142–6

[156] Gibbons C S, Reinsborough V C and Whitla W A 1975 Crystal Structures of K 2 MgCl 4 and Cs 2 MgCl 4 *Can. J. Chem.* **53** 114–8

[157] Sato T, Kyoi D, Rönnebro E, Kitamura N, Sakai T and Noréus D 2006 Structural investigations of two new ternary magnesium-niobium hydrides, Mg6.5NbH∼14 and MgNb2H∼4 *J. Alloys Compd.* **417** 230–4

[158] Demazeau G 1987 New Problems in Solid-State Chemistry Solved By High Pressure Conditions: an Exciting Perspective for Preparing New Materials. *Chem. Scr.* **28** 21–4

[159] Demazeau G 2002 High pressure in solid-state chemistry *J. Phys. Condens. Matter* **14** 11031–5

[160] Zhang L, Wang Y, Lv J and Ma Y 2017 Materials discovery at high pressures *Nat. Rev. Mater.* **2**

[161] Manjón F J, Tresserras J A S, Ibáñez J and Pereira A L J 2019 *Pressure-induced phase transitions in sesquioxides* vol 9

[162] Wang H, Tse J S, Tanaka K, Iitaka T and Ma Y 2012 Superconductive sodalite-like clathrate calcium hydride at high pressures *Proc. Natl. Acad. Sci. U. S. A.* **109** 6463–6

[163] Struzhkin V V., Kim D Y, Stavrou E, Muramatsu T, Mao H K, Pickard C J, Needs R J, Prakapenka V B and Goncharov A F 2016 Synthesis of sodium polyhydrides at high pressures *Nat. Commun.* **7** 1–8

[164] Parker L J and Atou T 1998 Pressure Synthesis of Alkali Metal-Transition Mewl Compounds Department of Chemistry , Pennsylvania State University , University Park , PA 16802 , USA *Rev. High Press. Sci. Technol.* **7** 1049–53

[165] Kusadome Y, Ikeda K, Nakamori Y, Orimo S and Horita Z 2007 Hydrogen storage capability of MgNi2 processed by high pressure torsion *Scr. Mater.* **57** 751–3

[166] Reilly J J and Wiswall R H 1968 The Reaction of Hydrogen with Alloys of Magnesium and Nickel and the Formation of Mg2NiH4 *Inorg. Chem.* **7** 2254–6

[167] Yartys V A, Antonov V E, Beskrovnyy A I, Crivello J C, Denys R V., Fedotov V K, Gupta M, Kulakov V I, Kuzovnikov M A, Latroche M, Morozov Y G, Sheverev S G and Tarasov B P 2015 Hydrogen-assisted phase transition in a trihydride MgNi2H3 synthesized at high H2 pressures: Thermodynamics, crystallographic and electronic structures *Acta Mater.* **82** 316–27

[168] Kozlenko D P, Dubrovinsky L S, Kichanov S E, Lukin E V., Cerantola V, Chumakov A I and Savenko B N 2019 Magnetic and electronic properties of magnetite across the high pressure anomaly *Sci. Rep.* **9** 1–9

[169] Monteseguro V, Sans J A, Cuartero V, Cova F, Abrikosov I A, Olovsson W, Popescu C, Pascarelli S, Garbarino G, Jönsson H J M, Irifune T and Errandonea D 2019 Phase stability and electronic structure of iridium metal at the megabar range *Sci. Rep.* **9** 1–9

[170] Walsh J P S and Freedman D E 2018 High-Pressure Synthesis: A New Frontier in the Search for Next-Generation Intermetallic Compounds *Acc. Chem. Res.* **51** 1315–23

[171] Chen B, Lin J F, Chen J, Zhang H and Zeng Q 2016 Synchrotron-based high-pressure research in materials science *MRS Bull.* **41** 473–8

[172] Huppertz H 2004 Multianvil high-pressure/high-temperature synthesis in solid state chemistry *Zeitschrift fur Krist.* **219** 330–8

[173] Jaffe A, Lin Y and Karunadasa H I 2017 Halide Perovskites under Pressure: Accessing New Properties through Lattice Compression *ACS Energy Lett.* **2** 1549–55

[174] Zhang L, Zeng Q and Wang K 2017 Pressure-Induced Structural and Optical Properties of Inorganic Halide Perovskite CsPbBr3 *J. Phys. Chem. Lett.* **8** 3752–8

[175] Jaffe A, Lin Y, Mao W L and Karunadasa H I 2015 Pressure-induced conductivity and yellow-to-black piezochromism in a layered Cu-Cl hybrid perovskite *J. Am. Chem. Soc.* **137** 1673–8

[176] Gainza J, Serrano-Sánchez F, Rodrigues J E F S, Nemes N M, Martínez J L and Alonso J A 2021 Metastable materials accessed under moderate pressure conditions (P ≤ 3.5 gpa) in a piston-cylinder press *Materials (Basel).* **14**

[177] Shimura G, Shirako Y, Niwa K and Hasegawa M 2016 High-pressure synthesis and relationship between A-site ordering and local structure of multicomponent perovskites (Ln0.25Mn0.75)(Al0.25Ti0.75)O3, Ln=La, Pr, Nd, Sm, Gd, Tb, Dy, Y *J. Solid State Chem.* **242** 55–62

[178] Takagi S, Saitoh H, Endo N, Sato R, Ikeshoji T, Matsuo M, Miwa K, Aoki K and Orimo S I 2013 Density-functional study of perovskite-type hydride LiNiH3 and its synthesis: Mechanism for formation of metallic perovskite *Phys. Rev. B - Condens. Matter Mater. Phys.* **87** 1–6

[179] Kyoi D, Sakai T, Kitamura N, Ueda A and Tanase S 2008 Synthesis of FCC Mg-Zr and Mg-Hf hydrides using GPa hydrogen pressure method and their hydrogen-desorption properties *J. Alloys Compd.* **463** 311–6

[180] Torres B, Martínez-Lope M J, Alonso J A, Serafini D, Fernández-Díaz M T and Martínez-Coronado R 2013 Short communication: High-pressure synthesis and crystal structure of a novel Mg3CuHx ternary hydride *Int. J. Hydrogen Energy* **38** 15264–8

[181] Martínez-Coronado R, Retuerto M, Torres B, Martínez-Lope M J, Fernández-Díaz M T and Alonso J A 2013 High-pressure synthesis, crystal structure and cyclability of the Mg 2NiH4 hydride *Int. J. Hydrogen Energy* **38** 5738–45

[182] Goto Y, Kakuta H, Kamegawa A, Takamura H and Okada M 2005 High-pressure

synthesis of novel hydride in Mg-M systems (M = Li, Pd) *J. Alloys Compd.* **404–406** 448–52

[183] Kamegawa A, Goto Y, Kakuta H, Takamura H and Okada M 2006 High-pressure synthesis of novel hydrides in Mg-RE-H systems (RE = Y, La, Ce, Pr, Sm, Gd, Tb, Dy) *J. Alloys Compd.* **408–412** 284–7

[184] Takasaki T, Mukai T, Kitamura N, Tanase S and Sakai T 2010 High-pressure synthesis of novel hydrides Mg7-xAxTiH16-x (A = Li, Na, K; x = 0-1.0) and their reversible hydrogen storage properties *J. Alloys Compd.* **494** 439–45

[185] Rodgers J A, Williams A J and Attfield J P 2006 High-pressure / high-temperature synthesis of transition metal oxide perovskites *Zeitschrift fur Naturforsch. - Sect. B J. Chem. Sci.* **61** 1515–26

[186] Ayukawa S Y, Ikeda K, Kato M, Noji T, Orimo S I and Koike Y 2012 Synthesis and specific heat of CaPdH 3-δ with the perovskite structure *J. Phys. Soc. Japan* **81** 1–5

[187] Yagyu H, Kato M, Noji T and Koike Y 2013 Synthesis of perovskite-type hydrides APdH3 (A = Sr, Ba) by a new method using CaH2 as a H2-source *Phys. Procedia* **45** 109–12

[188] Wiedemann D, Heppke E M and Franz A 2019 And Yet It Moves: A High-Temperature Neutron Diffraction Study of Ion Diffusion in the Inverse Perovskites BaLiX3 (X = F, H, D) *Eur. J. Inorg. Chem.* **2019** 5085–8

[189] Greedan J E 1970 Synthesis and crystal growth of SrLiH3 and EuLiH3; Ternary hydrides with the perovskite structure *J. Cryst. Growth* **6** 119–24

[190] Cooper M J, Rouse K D and Sakata M 1981 An alternative to the Rietveld profile refinement method *Zeitschrift fur Krist. - New Cryst. Struct.* **157** 101–17

[191] Izumi F, Mitomo M and Bando Y 1984 Rietveld refinements for calcium and yttrium containing α-sialons *J. Mater. Sci.* **19** 3115–20

[192] Mccusker L B, Von Dreele R B, Cox D E, Louër D and Scardi P 1999 Rietveld refinement guidelines *J. Appl. Crystallogr.* **32** 36–50

[193] Le Godec Y, Dove M T, Redfern S A T, Tucker M G, Marshall W G, Syfosse G and Besson J M 2001 A new high P-T cell for neutron diffraction up to 7 GPa and 2000 K with measurement of temperature by neutron radiography *High Press. Res.* **21** 263–80

[194] Besson J M, Nelmes R J, Hamel G, Loveday J S, Weill G and Hull S 1992 Neutron powder diffraction above 10 GPa *Phys. B Phys. Condens. Matter* **180–181** 907–10

[195] Morard G, Mezouar M, Rey N, Poloni R, Merlen A, Le Floch S, Toulemonde P, Pascarelli S, San-Miguel A, Sanloup C and Fiquet G 2007 Optimization of Paris-

Edinburgh press cell assemblies for in situ monochromatic X-ray diffraction and X-ray absorption *High Press. Res.* **27** 223–33

[196] Godec Y L E, Hamel G and Hammouda T 2005 Compact multianvil device for in situ studies at high **25** 243–53

[197] Besson J M and Nelmes R J 1995 New developments in neutron-scattering methods under high pressure with the Paris-Edinburgh cells *Phys. B Phys. Condens. Matter* **213–214** 31–6

[198] Toulemonde P, Goujon C, Laversenne L, Bordet P, Bruyère R, Legendre M, Leynaud O, Prat A and Mezouar M 2014 High pressure and high temperature in situ X-ray diffraction studies in the Paris-Edinburgh cell using a laboratory X-ray source *High Press. Res.* **34** 167–75

[199] Brown J M 1999 The NaCl pressure standard *J. Appl. Phys.* **86** 5801–8

[200] Birch F 1986 Equation of state and thermodynamic parameters of NaCl to 300 kbar in the high-temperature domain *J. Geophys. Res.* **91** 4949

[201] Decker D L 1971 High-pressure equation of state for NaCl, KCl, and CsCl *J. Appl. Phys.* **42** 3239–44

[202] Anon Properties_Earth_Planetary_p327_Utsumi.pdf

[203] Saxena S K and Zhang J 1990 Thermochemical and pressure-volume-temperature systematics of data on solids, examples: Tungsten and MgO *Phys. Chem. Miner.* **17** 45–51

[204] Greeff C W, Boettger J C, Graf M J and Johnson J D 2006 Theoretical investigation of the Cu EOS standard *J. Phys. Chem. Solids* **67** 2033–40

[205] Pathak P D and Vasavada N G 1970 Thermal expansion of alkali halides and the law of corresponding states *J. Phys. C Solid State Phys.* **3** 77–9

[206] Shinzato Y, Yukawa H, Morinaga M, Baba T and Nakai H 2007 Energy density analysis of the chemical bond between atoms in perovskite-type hydrides *J. Alloys Compd.* **446–447** 96–100

[207] Katsura T and Tange Y 2019 A simple derivation of the Birch–Murnaghan equations of state (EOSs) and comparison with EOSs derived from other definitions of finite strain *Minerals* **9**

[208] Birch F 1978 Finite strain isotherm and velocities for single-crystal and polycrystalline NaCl at high pressures and 300°K *J. Geophys. Res.* **83** 1257

[209] Chihi T, Fatmi M and Ghebouli B 2017 Ab initio study of the structural stability, elastic, electronic and optical properties of NaMgHiFj [(i, j) = (3, 0), (2, 1), (1, 2), (0,

3)] compounds *Solid State Commun.* **261** 10–6

[210] Gupta M 1989 Review of Recent Theoretical Investigations of the Electronic Structure of Intermetallic Hydrides *Zeitschrift fur Phys. Chemie* **163** 517–20

[211] Berger C, Bucher E, Lammer J, Nader C and Sitte W 2021 Fundamental material property trends in the La0.8-xNdxCa0.2FeO3-δ series: crystal structure and thermal expansion *J. Mater. Sci.* **56** 10191–203

[212] Keskar M, Patkare G, Shafeeq M, Phatak R A and Kannan S 2021 Structural and thermal study of Sr(Th1-xUx)(PO4)2 compounds *J. Solid State Chem.* **300** 122228

[213] Angel R J, Gonzalez-Platas J and Alvaro M 2014 EosFit7c and a Fortran module (library) for equation of state calculations *Zeitschrift fur Krist.* **229** 405–19

[214] Salje E K H, Wruck B and Thomas H 1991 Order-parameter saturation and low-temperature extension of Landau theory *Zeitschrift für Phys. B Condens. Matter* **82** 399–404

[215] Duthil P 2014 Material properties at low temperature *CAS-CERN Accel. Sch. Supercond. Accel. - Proc.* 77–95

[216] Grochala W and Edwards P P 2004 Thermal decomposition of the non-interstitial hydrides for the storage and production of hydrogen *Chem. Rev.* **104** 1283–315

[217] Li Q, Lu Y, Luo Q, Yang X, Yang Y, Tan J, Dong Z, Dang J, Li J, Chen Y, Jiang B, Sun S and Pan F 2021 Thermodynamics and kinetics of hydriding and dehydriding reactions in Mg-based hydrogen storage materials *J. Magnes. Alloy.* **9** 1922–41

[218] Li D, Zhang T, Yang S, Tao Z and Chen J 2011 Ab initio investigation of structures, electronic and thermodynamic properties for Li-Mg-H ternary system *J. Alloys Compd.* **509** 8228–34

[219] Li Y, Rao B K, Mcmullen T, Jena P, Khowash P K and Virginia W 2000 Cluster calculations **44** 6030–6

[220] Pluengphon P, Tsuppayakorn-aek P, Sukmas W, Inceesungvorn B and Bovornratanaraks T 2021 Dynamical stabilization and H-vacancy diffusion kinetics of lightweight complex hydrides: Ab initio study for hydrogen storage improvement *Int. J. Hydrogen Energy* **46** 22591–8

[221] Peltzer Y B E L 2016 First principle predictions of new crystal structures for hydrogen reservoirs *Int. J. Hydrogen Energy* **41** 5682–7

[222] Heslop G E C and J A 1968 Some t-Butylmagnesium and Related Complexes. Reactions between Hydrides and Organomagnesium Compounds *J. Chem. Soc. A Inorganic, Phys. Theor.* 514–8

[223] Bouamrane A and Soulie J 2001 Standard enthalpies of formation of KCaH 3 À x F x with x ˆ 1 , 1 . 5 , 2 , 2 . 5 **375** 5–8

[224] Vajeeston P, Ravindran P and Fjellvåg H 2010 Structural investigation and thermodynamical properties of alkali calcium trihydrides *J. Chem. Phys.* **132**

[225] Sartori S, Léon A, Zabara O, Muller J, Fichtner M and Hauback B C 2009 Studies of mixed hydrides based on Mg and Ca by reactive ball milling *J. Alloys Compd.* **476** 639–43